

MODELING AND OPTIMIZATION OF ULTRASONIC LINEAR MOTORS

THÈSE N° 3665 (2006)

PRÉSENTÉE LE 10 NOVEMBRE 2006

À LA FACULTÉ DES SCIENCES ET TECHNIQUES DE L'INGÉNIEUR

Laboratoire d'actionneurs intégrés

PROGRAMME DOCTORAL EN SYSTÈMES DE PRODUCTION ET ROBOTIQUE

ÉCOLE POLYTECHNIQUE FÉDÉRALE DE LAUSANNE

POUR L'OBTENTION DU GRADE DE DOCTEUR ÈS SCIENCES

PAR

José FERNANDEZ LOPEZ

ingénieur électricien diplômé EPF
de nationalité espagnole

acceptée sur proposition du jury:

Prof. A. Billard, présidente du jury
Prof. Y. Perriard, directeur de thèse
Prof. H. Bleuler, rapporteur
Dr C. Péclat, rapporteur
Prof. B. Semail, rapporteur



ÉCOLE POLYTECHNIQUE
FÉDÉRALE DE LAUSANNE

Suisse
2006

ACKNOWLEDGEMENTS

This thesis is a result of my efforts as a research assistant between 2002 and 2006 at the Integrated Actuators Laboratory (LAI) of the Swiss Federal Institute of Technology (EPFL). During that time, I have been supported by various people to whom I wish to express my gratitude.

I am indebted to Prof. Y. Perriard; he offered me the possibility to work in a liberal environment and gave me the freedom to conduct my research in an independent way. Its advices, support and encouragements gave me the necessary motivation for the achievement of this thesis work.

I would also like to thank Prof. B. Semail, Prof. H. Bleuler and Dr C. Péclat for being my co-examiners and for the time they spent to read my work and for their constructive remarks.

Many people have contributed to this thesis, students as well as members of the LAI. All my gratitude for the many conversations, the ideas and the developments which contributed to the advance of my work.

Finally, I would like to thank my parents, who always supported me in my choices and who gave me the means of achieving my goals. And of course many thanks to my tender Marija, for the support and love she gave me throughout my work.

Lausanne, October 2006

José Fernandez

*If we know from where we come,
We know where we go.
If we do not honour our past,
We lose our future.*

Matteo Bullo & José Fernandez

TABLE OF CONTENTS

Abstract	xi
Résumé	xiii
List of Publications	xv
1. Introduction	1
1.1 Background and motivation	1
1.2 Objective and scope of the research	2
1.3 Thesis outline	3
2. Piezoelectric materials in devices	5
2.1 Introduction	5
2.2 Piezoelectric materials	6
2.2.1 Piezoelectric ceramic	6
2.2.2 Polarization	6
2.2.3 Soft <i>PZT</i> and hard <i>PZT</i> ceramics	8
2.2.4 Limitations in piezoelectric materials	10
2.2.5 Bonding <i>PZT</i> ceramics	10
2.2.6 Behavior of a <i>PZT</i> ceramic	11
2.3 Piezoelectric theory	12
2.3.1 Piezoelectric constants	12

2.3.2	Fundamental piezoelectric relations	16
2.3.3	Vibration modes	18
2.4	Applications	19
2.4.1	Introduction	19
2.4.2	Generators	21
2.4.3	Sensors	21
2.4.4	Transducers	22
2.4.5	Transformers	23
2.4.6	Actuators	24
2.5	Conclusion	25
3.	<i>Ultrasonic motors: state of the art</i>	26
3.1	Introduction	26
3.2	Historical background	27
3.3	Brief description of the operating principle	29
3.4	Classification of ultrasonic motors	30
3.4.1	Classification by excitation	30
3.4.2	Classification by motor function	36
3.5	Conclusion	49
4.	<i>Ultrasonic linear motors: modeling, simulation and validation</i>	51
4.1	Introduction	51
4.2	Theoretical modeling	52
4.2.1	Standing and traveling waves	52
4.2.2	Electric equivalent circuit	62
4.2.3	Numerical modeling using FEM	70

4.2.4	Simulations	75
4.3	Experimental results	79
4.3.1	Prototype	80
4.3.2	Measurements	80
4.4	Modeling validation	82
4.5	Conclusion	83
5.	<i>Sensitivity analysis and optimization</i>	85
5.1	Introduction	85
5.2	State of the art of optimization of piezoelectric actuators	86
5.3	Sensitivity analysis	87
5.3.1	Introduction	87
5.3.2	Design of experiments (DOE)	88
5.3.3	Sensitivity analysis methodology	90
5.3.4	Results	98
5.4	FE optimization	106
5.4.1	Introduction	106
5.4.2	Optimization tools	107
5.4.3	Results	109
5.5	Discussion and methodology validation	118
5.6	Application case: optimization of an ultrasonic linear motor for the auto-focus function of an optical system	119
5.6.1	Introduction	119
5.6.2	The MINISWYS Ultrasonic Motor (MUM)	120
5.6.3	Numerical modeling of the motor	126

5.6.4	Optimization	132
5.6.5	Methodology validation	142
5.7	Multi-objective optimization methods	147
5.7.1	Introduction	147
5.7.2	Traditional multi-objective optimization methods	147
5.7.3	Multi-objective evolutionary algorithms	148
5.7.4	Multi-objective genetic algorithms	151
5.8	Conclusion	152
6.	<i>Piezoelectric transformers: a new way to supply ultrasonic motors</i>	154
6.1	Introduction	154
6.2	Working principle of the piezoelectric transformers	155
6.2.1	Rosen type	155
6.2.2	Radial mode type	156
6.3	Analytical and numerical modeling	158
6.3.1	Introduction	158
6.3.2	Analytical modeling	158
6.3.3	Numerical modeling	163
6.4	Experimental results and validation	168
6.4.1	Introduction	168
6.4.2	Measurements	168
6.4.3	Comparison and validation	170
6.5	Applications	175
6.5.1	Introduction	175
6.5.2	Ultrasonic motors power supply	175

6.5.3	High voltage applications	177
6.5.4	Low voltage and high power applications	178
6.6	Conclusion	182
7.	Conclusion and perspectives	183
7.1	Overview	183
7.2	Main results and innovative contribution	184
7.3	Perspectives and future developments	186
	Bibliography	189
	List of Abbreviations	207
	List of Symbols	209
	List of Figures	215
	List of Tables	225
	Appendix	228
	Curriculum Vitae	281

ABSTRACT

Ultrasonic motors have received much attention these last years, in particular with regard to their modeling and their design principle. Their operating principle is based on piezoelectric ceramics that convert electrical energy into mechanical energy in the form of vibrations of an elastic body whose surface points perform an elliptic motion with a frequency in the ultrasonic range ($\geq 20kHz$). The moving part, which is pressed against the vibrating body by a prestressing force, can move thanks to the friction forces presented at the interface between the stator (resonator) and the rotor (slider).

Their specific properties make ultrasonic motors a very attractive solution for a direct transmission for different applications like precise positioning devices. Indeed, they present the possibility to obtain unlimited motions, high resolution and excellent dynamics of positioning. Then, it is obvious that ultrasonic motors could be used in new application fields, in particular to replace conventional electromagnetic motors. However, they have to overcome two principal difficulties: their efficiency is rather poor and they are often too expensive. Moreover, their use in the car industry or for the positioning of axes in machine tools for example requires driving forces and velocities higher than those which they currently present.

Analytical modeling of such motors is not obvious and assumptions that are made are often too restrictive. This is why the use of a numerical modeling (3-D) is necessary to model the behavior of this type of motors. Thus, finite element simulations are used but they often require high computing times. To avoid it, the number of simulations can be decreased by choosing the input parameters (dimensions, materials, boundary conditions,...) more judiciously according to

their influence on the output parameters. Thus, one can obtain the sensitivity of an input parameter on the value of the output parameter. With this intention, the application of design of experiments has been adopted in this thesis work. This methodology, applied to finite element simulations, is an innovative technique in the field of theoretical modeling of such motors. This methodology is particularly interesting in sight of predicting the results but also to find out an optimal set of input parameters for the motor. According to the results obtained and presented in this thesis work, the use of design of experiments in the field of ultrasonic motors modeling proves to be very promising and demonstrates to be a powerful tool. The application of the proposed methodology for the optimization of an ultrasonic linear motor used for the auto-focus function of the lens of an optical system also made it possible to show the validity and the potential of this optimization method.

Keywords: Ultrasonic linear motor, modeling, FEM simulations, design of experiments, sensitivity analysis, optimization, piezoelectric transformer.

RÉSUMÉ

Les moteurs ultrasoniques ont fait l'objet ces dernières années de beaucoup de recherches, notamment en ce qui concerne leur modélisation et leur dimensionnement. Leur principe de fonctionnement est basé sur la conversion d'une énergie électrique en une énergie mécanique de vibration par l'intermédiaire de l'effet piézoélectrique inverse. La plupart du temps, la partie vibrante est excitée de telle sorte que les points à la surface de celle-ci décrivent une trajectoire elliptique à une fréquence dite ultrasonique ($\geq 20\text{kHz}$). La partie mobile est pressée contre la partie vibrante à l'aide d'une force normale de telle sorte que grâce aux vibrations entretenues sur la partie vibrante, un déplacement continu (ou discontinu) de la partie mobile est obtenu à partir des forces de friction présentes dans la zone de contact.

Leurs différentes propriétés font des moteurs ultrasoniques une solution très attrayante pour une transmission directe pour différentes applications comme les dispositifs de positionnement précis car ils remplissent à la fois des conditions de course illimitée, de haute résolution et de dynamique de positionnement excellentes. Il est alors évident que les moteurs ultrasoniques pourraient être utilisés dans de nouveaux domaines d'application, notamment en remplacement des moteurs électromagnétiques conventionnels. Pour ce faire, ils doivent surmonter deux difficultés principales: leur rendement est assez faible et ils sont souvent trop chers. De plus, leur utilisation dans l'industrie automobile ou le positionnement d'axes pour des machines-outils par exemple exige des forces et des vitesses plus élevées que celles qu'ils présentent actuellement.

Leur modélisation analytique n'étant pas évidente et faisant appel à des hypothèses souvent trop restrictives, l'utilisation d'une modélisation numérique (3-

D) est nécessaire afin de modéliser le comportement de tels moteurs. Des simulations par éléments finis sont donc employées mais requièrent souvent beaucoup de temps de calcul. Pour éviter cela, le nombre des simulations peut être diminué en choisissant les paramètres d'entrée (dimensions, matériaux, bornes,...) plus judicieusement en fonction de leur influence sur les paramètres de sortie. On obtient ainsi la sensibilité d'un paramètre d'entrée sur la valeur du paramètre de sortie. C'est dans cette optique que l'application de la planification d'expériences a été adoptée dans ce travail de thèse. Cette méthodologie, appliquée aux simulations par éléments finis est innovatrice dans le domaine du dimensionnement de tels moteurs. Elle est particulièrement intéressante en vue de la prédiction des résultats mais également en vue de la détermination d'un jeu de paramètres optimal du moteur. D'après les résultats obtenus et présentés dans ce travail de thèse, l'utilisation des plans d'expériences dans ce domaine s'est révélée être très prometteuse et surtout être un outil puissant de dimensionnement. L'application de la méthodologie proposée pour l'optimisation de la course de l'objectif d'un système optique a également permis de démontrer la validité et le potentiel de cette méthode d'optimisation.

Mots-clés: Moteur ultrasonique linéaire, modélisation, simulations par éléments finis, planification d'expériences, analyse de sensibilité, optimisation, transformateur piézoélectrique.

LIST OF PUBLICATIONS

Parts of this work have already been published in terms of conference contributions or journal papers. In the text, these publications are referred to as [Fer #].

- [Fer01] J. Fernandez, Y. Perriard, "*Comparative Analysis and Modeling of Both Standing and Traveling Wave Ultrasonic Linear Motor*", in Proceedings of the IEEE International Ultrasonics Symposium, Honolulu, USA, 5-8 October 2003, vol. 2, pp. 1770-1773.
- [Fer02] J. Fernandez, Y. Perriard, "*Characteristics, Modeling and Simulation of a Traveling Wave Ultrasonic Linear Motor*", in Proceedings of the IEEE International Ultrasonics, Ferroelectrics, and Frequency Control 50th Anniversary Joint Conference, Montreal, Canada, 23-27 August 2004, vol. 3, pp. 2247-2250.
- [Fer03] J. Fernandez, Y. Perriard, "*Numerical Analysis and Simulation of Ultrasonic Linear Actuators*", World Congress on Ultrasonics / Ultrasonic International, Beijing, China, 28th August - 1st September 2005.
- [Fer04] J. Fernandez, Y. Perriard, "*Sensitivity Analysis of an Ultrasonic Linear Actuator Using Design of Experiments*", World Congress on Ultrasonics / Ultrasonic International, Beijing, China, 28th August - 1st September 2005.
- [Fer05] J. Fernandez, Y. Ruffieux, Y. Perriard, "*Design Optimization Analysis of a Standing Wave Ultrasonic Linear Actuator*", in Proceedings of the IEEE International Ultrasonics, Ferroelectrics, and Frequency

Control Conference, Rotterdam, The Netherlands, 18-21 September 2005, vol. 1, pp. 311-314.

- [Fer06] J. Fernandez, M. Krummen, Y. Perriard, "*Analytical and Numerical Modeling of an Ultrasonic Stepping Motor Using Standing Waves*", in Proceedings of the IEEE International Ultrasonics, Ferroelectrics, and Frequency Control 50th Anniversary Joint Conference, Montreal, Canada, 23-27 August 2004, vol. 2, pp. 1173-1176.
- [Fer07] J. Fernandez, J. Holzbecher, M. Stutz, Y. Perriard, "*Modeling and Characteristics Comparison of Two Different Piezoelectric Transformers*", in Proceedings of the IEEE International Ultrasonics, Ferroelectrics, and Frequency Control Conference, Rotterdam, The Netherlands, 18-21 September 2005, vol. 3, pp. 1530-1533.
- [Fer08] J. Fernandez, Y. Perriard, "*Sensitivity Analysis and Optimization of a Standing Wave Ultrasonic Linear Motor*", IEEE Transactions on Ultrasonics, Ferroelectrics and Frequency Control, vol. 53, n°7, pp. 1352-1361, 2006.
- [Fer09] J. Fernandez, L. A. Berger, Y. Perriard, "*Optimization of a New Type of Ultrasonic Linear Motor*", accepted for IEEE International Ultrasonics Symposium, Vancouver, Canada, 3-6 October, 2006.

1. INTRODUCTION

1.1 Background and motivation

Industrial requirements have in the past focused mainly on improving the quality and quantity of electromagnetic motors. This has resulted in a huge amount of motors found in almost all areas of applications. Recently, the advance in the field of smart structures and active materials has led to new kinds of motors. Indeed, over the last decades, the demand for piezoelectric motors has been increased significantly. There exist numerous examples from different application areas where piezoelectric motors developed recently have shown to be superior to their electromagnetic counterparts. These new devices are widely used in engineering fields like micro-positioning, active vibration control, ultrasonic welding and machining. Moreover, they are already present in aerospace, aviation, shipping, cars and camera applications.

Piezoelectric ultrasonic motors were first invented by H. V. Barth [Bar73] and later by the ex-Soviets ([Vis77], [Vas79] and [Rag88]), first commercialized by the Japanese ([SB82], [Sas85], [Ina87], [OM87], [Shi89], [Hos89], [Kas92] and [UT93]) and first micro-fabricated by the Americans ([MWH89], [Fly92]). Nowadays, most of the research works and developments are devoted to the modeling of ultrasonic motors for the purpose of predicting the performances of the motor. As large numbers of motors cannot be built and tested easily and cost effectively, it becomes advantageous, in the preliminary design stage, to have the ability to predict how a given design will perform.

Unfortunately, the mathematical model of ultrasonic motors is complex and difficult to derive due to its driving principle based on high-frequency mechanical vi-

brations and frictional forces. Therefore, it is difficult to predict the performances and the characteristics of an ultrasonic motor under various working conditions. Most of the existing work in the field of piezoelectricity has been carried out by scientists in order to establish linear relationships between different parameters that describe piezoelectric phenomena ([Ike96]). Moreover, Sashida et al. proposed a model ([SK93]) but the method proved to be too laborious. Another approach was carried out by Hirata et al. [HU93], [HU95]. On the other hand, Haggood et al. utilized the Rayleigh-Ritz assumed mode energy method [HA95]. Analytical modeling of piezoelectric motors has also been the subject of extensive research all over the world. Furthermore, attempts using finite element method (FEM) for vibration analysis were also conducted [KW95], [Jeo97].

Thus, although ultrasonic motors present interesting advantages like simple mechanical structure, large speed range without gear-mechanism, high force density, braking force without energy supply, absence of noise in the audible range, insensitivity to electromagnetic fields but also negligible electromagnetic emissions, there are many phenomena which are not well understood. But also a lack of optimization techniques upstream from their design does not make them the most often considered solution. The form of the friction law describing rotor-stator interaction, impact processes, effects of surface roughness, material hardness, wear or boundary layer regimes need to be studied in order to design efficient ultrasonic motors and optimize their performances. Within the framework of this thesis work, interest has been laid on ultrasonic linear motors [HW00] and the goal of the present research is precisely to develop an optimization methodology allowing to improve the motor characteristics (output amplitude, torque, efficiency, etc.) by varying the motor design parameters.

1.2 Objective and scope of the research

The design of piezoelectric motors is a difficult task because their overall characteristics are affected by various factors such as dimensions, materials properties, electrical and mechanical boundary conditions, etc. The design of piezoelectric motors can be described as a process of finding optimal design variables like

dimensions and material types of piezoelectric elements and mechanical parts which minimize or maximize a certain number of objectives like e.g. the output amplitude, the input or output power that are subject to a certain set of specified requirements like resonance frequency, limits on input voltage, pre-stressing force, geometric constraints, etc. Thus, the objective of this thesis work is to present a procedure for piezoelectric motor design via objective optimization methods. In particular, the use of design of experiments (DOE) for the sensitivity analysis of an ultrasonic linear motor will be described and explained. This method, applied to finite element simulations, is an innovative way to analyze the effects of the different design variables on the objective function but can be also considered as a pre-optimization stage of the study.

So, this thesis work mainly deals with the study, the modeling and the optimization of ultrasonic linear motors. The scope includes the following areas:

- i) Description of the operating principle of ultrasonic linear motors
- ii) Theoretical modeling and FE simulations
- iii) Validation of the theoretical model with experimental results
- iv) Sensitivity analysis using design of experiments (DOE)
- v) Finite element (FE) optimization
- vi) Validation of the methodology

1.3 Thesis outline

The thesis is organized as follows:

Chapter 2 briefly describes the general background of piezoelectricity, considering ceramic materials, fundamental relations but also the description of some application fields and in particular ultrasonic motors.

Chapter 3 presents the state of the art of ultrasonic motors, describing the different motor types as well from the point of view of the vibration mode, standing or traveling wave, as of the motor function, rotary or linear.

Chapter 4 focuses on the theoretical modeling of ultrasonic linear motors. First of all, theory of standing and traveling waves is briefly presented. Then, numerical modeling is introduced using finite element method (FEM) and simulation results are presented. Experimental results are then presented with the aim of validating the model.

Chapter 5 is devoted to the optimization study of linear ultrasonic motors. Firstly, sensitivity analysis is introduced. Design of experiments (DOE) methods are explained, in particular factorial designs and response surfaces method (Doehlert). This step of the study allows to find out the most influential parameters by determining the effects of the different design variables on the objective function in order to reduce the variation ranges of the input parameters. Then, the results obtained in the pre-optimization stage are applied to FE optimization and the methodology is discussed and validated. Moreover, an application case dealing with the optimization of an ultrasonic linear motor for the auto-focus function of the lens of an optical system is presented. Finally, the chapter concludes with some considerations about multi-objective optimization methods.

Chapter 6 describes a new way to supply ultrasonic motors using piezoelectric transformers. The analysis of two different piezoelectric transformers, a Rosen type one and a radial mode type one, is presented by means of analytical modeling, finite element simulations and measurements. With regard to the power supply of an ultrasonic motor, which requires a high voltage at high frequencies, the idea of matching the resonance frequency of a piezoelectric transformer with the one of the motor is discussed and perspectives are presented.

Chapter 7 finalizes this thesis by providing an overview of its contents and the main results obtained, concluding with some perspectives and aspects for future developments.

2. PIEZOELECTRIC MATERIALS IN DEVICES

2.1 Introduction

The piezoelectric¹ effect was discovered in 1880 by Pierre and Jacques Curie. Piezoelectricity is the property of some materials to develop electric charge on their surface when mechanical stress is exerted on them [Ike96]. The electrical response to mechanical stimulation is called the direct piezoelectric effect and the mechanical response to electrical stimulation is called the converse piezoelectric effect. Piezoelectricity is the property of all materials that have non-centrosymmetric crystal structure. It is found in inorganic materials such as quartz (SiO_2) or lead zirconate titanate (*PZT*), in organic materials and in biological matter (hair, bones). For technical applications of piezoelectrics, the focus is on inorganic materials, ceramics and single crystals. More details will be given in the section dealing with piezoelectric materials. Then, the fundamental piezoelectric relations and the basic properties of piezoelectric materials will be introduced. Moreover, the coupling of electrical and mechanical energy, making piezoelectric materials useful in a wide range of other applications such as sensors, actuators and transducers will be discussed in the last part of the chapter.

¹ the prefix 'piezo-' is derived from the Greek word for 'press'

2.2 Piezoelectric materials

2.2.1 Piezoelectric ceramic

To prepare a piezoelectric ceramic, fine powders of the component metal oxides are mixed in specific proportions, then heated to form a uniform powder. The powder is mixed with an organic binder and is formed into structural elements having the desired shape (discs, rods, plates, etc.). The elements are fired according to a specific time and temperature program, during which the powder particles sinter and the material reaches a dense crystalline structure. The elements are cooled, then shaped or trimmed to specifications, and electrodes are applied to the appropriate surfaces.

Most piezoelectric devices are based on oxide piezoelectrics: lead zirconate titanate (*PZT*) is the most widely used piezoelectric ceramic. Quartz crystals are also widely used. The crystalline structure of *PZT* and of many other useful piezoelectrics is the perovskite structure or a derivative of perovskite. Now, the lead containing perovskites such as *PZT* is by far the best performing for actuators, transducers and a range of sensors. Some essential materials and materials related issues are now described.

2.2.2 Polarization

A traditional piezoelectric ceramic is a mass of perovskite crystals, each consisting of a small, tetravalent metal ion, usually titanium or zirconium, in a lattice of larger, divalent metal ions, usually lead or barium, and O_2^- ions (Fig. 2.1) [Cad64]. Under conditions that confer tetragonal or rhombohedral symmetry of the crystals, each crystal has a dipole moment (Fig. 2.1b). Above a critical temperature, the Curie point, each perovskite crystal in the fired ceramic element exhibits a simple cubic symmetry with no dipole moment (Fig. 2.1a). However, at temperatures below the Curie point, each crystal has tetragonal or rhombohedral symmetry and a dipole moment (Fig. 2.1b).

Adjoining dipoles form regions of local alignment called domains. The align-

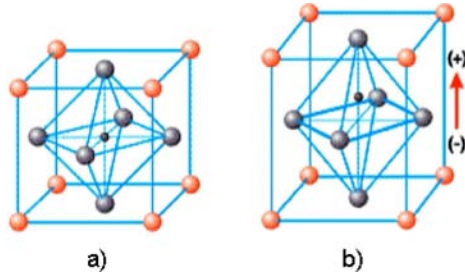


Fig. 2.1: Crystal structure of a traditional piezoelectric ceramic: a) temperature above Curie point, b) temperature below Curie point

ment gives a net dipole moment to the domain, and thus a net polarization. The direction of polarization among neighboring domains is random, so that the ceramic element has no overall polarization (Fig. 2.2a).

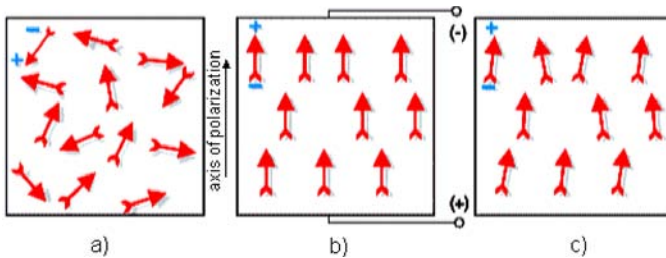


Fig. 2.2: Polarizing (poling) a piezoelectric ceramic: a) random orientation of polar domains prior to polarization, b) polarization in DC electric field, c) remanent polarization after electric field removed

The domains in a ceramic element are aligned by exposing the element to a strong, direct current electric field, usually at a temperature slightly below the Curie point (Fig. 2.2b). Through this polarizing (poling) treatment, domains most nearly aligned with the electric field expand at the expense of domains that are not aligned with the field, and the element lengthens in the direction of the field. When the electric field is removed, most of the dipoles are locked into a configuration of near alignment (Fig. 2.2c). Now, the element has a permanent polarization, the remanent polarization, and is permanently elongated.

Note: Analogous to corresponding characteristics of ferromagnetic materials, a poled ferroelectric material exhibits hysteresis [Uch97].

Fig. 2.3a shows a typical hysteresis curve created by applying an electric field E to a piezoelectric ceramic element until maximum polarization P is attained, reducing the field to zero to determine the remanent polarization, reversing the field to attain a negative maximum polarization and negative remanent polarization, and reversing the field to restore the positive remanent polarization. Moreover, Fig. 2.3b shows the relative change in the dimension of the ceramic element (strain S) along the direction of polarization, corresponding to the change in the electric field. The relative increase / decrease in the dimension parallel to the direction of the electric field is accompanied by a corresponding, but approximately 50% smaller, relative decrease / increase in the dimension perpendicular to the electric field.

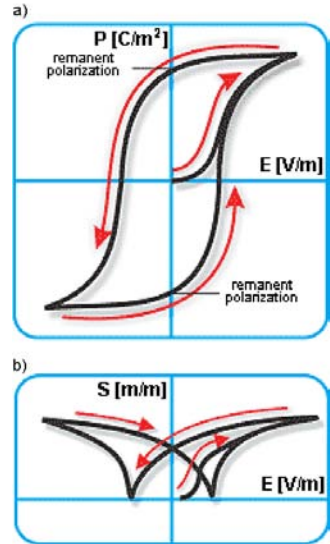


Fig. 2.3: a) hysteresis curve for polarization, b) elongation / contraction of a ceramic element

2.2.3 Soft PZT and hard PZT ceramics

Lead zirconate titanate is the most widely used piezoelectric ceramic. *PZT* is a solid-solution (alloy) of lead titanate and lead zirconate. Small amounts of a donor dopant added to a ceramic formulation create metal (cation) vacancies in the crystal structure, enhancing the effects of extrinsic factors on the piezoelectric properties of the ceramic. The products of such formulations, soft ceramics, are characterized by large electromechanical coupling factors, large piezoelectric constants, high permittivity, large dielectric constants, high dielectric losses, low mechanical quality factors, and poor linearity. Soft ceramics produce larger displacements and wider signal band widths, relative to hard ceramics, but they

exhibit a bigger hysteresis, and are more susceptible to depolarization or other deterioration. Lower Curie points (generally below $300^{\circ}C$) explain that soft ceramics are used at lower temperatures. Generally large values for permittivity and dielectric dissipation factor restrict or eliminate soft ceramics from applications requiring combinations of high frequency inputs and high electric fields. Consequently, soft ceramics are used primarily in sensing applications, rather than in power applications.

Hard ceramics have characteristics generally opposite those of soft ceramics, including Curie points above $300^{\circ}C$, small piezoelectric charge constants, large electromechanical coupling factors, and large mechanical quality factors. They are also more difficult to polarize or depolarize. Although hard ceramics generally are more stable than soft ceramics, they cannot produce the same large displacements. Hard ceramics are compatible with high mechanical loads and high voltages. Be aware, a soft ceramic can be prepared to exhibit some characteristics approaching those of a hard ceramic, or vice versa. Thus, when choosing a ceramic for a particular application, it can be useful to look beyond general categorization, and carefully compare specific characteristics (see Table 2.1).

Table 2.1: Characteristics of soft ceramics and hard ceramics compared

Characteristic	Soft ceramic	Hard ceramic
Piezoelectric constants	larger	smaller
Permittivity	higher	lower
Dielectric constants	larger	smaller
Dielectric losses	higher	lower
Electromechanical coupling factors	larger	smaller
Electrical resistance	very high	lower
Mechanical quality factor	low	high
Coercive field	low	higher
Linearity	poor	better
Polarization / depolarization	easier	more difficult

2.2.4 Limitations in piezoelectric materials

There are many shortcomings of piezoelectric materials, for instance:

- Fatigue failure resulting from the alternating stress in the ceramic elements
- Looseness of the piezoelectric properties in the neighborhood of the Curie temperature point ($> 300^{\circ}\text{C}$)
- Weakening of the adhesive bond occurring below the Curie point
- Change in Young's modulus with temperature causing a change in the resonant frequency and thereby resulting in lowering the performance of the device
- Short life span owing to rapid wear and tear
- Large frictional losses due to the complex nature of vibrations together with other phenomena (sliding and deformation losses lead to lower efficiencies, for example at most $\sim 50\%$ in ultrasonic motor applications)

2.2.5 Bonding PZT ceramics

In most applications, *PZT* ceramics have to be fixed to some substrate. The three principal methods to do so are:

- clamping
- welding
- gluing

Clamping is often found to be an unreliable method and is not often used. Welding has the advantage of giving a conductive connection but the motion will cause fatigue in the bond. Gluing is usually the best approach. Epoxy or acrylate glues provide strong but still flexible joints between adjacent surfaces. There is no fatigue and operating temperatures up to 150°C are not a problem for some of

the glues. Electrical contact between the substrate and the electrode on the *PZT* is nearly always required. One possibility is to use conductive glue, usually an epoxy filled with particles. A drawback of these glues is that they are so heavily loaded with conductive particles that the glue line is often weak. A solution to this problem is to mix nickel powder into the glue or use glues containing silver.

The electrodes on *PZT* ceramics are of nickel or silver. Welding on surfaces of these material types is possible, but a special attention to depolarization has to be done. Indeed, temperatures can be so high that they affect the piezoelectric activity of the ceramic and this would result in a partial or even total loss of its piezoelectric properties. More details concerning the fabrication of piezoelectric ceramics are described in [JC71] and [Set02].

2.2.6 Behavior of a PZT ceramic

A piezoelectric ceramic element exposed to an alternating electric field changes dimensions cyclically, at the frequency of the field. The typical response graph of a ceramic element is depicted in Fig. 2.4.

The frequency at which the vibrating element converts most efficiently the electrical input energy into mechanical energy is determined by the composition of the ceramic material and by the shape and volume of the element. As the frequency increases, the element's oscillations first approach a frequency at which impedance is minimum (max. admittance). This minimum impedance frequency f_m approximates the series resonance frequency f_s , the frequency at which impedance in an electrical circuit describing the element is zero (neglecting resistance caused by mechanical losses). This frequency is also called the resonance frequency f_r .

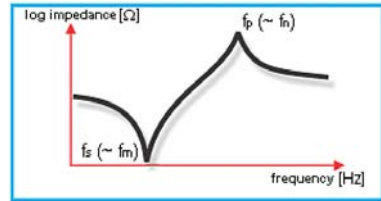


Fig. 2.4: Impedance as a function of frequency

As the frequency is further increased, impedance increases to a maximum (min. admittance). This maximum impedance frequency f_n approximates the paral-

parallel resonance frequency f_p , the frequency at which parallel resistance in the equivalent electrical circuit is infinite (neglecting resistance caused by mechanical losses). This frequency is also called the anti-resonance frequency f_a . The values for minimum impedance frequency and maximum impedance frequency can be used to calculate the electromechanical coupling factor, an indicator of the effectiveness with which a piezoelectric material converts electrical energy into mechanical energy or mechanical energy into electrical energy. Dielectric losses and mechanical losses also affect the efficiency of energy conversion. These different aspects are presented more in detail in the following section.

2.3 Piezoelectric theory

2.3.1 Piezoelectric constants

Because a piezoelectric ceramic is anisotropic, physical constants relate to both the direction of the applied mechanical or electric force and the directions perpendicular to the applied force.

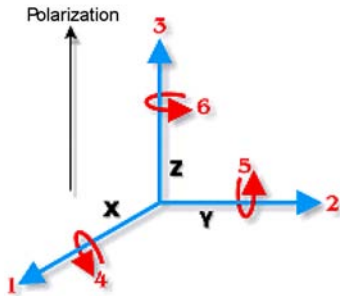


Fig. 2.5: Axes notation

Consequently, each constant generally has two subscripts that indicate the directions of the two related quantities, such as stress (force on the ceramic element / surface area of the element) and strain (change in length of element / original length of element) for elasticity. The direction of positive polarization usually is made to coincide with the z-axis of a rectangular system of x, y, and z axes (see Fig. 2.5). Direction x, y, or z is represented by the subscript 1, 2, or 3, respectively, and shear

about one of these axes is represented by the subscript 4, 5, or 6, respectively. Definitions of the most frequently used constants, and equations for determining and interrelating these constants are presented in the next paragraphs.

i. Piezoelectric charge constant

The piezoelectric charge constant \mathbf{d} is the polarization generated per unit of mechanical stress (\mathbf{T}) applied to a piezoelectric material or, alternatively, is the mechanical strain (\mathbf{S}) experienced by a piezoelectric material per unit of electric field applied (\mathbf{E}). The first subscript to \mathbf{d} indicates the direction of polarization generated in the material when the electric field is zero or, alternatively, is the direction of the applied field strength. The second subscript is the direction of the applied stress or the induced strain, respectively. Because the strain induced in a piezoelectric material by an applied electric field is the product of the value for the electric field and the value for \mathbf{d} , \mathbf{d} is an important indicator of a material's suitability for strain-dependent applications (actuators).

ii. Piezoelectric voltage constant

The piezoelectric voltage constant \mathbf{g} is the electric field generated by a piezoelectric material per unit of mechanical stress applied or, alternatively, is the mechanical strain experienced by a piezoelectric material per unit of electric displacement applied. The first subscript to \mathbf{g} indicates the direction of the electric field generated in the material, or the direction of the applied electric displacement (\mathbf{D}). The second subscript is the direction of the applied stress or the induced strain, respectively. Because the strength of the induced electric field produced by a piezoelectric material in response to an applied physical stress is the product of the value for the applied stress and the value for \mathbf{g} , \mathbf{g} is important for assessing a material's suitability for sensing applications (sensors).

iii. Permittivity

The permittivity or dielectric constant ϵ , for a piezoelectric ceramic material, is the dielectric displacement per unit electric field. $\epsilon^{\mathbf{T}}$ is the permittivity at constant stress, $\epsilon^{\mathbf{S}}$ is the permittivity at constant strain. The first subscript to ϵ indicates the direction of the dielectric displacement; the second is the direction of the electric field.

iv. Elastic compliance

Elastic compliance \mathbf{s} is the strain produced in a piezoelectric material per unit of stress applied and, for the 11 and 33 directions, is the reciprocal of the modulus of elasticity (Young's modulus, \mathbf{Y}). \mathbf{s}^D is the compliance under a constant electrical displacement; \mathbf{s}^E is the compliance under a constant electric field. The first subscript indicates the direction of strain, the second is the direction of stress.

v. Young's modulus

Young's modulus \mathbf{Y} is an indicator of the stiffness (elasticity) of a ceramic material. \mathbf{Y} is determined from the value for the stress applied to the material divided by the value for the resulting strain in the same direction.

vi. Electromechanical coupling factor

The electromechanical coupling factor k is an indicator of the effectiveness with which a piezoelectric material converts electrical energy into mechanical energy, or converts mechanical energy into electrical energy. The first subscript to k denotes the direction along which the electrodes are applied; the second denotes the direction along which the mechanical energy is applied or developed. k values quoted in ceramic suppliers' specifications typically are theoretical maximum values. At low input frequencies, a typical piezoelectric ceramic can convert 30% to 75% of the energy delivered to it in one form into the other form, depending on the formulation of the ceramic and the directions of the forces involved. A high k usually is desirable for efficient energy conversion, but k does not account for dielectric losses or mechanical losses, nor for recovery of unconverted energy. The accurate measure of efficiency is the ratio of converted, useable energy delivered by the piezoelectric element to the total energy taken up by the element. By this measure, piezoelectric ceramic elements in well designed systems can exhibit efficiencies that exceed 90%.

The dimensions of a ceramic element can dictate unique expressions of k . For a

thin disc of piezoelectric ceramic, the planar coupling factor k_p expresses radial coupling, i.e. the coupling between an electric field parallel to the direction in which the ceramic element is polarized (direction 3) and mechanical effects that produce radial vibrations, relative to the direction of polarization (direction 1 and direction 2). For a disc or plate of material whose surface dimensions are large relative to its thickness, the thickness coupling factor k_t , a unique expression of k_{33} , expresses the coupling between an electric field in direction 3 and mechanical vibrations in the same direction. The resonance frequency for the thickness dimension of an element of this shape is much higher than the resonance frequency for the transverse dimensions. At the same time, strongly attenuated transverse vibrations at this higher resonance frequency make k_t lower than k_{33} , the corresponding factor for longitudinal vibrations of a thin rod of the same material, for which a much lower longitudinal resonance frequency more closely matches the transverse resonance frequency. This is the result of the transverse contraction / expansion that accompanies the expansion / contraction in thickness.

vii. Dielectric dissipation factor

The dielectric dissipation factor (dielectric loss factor) $\tan \delta$, for a ceramic material, is the tangent of the dielectric loss angle. $\tan \delta$ is determined by the ratio of effective conductance to effective susceptance in a parallel circuit, measured by using an impedance bridge. Values for $\tan \delta$ typically are determined at 1 kHz.

viii. Mechanical quality factor

In analogy to the electrical quality factor Q , the mechanical quality factor Q_m describes the ratio of the strain in phase with the stress to the strain out of phase with the stress in the vibrating body. Q_m is the 3dB width of the piezoelectric resonance divided to the resonance frequency. 'Hard' materials have a superior Q_m in comparison to 'soft' materials, this is why they are more adapted for applications requiring a high mechanical quality factor, such as resonators. On the

contrary, for applications that need a given band-width, such as filters, the use of 'soft' (low Q_m) materials is more suitable.

2.3.2 Fundamental piezoelectric relations

The electrical behavior of an unstressed medium under the influence of an electric field is defined by two quantities, the field strength \mathbf{E} and the dielectric displacement \mathbf{D} . Their relationship is:

$$\mathbf{D} = \epsilon \mathbf{E} \quad (2.1)$$

The mechanical behavior of the same medium at zero electric field strength is defined by two mechanical quantities, the stress applied \mathbf{T} and the strain \mathbf{S} . The relationship here is:

$$\mathbf{S} = s \mathbf{T} \quad (2.2)$$

The piezoelectric effect couples the electrical and the mechanical behaviors. It can be approximately described by the following linear piezoelectric constitutive fundamental equations [Waa91]:

$$\begin{aligned} \mathbf{S} &= \mathbf{s}^E \mathbf{T} + \mathbf{d}^t \mathbf{E} \\ \mathbf{D} &= \mathbf{d} \mathbf{T} + \epsilon^T \mathbf{E} \end{aligned} \quad (2.3)$$

In the above equations, the full tensor notation has been abbreviated into simpler matrix notation. These different matrices are defined as follows:

The superscripts \mathbf{T} and \mathbf{E} refer to the quantities to be kept constant ($\mathbf{T} = \mathbf{E} = \mathbf{0}$) when measuring material constants [IEE87]. Similar relations are found for various choices of independent variable sets. The constitutive equations can be arranged in several ways. The four types of piezoelectric constitutive equation sets are shown in Table 2.3. By calculations, one set of constants can be expressed by another [Ike96].

Table 2.2: Definition of the piezoelectric constants

D	$[C/m^2]$	Dielectric displacement	3×1 vector
E	$[V/m]$	Electric field strength	3×1 vector
S	$[m/m]$	Strain	6×1 vector
T	$[N/m^2]$	Stress	6×1 vector
s^E	$[m^2/N]$	Elastic compliance	6×6 matrix
ε^T	$[F/m]$	Absolute dielectric constant	3×3 matrix
d	$[C/N]$	Piezoelectric charge constant	3×6 matrix

Table 2.3: Types of fundamental piezoelectric constitutive equations

Independent variables	Piezoelectric constitutive equations	Form
T, E	$\mathbf{S} = \mathbf{s}^E \mathbf{T} + \mathbf{d}^t \mathbf{E}$ $\mathbf{D} = \mathbf{d} \mathbf{T} + \epsilon^T \mathbf{E}$	d-form
S, D	$\mathbf{T} = \mathbf{c}^D \mathbf{S} - \mathbf{h} \mathbf{D}$ $\mathbf{E} = -\mathbf{h} \mathbf{S} + \beta^S \mathbf{D}$	h-form
S, E	$\mathbf{T} = \mathbf{c}^E \mathbf{S} - \mathbf{e} \mathbf{E}$ $\mathbf{D} = \mathbf{e} \mathbf{S} + \epsilon^S \mathbf{E}$	e-form
T, D	$\mathbf{S} = \mathbf{s}^D \mathbf{T} - \mathbf{g} \mathbf{D}$ $\mathbf{E} = -\mathbf{g} \mathbf{T} + \beta^T \mathbf{D}$	g-form

The material constants are compiled in the elastoelectric matrix given in Table 2.4. It is worth noticing that not all elements of this matrix are occupied. Moreover, due to the fact that the components of the **d** matrix are reduced to three non zero elements d_{33} , d_{31} and d_{15} , the electromechanical coupling in the piezoelectric ceramics is achieved through three principal modes of vibrations. These different vibration modes are described in the next paragraphs.

2.3.3 Vibration modes

In practice, the variation of the electric field will deform a piezoelectric body in different directions with different intensities. According to the type of the used piezoelectric effect (the directions of the applied electric field and the extension), three main groups of vibration modes can be achieved. These modes are the longitudinal mode (d_{33}), the transversal mode (d_{31}) and the shear mode (d_{15}).

Table 2.4: Elastoelectric matrix for \mathbf{T} and \mathbf{E} taken as independent variables

	T_1	T_2	T_3	T_4	T_5	T_6	E_1	E_2	E_3
S_1	s_{11}	s_{12}	s_{13}						d_{31}
S_2	s_{12}	s_{11}	s_{13}						d_{31}
S_3	s_{13}	s_{13}	s_{33}						d_{33}
S_4				s_{44}				d_{15}	
S_5					s_{44}		d_{15}		
S_6						$2(s_{11} - s_{12})$			
D_1					d_{15}		ϵ_{11}		
D_2				d_{15}				ϵ_{11}	
D_3	d_{31}	d_{31}	d_{33}						ϵ_{33}

- **Longitudinal mode (33):** in the longitudinal mode, the deformations take place parallel to the applied electric field and the polarization, as shown in Fig. 2.6. This mode is usually used for small movements and high forces.



Fig. 2.6: The longitudinal vibration mode

- **Transversal mode (31):** in the transversal mode, the deformations take place perpendicular to the electric axis as shown in Fig. 2.7. This mode is also used for small movements and high forces and also has high stiffness.

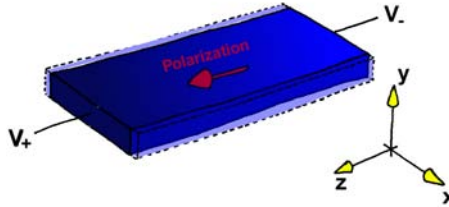


Fig. 2.7: The transversal vibration mode

- **Shear mode (15):** in the shear mode, the deformations take place around the axis perpendicular to the plan containing the electrical field vector and the polarization as shown in Fig. 2.8. They are mainly used for large movements and have low stiffness.

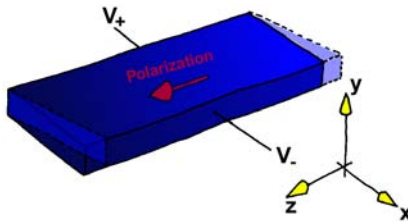


Fig. 2.8: The shear vibration mode

2.4 Applications

2.4.1 Introduction

As explained previously, mechanical compression or tension on a polarized piezoelectric ceramic element changes the dipole moment, creating a voltage. Com-

pression along the direction of polarization, or tension perpendicular to the direction of polarization, generates a voltage of the same polarity as the poling voltage (Fig. 2.9b). Tension along the direction of polarization, or compression perpendicular to the direction of polarization, generates a voltage with polarity opposite to the poling voltage (Fig. 2.9c). These actions are generator actions: the ceramic element converts the mechanical energy of compression or tension into electrical energy. This behavior is used in fuel-igniting devices, solid state batteries, force-sensing devices and other products. Values for compressive stress and the voltage (or field strength) generated by applying stress to a piezoelectric ceramic element are linearly proportional up to a material-specific stress. The same is true for applied voltage and generated strain. The same is true for applied voltage and generated strain.

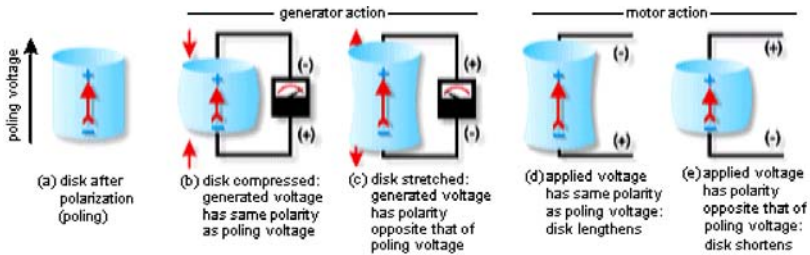


Fig. 2.9: Generator and motor actions of a piezoelectric element

If a voltage of the same polarity as the poling voltage is applied to a ceramic element in the same direction, the element will lengthen and its diameter will become smaller (Fig. 2.9d). If a voltage of polarity opposite to the poling voltage is applied, the element will become shorter and broader (Fig. 2.9e). If an alternating voltage is applied, the element will lengthen and shorten cyclically, at the frequency of the applied voltage. This is motor action: electrical energy is converted into mechanical energy. The principle is adapted to piezoelectric motors, sound or ultrasound generating devices and many other products.

A piezoelectric system can be constructed for virtually any application for which any other type of electromechanical transducer can be used. For any particular application, however, limiting factors include the size, weight and cost of the

system. Piezoceramic devices fit into five general categories: generators, sensors, transducers, transformers and actuators. Characteristics of each group are briefly summarized below.

2.4.2 Generators

Piezoelectric ceramics can generate voltages sufficient to spark across an electrode gap, and thus can be used as ignitors in fuel lighters, gas stoves, welding equipment and such other apparatus.

Piezoelectric ignition systems are small and simple, distinct advantages relative to alternative systems that include permanent magnets or high voltage transformers and capacitors. Fig. 2.10 shows the principal assembly of a piezoelectric ignition system [Hel74]. Usually, two piezoelectric cylinders are stacked and operated in parallel, so that no further high voltage insulation is required. Alternatively, the electrical energy generated by a piezoelectric element can be stored. Techniques used to make multilayer capacitors have been used to construct multilayer piezoelectric generators. Such generators are excellent solid state batteries for electronic circuits.

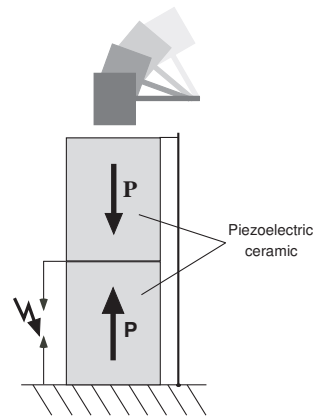


Fig. 2.10: Piezoelectric ignition system

2.4.3 Sensors

A sensor converts a physical parameter, such as acceleration or pressure, into an electrical signal. In some sensors the physical parameter acts directly on the piezoelectric element; in other devices an acoustical signal establishes vibrations in the element and the vibrations are converted into an electrical signal. Often, the system provides a visual, audible, or physical response to the input from the sensor, automobile seat belts lock in response to a rapid deceleration for example.

A representation of a typical force, pressure and acceleration sensor is shown in Fig. 2.11 [Kle82]. The gray color represents the test structure. The blue color corresponds to the sensor housing. The piezoelectric crystals are colored in red. The black electrode is where the charges from the crystals accumulate before it is conditioned by the yellow, micro-circuit. The accelerometer also incorporates a mass which is shown by the green color. Note that they differ very little in internal configuration. In accelerometers, which measure motion, an invariant seismic mass is forced by the crystals to follow the motion of the base and structure to which it is attached. The resulting force F on the crystals is easily calculated using Newton's second law of motion. Pressure and force sensors are nearly identical and rely on an external force to strain the crystals. The major difference being that the pressure sensors utilize a diaphragm to collect pressure, which is simply a force applied over an area.

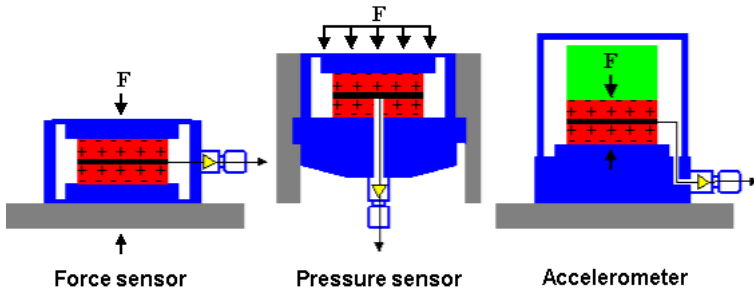


Fig. 2.11: Sensor constructions

2.4.4 Transducers

Piezoelectric transducers convert electrical energy into vibrational mechanical energy, often sound or ultrasound, that is used to perform a task. The scheme of an ultrasound transducer is represented in Fig. 2.12 [Wer86]. Piezoelectric transducers that generate audible sounds afford significant advantages, relative to alternative electromagnetic devices: they are compact, simple, highly reliable and minimal energy can produce a high level of sound. These characteristics

are ideally matched to the needs of battery powered equipment. Because the piezoelectric effect is reversible, a transducer can both generate an ultrasound signal from electrical energy and convert incoming sound into an electrical signal. Some devices designed for measuring distances, flow rates or fluid levels incorporate a single piezoelectric transducer in the signal sending and receiving roles. Other designs incorporate two transducers and separate these roles. Piezoelectric transducers are also used to generate ultrasonic vibrations for cleaning, atomizing liquids, drilling or milling ceramics, or other difficult materials, welding plastics, medical diagnostics, or for other purposes [Smi92].

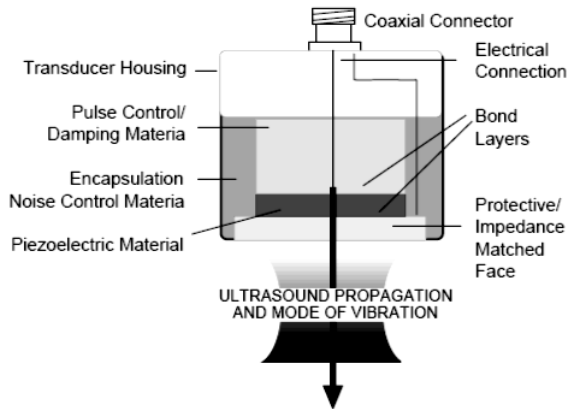


Fig. 2.12: Scheme of an ultrasound transducer

2.4.5 Transformers

Piezoelectric transformers have several advantages in comparison to the electromagnetic transformer, such as lower weight and volume, better isolation and absence of electromagnetic noise. They can have a very flat design making them especially attractive in miniaturized high voltage sources for cold cathode fluorescent lamps in hand-held computers and in cars. The principle of a piezoelectric transformer (Rosen type) is shown in Fig. 2.13. The electrical input voltage

V_{in} generates a mechanical vibration, usually at the resonance frequency of the piezoelectric element, which then is reconverted into an electrical voltage, the output voltage V_{out} of the transformer. The output to input voltage ratio depends on the geometrical dimensions, the electromechanical coupling factor, the mechanical quality factor and the load resistance R_L .

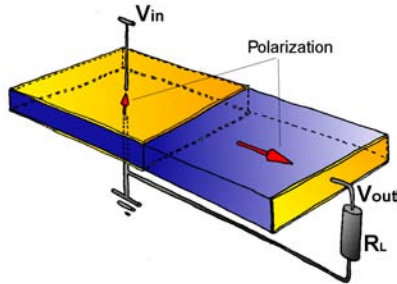


Fig. 2.13: Principle of a Rosen type piezoelectric transformer

Recent improvements in transformer design and piezoelectric materials open up new prospects for the application of piezoelectric transformers [HLW02]. Chapter 6 deals with the application of a piezoelectric transformer in the power supply system of an ultrasonic motor.

2.4.6 Actuators

A piezoelectric actuator converts an electrical signal into a precisely controlled physical displacement, to finely adjust precision machining tools, lenses, or mirrors. Piezoelectric actuators are also used to control hydraulic valves, act as small-volume pumps or special-purpose motors, and in other applications. A potentially important advantage of piezoelectric actuators is the absence of electromagnetic noise. Furthermore, if physical displacement is prevented, an actuator will develop an useable force. As an example, the scheme of a propagating wave type ultrasonic motor is shown for the rotary motor developed by Sashida [Sas83] in Fig. 2.14a) and the application of this motor in a camera auto-focusing mech-

anism is represented in Fig. 2.14b). The rotor in contact with the elastic rippled stator will be driven by means of a traveling elastic wave induced in the stator by a piezoelectric ring ceramic bonded onto the stator. The great advantage of this kind of motor is its low speed and its high torque, which can be achieved without gears by using the small movement amplitudes. In addition, the piezoelectric motor starts and stops fast, it is insensitive to strong magnetic fields and does not generate magnetic disturbances. Further details will be described in the following chapter and also other types of ultrasonic motors will be presented.

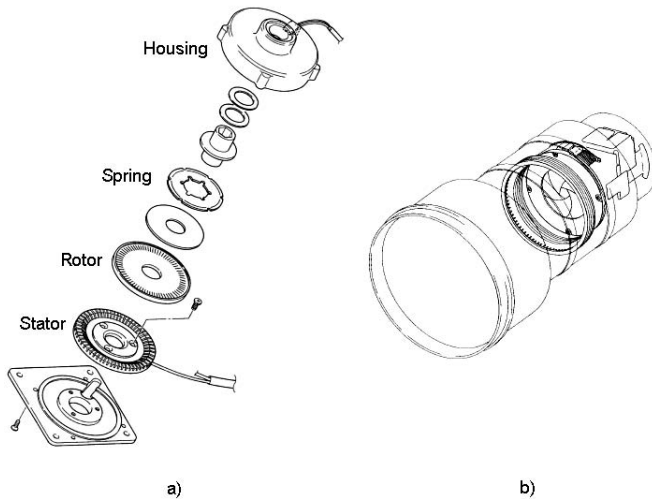


Fig. 2.14: a) Traveling wave ultrasonic motor developed by Sashida, b) application in a camera auto-focusing mechanism

2.5 Conclusion

Piezoelectricity and piezoelectric materials have been introduced. The development of some application fields has been shown, in particular in the field of ultrasonic motors. In the next chapter, the theme which deals with the state of the art of the different types of piezoelectric motors will be developed.

3. ULTRASONIC MOTORS: STATE OF THE ART

3.1 Introduction

Piezoelectric ultrasonic motors, whose efficiency is insensitive to size, are frequently used in the mm-size motor area. In general, piezoelectric motors are classified into two categories, based on the type of driving voltage applied to the device and the nature of the strain induced by the voltage: rigid displacement devices for which the strain is induced unidirectionally along an applied DC field, and resonating displacement devices for which the alternating strain is excited by an AC field at the mechanical resonance frequency. The first category can be further divided into two types: servo displacement transducers and pulse-drive motors. The AC resonant displacement is not directly proportional to the applied voltage, but is dependent on the adjustment of the drive frequency. Very high speed motion due to the high frequency is also an attractive feature of the ultrasonic motors. The materials requirements for these classes of devices are somewhat different, and certain compounds will be better suited for particular applications. The ultrasonic motor, for instance, requires a very hard piezoelectric with a high mechanical quality factor Q_m , in order to minimize heat generation and maximize displacement. The servo displacement transducer suffers most from strain hysteresis. The pulse-drive motor requires a low-permittivity material rather than a small hysteresis, so that soft *PZT* materials are preferred. This thesis deals with ultrasonic motors using resonant vibrations. However, after a brief historical background review, different ultrasonic motors are introduced. Working principles and motor characteristics are explained.

3.2 Historical background

Electromagnetic motors were invented more than a hundred years ago. While these motors still dominate the industry, a drastic improvement cannot be expected except through new discoveries in magnetic materials or superconductors. Regarding conventional electromagnetic motors, tiny motors smaller than 1 cm^3 are rather difficult to produce with sufficient energy efficiency. Therefore, a new class of motors using high power ultrasonic energy, the ultrasonic motors, is gaining widespread attention. Ultrasonic motors made with piezoceramics whose efficiency is insensitive to size are superior in the mini-motor area. Figure 3.1 shows the basic construction of ultrasonic motors, in the case of a motor configuration using the elliptic motion of the surface points of the vibrator to create the movement. It consists of a high frequency power supply, a vibratory piece (stator) and a slider (rotor). Further, the vibratory piece is composed of a piezoelectric driving component and an elastic vibratory part. The slider has generally a friction coat.

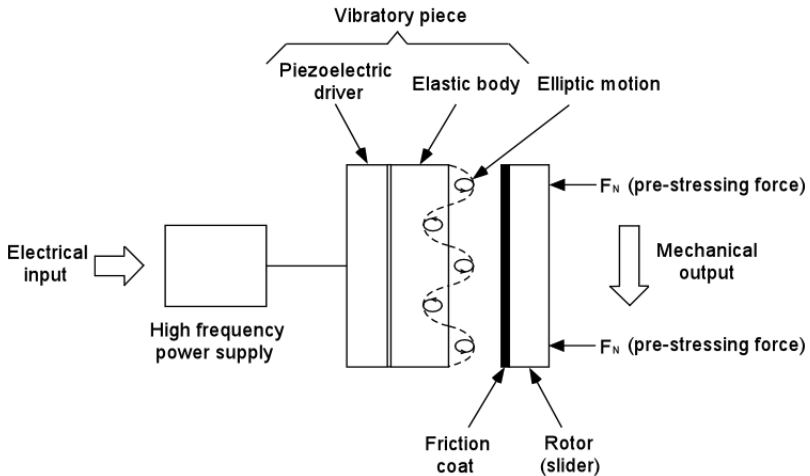


Fig. 3.1: Basic scheme of ultrasonic motors

Though there had been some earlier attempts, the practical ultrasonic motor was proposed firstly by H. V. Barth of IBM in 1973 [Bar73].

As shown in Fig. 3.2, the rotor was pressed against two horns placed at different locations. By exciting one of the horns, the rotor was driven in one direction, and by exciting the other one, the rotation direction was reversed. Because of the difficulty in maintaining a constant vibration amplitude with temperature rise, wear and tear, the motors were not of much practical use at that time. In the 1980's, with increasing chip pattern density, the semiconductor industry began to request much more precise and sophisticated sensors which did not generate magnetic field noise. This urgent request has accelerated the developments in ultrasonic motors. Let now summarize the advantages and drawbacks of the ultrasonic motors.

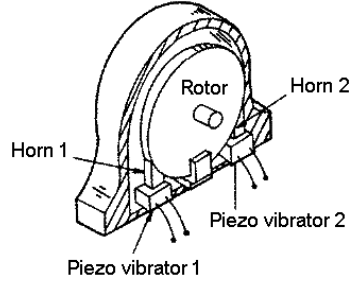


Fig. 3.2: Ultrasonic motor by Barth

Table 3.1: Advantages and drawbacks of ultrasonic motors

Advantages
Low speed and high torque—direct drive
Quick response and wide velocity range
Hard brake and no backlash: excellent controllability
Fine position resolution
High power/weight ratio and high efficiency
Simple and compact structure (easy production process) and light weight
Negligible effect from external magnetic or radioactive fields
No generation of magnetic fields and audible disturbances
Drawbacks
Necessity for a high frequency power supply
Less durability due to frictional drive
Drooping torque—speed characteristics

This review of history of piezoelectric ultrasonic motors is not complete. Indeed, many different designs of piezoelectric motors have appeared recently. Theoretical evaluation of the conversion process, conception of more powerful motors and micromotors as well as design optimization are also being undertaken.

3.3 Brief description of the operating principle

A piezoelectric motor operating principle is based on the use of reverse piezoelectric effect for continuous conversion of electric power into mechanical energy. The process of energy conversion which takes place in the piezoelectric motor can be separated into two parts. One is the ultrasonic vibration generation and the second is the conversion of this vibration into the slider (rotor) movement. When a voltage is applied to the piezoelectric ceramic element, alternating expansions and contractions occur either in the ceramic body itself or in the attached elastic body. The magnitude of these oscillations is very small, about some micrometers. In order to obtain a bigger deformation amplitude, the resonance effect of the vibratory piece in the ultrasonic range is used. The conversion of the ultrasonic vibrations in the rotor movement is based on the elliptic motion displacement of the surface points of the contact zone between stator and rotor. The displacements can be produced independently through two individually vibrating bodies or by a single vibrator. Depending of the method of realizing such a motion, different motor structures can be developed. Various shapes and constructions are possible, because there are many ways of creating the elliptic motion present between the contacting surfaces. Many researchers have classified piezoelectric ultrasonic motors into two groups according to the vibration modes used to generate the elliptic motion. However, there are some structures that generate neither traveling wave nor standing waves. So, in the next section, piezoelectric ultrasonic motors are classified into different categories, in particular based on the excitation type and the motor function.

3.4 Classification of ultrasonic motors

3.4.1 Classification by excitation

The form of an ultrasonic motor can be recognized by the way in which the elliptic motion of the contact zone is obtained. Motors are classified into two forms: one utilizes a single vibration mode and the other two vibration modes.

Ultrasonic motor using single vibration mode

The ultrasonic motor using a single vibration is further classified into two groups, a standing wave motor and a traveling wave motor [Fer01].

Standing Wave Ultrasonic Motor (SWUM):

There are two different designs of piezoelectric ultrasonic motors of the standing wave type. In the first class, only the longitudinal vibration of the piezoelectric actuator is excited (Fig. 3.3). The oblique impact between the stator and slider/rotor element causes an indirect bending mode excitation, converting longitudinal vibration into tangential vibration in the case of rotary motors ([Bar73], [Vis77] and [SB82]). This principle is also applicable to the longitudinal vibration of a bar ([Iij87] and [Tom88]).

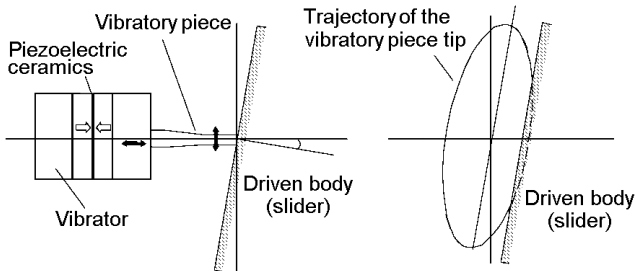


Fig. 3.3: Example of SWUM [SB82]

In the second class, two groups of electrodes on the vibratory piece, such as on a ring, are excited in order to have clockwise and counterclockwise rotation. Such a motor design was proposed by Takano et al. [TTK92] and the principle is illustrated in Fig. 3.4.

The circular shape of the piezoelectric element shown in Fig. 3.4 is divided into 12 parts of $1/4$ wavelength. The parts of each pattern are alternately polarized in positive (+) and negative (-) pairs. The six projections on the vibrator are placed on the border between parts of the same polarity and are adhered to the piezoelectric element. When the shaded (group A) electrodes are excited at the operating frequency of the motor, the projections leading to the left rise and ones leading to the right fall (the position of the wave crests and wave hollows alternate in half periods). The rotor is then driven to the left by the 3 rising projections. When the drive signal is applied to the non-shaded area (group B), the entire process is reversed. By driving the rotor in this manner, it is possible to easily change the direction of the rotor. The principle described above is also valid for linear piezoelectric ultrasonic motors.

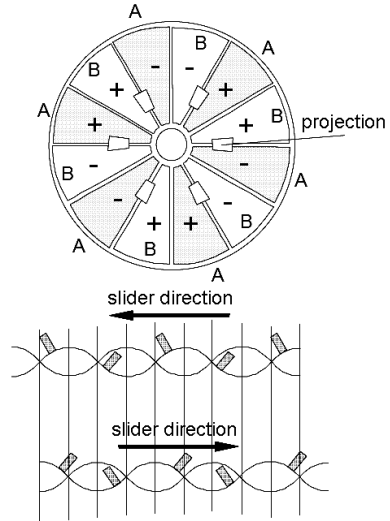


Fig. 3.4: Example of SWUM [TTK92]

Traveling Wave Ultrasonic Motor (TWUM):

A wave traveling along a bounded solid body is composed of longitudinal and transverse waves, and the particles on the surface move elliptically by themselves. An object pressed on it is forced to move by frictional force as shown in Fig. 3.5. The direction of motion is determined by the directions of wave propagation and motion of the particles. In the literature, the operating principle of a travel-

ing wave motor is described more in detail ([Ina87], [HW92], [SK93], [UT93] and [Uch97]). Although the most common structure for rotary motors is a disk, ring or cylinder, a traveling wave type piezoelectric motor using a rectangular plate is also realizable [MBB98]. Motor using high frequency surface acoustic waves (SAW) may also be classified in this group [KTH96].

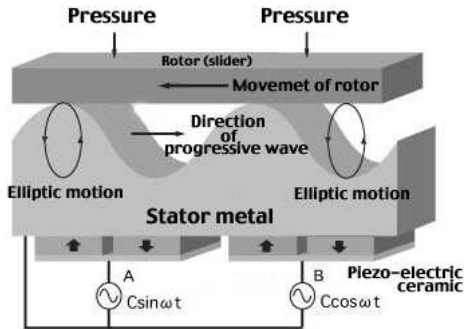


Fig. 3.5: Principle of TWUM

Ultrasonic motor using two vibration modes

If two vibration modes whose displacement components are perpendicular to each other are combined, the synthesized particle motion can be made elliptical. Ultrasonic motors using two vibration modes fall into three groups: mode conversion, multi-mode and hybrid transducer motors.

Mode Conversion Ultrasonic Motor (MCUM):

This motor utilizes a mode conversion to obtain the two vibration modes from a single piezoelectric element. There exist different kinds of MCUM. One is the motor already presented in Fig. 3.3 and explained in detail in [SB82]. Another type uses a torsion coupler which converts a longitudinal vibration to a torsional vibration, as depicted in Fig. 3.6 [Kum85]. The tip of the torsional coupler moves elliptically as a combination of torsional and longitudinal vibrations. These motors are driven by a single power source and are difficult to be reversely moved

without a change of frequency. On the other hand, it is easy to change the direction of motion of ultrasonic motors which employ two piezoelectric elements, because the direction is changed by switching the relative phase difference between two sources.

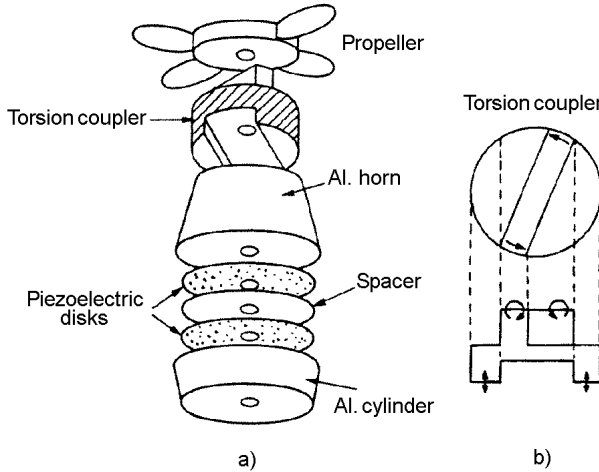


Fig. 3.6: a) Configuration of longitudinal torsional vibrator b) motion of the torsional coupler

Multi-Mode Ultrasonic Motor (MMUM):

This motor uses a coupled vibration or a multi-mode vibrator excited by one or two piezoelectric elements. Several vibration modes can be used; one is a longitudinal-flexural coupled vibration of a circular hollow cylinder. In this case, the motor can be hold at the axial vibration node. Figure 3.7 shows an example of coupled vibration of concentric shear and radial modes generated in a circular piezoelectric element [Tom88]. The particles of the outer surface move elliptically if the driving conditions are appropriate. Other ultrasonic motors use: a coupling of non-axisymmetric vibration with radial extensional vibration of a circular plate [Tak88]; longitudinal and flexural vibrations of a cross-shaped vi-

brator [Tom88]; two bending vibrations of a rectangular bar where the directions of the two vibrations are perpendicular with each other [Tom87]; a coupled vibration between longitudinal and flexural vibration of a plate [Tom87]. The last three were developed for linear motors.

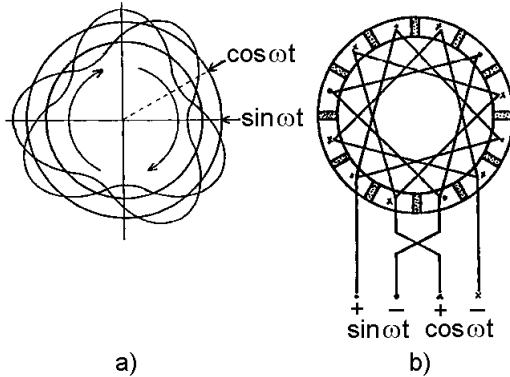


Fig. 3.7: a) Scheme of the rotation mode b) piezoelectric element with divided electrode for the rotation mode

Hybrid Transducer Ultrasonic Motor (HTUM):

This motor uses two separate vibrations which are independently excited by two separate piezoelectric elements. There are several kinds of HTUM. Figure 3.8 is a schematic drawing of a hybrid transducer ultrasonic motor prototype [UK88]. The stator is composed of a torsional vibrator and a longitudinal multilayered piezoelectric actuator. The actuator is bonded on the flat surface of the vibrator. These two kinds of piezoelectric elements are driven by two electrical sources with the same frequency and the phase difference between them is controlled appropriately. Since only the mechanical output of the torsional transducer contributes to the motor output, it should be operated with high efficiency and converts a large electrical power input into a mechanical output. Figure 3.8b shows the four typical phases in one cycle:

1. The vibrator is at its maximum speed and the actuator is elongated up to its maximum point to generate the frictional force.
2. The displacement of the vibrator becomes at its maximum and the displacement of the actuator becomes zero. Then the actuator is apart from the rotor at this phase.
3. The vibration velocity of the vibrator is at its maximum in the opposite direction to that of the first step. The actuator is at its minimum size without any contact with the rotor.
4. The vibrator is at the maximum point, but in the opposite direction to that of the second step and the displacement of the actuator is zero. Also in this phase, the actuator does not contact with the rotor.

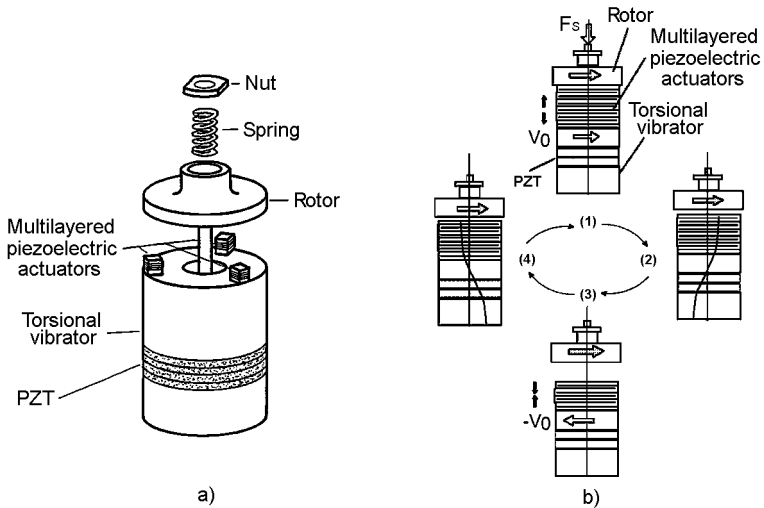


Fig. 3.8: a) Scheme of the HTUM b) principle of the HTUM

The advantage of this kind of HTUM is that since the two piezoelectric elements are independent of each other, the output of the motor can be changed accordingly by adjusting only one of the transducers. The vibration Lissajous figure of this motor depicted in Fig. 3.9 illustrates this point.

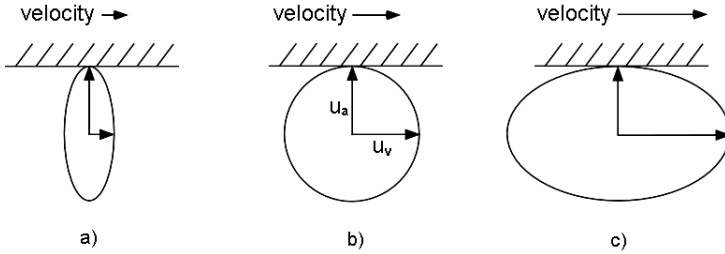


Fig. 3.9: The contact surface of the actuator at different vibration amplitude ratios: u_v is the amplitude of the vibrator and u_a the amplitude of the actuator: a) low speed, c) high speed

Another sandwich transducer can also be used for the stator, where longitudinal and torsional piezoelectric elements are built in and their resonance frequencies coincide with each other [UNM87]. The combination of two orthogonal bimorph vibrators can also be used for linear ultrasonic motors [Tom87].

3.4.2 Classification by motor function

As presented in the preceding section, ultrasonic motors can be classified according to the excitation but also according to the motor function (linear or rotary). In the following paragraphs, some examples of linear and rotary ultrasonic motors are presented, the majority of them having been the subject of studies within the framework of this thesis work.

Rotary ultrasonic motors

Continuous:

In general, when a vibration source is driven at one position on a closed ring (circular or square) at a frequency corresponding to the resonance of this ring, only a standing wave is excited, because the vibration propagates in two directions symmetrically to the vibration source and these interfere with each other.

When multiple vibration sources are installed on the ring, displacements can be obtained by superimposing all the waves (two waves from each vibration source). Using this superposition principle, we can generate a propagating wave which is a rotation of the standing wave shape, even in a closed ring. In principle, the excitation at only two parts of the ring is sufficient to generate a traveling wave. However, in practice, the number of the vibration sources is increased to as many as possible to increase the mechanical output. The symmetry of the electrode structure needs to be considered.

Figure 3.10 shows the famous Shinsei motor [Shi87]. By means of the traveling elastic wave induced by a thin piezoelectric ring, a ring-type slider in contact with the surface of the elastic body bonded onto the piezoelectric is driven in both directions by exchanging the sine and cosine voltage inputs. Another advantage is its thin design, which makes it suitable for installation in cameras as an automatic focusing device. Developments on the analytical and numerical modeling as well as the control and driving methods for this type of motor have been the subject of research studies within the laboratory and led to a master project [FerMs] and a thesis dissertation [Bul05].

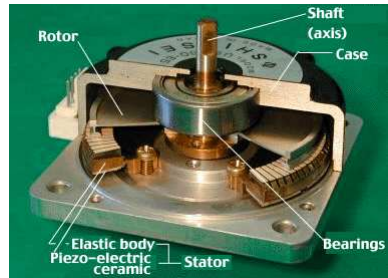


Fig. 3.10: Shinsei ultrasonic motor

Stepping:

These types of motors are based on the phenomenon that an object on a vibrating body moves to the nodal point of the vibration and rests there. The use of circular structures (i.e. ring, disk or cylinder) as a stator element simplifies the motor structure. The operating principle of the motor is based on a piezoelectric actuator that converts electrical energy into mechanical energy in the form of standing vibrations of an elastic body with a frequency in the ultrasonic range. Another body is pressed against the vibrating body by a normal force and the

vibrations are transformed into a step by step motion by the way of small leaps of the rotor's teeth. Figure 3.11 shows the principle of a step motion for the ultrasonic motor. When the electrode A is activated by an AC voltage, a standing wave vibration is created in the stator (dashed curve). When the excitation is switched to the electrode B, a spatial phase shift of the standing wave vibration occurs (solid curve). Thus, the rotor moves from the point P_1 to the point P_2 , which corresponds to one step. By exciting the electrodes one after the other in sequence, the rotor rotates step by step along the stator surface. The direction of the motion can be reversed by changing the phase-shift sequence.

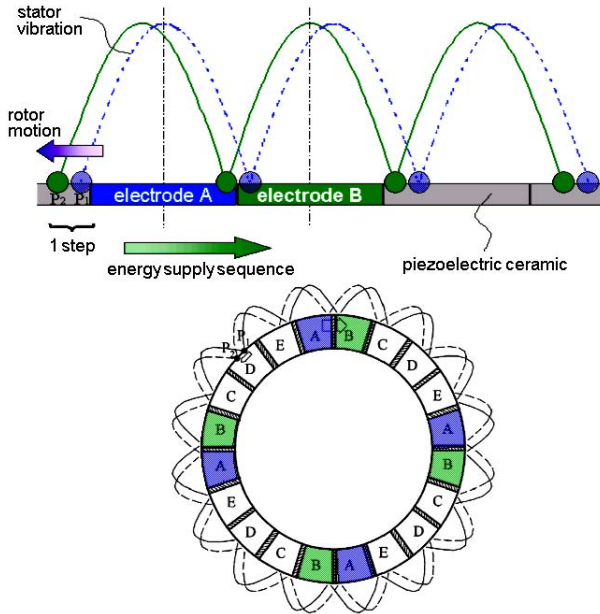


Fig. 3.11: Operating principle of the step by step ultrasonic motor

The Fig. 3.12a shows a prototype built at the laboratory within the framework of a student project about a step by step ultrasonic actuator [KruMs]. In order to determine the stator vibration modes, the software ANSYS [Ans81] has been used. The result obtained for the $n=10$ mode of vibration is presented in Fig. 3.12b.

The applied voltage to the piezoceramic is about 283 V. The resonance frequency found is about 23.2 kHz. Finally, Fig. 3.12c shows the distribution of the standing wave for the $n=10$ mode of vibration found through speckle interferometry. The 10 wavelengths are uniformly distributed in the stator. The amplitude of vibration is $0.1 \mu\text{m}$. The frequency of this vibration mode is about 19.8 kHz for an applied voltage of 79.8 V (peak to peak). More detailed information about the results of this study can be found in [Fer06].

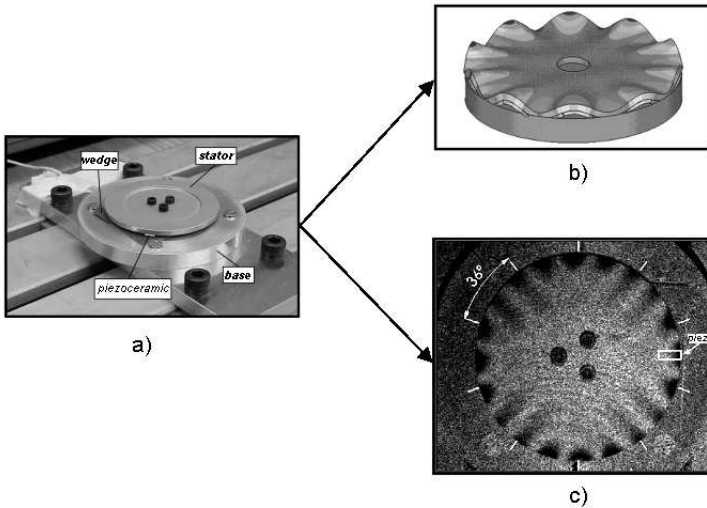


Fig. 3.12: a) prototype built at the laboratory, b) vibration mode for $n=10$ obtained with Ansys, c) experimental result through speckle interferometry

Other typical examples of these types of motors can also be found in the literature [Nak97], [LIP98] and [MKH96].

Non-contact:

Since objects levitate at a distance of several tens to hundreds of micrometers above a radiating surface, this phenomenon is called "near field acoustic levitation". In the case of a non-contact ultrasonic motor, the vibrating body is

actuated by a piezoelectric element and emits an acoustic wave in the ultrasonic range [Vil05]. In order to obtain a movement of the object in levitation (rotor), this plate does not only vibrate in the vertical direction but also in a transverse mode, which makes it possible to obtain an output mechanical torque. The levitation force can be considerable and even objects of a few kilograms can be levitated.

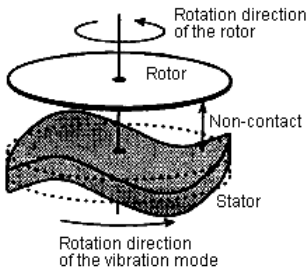


Fig. 3.13: A non-contact type ultrasonic rotary motor

Figure 3.13 shows the fundamental set-up of the non-contact type ultrasonic rotary motor [HYO93]. The rotor made of the light thin rigid paper is set with a small gap on the stator made of the piezoelectric ceramic disk. The stator is vibrating flexurally in the direction vertical to the disk-surface, and the vibration mode rotates in the circumferential direction. The sound waves are radiated from this traveling flexural waves, and the radiation pressure of the sound waves are assumed to act as a driving force of the ultrasonic motor.

Linear motors can also be designed using the same principle. This will be explained at the end of the chapter, giving in particular an example of non-contact ultrasonic linear motor using the radiation pressure effect.

Linear ultrasonic motors

Continuous:

Rotary traveling wave motors, which are used in the lens drives of autofocus objectives produced by Canon, have been well known for many years. The same operating principle can be used for a linear motor, see Fig. 3.14a [HSH98], [NEY90]. An other type of ultrasonic linear motor using a traveling wave can be achieved by pressing a linear rod tangentially onto the stator of a rotary motor, as shown in Fig. 3.14b [HS96]. Unfortunately, this motor construction suffers from its complexity and low efficiency. Thus, no linear traveling wave motor made

its way to market until today. Some new proposals, e.g. [Cla99], use Rayleigh waves instead of bending waves. These devices can be miniaturized easily and thus may be quite successful in the future.

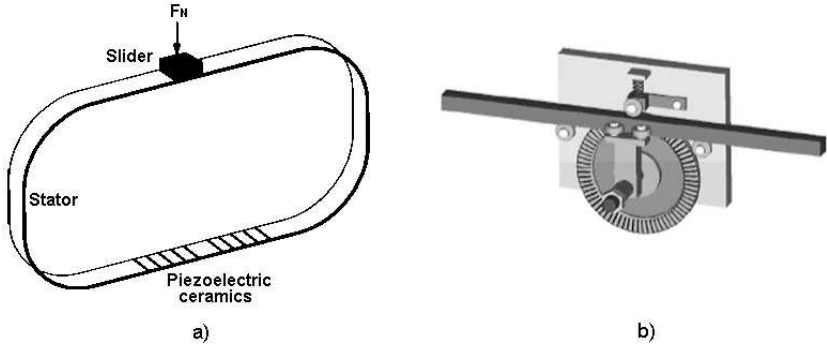


Fig. 3.14: Traveling wave linear ultrasonic motors: a) linear TWUM with ring-type stator, b) linear TWUM with a straight rod pressed tangentially onto rotational symmetric stator

The study of this type of motors has also been the object of a paper based on the research undertaken within the laboratory and presented in [Fer02].

Inchworm:

Inchworm motors were first introduced to the commercial market by Burleigh Instruments [MW75], [HW00]. An inchworm motor uses piezoelectric properties to perform multiple steps at high frequencies to realize large displacement and velocity. Figure 3.15 shows the schematic operation diagram of a typical inchworm motor. The motor consists of the left and right clamping actuators (LCA and RCA) which grip, when extended, onto a shaft to provide a positive holding force. Between the two clamping actuators is the longitudinal piezoelectric vibrator (LPV) providing the extension and contraction motion for the system. Referring to Fig. 3.15, the operating cycle is as follows:

1. The LCA is extended to clamp onto the shaft

2. The LPV extends to provide a positive step
3. With the LPV extended, the RCA extends to clamp onto the shaft
4. The LCA then releases the shaft
5. The LPV contracts to bring the rear of the motor into its advanced position
6. The LCA then extends to provide a positive holding force
7. The RCA contracts to complete the cycle

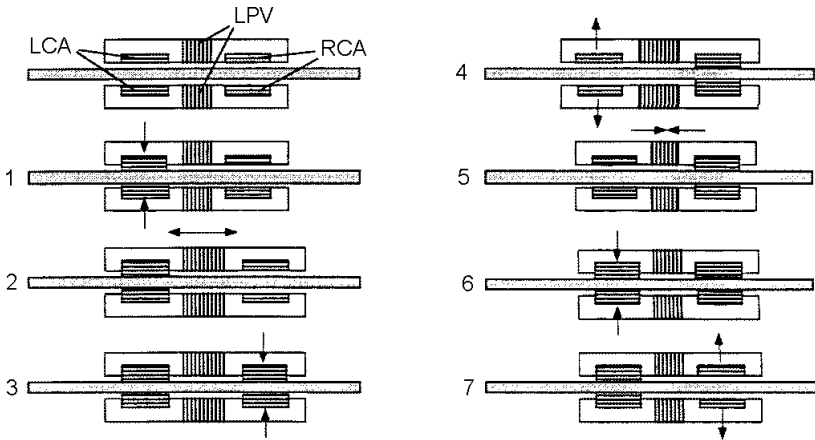


Fig. 3.15: Schematic operation diagram of an inchworm motor

Continuous motion is realized through repetition of the cycle. A positive holding force is achieved by applying a positive DC voltage to both of the clamping actuators (similar to positions 3 and 6 in Fig. 3.15). The motor is free to slide when a negative DC voltage is applied to both clamping actuators. Because of the capacitive nature of the piezoelectric ceramics, the hold and free states can be achieved with very little power consumption. There are two ways to control the velocity of the motor. One method is to vary the step size per cycle by adjusting the voltage across the LPV. The second method is to vary the steps per second by adjusting the frequency of operation. For large motions, the operating cycle

described in Fig. 3.15 is used. The direction of the motor is reversed by switching the left and right clamping actuator signals. For precise microscopic motion, one clamping actuator is clamped while the load bearing side is free (as in position 2 in Fig. 3.15). Voltage across the LPV can then be used for precise motion. Internal position sensing can be added to the motor to increase the resolution of the micro-motion.

Micro-push:

An other group of linear piezoelectric motors are the so-called micro-push motors. Herein, elliptical motions of surface points are generated by the superposition of extension and bending modes of oscillating structures. By pressing a slider against the driving tip of the actuator, these microscopic small motions are transformed into a macroscopic linear motion through friction forces.

A very simple working principle to achieve the desired elliptic motion is given in Fig. 3.16 [Vis81]. This motor is marketed by Nanomotion [Nanom].

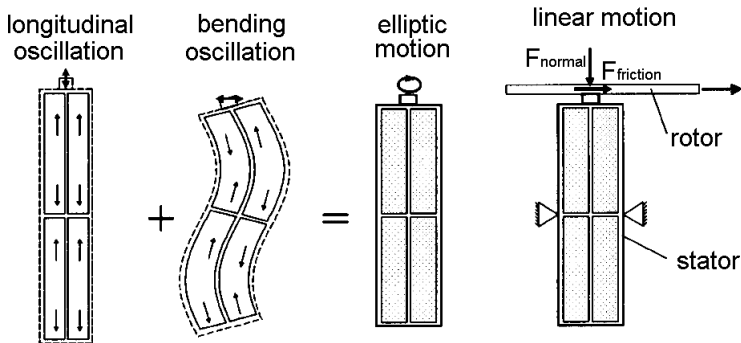


Fig. 3.16: Micro-push motor using a piezoelectric rectangular plate

In [TT95], a motor that uses radial and non-axisymmetric vibrations of an annular plate to achieve elliptic motions at two points lying opposite each other has been designed. Another micro-push device using two stacks of piezoelectric elements

that are positioned perpendicular to each other to produce the desired elliptic motion of the driving tip is depicted in Fig. 3.17 [UT93], [Kur98].

Two bolt-clamped Langevin transducers are arranged in orthogonal manner for high output mechanical power. When the two vibrators operate in-phase, the tip of the transducer vibrates along the center line which is drawn by a dotted and broken line. This vibration direction is normal to a driving surface. On the contrary, if the vibrators operate at anti-phase, the transducer tip moves in orthogonal direction of the line. This component is tangential to the driving surface. For the operation of an ultrasonic motor, the two vibrators are driven by two electrical sources. The two drivers have the same

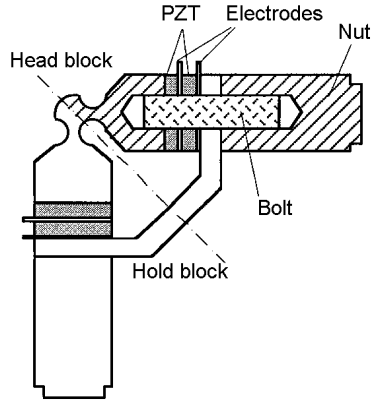


Fig. 3.17: Micro-push motor using piezoelectric stacks

frequency, and they are tuned to the resonance of the transducer. They have a temporal 90 degrees phase shift with respect to each other, so that two vibration modes are excited. As a result, the tip of the transducer moves in an elliptical motion. The rotation direction of the elliptical motion is changed by the phase relation of the electrical sources of +90 degrees or -90 degrees.

This type of actuation system and its corresponding operating principle are those which have been chosen within the framework of this thesis (as design and model) and will be presented in the Chapters 4 and 5.

Finally, a last micro-push type motor is presented. This motor has been studied in the laboratory because of its simplicity and very interesting characteristics. The piezoelectric Elliptec motor [Ellip] consists only of a stator; the rotor (slider) is not necessarily considered as an integral part of the motor. In this micro-push device, the slider receives many thousands of tiny thrusts per second from the stator. These micro-pushes are generated using a piezoelectric element in combination with a mechanical resonator. In the Elliptec design, a multilayered piezoelectric ceramic is inserted into a long mechanical resonator made from

aluminum. When the piezoelectric ceramic is excited with an appropriate AC signal, it generates mechanical oscillations which are amplified by the resonator in a manner that the actuator tip performs flat-elliptical motion in the micrometer range. Figure 3.18 illustrates the Elliptec motor as well as its operating principle.

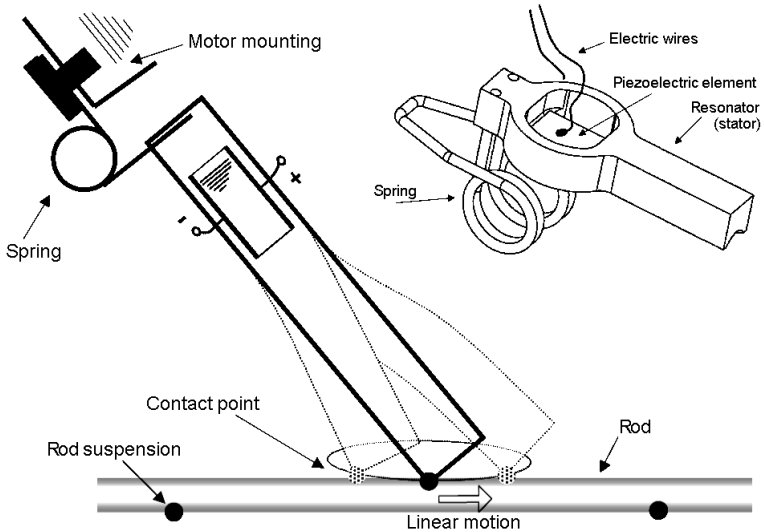


Fig. 3.18: Elliptec motor and its operating principle

Simulations have been realized and the harmonic response obtained shows that there are two natural frequencies located at about 83kHz and 100kHz . At an operating frequency of 83kHz the slider moves in one direction and at a frequency of 100kHz the slider moves in the opposite direction. Figure 3.19 presents the deformations and the Elliptec prototype. More complete results are presented in a conference paper [Fer03].

Stick and slip:

Stick and slip motors have several advantages which make them attractive for

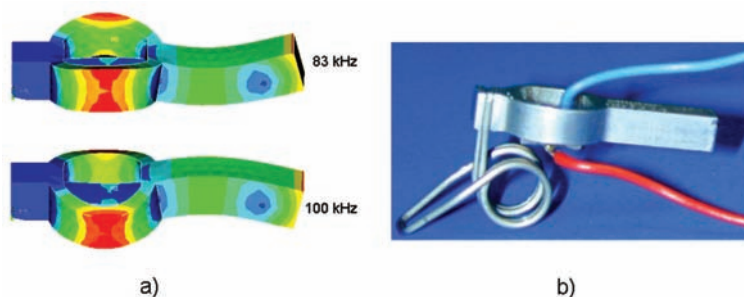


Fig. 3.19: Elliptec actuator: a) harmonic responses, b) Elliptec prototype

many purposes. They are simple (few components, low cost material, etc.), they have an intrinsic high resolution and rigidity, the guiding and driving functions can be combined and long displacements are possible [BC98], [Poh87]. An inertial mass (m) is supported and guided by deformable legs (piezoelectric ceramics) as shown in Fig. 3.20. Two modes of operation are defined, stepping- and scanning-modes. In the stepping-mode, each step consists of a slow deformation of the legs followed by an abrupt jump backward. During the slow deformation, the mass follows the legs because of friction (stick), whereas it cannot follow the sudden jump because of its inertia (slip). The stepping mode allows long displacements at a relatively high speed, but the resolution is limited. Once the position is within less than a step distance of the target, the legs are deformed slowly until the final position is reached. In this mode, called scanning-mode, the resolution is better and is equivalent to a fraction of a step.

A possible application of a stick and slip actuation system is presented in Fig. 3.21, representing a linear stage for micro-positioning [Ber04].

A motor, based on a similar operating principle is marketed by Owis [OWIS].

Non-contact:

As explained previously, there is a category of motors known as non-contact

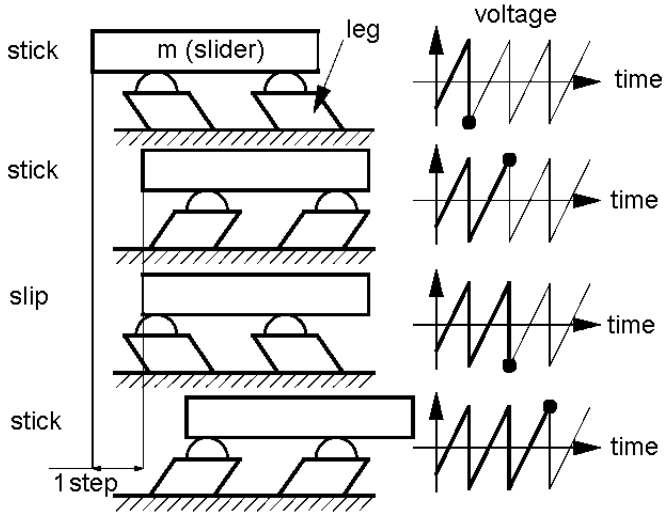


Fig. 3.20: Operating principle of a stick and slip motor

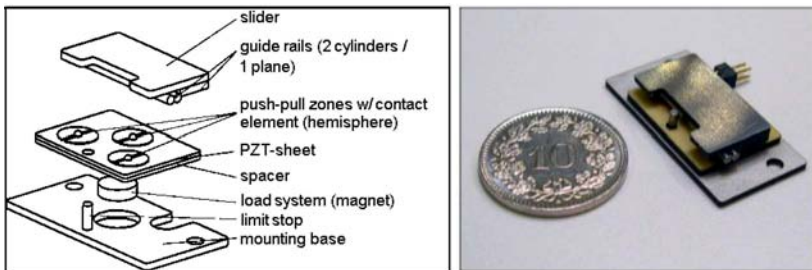


Fig. 3.21: Application example: linear stage for micro-positioning

ultrasonic motors. It has been shown how to obtain a rotary movement using the phenomenon of near field acoustic levitation. But it is also possible to design linear motors. Figure 3.22 shows a schematic diagram of a non-contact transportation system which uses a flexural traveling wave. The operation mechanism can be explained as follows [HKU98]. The traveling sound field in the gap produces two unidirectional forces on the object. One is in the normal direction and levitates the object, and the other induces near-boundary streaming along the sur-

face of the object. The velocity gradient of the near-boundary streaming on the surface of the object produces a viscous force which causes the object to move in the horizontal direction. If the plate begins to vibrate, the object is quickly levitated and gradually accelerated in the same direction by the viscous force. Non-contact ultrasonic linear motors can also be obtained using standing waves as explained in [Hu01].

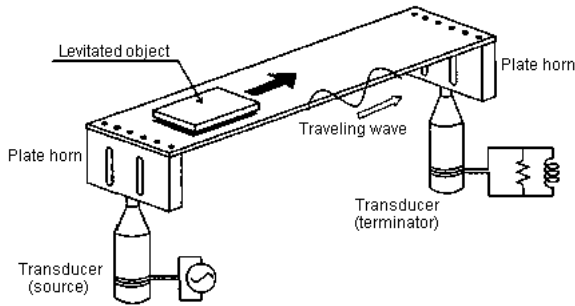


Fig. 3.22: A non-contact type ultrasonic linear motor

Moreover, the effect of radiation pressure can be used in other applications. Many researchs were carried out on bearings without contact to obtain guidance without friction forces. A thesis work relating to a linear slider bearing has been in particular carried out. The piezoelectric elements are placed on the slider as shown in Fig. 3.23b. The slider is then guided by levitation on a glass rail (Fig. 3.23a). For more details about this study, see [Wie01]. A similar application but using acoustic streaming relates to micro-pumps [Ngu98].

Finally, after this outline of the various types of ultrasonic motors and the different possible applications, the flowchart in Fig. 3.24 presents an overall summary of the ultrasonic motors classification. This classification is a proposal made by the author. Of course, other classifications could be made, in particular by adding interactions between the various groups presented in Fig. 3.24.

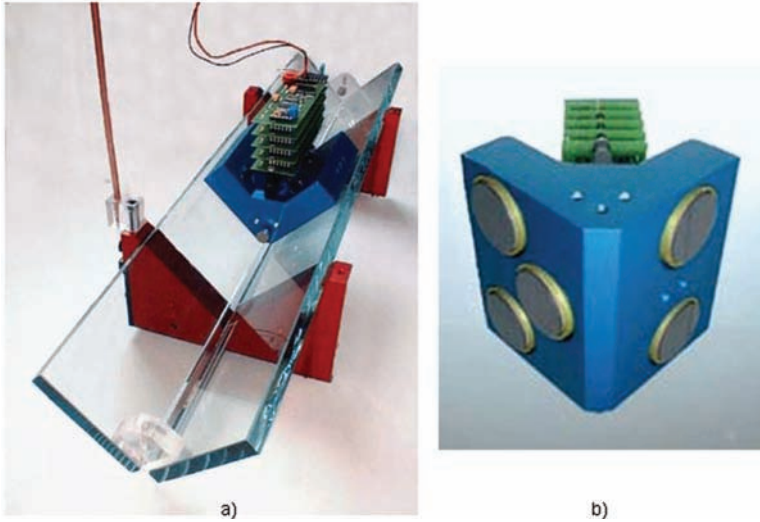


Fig. 3.23: Linear slider bearing: a) complete system with glass rail ; b) bottom view of the slider with five bearing elements

3.5 Conclusion

The principle and classification of several ultrasonic motors have been briefly described. Of course, this list is not exhaustive but already gives a good overview of different configurations and operating principles of ultrasonic motors. Furthermore, ultrasonic motors have not yet demonstrated their full potential, because they are still in the developing stage. However, they are being widely studied and developed for their specific characteristics. For this purpose, limits to performance shown by torque, efficiency and output power should be analyzed theoretically and experimentally. A better efficiency could be obtained for example by changing the construction or vibration amplitude distribution of the stator. In order to achieve this goal, modeling is necessary. This work is treated in the next chapter, where a micro-push ultrasonic motor developed in the laboratory is taken as a case study. Thereafter, based on this model, a sensitivity analysis will be undertaken and an optimization study will be carried out (Chapter 5).

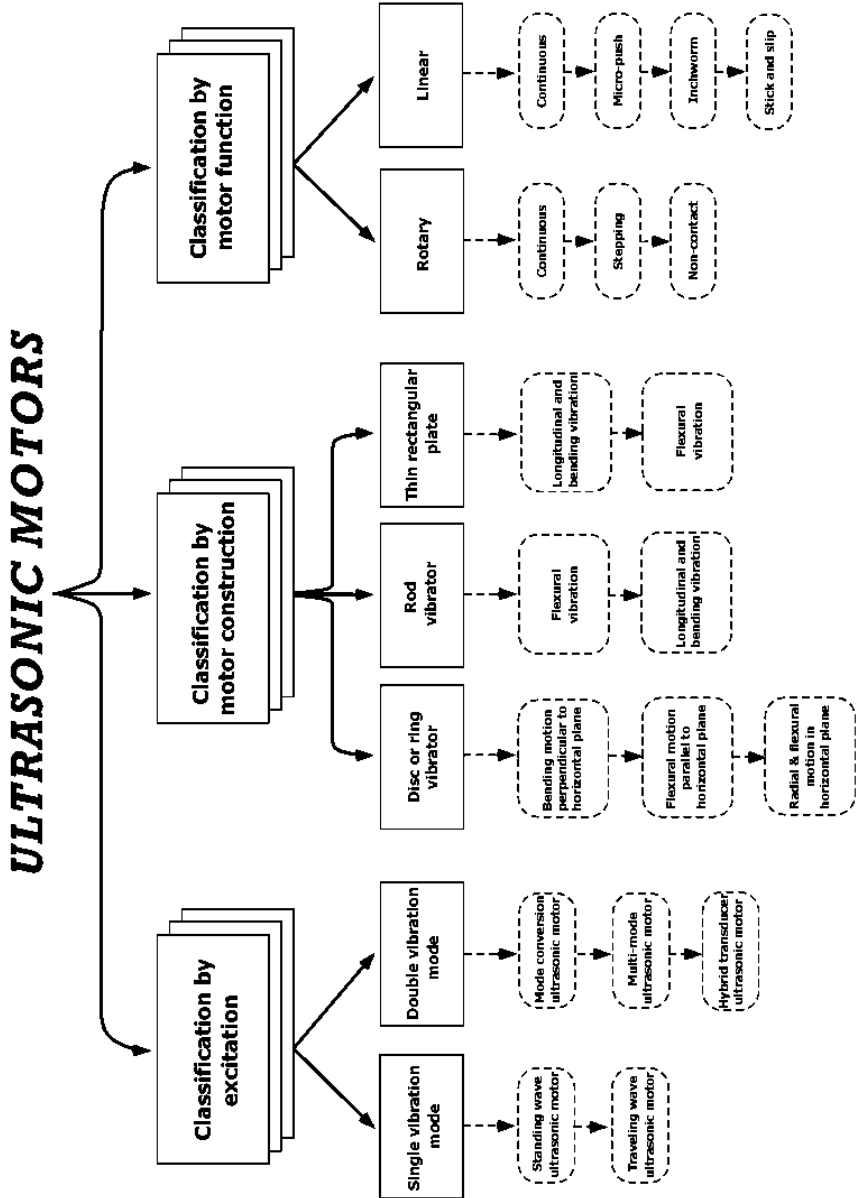


Fig. 3.24: Classification of ultrasonic motors

4. ULTRASONIC LINEAR MOTORS: MODELING, SIMULATION AND VALIDATION

4.1 Introduction

In this chapter, theoretical modeling and simulations of ultrasonic linear motors are presented. Only the vibrator (piezoelectric ceramics and stator) will be taken into account. Contact problems between stator and rotor (slider) are not treated here. However, many studies dealing with this research field can be easily found in the literature [Let94], [MMF96] and [Hel98]. So, first, standing and traveling waves will be briefly presented, since the majority of the motors uses one or the other wave type to generate the stator vibration and thus obtain the elliptic trajectory of the points on the surface of the stator. Then, electric equivalent circuit will be presented with the aim of giving a general idea of another way of modeling the vibrator analytically. Numerical modeling using finite element method (FEM) is then introduced and developed. Simulations of an ultrasonic linear motor are then performed and experimental results on a prototype built at the laboratory are presented. Finally, validation of the theoretical modeling is carried out, comparing both simulations and experiments.

4.2 Theoretical modeling

4.2.1 Standing and traveling waves

Generally, ultrasonic piezoelectric motors can be designed to use either traveling waves or standing waves to generate motion. Piezoelectric standing wave motors use a combination of flexural, torsional or longitudinal vibrations of a piezoelectric actuator. One vibration produces a normal force while the other generates motion that is perpendicular to the normal force. This combination creates a friction based driving force between one stationary component, the vibrator, and the object to be moved, the slider. On the other hand, in a piezoelectric traveling wave motor, traveling waves are generated and propagate in both directions. Such waves can be classified into two general types. The first type is known as Rayleigh wave [Rao84]. An analogy to this kind of wave are the earthquakes. The other type of wave known as flexural wave ([Sas85] and [UT93]) propagates with a snake-like motion. For both Rayleigh and flexural waves, a point on the surface will move following an elliptical trajectory. It is this elliptical motion that provides the drive in traveling wave motors. In the following sections, these two wave types are described more in details.

Ultrasonic linear motors using standing waves

A standing wave pattern is a vibrational pattern created within a medium. The vibrational frequency of the source causes reflected waves from one end of the medium that interfere with incident waves from the source. In this manner, specific points along the medium appear to be standing still. Because the observed wave pattern is characterized by points which appear to be standing still, the pattern is often called a "standing wave pattern". Such patterns are only created within the medium at specific vibration frequencies; these frequencies are known as harmonic frequencies. At any frequency other than a harmonic frequency, the interference of reflected and incident waves results in a resulting disturbance of the medium which is irregular and non-repeating.

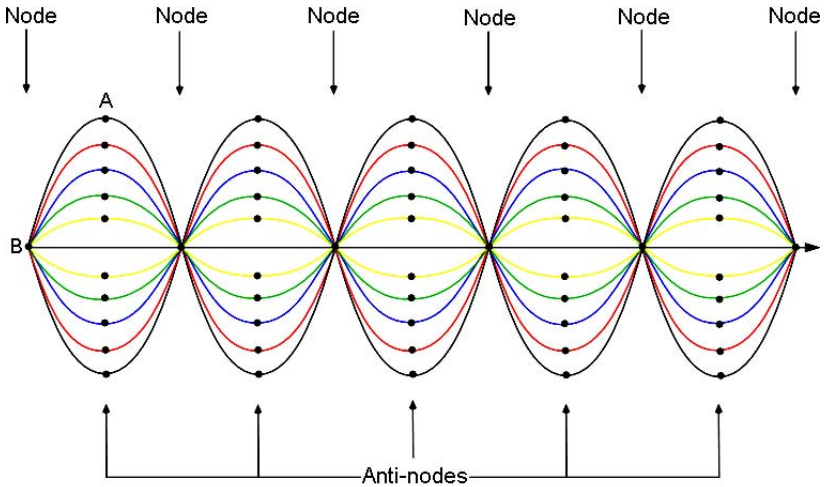


Fig. 4.1: Standing wave pattern

Figure 4.1 depicts a standing wave pattern in a medium. A snapshot of the medium over time is depicted using various colors. Note that point A on the medium moves from a positive to a negative displacement over time. The diagram only shows one-half cycle of the motion of the standing wave pattern. The motion would continue and persist, with point A returning to the same positive displacement and then continuing its back-and-forth vibration between the up to the down position. Note that point B on the medium is a point which never moves. Point B is a point of no displacement; such points are known as nodes. Nodes and anti-nodes should not be confused with crests and hollows. When the motion of a traveling wave is discussed, it is customary to refer to a point of large maximum displacement as a crest and a point of large negative displacement as a hollow. These represent points of the disturbance which travel from one location to another through the medium. On the contrary, an anti-node is a point on the medium which is staying at the same location. Furthermore, an anti-node vibrates back and forth between a large upward and a large downward displacement.

Driving process of standing wave motors:

The first step in understanding how standing wave motors work requires better knowledge of how the oscillating motion of a vibrator surface point (tip) generates motion of the slider. The curves shown in Fig. 4.2 represent the motion of a single point at the end of the tip that is in contact with the surface of the slider.

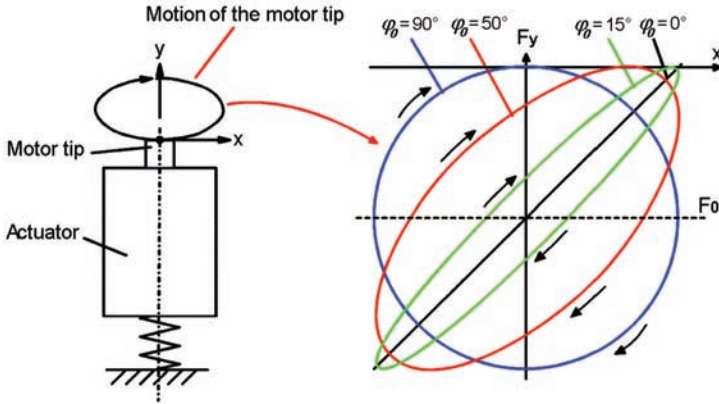


Fig. 4.2: Motion of the motor tip for different phase angles

The tip motion is the product of a two-dimensional vibration at the interface between the vibrator tip and the slider. The motion in each direction can be represented with a sinusoidal function. As the vibration in both directions has the same frequency, the phase between them is constant. The amplitudes of each of the two components as well as the phase between them are the three quantities that determine the shape of the curves as shown in Fig. 4.2. For simplicity, the amplitudes are normalized. During operation, the vibrator is preloaded against the slider (through a pre-stressing force) in such a way that the tip does not move away from the slider surface. The actuator vibration then causes strain in the actuator, which is experienced as a normal force through the stiffness of the contact point. To generate motion of the slider, the vibrator tip slides back and forth along the slider surface. Vibrator and slider interact via a friction-based force, which depends on the direction of relative motion, the coefficient of friction and

the magnitude of the normal force. The direction of the relative sliding velocity between the tip and the slider changes, which determines the direction of the friction force, which then accelerates (and decelerates) the slider in the respective direction. In order to obtain a continuous slider motion, the average normal force must be larger during the part of the cycle when the tip is sliding in the direction of the desired slider motion. The slider is accelerated more during this part of the cycle than it is decelerated when the tip retracts under the influence of a force smaller than the average normal force. The phase angle between the sliding motion and the normal force controls the time during a cycle when the slider is accelerated and decelerated, because the magnitude of the dynamic normal force influences the amount of frictional force that is present in the system. A relative phase angle of 90° means that the normal force, and thus the friction force, is smaller than the average when the tip moves from the left to the right, resulting in a minimal acceleration in this direction. In this case, the friction force at any time during the second part of the cycle is larger than during the first half, meaning that the acceleration from the right to the left is at a maximum. In addition, at a 90° phase angle, the maximal tip velocity coincides with the maximal friction force. Smaller as well as larger phase angles result in a lesser overall slider acceleration, smaller maximum slider velocity and lower motor efficiency. A phase of 270° reverses the slider direction. The tip motion has then the same shape as shown in Fig. 4.2 for 90° , but the motion is in the opposite direction.

Equation of motion:

The equation of motion can be derived using the driving process described previously. To verify the concept mentioned above and to be able to analyze the influence of phase, sliding motion, normal force and pre-stressing force on the slider motion, a model of this process has to be developed. A model that can be used to obtain the equation of motion for the slider is shown in Fig. 4.3 [Bau01]. The slider (mass m and coordinate x) is accelerated by the friction force F_F . The direction of the friction force depends on the direction of the relative speed of the slider and the vibrator tip. The two main assumptions for creating the slider motion model are that the normal force at the tip is always compressive and that

only sliding friction acts between the vibrator and the slider. A non-compressive normal force would mean that vibrator and slider lose contact, which is a potential complication not taken into account in this model. Furthermore, the impact of the tip coming back onto the slider surface would cause a lot of wear and in addition excite all resonances in the system, which is not desirable.

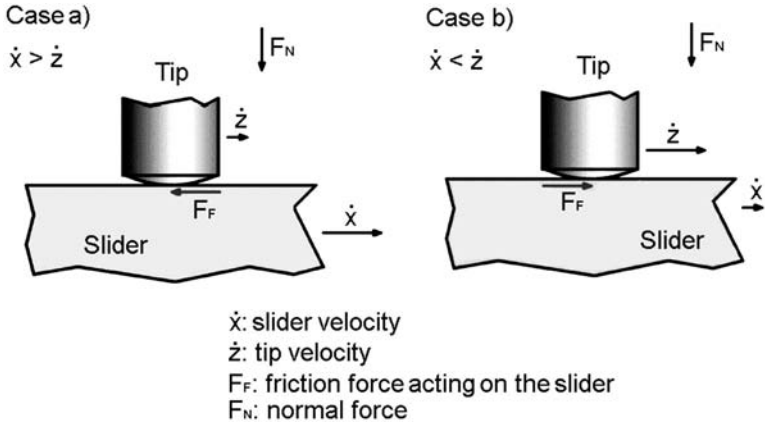


Fig. 4.3: Motion model for the slider

Case a) $\dot{x} > \dot{z}$:

$$m\ddot{x}(t) = -F_F(t) = -\mu F_N(t) \quad (4.1)$$

Case b) $\dot{x} < \dot{z}$:

$$m\ddot{x}(t) = F_F(t) = \mu F_N(t) \quad (4.2)$$

Both cases combined:

$$m\ddot{x}(t) = \text{sign}[\dot{x}(t) - \dot{z}(t)] \cdot F_N(t) \quad (4.3)$$

With:

$$F_N(t) = F_0 + F \cdot \cos(\omega t) \quad (4.4)$$

$$z(t) = z_0 \cdot \sin(\omega t - \varphi_0) \quad (4.5)$$

$$\dot{z}(t) = z_0 \omega \cdot \cos(\omega t - \varphi_0) \quad (4.6)$$

Where:

- $x(t)$: coordinate of the slider (in the direction of slider motion)
- $z(t)$: coordinate of the tip motion (in the direction of slider motion)
- F_0 : pre-stressing force
- F : amplitude of the sinusoidal normal force ($< F_0$)
- z_0 : amplitude of the tip motion
- φ_0 : phase between the tip motion and the force
- m : mass of the slider
- μ : coefficient of friction between the tip and the slider surface
- ω : angular frequency

Substituting equations (4.4) and (4.6) into (4.3) yields the complete equation of motion for the slider:

$$\ddot{x}(t) = \frac{\mu}{m} \text{sign} [\dot{x}(t) - z_0 \omega \cdot \cos(\omega t - \varphi_0)] (F_0 + F \cdot \cos(\omega t)) \quad (4.7)$$

This model is rather simple but makes it possible to define the equation of motion of the slider in the case of a standing wave ultrasonic motor. Other more complex models exist, but this one gives already a general idea of how to model easily the motion of the slider.

Ultrasonic linear motors using traveling waves

A mechanical wave is a disturbance which is created by a vibrating object and subsequently travels through a medium from one location to another, transporting energy as it moves. The mechanism by which a mechanical wave propagates itself through a medium involves particle interaction; one particle applies a push or pull on its adjacent neighbor, causing a displacement of that neighbor from the equilibrium or rest position. As a wave is observed traveling through a medium, a crest is seen moving along from particle to particle as shown in Fig. 4.4. This crest is followed by a hollow which is in turn followed by the next crest. In fact, one would observe a distinct wave pattern (in the form of a sine wave) traveling through the medium. This sine wave pattern continues to move in uninterrupted

fashion until it encounters another wave along the medium or until it encounters a boundary with another medium. This type of wave pattern which is seen traveling through a medium is referred to as a traveling wave.

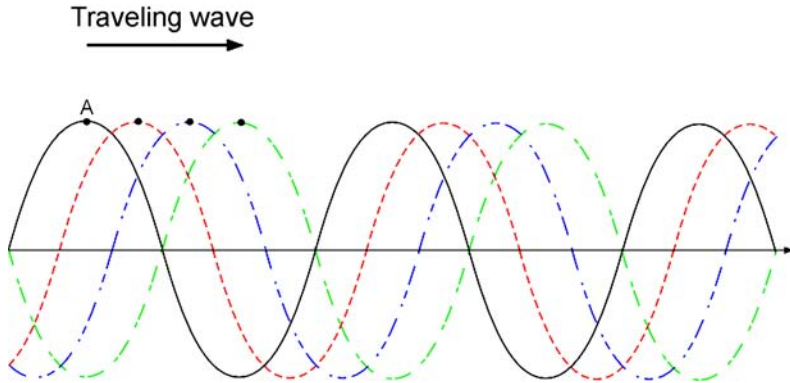


Fig. 4.4: Traveling wave

Note: a traveling wave can be generated by superimposing two standing waves whose phase differs by 90° each other in time and in space.

Driving process of traveling wave motors:

When a slider is pressed against the vibrator, where a traveling wave is propagating, the slider contacts the vibrator only intermittently as shown in Fig. 4.5, because the time constant of the slider is larger than the period at which the vibrating stator is driven. If the slider is movable along the contacting surface and the vibrator has a displacement component parallel to the surface, the frictional force between the two causes the slider to move during the period of contact. At other times during a cycle, the frictional force does not act on the slider because the compressive force between the two parts becomes negative in the direction of the contact and the slider continues the motion.

The vibration amplitude of the ultrasonic vibrator is usually no more than several microns. With regard to the involved forces, Fig. 4.5 shows the normal force F_N

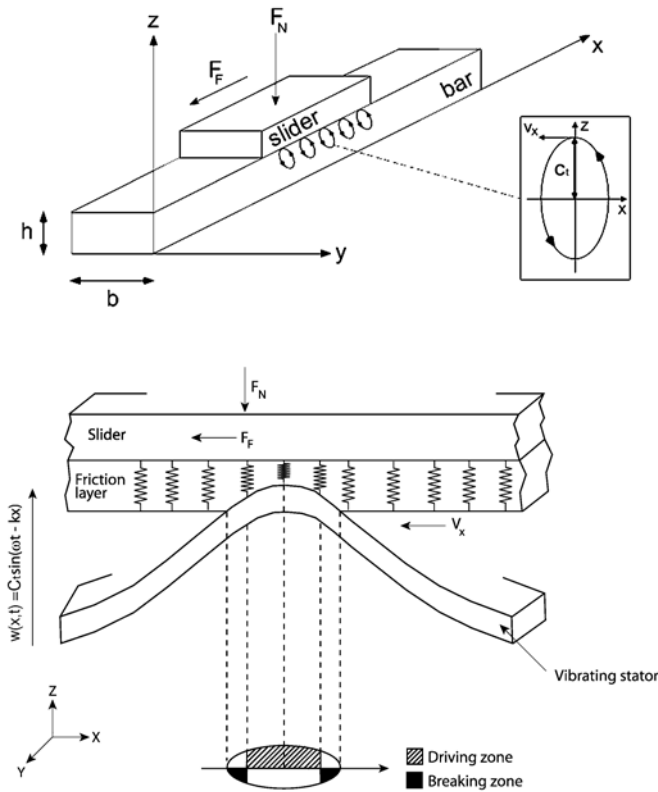


Fig. 4.5: Driving process of linear traveling wave motors

and the friction force F_F acting on the slider. In the contact zone (elliptic shape), the points of the vibrator which have the same tangential speed of the slider make it possible to locate, as shown in Fig. 4.5, the braking and traction zones. The force F_F is produced by the friction between the bar and the friction layer. If the normal force is strong enough, the thrust or torque can be quite large. The x -axis speed v_x is expected to be reduced when the normal force F_N is applied to the slider because the traveling wave is distorted ([HK93] and [KT91]).

Equation of motion:

Theory of beam vibration is used in the analysis of a linear traveling ultrasonic motor [KUM85]. The analysis of beam vibration is complicated because the equation solved includes a fourth-order derivative with respect to x , which is the moving direction axis variable. The wave equation of a bending beam in a homogeneous isotropic solid bar is expressed as [Gra77]:

$$\frac{\partial^4 w}{\partial x^4} + \frac{\rho S_b}{Y_b I_S} \frac{\partial^2 w}{\partial t^2} = 0 \quad (4.8)$$

The solution of (4.8) is:

$$w(x, t) = C_t \sin(\omega t - kx) \quad (4.9)$$

Where:

- w : transverse displacement (in z direction)
- ρ : density of the bar
- S_b : cross section of the bar
- Y_b : Young's modulus of the bar
- I_S : moment of inertia of the cross section
- C_t : constant
- ω : angular frequency of the flexural wave
- $k = \frac{2\pi}{\lambda}$, λ : wavenumber and wavelength, respectively
- b, h : width and thickness of the bar, respectively

In addition to the transverse displacement, the variation in the x axis (longitudinal displacement) is given by:

$$u(x, z, t) = -z \frac{\partial w}{\partial x} = C_t z k \cos(\omega t - kx) \quad (4.10)$$

With the relations (4.9) and (4.10), the trajectory of the points at the surface of the bar can be achieved:

$$\left(\frac{u}{C_t z k} \right)^2 + \left(\frac{w}{C_t} \right)^2 = 1 \quad (4.11)$$

Equation (4.11) shows that the the points move elliptically as shown in Fig. 4.6, just below. By placing a slider in contact with the traveling wave, the slider will be forced to move along with the velocity of the particles at the crests of the traveling wave propagating down the beam. This velocity, when the coupling between the slider is neglected, is obtained by the derivate of (4.10):

$$v_x = -C_t z k \omega \sin(\omega t - kx) \tag{4.12}$$

Equation (4.12) represents the maximum speed reachable by the slider. The slider moves opposite to the wave direction but it can be easily changed by altering the phase difference ϕ to $-\phi$ and vice-versa. The particular case $\phi = 0$ means that the two displacements (u_x, u_z) are driven with the same phase and the elliptical motion is not realized; instead, straight-line motion occurs (standing wave).

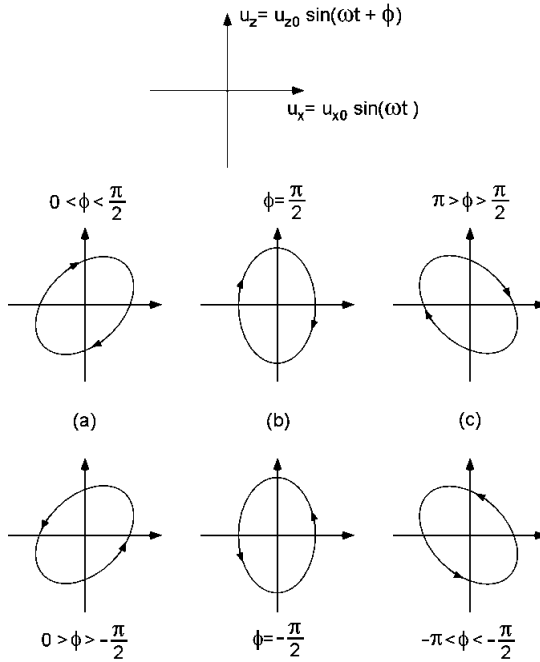


Fig. 4.6: Elliptic displacement motion

Resonance frequency:

Traveling waves are produced by the vibration of the piezoelectric elements glued under the bar (beam). Considering that the cross section inertia of the bar is given by:

$$I_S = \frac{bh^3}{12} \quad (4.13)$$

The resonance frequency f_r can be obtained from (4.8) and (4.9):

$$f_r = \frac{\pi h}{\lambda^2} \sqrt{\frac{Y_b}{3\rho}} \quad (4.14)$$

Equation (4.14) is approximative. The calculation of the exact value is very complex and needs a precise knowledge of the geometry and different material properties of the motor.

In the following section, another method to model the motor analytically is presented. The motor is represented by an electric equivalent circuit, making it possible to simply characterize the motor close to its principal resonance frequency.

4.2.2 Electric equivalent circuit

Introduction

The details involved in the working mechanism of an ultrasonic motor are rather complex and analytical modeling is quite difficult. This is why theory of equivalent circuits is often useful to represent a problem in mechanics in order to determine the static or dynamic behavior of the system. Thus, equivalent circuit method is widely used in the modeling of ultrasonic motors, as it is extremely efficient in solving complex problems. An equivalent circuit model will be presented in this section for the modeling of linear ultrasonic motors.

Electromechanical equivalent scheme

First of all, in describing the behavior of systems that employ piezoelectric ceramics, the equivalent electromechanical scheme represented in Fig. 4.7 is important.

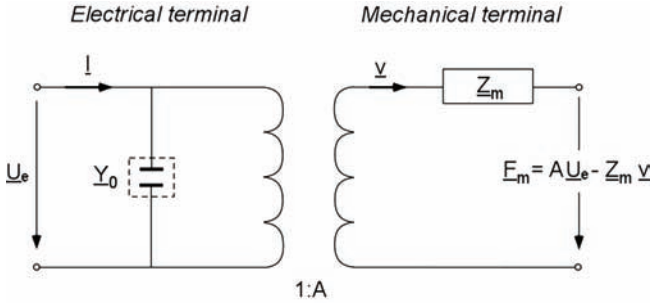


Fig. 4.7: Electromechanical equivalent scheme

This scheme is characterized by the following equations ([Pec95], [Mer81] and [Ros88]):

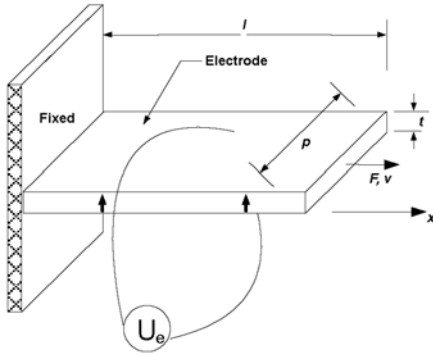
$$\begin{aligned} -\underline{F}_m &= A\underline{U}_e - \underline{Z}_m \underline{v} \\ \underline{I} &= \underline{Y}_0 \underline{U}_e + A\underline{v} \end{aligned} \quad (4.15)$$

Where:

- \underline{F}_m : force at the mechanical terminal
- A: force factor
- \underline{U}_e : voltage at the electrical terminal
- \underline{Z}_m : mechanical impedance of the piezoelectric ceramic
- \underline{v} : velocity at the mechanical terminal
- \underline{I} : current at the electrical terminal
- \underline{Y}_0 : electrical admittance of the piezoelectric ceramic

In the first line of equation (4.15), the first term on the right side is the force generated within the ceramic body, which is equal to the applied voltage \underline{U}_e mul-

multiplied by A . Subtracting the product of the internal mechanical impedance Z_m by the velocity \underline{v} from this force, the result is the force exerted by the motor externally. Thus, the force factor A is the force created when an unit voltage is applied. Moreover, from equation (4.15), $Y_0 \underline{U}_e$ is the current flowing through the capacitor and $A \underline{v}$ is the current which causes the ceramic body to deform. Thus, the force factor A is the current generated when the unit velocity is transmitted to the ceramic body. In general, A depends on the properties and dimensions of the ceramic and how it is used. Taking an example, the expression for A will be analytically determined.



The model (ceramic plate) shown in Fig. 4.8 will be used. With reference to this model, the following relationships exist:

$$\text{Electric field strength: } \underline{E} = \underline{U}_e / t$$

$$\text{Mechanical stress: } \underline{T} = \underline{F} / p t$$

$$\text{Strain: } \underline{S} = \underline{x} / l$$

$$\text{Velocity: } \underline{v} = d\underline{x} / dt = j\omega \underline{x} = j\omega \underline{S} l$$

$$\text{Current: } \underline{I} = p l d\underline{D} / dt = j\omega p l \underline{D}$$

Fig. 4.8: Ceramic plate deformed in its length

Where t , p and l are the thickness, width and length of the ceramic element, respectively. The displacement is represented by x .

Now, substituting these values into equation (4.15), we obtain:

$$\begin{aligned} -\underline{T} p t &= A \underline{E} t - j\omega Z_m \underline{S} l \\ j\omega p l \underline{D} &= Y_0 \underline{E} t + j\omega A \underline{S} l \end{aligned} \quad (4.16)$$

Therefore,

$$\begin{aligned}\underline{T} &= j\omega Z_m \frac{l}{pt} \underline{S} - \frac{A}{p} \underline{E} \\ \underline{D} &= \frac{A}{p} \underline{S} + \frac{Y_0 t}{j\omega pl} \underline{E}\end{aligned}\quad (4.17)$$

Equation (4.17) is identical to the third type of fundamental piezoelectric constitutive equation presented in Table 2.3 with \underline{S} and \underline{E} taken as independent variables (e-form) and with the following constants:

$$c^E = j\omega Z_m \frac{l}{pt} \quad (4.18)$$

$$e = \frac{A}{p} \quad (4.19)$$

$$\epsilon^S = \frac{Y_0 t}{j\omega pl} \quad (4.20)$$

From (4.18), the force factor can be determined. It is given by the multiplication of the width of the ceramic plate p by the piezoelectric constant e , with subscripts 3 for the electric direction and 1 for the mechanical direction taken into account the axes notation presented in Fig. 2.5:

$$A = pe_{31} \quad (4.21)$$

Hence [IEE87]:

$$A = s_{11} d_{31} p \quad (4.22)$$

The above equation for the force factor A is generally determined not only by the dimensions and material properties of the piezoelectric ceramic element but also by the properties of the metal plate with which it is combined (forming the vibrator). Now, a simplifying equivalent circuit can be obtained by incorporating the transformer element into the internal impedance Z_m . This new equivalent circuit, which is then the electric equivalent circuit, is presented in the following section.

Electric equivalent circuit and its components

The electromechanical equivalent scheme presented in Fig. 4.7 can be replaced by an electric circuit, where the vibrator is characterized by an equivalent electrical impedance representing its mass and a capacitor related to its rigidity. Furthermore, this scheme can be completed by taking into account the dielectric and mechanical losses of the vibrator. In this way, an electric equivalent circuit is obtained. It is depicted in Fig. 4.9.

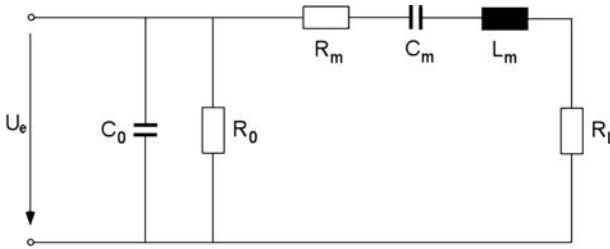


Fig. 4.9: Electric equivalent circuit

This circuit allows to model easily the behavior of a piezoelectric transducer operating at or near its principal resonance frequency. It is composed of three distinct parts:

- the dielectric part, which is composed of C_0 and R_0 , corresponding to the dielectric properties of the ceramic element
- the motional part, which is composed of R_m , C_m and L_m that are specific to piezoelectric materials; the admittance composed of these three components in series is called the motional admittance Y_m
- the dissipative part, which is composed of R_L , corresponding to the mechanical load

The different components of the electric equivalent circuit are now described and defined.

Static capacitance C_0 :

The value of the static capacitance is given by [SK93]:

$$C_0 = \epsilon_0 \epsilon_r \frac{S_{el}}{d_{el}} \quad (4.23)$$

where ϵ_0 is the free space permittivity, ϵ_r the relative permittivity, S_{el} the surface of the electrodes of the piezoelectric ceramic and d_{el} the distance between the electrodes.

Dielectric resistance R_0 :

This resistance, which is in parallel with the static capacitance, represents the dielectric losses. For a given frequency, it is given by [UT93]:

$$R_0 = \frac{1}{\omega C_0 \tan \delta} \quad (4.24)$$

where ω is the angular frequency of the considered frequency and $\tan \delta$ is the dielectric dissipation factor.

Motional resistance R_m :

The motional resistance R_m represents the mechanical losses of the vibrator. It also includes the losses by friction in the air, the losses due to the glue between the ceramic and the stator. The losses caused by the welding of the connection wires as well as the losses in the electrodes.

Motional capacitance C_m and motional inductance L_m :

C_m and L_m represent the rigidity and the inertia of the vibrator, respectively.

They are given by [Pec95]:

$$C_m = \frac{A^2}{K} \quad (4.25)$$

$$L_m = \frac{m_v}{A^2} \quad (4.26)$$

where K is a spring constant and m_v the mass of the vibrator, linked by the following relation:

$$\omega_r = \sqrt{\frac{K}{m_v}} \quad (4.27)$$

with ω_r the resonant angular frequency of the vibrator.

Load resistance R_L :

The resistance R_L represents in a very simplified way the load imposed to the vibrator.

Resonance frequency:

As explained earlier, in order to achieve high efficiencies of ultrasonic motors, they should be driven at or close to the frequency that will create resonance between C_m and L_m in the equivalent circuit. This frequency is called the resonance frequency f_r and is given by:

$$f_r = \frac{\omega_r}{2\pi} = \frac{1}{2\pi\sqrt{L_m C_m}} \quad (4.28)$$

The anti-resonance frequency is given by:

$$f_a = \frac{1}{2\pi} \sqrt{\frac{C_0 + C_m}{L_m C_0 C_m}} \quad (4.29)$$

These frequencies have been introduced in Chapter 2 and have already been explained in details (see Fig. 2.4).

Other parameters:

The sharpness of the resonance is indicated by the electrical quality factor Q given by:

$$Q = \frac{\omega_r L_m}{R_m} = \frac{1}{\omega_m C_m R_m} \quad (4.30)$$

Moreover, from f_r and f_a , the electromechanical coupling factor k can be determined using the following equation:

$$k = \sqrt{\frac{C_m}{C_m + C_0}} = \sqrt{1 - \left(\frac{f_r}{f_a}\right)^2} \quad (4.31)$$

It is then possible, using an analogical tool for the simulation of electric circuits, to study the behavior of the equivalent circuit according to its parameters.

Comments:

In the preceding sections, analytical modeling of linear ultrasonic motors has been presented. As it has been shown, equations defining the vibrator or even the motion of the slider are sometimes complex (4th order derivative wave equation for example). Moreover, each structure or working principle of ultrasonic motors may be different (using standing or traveling waves, considering small leaps of the stator in the contact zone [KruMs], ...) requiring different analytical modeling strategies and using most of time too restrictive assumptions. Furthermore, the analysis of an ultrasonic motor using an electric equivalent circuit requires some care. Indeed, it should be specified that for the piezoelectric stator of an ultrasonic motor, the force factor A is more difficult to be determined analytically that presented in this work, the deformation mode of the stator being generally more complex. Moreover, the real influence of the slider on the resonance frequency of the stator has not been taken into account (rigidity variations due to the radial forces, effect of non-continuous contact, conditions of friction between stator and rotor, ...). More complete and advanced equivalent circuits making it possible to take into account all these parameters exist ([SK93], [UT93]) but

they are limited because they require the numerical knowledge of the components constituting the circuit and these can only be determined experimentally.

So, the analytic way of modeling has not been used within the framework of this thesis for the modeling of linear ultrasonic motors, in particular for the different reasons explained previously but also taking into account the optimization study which would then have been very difficult, even impossible. This is the reason why numerical modeling has been chosen and will be explained in the next sections. Nevertheless, the analytical approach is an interesting way to describe piezoelectric transducers and this is why it has been used for the modeling of piezoelectric transformers, which will be presented in Chapter 6.

4.2.3 Numerical modeling using FEM

Introduction

The finite element method (FEM) is an approximation of the governing equations that is particularly well suited to computation. Whereas the differential form of the governing equations requires the solution to be exact at every point in space, the FEM is based on an equivalent variational statement that enforces the accuracy of the solution in a weighted average sense over small sub-regions of the space (the finite elements). Since the problem is replaced by a simpler one, only an approximate solution rather than the exact one will be determined. Nevertheless, it is often possible to improve or refine the approximate solution by spending more computational effort and time.

The analytical models used to simulate the mechanical and electrical behavior of piezoelectric motors generally introduce simplifying assumptions that are often incomplete or invalid (as mentioned previously). Thus, finite element modeling is being widely adopted in the design of ultrasonic motors. For the 3-D simulation of piezoelectric motors, the complete set of fundamental equations governing piezoelectricity has to be solved. The finite element method is however sufficiently general to handle these differential equations.

Finite Element Method (FEM)

FEM has been preferred in our study because it is capable of handling complex geometries and boundary conditions. In the FEM, the continuous structure of the piezoelectric motor is discretized into a number of finite elements. Besides the mechanical degrees of freedom (represented by the nodal displacement vector γ), an electrical degree of freedom ξ (nodal potential vector) is added at each node. The FEM solution vector consists of the displacement values and electric potential values at the different nodes. The displacement and voltage fields at arbitrary locations within the elements are assumed to be a linear combination of the nodal values of these fields, respectively. The coupled electromechanical field is described by means of the linear piezoelectric constitutive equations. The analysis then proceeds to writing a set of differential equations of motion and Maxwell's equations [Abb98], [Ler90]. Basic equations for the motion of the motor can be written in matrix form as follows [AH70]:

$$\begin{aligned} [M_M] \frac{\partial^2 \{\gamma\}}{\partial t^2} + [K_1] \frac{\partial \{\gamma\}}{\partial t} + [K_2] \{\gamma\} + [K_3] \{\xi\} &= \{F_V\} \\ [K_3]^T \{\gamma\} + [K_4] \{\xi\} &= \{Q_E\} \end{aligned} \quad (4.32)$$

Where:

- M_M**: Mass matrix
- K₁**: Damping matrix
- K₂**: Stiffness matrix
- K₃**: Piezoelectric matrix
- K₄**: Dielectric matrix
- F_V**: Nodal mechanical force vector
- Q_E**: Nodal electrical charge vector
- γ : Nodal displacement vector
- ξ : Nodal potential vector

Equation (4.32) can be solved by applying FEM. Numerical modeling has been carried out using ANSYS software [Ans81] which is used to create a solid finite

element model and make different analyses. The next sections describe the structure and the numerical model of the linear ultrasonic motor chosen in our study and then the different simulations carried out are presented.

Structure and numerical model of the linear ultrasonic motor

The FE model of the motor (vibrating part) is represented by the Fig. 4.10. Figures 4.11 and 4.12 show more in details the vibrating part of the motor which is composed of the piezoelectric ceramics and the vibrator (stator). Moreover, dimensions and materials of the vibrator and the piezoelectric ceramics used for the simulations are given in Table 4.1 and in Appendix A.

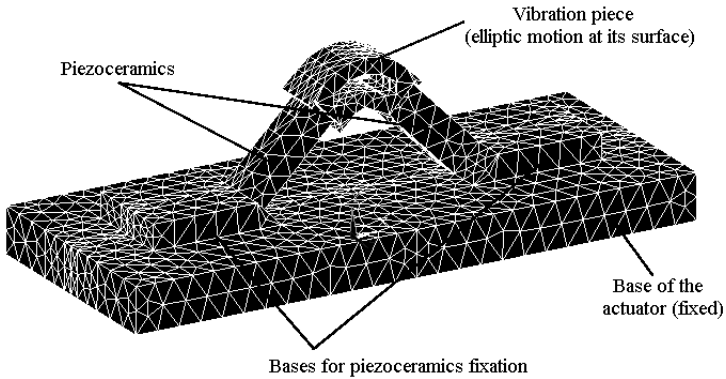


Fig. 4.10: FE model of the ULM

The piezoceramics are arranged to yield two displacements in longitudinal motion and by providing a phase difference between them, elliptical motion is obtained. Multilayered piezoceramics are used because they can yield relatively large displacements at lower driving voltages. Then, the flat elliptical displacement motion on the surface of the vibrator (stator), obtained thanks to the standing waves created by each piezoceramic, in contact with a slider, is used to yield the linear motion of the slider as already explained in section 3.4.2 (Fig. 3.17).

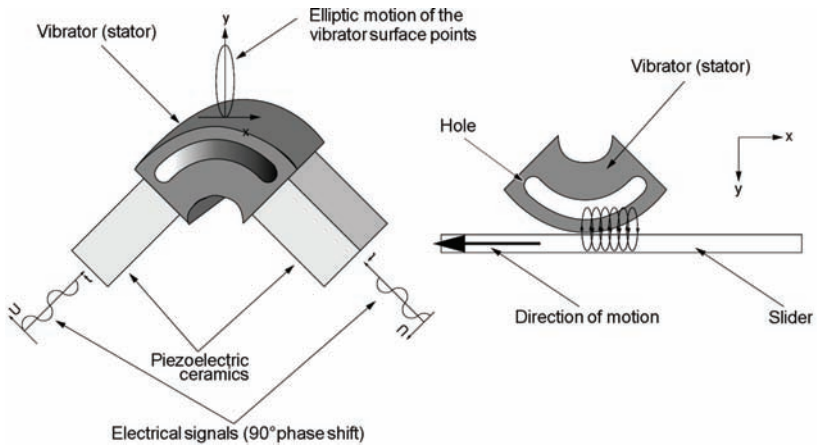


Fig. 4.11: Operating principle of the ULM

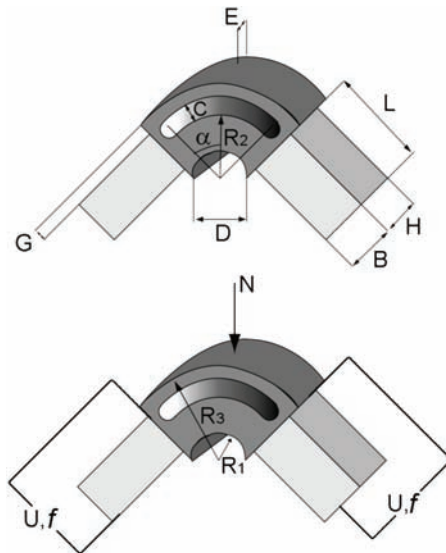


Fig. 4.12: Parametrization of the vibrating part of the ULM

Table 4.1: Dimensions and materials of the simulated vibrator

Parameter	Value
D	4.4mm
B	3mm
H	2mm
L	9mm
E	1.55mm
G	0.5mm
α	45°
C	1.4mm
R_1	1.2mm
R_2	2.55mm
R_3	5.3mm
Material of the vibrator: steel	
Density	7900 kg/m ³
Young's modulus	2.1 · 10 ¹¹ N/m ²
Poisson's ratio	0.32

For our study, the main interesting parameter is the deformation amplitude (vertical displacement) of the vibrating piece (stator) describing the elliptical trajectory. The parametrization of the motor and the external parameters are described in Fig. 4.12, where it is possible to obtain structures with or without a hole. The different dimensional and external parameters of the motor presented in Table 4.1 are defined as follows:

- D: spacing between piezoceramics
- B: width of piezoceramics
- L: length of piezoceramics
- H: thickness of piezoceramics
- E: half-thickness of the stator

- G: supplementary width added to the stator
- α : angle defining stator's hole
- R_1 : stator's inner radius
- R_2 : hole's inner radius
- R_3 : stator's outer radius
- C: width of the hole
- U: voltage applied to piezoceramics
- f: frequency of the input voltage
- N: pre-stressing force

Once the structure has been defined, several simulations have been carried out using ANSYS software. In the following sections, the characteristics and the possibilities of this software are first briefly presented and the different simulation results are then presented.

4.2.4 Simulations

Finite element software

The finite element software used, ANSYS [Ans81], is a general-purpose finite element analysis (FEA) software package. Finite element analysis is a numerical method of decomposing a complex system into very small parts (of user-designated size) called elements. The software implements equations that govern the behavior of these elements and solves them all, creating a comprehensive explanation of how the system acts as a whole. Then, these results can be presented in tabulated or graphical forms. This type of analysis is typically used for the design and optimization of systems too complex to be studied analytically or even experimentally. Systems that may fit into these categories are too complex due to their geometry, scale, governing equations or manufacturing price and time.

ANSYS can solve numerically a wide variety of problems. These problems include: static/dynamic structural analyses (both linear and non-linear), heat transfer and fluid problems, as well as acoustic, electromagnetic and piezoelectric problems. In general, a finite element solution may be broken into the following three stages:

- i. Preprocessing: defining the problem. The major steps in preprocessing are: the definition of key points, lines, areas and volumes; the definition of the element type and material/geometric properties; the mesh of lines, areas or volumes, as required. The amount of detail required will depend on the dimensionality of the analysis (i.e. 1-D, 2-D, axi-symmetric, 3-D).
- ii. Solution: assigning loads, constraints and solving. Here, loads (point or pressure) and constraints (translational and rotational) are specified and finally the resulting set of equations is solved.
- iii. Postprocessing: further processing and viewing of the results. In this stage, it is possible to see the lists of nodal displacements, element forces or moments, deflection plots and stress contour diagrams.

ANSYS distinguishes two different models that are built by the user throughout a FE analysis: the solid model and the FE model. The solid model is a geometric description of the structure to be analyzed and is best compared to a model built using a CAD software. In ANSYS, the solid model consists of key points, lines, areas and volumes. In general, the solid model is used to create the FE model, consisting of nodes and elements only. This process is called meshing. During meshing, ANSYS automatically places nodes and elements into the solid model, such that it fills out the solid model in an optimal way. This is done to ease the very elaborate tasks of defining every single node and element individually by the user. However, it needs to be kept in mind that the subsequent FE analysis will be based on the FE model only and is completely independent of the original solid model. Therefore, the analyst should plan ahead carefully how much detail is to be included into a solid model in order to not perform unnecessary work. The FE model can also be created manually, which sometimes proves to be easier for specific modeling purposes.

Configuration of simulation

First of all, it is to be raised that simulations have been made in air although other mediums could be considered if necessary. Furthermore, the driving process of the slider has not been simulated. Such a simulation by FE is possible in the case of an ultrasonic motor using traveling waves in which the stator is in permanent contact with the slider. But in the case of an ULM using standing waves, the contact is periodic and cannot be simulated simply by a modal analysis program. For this reason we have limited our study to the case of the stator structure only.

Another important point for simulations is the mesh. Indeed, its size influences the precision of the results and the computing time. Thus, a compromise had to be found not to exceed the limiting number of nodes of the current software version while keeping reasonable computing times. With regard to the boundary conditions, fixation nodes have been imposed, representing the base of the motor, voltage nodes have been specified on both ends of the piezoceramics and a normal force has been applied at a node of the top of the vibrator, representing the pre-stressing force.

The three-dimensional FE model presented in Fig. 4.10 allows then the modal analysis of the three-dimensional vibrating structure (piezoceramics + vibrator). ANSYS can then calculate: the eigen -frequencies, strain, stress and displacements of the structure, the displacement motion of the points at the surface of the vibrator but also the admittance according to the frequency. These different simulations have been performed and results are presented below.

Results

The modal shape obtained and the vertical displacement as a function of the frequency are presented in Fig. 4.13 and 4.14, respectively.

The harmonic response of the motor shows that the natural frequency is located at 30.09kHz . With this frequency, flat elliptical displacement motion is obtained at the surface points of the vibrator as shown in Fig. 4.15.

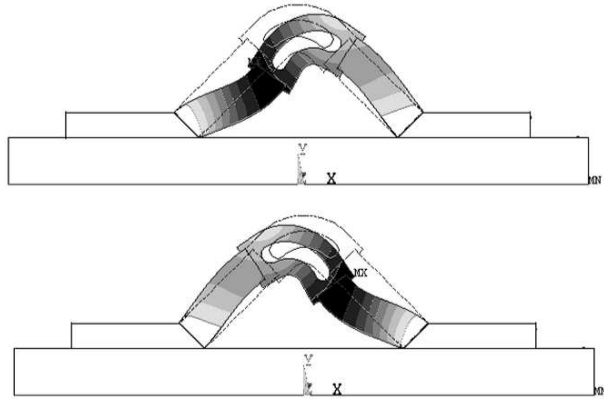


Fig. 4.13: Modal shape at resonance frequency

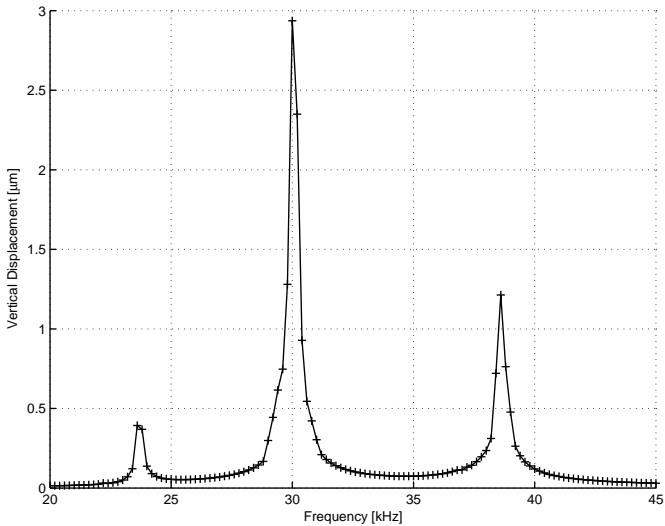


Fig. 4.14: Vertical displacement of a surface point

In the case of the harmonic analysis, another important constraint has to be taken into account. Indeed, a damping coefficient should be considered. This coeffi-

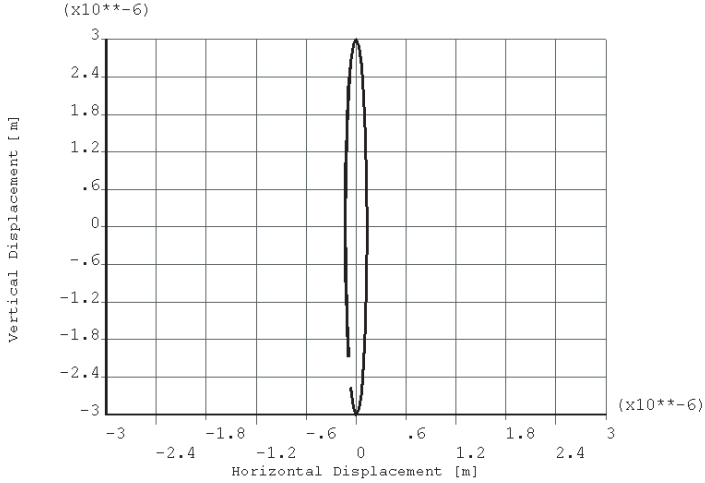


Fig. 4.15: Elliptic motion of a surface point

cient is, in simulation, represented by the addition of a specific command. This command introduces an attenuation factor representing the damping coefficient of the entire structure. Usually, this factor is evaluated by experiments, but as it is difficult in our case, an approximate value has been considered (approximately 1%).

4.3 Experimental results

Some experiments with a prototype built at the laboratory have been performed to confirm the numerical modeling and simulations. Materials used and dimensions of the motor are given in Table 4.1 and in Appendix A. Unfortunately, after various measurements, the prototype did not work any more in an optimal way, surely because of the bonding of the piezoceramics which was not easy and not very well done. This made the motor unusable. After all, some measurements could be carried out at the beginning and have in particular allowed the modeling validation, as it will be shown at the end of the chapter.

4.3.1 Prototype

Figure 4.16 shows the prototype built at the laboratory.

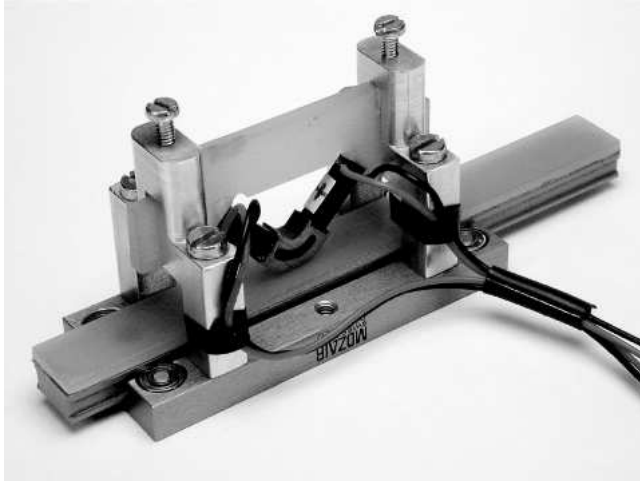


Fig. 4.16: Prototype of the motor realized at the laboratory

4.3.2 Measurements

The admittance (amplitude and phase) of the motor has been obtained using an impedance analyzer. This enables to determine experimentally the value of the resonance frequency. Figure 4.17 represents the measured admittance and it shows that there are two resonance frequencies located at about 30kHz and 38kHz respectively. These values validate the results obtained by simulation (Fig. 4.14) and confirm that the resonance frequency which gives a maximum of deformation amplitude is indeed 30.09kHz .

Moreover, the comparison of the vertical displacement (of a surface point of the vibrator) as a function of the applied voltage at the resonance frequency between simulations and experiments has been carried out. The power consumption of the

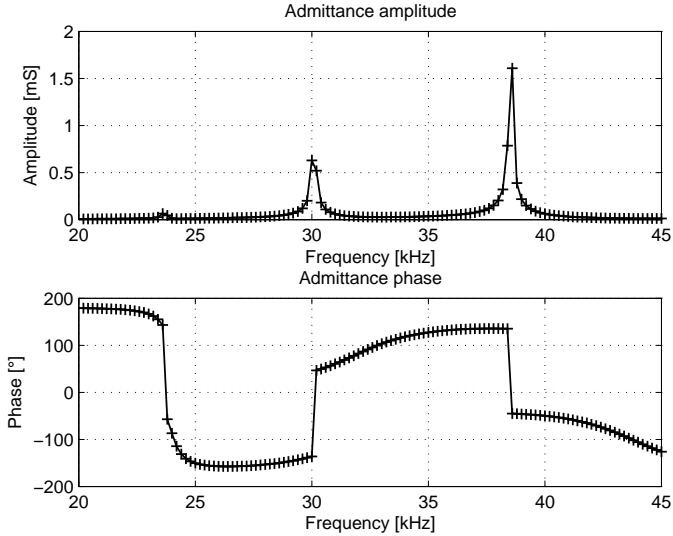


Fig. 4.17: Admittance versus frequency of the vibrating part of the ULM

motor has also been measured. Results are presented in Fig. 4.18. They show that the model simulation results could be fitted with the experimental values by adjusting the damping coefficient used in the simulations. Indeed, the value of 1% ($\sim 1/Q_m$) considered in our case could be decreased within sight of the results obtained. This has not been taken into account for the continuation of the study, but should be kept in mind.

As the results show it, a deformation amplitude of about $6.6\ \mu\text{m}$ is obtained in the vertical direction by applying a voltage of about 100V. The deformation amplitude obtained is sufficient to allow the motion of the slider (some tests showed it before the motor did not work any more). But in order to obtain a higher speed or a higher torque of the motor, it would be interesting to increase this deformation amplitude. Indeed, one makes the hypothesis that if the deformation amplitude in the vertical direction is bigger, then the torque of the motor would increase. In the same way, if the deformation amplitude in the horizontal direction is bigger,

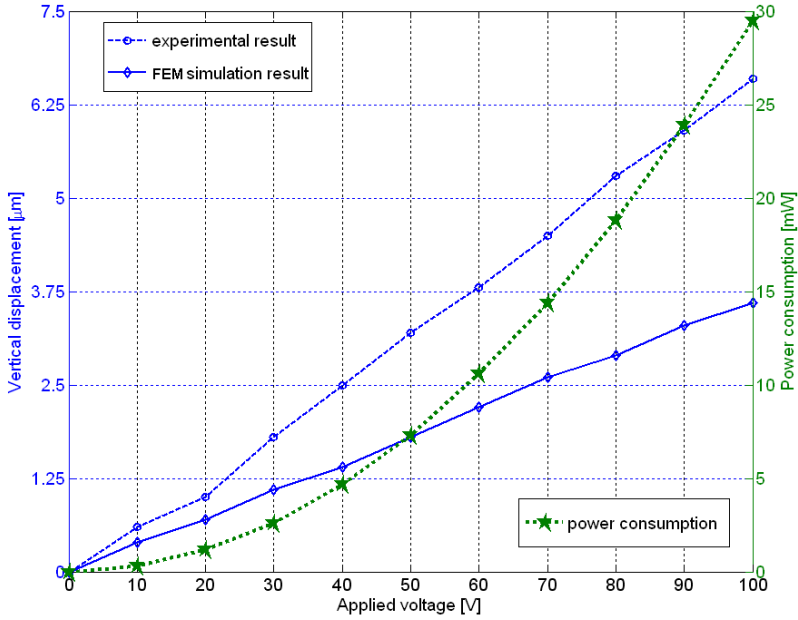


Fig. 4.18: Comparison of the vertical displacement versus applied voltage between ANSYS simulations and experimental data and power consumption of the motor

then the speed of the motor would increase. Thus, the goal of the following step of the study is to reach a bigger deformation amplitude (in the vertical direction in our study) by changing for example the vibrator dimensions. This will be the purpose of the next chapter.

4.4 Modeling validation

The results obtained show some differences between experiments and simulations. Indeed, the values found by measurements for the admittance as a function of the frequency show that the maximum is not located at the same frequency compared to the simulations. This can be explained by the fact that a

pre-stressing force has been taken into account in the FE simulations and this is not the case in experiments. However, the two different resonance frequencies have been observed, as well in simulations as in practice. Moreover, the model used for the simulation takes into account an attenuation factor representing the damping coefficient. As explained previously, this value is difficult to determine precisely and this can explain some differences between simulation results and experiments (simulation points could be fitted with the experimental ones by adjusting the damping coefficient). The difference of elasticity of the simulation model compared to the elasticity of the prototype realized can also be the cause of differences. With regard to the displacement motion of the vibrator surface points, the elliptic motion predicted is indeed obtained in the simulation results. So, qualitative and quantitative (to a lesser extent) agreement between simulations and experimental results has been established and allows to validate the numerical modeling.

4.5 Conclusion

Because of the ULM's complexity, precise analysis using analytic method is very difficult. Nevertheless, this modeling methodology (in particular using an electric equivalent circuit) has been presented in order to show that it is possible to model ultrasonic motors analytically. By the way, this methodology will be applied for the modeling of piezoelectric transformers presented in Chapter 6. In the same way, the method of Bond graph could be applied. Bond graph is an explicit graphical tool for capturing the common energy structure of systems. In the vector form, it gives a concise description of complex systems. By this approach, a physical system can be represented by symbols and lines, identifying the power flow paths. This method has not been presented in this study but could be considered as an interesting approach in the case of the ultrasonic motors analytical modeling (see [Blu82] and [MK99] for more details about the Bond graph method).

Then, numerical method is required to obtain more accurate analysis. So, the finite element software ANSYS has been used for the simulation of a standing

wave ultrasonic linear motor. Furthermore, experimental measurements obtained with a standing wave type ULM prototype designed at the laboratory made it possible to compare the results between theoretical modeling and practical experiments. This comparison has shown that numerical modeling is a good way to analyze the vibrating structure of the motor and this method has been validated.

So, it seems possible to use this numerical method to study the characteristics and the performances of the motor. Indeed, by varying its dimensions or/and the vibrating structure materials, it is obvious that it would be possible to increase for example the deformation amplitude of the vibrator, which would then make it possible to obtain a higher torque or speed of the motor. This optimization part of the study is treated in the following chapter, in particular by using design of experiments (DOE) as a pre-optimization stage before carrying out the optimization using the finite element method.

5. SENSITIVITY ANALYSIS AND OPTIMIZATION

5.1 Introduction

In Chapter 4, numerical modeling of an ULM has been performed and experiments with a prototype built at the laboratory have been carried out. A deformation amplitude of about $6.6\mu\text{m}$ has been obtained by applying a 100V voltage to the piezoceramics. The goal of the present chapter is to obtain a bigger deformation amplitude by varying the motor parameters and in particular the vibrator dimensions. First of all, a brief review of methods applied for the optimization of piezoelectric actuators is presented. Then, after a parametrization of the motor structure and with the aim of reducing the variation ranges of the input parameters but also to avoid performing a large number of simulations, a pre-optimization stage is performed. Thus, sensitivity analysis is carried out using design of experiments (DOE) which is a good way to obtain the influence of the input parameters on the objective function (deformation amplitude). Then, the optimization study, based on the results obtained thanks to the pre-optimization stage, is realized using the FEM software. The structure obtained is then analyzed to validate the optimization methodology.

In order to confirm the validity of the proposed methodology, an application case is presented at the end of the chapter. The optimization of a linear ultrasonic motor for the auto-focus function of an optical system will be performed. Finally, to complete the study, a brief approach of multi-objective optimization methods will be presented. The purpose is to show that it would be possible to optimize an ULM by considering several objective functions while keeping the same method-

ology presented in this dissertation work, in particular by applying methods such as evolutionary algorithms or even genetic algorithms.

5.2 State of the art of optimization of piezoelectric actuators

The performance of piezoelectric actuators and motors can usually be remarkably improved, in particular if mathematical optimization methods are applied in their development. As piezoelectric ultrasonic actuators couple electric and mechanical aspects, their optimization characterizes multidisciplinary optimization problems. In recent decades, a number of optimization problems of piezoelectric actuators have been studied and some algorithms have been used successfully. In this section, the state of the art of the optimization of piezoelectric actuators is briefly reviewed.

A large number of studies have been carried out into optimization problems of piezoelectric actuators in intelligent structures [SC93]. Such structures provide efficient methods to implement various tasks such as active control, shape control and health monitoring (see [CL87], [Cra94], [LOM02], [CTS02] and [Pre02]). Then, it is important to determine optimal dimensions, placement or control of piezoelectric actuators in an intelligent structure in order to improve the performances. As an example, genetic algorithms have been used to find the optimal placement of piezoelectric actuators and sensors for active vibration control of a plate ([SWW99], [HL99] and [Zha00]). Besides these works, there are also many other publications in the same subject: [YV96], [Bar00] and [HM03] for example.

Topology optimization of piezoelectric actuators is another subject widely studied. The purpose is to find the optimal layout of a structure in a specified domain in order to minimize (or maximize) defined objective functions or achieve specified properties [BS03]. Topology optimization methods have been applied to design amplifying mechanisms for the displacement of piezoelectric actuators (see [Lau00], [Du00], [CF00], [SNK00] and [BF02]). Topology optimization requires efficient and reliable large-scale nonlinear optimization algorithms because a fine mesh is required and a large number of design variables are in-

cluded in the problem. Although the topology of a structure obtained by using topology optimization methods is generally difficult to manufacture, the topology optimization technique is one rational systematic design methodology for the structural design. Furthermore, some researchers have also studied optimization problems concerning ultrasonic motors [Pon03], transducers [JNL00] and piezoelectric transformers [HLH03].

Although a number of studies concerning optimization of piezoelectric actuators have been reported in the above reviewed literature, there is a necessity for further investigations, in particular in the first stages of actuators and motors designs. This is concerned with the modeling, the problem formulation, the application of optimization methods and finally the selection of optimum results. In the next sections, the above mentioned aspects will be discussed.

5.3 Sensitivity analysis

5.3.1 Introduction

Finite element method has been chosen in this work for the modeling of an ultrasonic linear motor. FEM is a powerful tool but FE simulations often require large computing times. To avoid performing a large number of simulations, input parameters of the motor like geometrical dimensions, material properties or even boundary conditions could be judiciously chosen in function of their influence on the output parameters. In this manner, sensitivity of each input parameter can be achieved, in particular using design of experiments (DOE).

Sensitivity analysis refers to any numerical strategy which aims to get insight of the influence of input factors on the simulation output. It is becoming recently a research subject in itself and new methods are emerging to answer an urging demand originated in the every day more larger use of computer modeling [FP04]. Three main techniques have been used within the framework of this study. The first one is a Monte-Carlo analysis: it is a global and quantitative method based on factors sampling that facilitates the calculation of uncertainties. The second one, factorial design, consists of an identification method for additive models with

interactions (combination between two or more input parameters) while varying them simultaneously. The third method, response surfaces (Doehlert design), will allow to know the behavior of our system on a whole experimental field by carrying out many simulations distributed in the field in question. In this manner, it will be possible to predict the result in a point where no simulation was made (by interpolation) using response surfaces. These techniques have been integrated in Matlab and can interface with the finite element simulation program ANSYS working in batch mode.

In the next sections, design of experiments is initially introduced and then the different methods chosen are described. Finally these methods are applied for the study of the vibrating structure of the ultrasonic linear motor described at the end of Chapter 4.

5.3.2 Design of experiments (DOE)

A strategy for planning research known as design of experiments (DOE) was first introduced in the early 1920's when a scientist at a small agricultural research station in England, Sir Ronald Fisher, showed how one could conduct valid experiments in the presence of many naturally fluctuating conditions such as temperature, soil condition, and rainfall. The design principles that he developed for agricultural experiments have been successfully adapted to industrial and military applications since the 1940's. In the past decade, the application of DOE has gained acceptance as an essential tool for improving the quality of goods and services. This recognition is partially due to the work of Genichi Taguchi, a Japanese quality expert, who promoted the use of DOE in designing robust products, those relatively insensitive to environmental fluctuations. It is also due to the recent availability of many user-friendly software packages, improved training, and accumulated successes with DOE applications.

DOE techniques are not widely used in simulations, rather in practice. Properly designed and executed experiments will generate more precise data while using substantially fewer experimental runs than alternative approaches. They will lead to results that can be interpreted using relatively simple statistical techniques,

in contrast to the information gathered in observational studies, which can be exceedingly difficult to interpret.

One traditional method is to evaluate only one variable (or factor) at a time, all other variables being held constant during test runs or simulations except the one being studied. This type of experiment reveals the effect of the chosen variable under set conditions; it does not show what would happen if the other variables also changed. It was Fisher's idea [Fis71] that it was much better to vary all the factors at once using a factorial design, in which experiments are run for all combinations of levels for all of the factors. With such a study design, testing will reveal what the effect of one variable would be when the other factors are changing. Another advantage of the factorial design is its efficiency. Indeed, only one run would be needed for each point, since there will be two runs at each level of each factor. Thus, the factorial design allows each factor to be evaluated with the same precision as in the one-factor-at-a-time experiment, but with only two-thirds the number of runs. Montgomery has shown that this relative efficiency of the factorial experiments increases as the number of variables increases [Mon97]. In other words, the effort saved by such internal replication becomes even more dramatic as more factors are added to an experiment.

One disadvantage of two-level factorial designs is that the size of the study increases by a factor of two for each additional factor. For example, with eight factors, 256 runs would theoretically be necessary. Fortunately, because three-factor and higher-order interactions are rarely important, such intensive efforts are seldom required. For most purposes, it is only necessary to evaluate the main effects of each variable and the two-factor interactions, which can be done with only a fraction of the runs in a full factorial design. Such designs are called fractional factorial designs. If there are some two-factor interactions that are known to be impossible, one can further reduce the number of runs by using fractional factorial designs. For the example of eight factors, one can create an efficient design that may require as little as 16 runs. Another disadvantage of two-level designs is that the experimental runs cannot detect if there are curvilinear effects in the region of optimum settings. To check on this possibility, every factorial design should include a center point at the zero level of all the factors. If cur-

vature is present, the response at this point will be much larger or smaller than the response expected from the linear model. If curvature is present, the factorial design can be expanded to allow estimation of the response surface. One way to do this is to add experimental points. The result of such an expanded design is usually a contour plot of the response surface or a surface plot.

Factorial designs and response surfaces (Doehlert design) will be developed and explained more in details in the sensitivity analysis methods, in the following sections. The other method (Monte-Carlo), used in a preliminary study [Fer04], has also been used to roughly understand the relation linking the variation of the input parameters to the variation in the output data. Unfortunately, with this technique in its simple use, it is not possible to have a feedback on the input parameters and this is why it has not been used for the continuation of the study.

So, carefully planned, statistically designed experiments offer clear advantages over traditional one-factor-at-a-time alternatives. DOE provides an organized approach, with which it is possible to address both simple and tricky experimental, or, in our case, simulation problems. DOE requires fewer experiments (simulations) than any other approach. Since these few experiments belong to an experimental plan, they are mutually connected and thereby linked in a logical and theoretically favorable manner. Thus, by means of DOE, one obtains more useful and more precise information about the studied system, because the joint influence of all parameters is assessed.

5.3.3 Sensitivity analysis methodology

Parametrization

Through the use of more or less complex algorithms, the sensitivity analysis using design of experiments allows to reduce the number of simulations while obtaining a maximum of information. There are several kinds of experimental designs [BHH78], [Mon97], but two main types will be used in this study: factorial designs and Doehlert method. These methods will be explained in the following paragraphs.

First of all, a parametrization of the motor has to be carried out. For our study, the output parameter chosen for the optimization is the deformation amplitude (vertical displacement) of the vibrating piece (resonator) describing the elliptical trajectory. The parametrization of the motor and the external parameters have already been described in Fig. 4.12 (section 4.2.3), where it is possible to obtain structures with or without a hole. Once the dimensional parameters chosen, it remains to define the variation range of each one. This must be done, of course, by respecting the physical constraints as well as the constraints imposed by the voltage U applied to the piezoceramics and the pre-stressing force N . Table 5.1 gives the different variation ranges initially selected for the dimensional and external parameters to respect the constraints. These boundaries will be fitted more precisely thanks to the sensitivity analysis.

Now, the goal consists in analyzing the influence of each input parameter on the deformation amplitude of the vibrating piece of the motor. This is the pre-optimization stage of the study. To do this, design of experiments (DOE) is used. As explained previously, this technique makes it possible to characterize the influences of the parameters taken individually (order 1) but also those coupled with each other (order 2, 3, etc.). In this manner, it is possible to determine which parameter will be kept as variable (and so define a more precise variation range) and which will be fixed during the optimization stage. The different steps of the sensitivity analysis are now described.

Table 5.1: Variation ranges of the different input parameters

Param.	Min (-1)	Max (+1)	Unit
U ($\equiv a_1$)	20	40	[V]
f ($\equiv a_2$)	free	free	[Hz]
N ($\equiv a_3$)	0	100	[N]
D ($\equiv a_4$)	2	20	[mm]
B ($\equiv a_5$)	2	10	[mm]
H ($\equiv a_6$)	2	10	[mm]
L ($\equiv a_7$)	10	30	[mm]
E ($\equiv a_8$)	1	7	[mm]
G ($\equiv a_9$)	1	7	[mm]
α ($\equiv a_{10}$)	1	45	[°]
R_1	1	10	[mm]
R_3	4.8	31.8	[mm]
R_2 ($\equiv a_{11}$)	$R_1 + 0.1 \cdot (R_3 - R_1)$	$R_1 + 0.6 \cdot (R_3 - R_1)$	[mm]
C ($\equiv a_{12}$)	$0.1 \cdot (R_3 - R_1)$	$0.3 \cdot (R_3 - R_1)$	[mm]

With:

$$\begin{aligned}
 R_1 &= \frac{D}{2} \\
 R_3 &= \sqrt{\left[\frac{\sqrt{2}}{2}(2G+B) \right]^2 + \left[\frac{\sqrt{2}}{2}(2G+B) + \frac{D}{2} \right]^2} \quad (5.1)
 \end{aligned}$$

Sensitivity analysis steps

The sensitivity analysis is performed according to the following steps:

- a) Choice of the parameters
- b) Random draw or according to an experimental design of n sets of values of the parameters

- c) Simulations
- d) Storage of the output results to be analyzed
- e) Determination of the most dominating parameters

These different steps are carried out by using two programs: Matlab and ANSYS. The first allows to create simulation files by varying the input parameters according to the selected method. Once these files are created, they are used in a reference file which is launched n times towards the finite element program ANSYS via Matlab in batch mode. At the end of each simulation, a result file is created by ANSYS and treated with Matlab which stores the results obtained in a vector. This vector of answers is then analyzed to determine which are the most dominating input parameters. Fig. 5.1 describes the routine used as well as the various interactions between the two programs.

Sensitivity analysis methods

Factorial designs:

The experimental design most commonly used in research studies consists in varying only one parameter at the same time. This method has the disadvantage not to take into account the interactions between the factors. Nevertheless, factorial designs make a capital improvement of the research strategy. The method consists in choosing the simulation points at the edge of the multi-dimensional domain defined by the input parameter ranges and fitting the simulation results to an appropriate polynomial function corresponding to a Taylor series of the model being analyzed [Gun93]. A full factorial design allows to determine all coefficients of a linear model with all possible interactions within 2^q runs (see Eq. (5.2)). This design methodology has the disadvantage of requiring a lot of runs and is practicable only for a small number of input parameters.

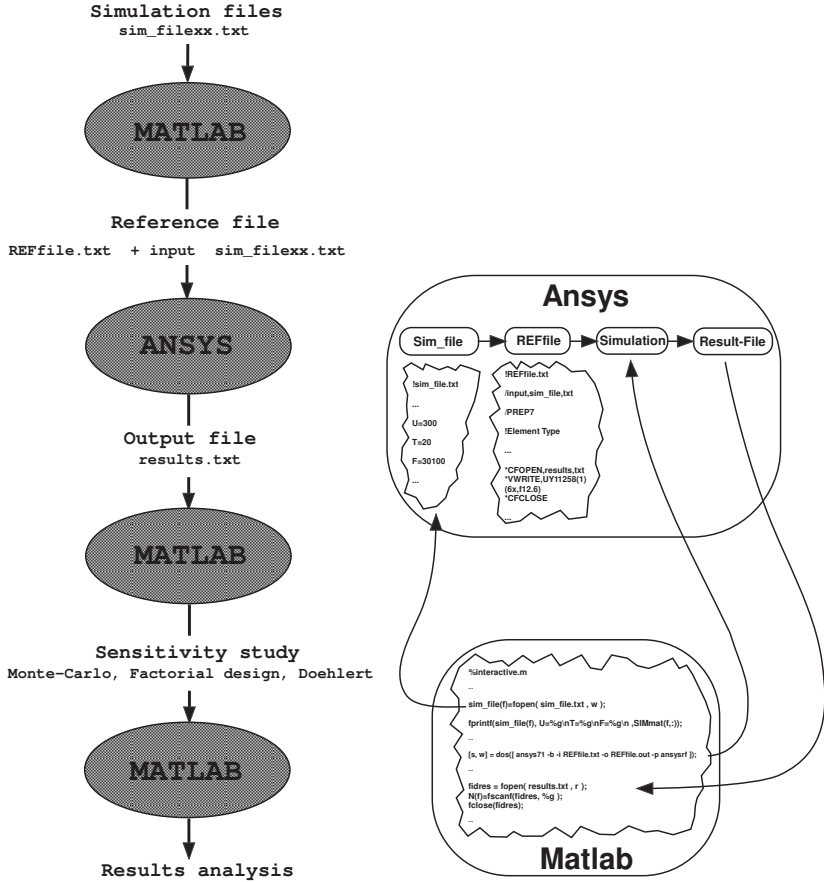


Fig. 5.1: Steps of the sensitivity analysis

$$\begin{aligned}
 R(x) = & a_0 + \sum_{i=1}^q a_i x_i + \sum_{i \neq j}^q a_{ij} x_i x_j + \dots \\
 & \dots + \sum_{i \neq j \neq k}^q a_{ijk} x_i x_j x_k + \dots + a_{i \dots n} x_i \dots x_q
 \end{aligned}
 \tag{5.2}$$

The coefficients a_0, a_1, \dots (see Table 5.1) are called the effects of the x_i parameters. One makes the distinction between:

- a_0 : constant effect (equal to the experiments mean)
- a_i : principal effects
- a_{ij} : effects of the first order interactions
- a_{ijk} : effects of the second order interactions

To explore an experimental space of q parameters, the lower and upper limits of their corresponding variation ranges are considered. This is represented by two states for the parameters (1 and -1). Then, the simulations to be carried out are all the possible combinations of the two states of each parameter ($= 2^q$). Once all these simulations performed, it is then possible to determine the coefficients a_0, a_1, \dots of the equation (5.2). Indeed, let us consider an experiments matrix \mathbf{E}_X gathering all the possibilities:

$$\mathbf{E}_X = \begin{bmatrix} e_{X11} & e_{X12} & \cdots & e_{X1q} \\ e_{X21} & \ddots & \cdots & e_{X2q} \\ \vdots & \vdots & \ddots & \vdots \\ e_{Xn1} & \cdots & \cdots & e_{Xnq} \end{bmatrix} \quad (5.3)$$

Where e_{Xij} is the state of the j^{th} parameter for the i^{th} experiment (simulation), with n the number of simulations and q the number of parameters.

As an example, the experiments matrix for three parameters is given by:

$${}^3\mathbf{E}_X = \begin{bmatrix} 1 & 1 & 1 \\ 1 & 1 & -1 \\ 1 & -1 & 1 \\ 1 & -1 & -1 \\ -1 & 1 & 1 \\ -1 & 1 & -1 \\ -1 & -1 & 1 \\ -1 & -1 & -1 \end{bmatrix} \quad (5.4)$$

Then, the model matrix \mathbf{X} can be built from the experiments matrix \mathbf{E}_X in the following way:

- The first column corresponds to the state of the constant effect a_0 and is thus always equal to 1
- The following columns correspond to the states of the principal effects (a_1, a_2, \dots); they are equal to the columns of the matrix \mathbf{E}_X
- The following columns correspond to the states of the coefficients of the first order interactions. They are obtained by the multiplication of the principal effects taking part in the interaction. Thus, the first term of the column corresponding to a_{12} is obtained by multiplying the first term of the column corresponding to a_1 and the first term of the column corresponding to a_2
- The following columns correspond to the terms of the second order interactions. Consequently, they are built by the multiplication of the three terms which interact the ones with the others
- ...

For the example of three parameters, the model matrix \mathbf{X} is given by:

$${}^3\mathbf{X} = \begin{bmatrix} 1 & 1 & 1 & 1 & 1 & 1 & 1 & 1 \\ 1 & 1 & 1 & -1 & 1 & -1 & -1 & -1 \\ 1 & 1 & -1 & 1 & -1 & 1 & -1 & -1 \\ 1 & 1 & -1 & -1 & -1 & -1 & 1 & 1 \\ 1 & -1 & 1 & 1 & -1 & -1 & 1 & -1 \\ 1 & -1 & 1 & -1 & -1 & 1 & -1 & 1 \\ 1 & -1 & -1 & 1 & 1 & -1 & -1 & 1 \\ 1 & -1 & -1 & -1 & 1 & 1 & 1 & -1 \end{bmatrix} \quad (5.5)$$

Let us now consider the response vector \mathbf{R} (from the responses $R(x)$ given by Eq. (5.2)) and the vector \mathbf{C} gathering all the effects given by:

$$\mathbf{C} = [a_0 \ a_1 \ a_2 \ \dots \ a_{12\dots g}]^T \quad (5.6)$$

Then, the system of equations can be written and solved in the following way:

$$\mathbf{X}\mathbf{C}=\mathbf{R} \Rightarrow \mathbf{C}=(\mathbf{X}^T\mathbf{X})^{-1} \mathbf{X}^T \mathbf{R} \quad (5.7)$$

By using factorial designs, it is possible to know the behavior of the system around a certain point, which is particularly useful for very complex systems since it is possible to quantify the influence of the different parameters. The disadvantage of this method is that the number of experiments (simulations) to carry out (2^q) increases in an exponential way according to the number of parameters (q). Another method is more suitable in the case of a system with much more input parameters. This method is called Doehlert design and it is explained in the next paragraph.

Doehlert design (response surfaces):

To know the behavior of a system on a whole experimental space, it is necessary to carry out experiments (simulations) distributed in all the space. In fact, the goal is to predict the response in a point of the experimental space where no simulation has been made (by interpolation). Then, it is necessary to use an empirical model, usually called response surfaces. This method, also called Doehlert design, makes it possible to easily move the center of interest in an experimental space (through an iterative way) according to the results ([BD87] and [FMP83]). Moreover, this design method is very interesting for optimization problems. As an example, the two dimensional Doehlert's network (two input parameters) and its corresponding model matrix \mathbf{X} are represented in Fig. 5.2.

The calculation methodology used in the factorial method can also be applied to Doehlert design (only the model matrix is different). The larger the number of input parameters, the larger the number of simulations n is and thus the experiments matrix is bigger. For a more precise analysis of our system, it would be judicious to consider more simulation points besides lower and upper bounds of the variables variation ranges, but the simulation time would then be larger. This is why, in a first approximation, less simulation points have been taken into account.

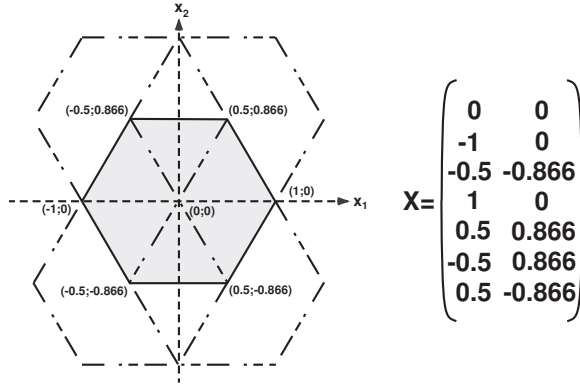


Fig. 5.2: Two dimensional Doehlert's network and the corresponding model matrix

In the next section, the results obtained applying these two methods are presented. The different input parameters vary according to the case of a structure with or without a hole. The output parameter is the deformation amplitude at the top of a vibrator surface point (vertical displacement). The analysis of the results will be done using two types of graphs. First, the graphs representing the effects. It is a graphical representation of the coefficients a_i , a_{ij} , a_{ijk} , ... shown in Eq. (5.2). This representation just makes it possible to see the parameters having the most important influence on the vertical displacement of the vibrator. As the number of analyzed parameters is large, only those being the most influential will be indicated by arrows on the graphs. It should be noted that, in this case, the analysis of the effects will be limited to those going until order 2. The quadratic effects will be also taken into account. The others (order 3 and higher) are neglected.

5.3.4 Results

Structure without a hole

First of all, an analysis of the input parameters effects on the deformation amplitude for a structure without a hole (see Fig. 4.12, $C=0$) has been carried out.

Figures 5.3, 5.4 and 5.5 show the results obtained.

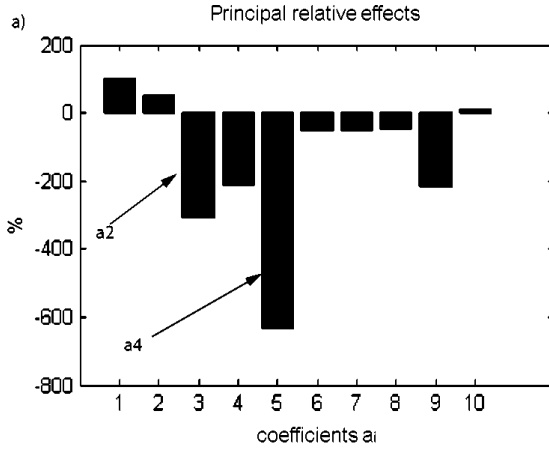


Fig. 5.3: Relative effects of the different input parameters for a structure without a hole:
a) principal effects

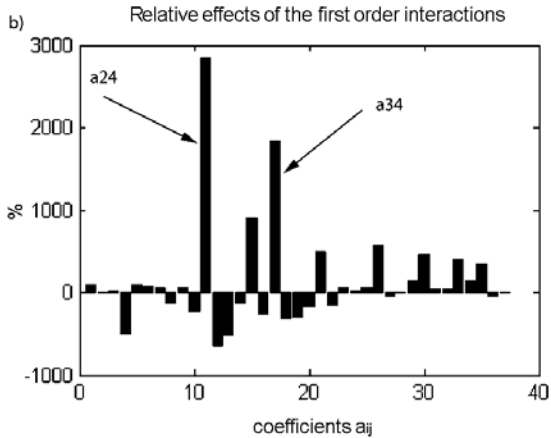


Fig. 5.4: Relative effects of the different input parameters for a structure without a hole:
b) first order interactions effects

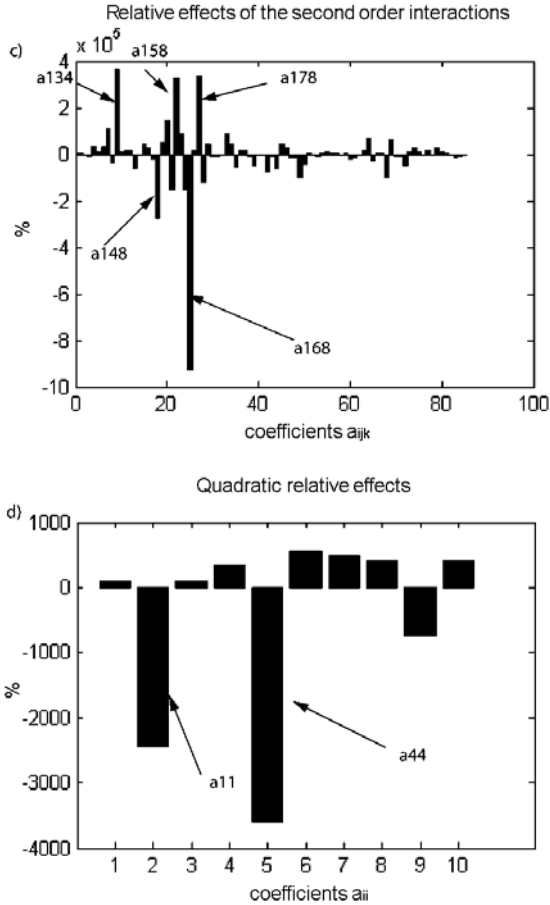


Fig. 5.5: Relative effects of the different input parameters for a structure without a hole: c) second order interactions effects, d) quadratic effects

Then a graph representing the influences can be obtained. Indeed, to better understand and see which are the most influential parameters, a program (Matlab) has been implemented and the influence of each parameter is calculated and then normalized in relation to the most influential one. In this manner, a more representative graph showing the parameters which are the most important is obtained. This is shown in Fig. 5.6.

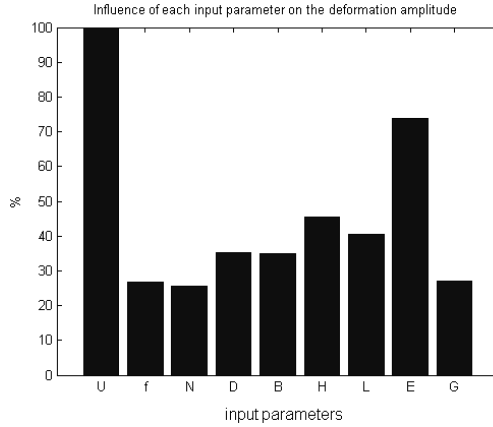


Fig. 5.6: Input parameters influences for a structure without a hole

Structure with a hole

The same methodology has been applied for a structure with a hole. The results are presented in Fig. 5.7, 5.8, 5.9, 5.10 and 5.11.

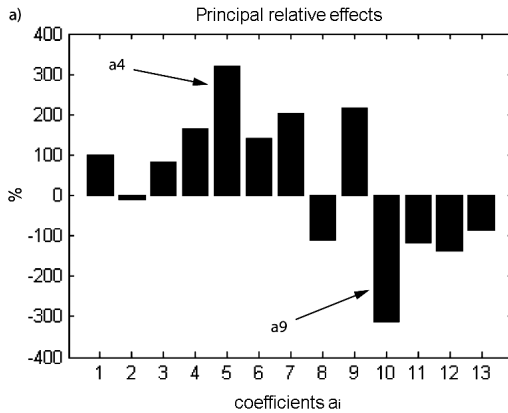


Fig. 5.7: Relative effects of the different input parameters for a structure with a hole: a) principal effects

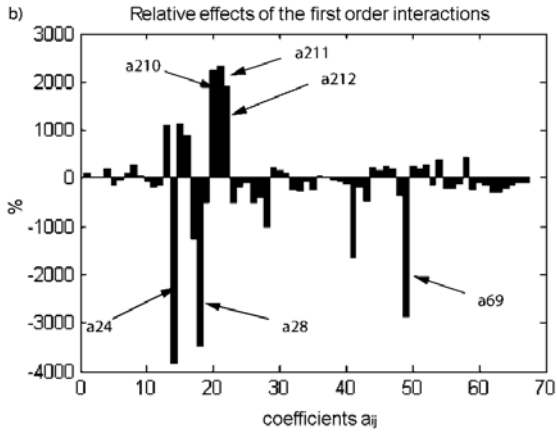


Fig. 5.8: Relative effects of the different input parameters for a structure with a hole: b) first order interactions effects

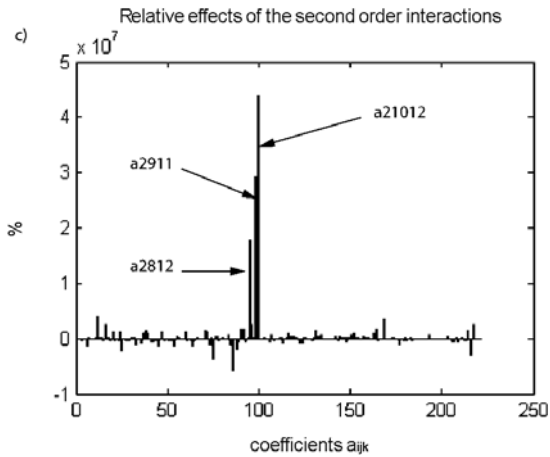


Fig. 5.9: Relative effects of the different input parameters for a structure with a hole: c) second order interactions effects

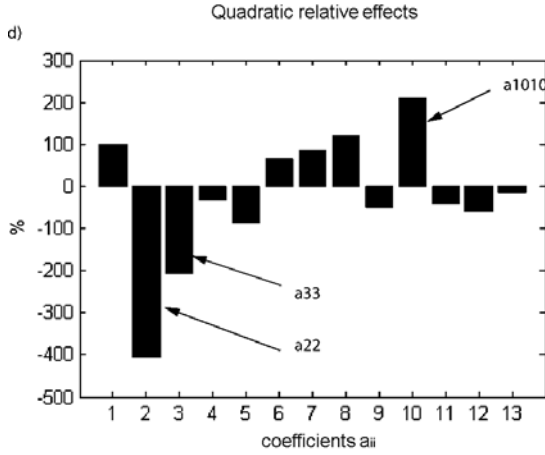


Fig. 5.10: Relative effects of the different input parameters for a structure with a hole: d) quadratic effects

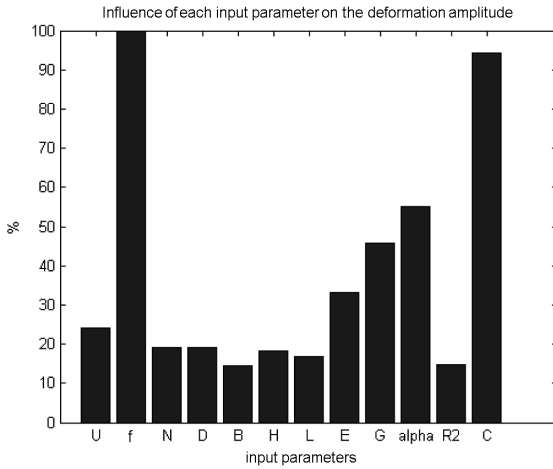


Fig. 5.11: Input parameters influences for a structure with a hole

Comments:

The results obtained for both structures, with and without a hole, are very interesting. It can be noticed that the influence of this hole is very important, as well from a point of view of the deformation amplitude as of the various influences of the input parameters. Indeed, in the case of a structure without a hole, the most significant input parameter is the voltage U applied to the piezoceramics. One can easily understand this result because of the direct relation between the displacement of the stator, the dilation of the piezoceramics and the applied voltage. Indeed, it is obvious that the higher the applied voltage the bigger the dilation and the displacement. Furthermore, the half-thickness of the stator E has also an important effect on the deformation amplitude while the other input parameters have a more or less equal influence but definitely lower than that of U and E . On the contrary, for a structure with a hole, the frequency f has a more influential effect than the applied voltage (see Fig. 5.11). This can be explained by the fact that the addition of a hole generates a considerable modification of the resonator structure and thus its resonance frequency. But in the case of a structure without a hole, the vibrator remains overall identical, only the variation of its thickness can lead to a slight modification of the resonance frequency but not as important as in the case of the presence of a hole. Moreover, the displacement amplitudes obtained in both cases are quite different. Indeed, the values for a structure with a hole are much more often positive than those obtained for a structure without a hole, but also bigger ($20\mu m$ compared to $10\mu m$). Table 5.2, Fig. 5.12 and Fig. 5.13 summarize the different results obtained.

It should be noted that there is a clear difference of calculation condition between a structure with a hole and one without. Indeed, the simulation of a structure shown in Fig. 5.12 takes three times less computing time than the simulation of a structure with a hole (Fig. 5.13). The size of the mesh is also smaller in the area of the hole, which also implies an increase in the computing time. Moreover, there are more parameters in a structure with a hole; this increases the computing time to a value of approximately 8 minutes per simulation.

The results found in the pre-optimization stage can then be applied to the FE optimization which is described in the following section.

Table 5.2: Input parameters and maximum deformation amplitude

	Without a hole	With a hole
Max. amplitude	9.1 μm	22.6 μm
External parameters	$U = 30V$ $f = 7.38\text{kHz}$ $N = 60.2N$	$U = 30V$ $f = 12.0\text{kHz}$ $N = 50N$
Dimensional parameters	$D = 18.1\text{mm}$ $B = 6\text{mm}$ $H = 6\text{mm}$ $L = 20\text{mm}$ $E = 4\text{mm}$ $G = 4\text{mm}$	$D = 11\text{mm}$ $B = 6\text{mm}$ $H = 8.6\text{mm}$ $L = 19.1\text{mm}$ $E = 3.7\text{mm}$ $G = 1.8\text{mm}$ $\alpha = 23^\circ$ $R_2 = 8.5\text{mm}$ $C = 1.7\text{mm}$

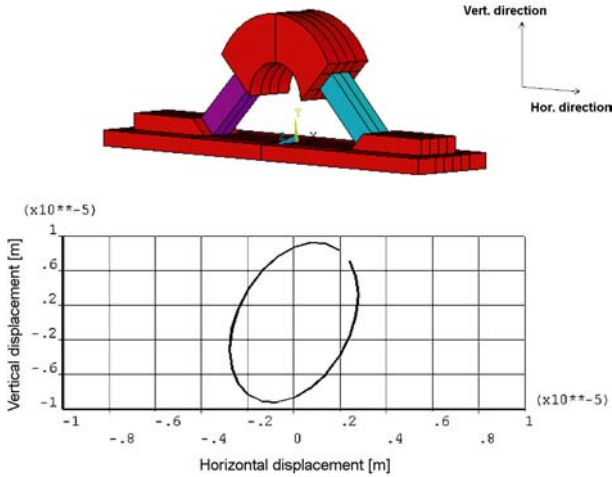


Fig. 5.12: Structures comparison: maximum amplitude without a hole

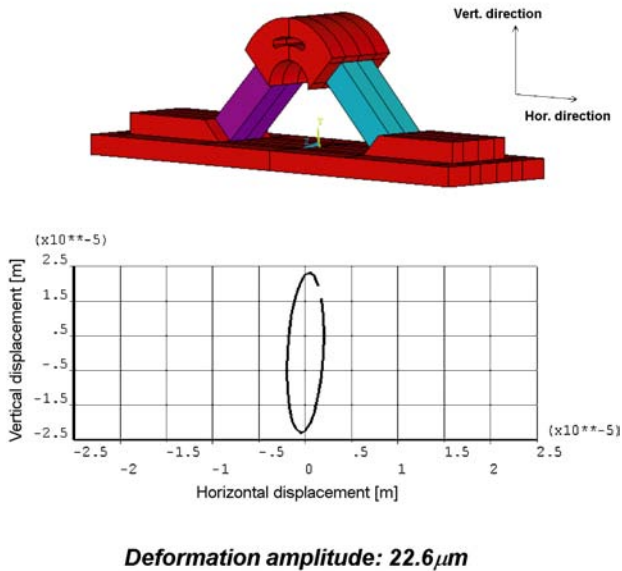


Fig. 5.13: Structures comparison: maximum amplitude with a hole

5.4 FE optimization

5.4.1 Introduction

The process involved in a FE optimization consists in following precise steps. First of all, an analysis file to be used during looping must be created. It will build the model parametrically, obtain the solution and finally retrieve and assign to parameters the response quantities that will be used as state variables and objective function. The next step is to declare the optimization variables (+ objective function) and choose an optimization method. Two different approaches have been chosen in our case: the first order method and the factorial design tool.

5.4.2 Optimization tools

First order method

The first order method uses gradients of the dependent variables with respect to the design specifications. For each iteration, gradient calculations (which may employ a steepest descent or conjugate direction method) are performed in order to determine a search direction and a line search strategy is adopted to minimize the unconstrained problem. Thus, each iteration is composed of a number of sub-iterations that include search direction and gradient computations. This is why one optimization iteration for the first order method performs several analysis loops. First order iterations continue until either convergence is achieved or termination occurs. The Gauss-Newton method is a class of methods for solving this type of problems. An improved and efficient version of the method is the so-called Levenberg-Marquardt algorithm. These methods are not discussed here, but detailed information can be easily found in the literature ([DS83]).

Factorial tool

Factorial design tool employs a 2-level, full or fractional factorial evaluation to generate design set results at all extreme points of the design space ([Mon97] and [Ans81]). In our case, a full evaluation will be performed: the program realizing $2 \cdot d_v$ loops, where d_v is the number of design variables. Every component of the design variable vector will take two extreme values (max. and min.). So, in a full factorial evaluation, every combination of design variable extreme values is considered in the dimensional design space.

Pre-optimization results

Using the results obtained in the pre-optimization stage (sensitivity analysis), it is then possible to determine a more precise variation range for each input parameter and fix some of them. Nevertheless, in order to minimize the computing

time of an optimization simulation performed with the FE method, these variation ranges have been still refined using iso-surfaces graphs. Indeed, the use of this type of graphs remains the best solution to easily understand the impact of the different input parameters on the deformation amplitude of the vibrator. The problem is that it is not conceivable to represent a graph with 9 or 12 input variables and one output value. This is why the problem has been divided into subproblems composed of several graphs with three input variables and the deformation amplitude as output value. As an example, a typical graph is presented in Fig. 5.14. This graph shows the influences of three input parameters (B, L, D) on the deformation amplitude obtained at the top of the vibrator (structure with a hole). Then, it is possible to identify for which values of the three parameters a maximum deformation amplitude is reached. In this particular case, we can see that there are different couples of values for which one obtains a maximum (red color). For example, values $B=10\text{mm}$, $L=30\text{mm}$ and $D=2\text{mm}$ give a deformation amplitude of about 0.3mm .

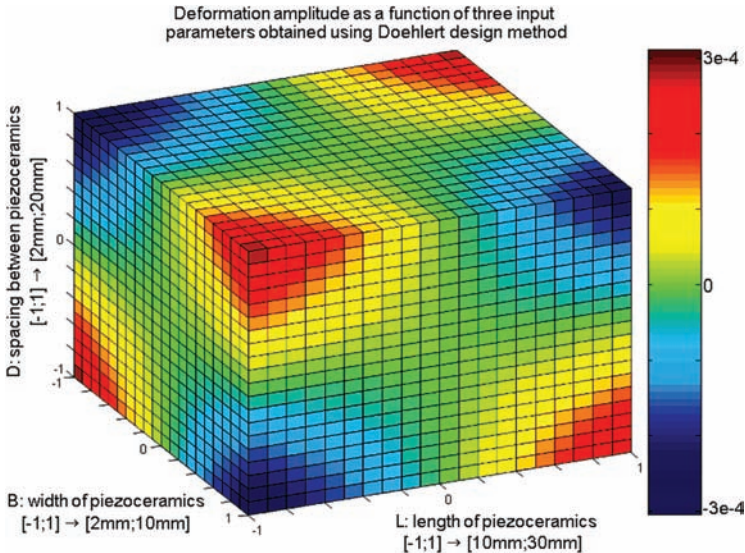


Fig. 5.14: Example of iso-surfaces graph for three input parameters (B, L, D)

With this method, the number of graphs to manage 9 to 12 variables (structures without and with a hole, respectively) is considerable. Some of the most significant are presented in Appendix B. But thanks to these results and after a pertinent analysis (with the aim of finding the input variables having the most influence on the deformation amplitude), the final variation ranges have been determined (see Table 5.3). In the next section, the results obtained using the first order method and the factorial tool are presented and compared.

5.4.3 Results

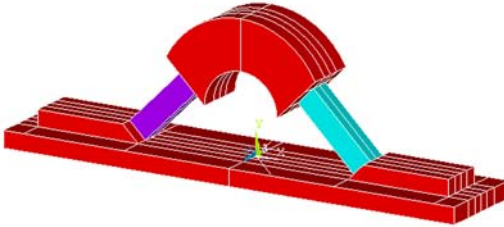
Structure without a hole

The initial structure chosen for the FE optimization is represented in Fig. 5.12. The maximum amplitude obtained in the pre-optimization stage using Doehlert design method was $9.1 \mu\text{m}$. The input parameters given in Table 5.2 have been taken as initial values and variation ranges have been chosen as shown in Table 5.3. First order method and factorial tool have been applied. Fig. 5.15 and 5.16 show the results obtained.

Table 5.3: Initial values and variation ranges of the different input parameters

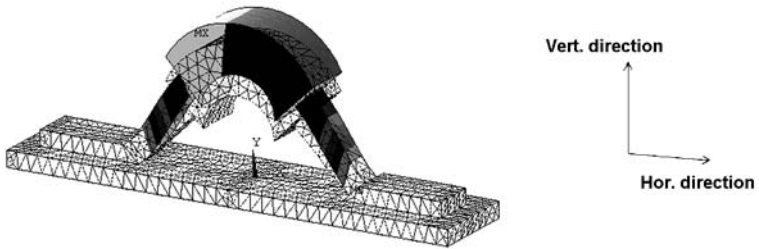
Parameter	Initial value	Variation range
U	30V	fixed
f	7.38kHz	[5.9kHz; 8.9kHz]
N	60.2N	fixed
D	18.1mm	[18.0mm; 18.2mm]
B	6mm	[5mm; 7mm]
H	6mm	[5mm; 7mm]
L	20mm	[15mm; 25mm]
E	4mm	[3mm; 5mm]
G	4mm	[3.9mm; 4.1mm]
Objective function		
Defor. ampl.	Init. val.: $9.1 \mu\text{m}$	Tol.: $0.1 \mu\text{m}$

Model:

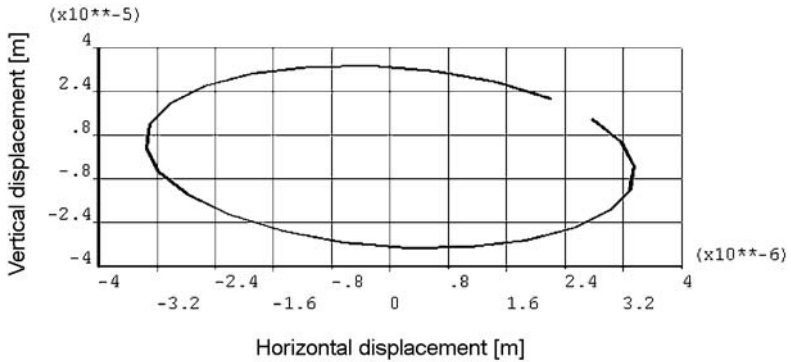


Final parameters: U = 30 V
 F = 6.6 kHz
 N = 60.2 N
 D = 18.1 mm
 B = 5.51 mm
 H = 5 mm
 L = 20.15 mm
 E = 3.98 mm
 G = 4 mm

Deformation:



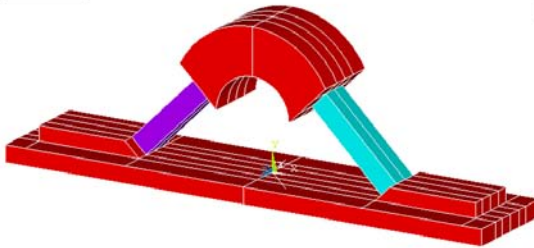
Elliptical trajectory of a surface point:



Deformation amplitude: 33.6 μ m

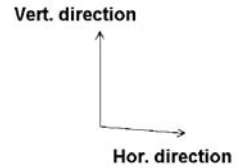
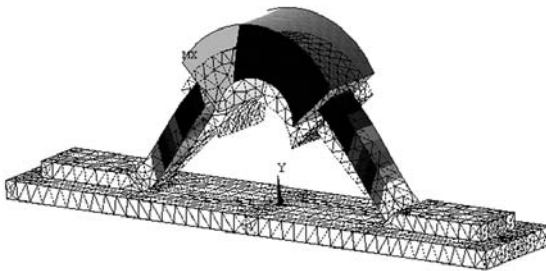
Fig. 5.15: FE Optimization (structure without a hole): first order method

Model:

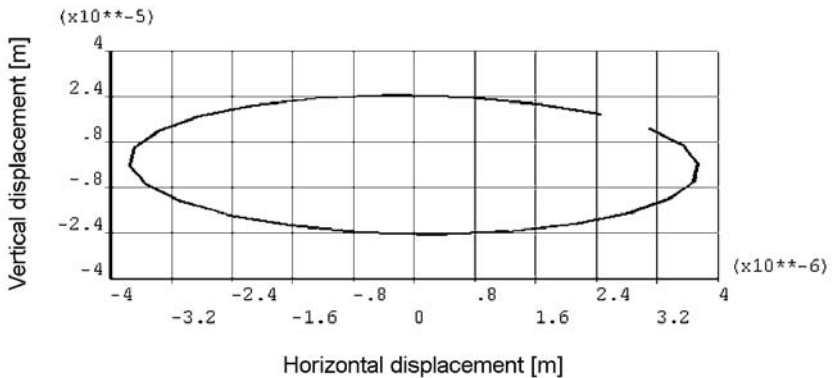


Final parameters: U = 30 V
 f = 5.9 kHz
 N = 60.2 N
 D = 18.1 mm
 B = 5 mm
 H = 7 mm
 L = 25 mm
 E = 5 mm
 G = 4 mm

Deformation:



Elliptical trajectory of a surface point:



Deformation amplitude: 24.1 μm

Fig. 5.16: FE Optimization (structure without a hole): factorial method

Structure with a hole

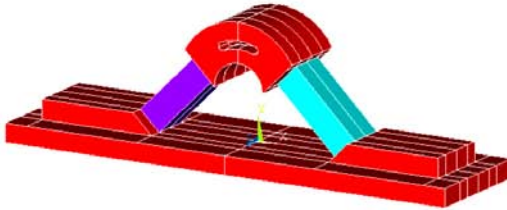
The structure chosen for the FE optimization is represented in Fig. 5.13. The maximum amplitude obtained in the pre-optimization stage using Doehlert design method was $22.6\mu m$. The input parameters given in Table 5.2 have been taken as initial values and variation ranges have been chosen as shown in Table 5.4. First order method and factorial tool have been applied. Fig. 5.17 and 5.18 show the results obtained.

Table 5.4: Initial values and variation ranges of the different input parameters

Parameter	Initial value	Variation range
U	30V	fixed
f	12.0kHz	[9.6kHz; 14.4kHz]
N	50N	fixed
D	11.0mm	[10.9mm; 11.1mm]
B	6mm	[5.9mm; 6.1mm]
H	8.6mm	[8.5mm; 8.7mm]
L	19.1mm	[19.0mm; 19.2mm]
E	3.7mm	[3.2mm; 4.3mm]
G	1.8mm	[1.2mm; 2.8mm]
α	$\alpha = 23^\circ$	[20.0°; 28.7°]
R_2	8.5mm	[6.5mm; 10.5mm]
C	1.7mm	[0.7mm; 2.2mm]
Objective function		
Defor. ampl.	Init. val.: $22.6\mu m$	Tol.: $0.1\mu m$

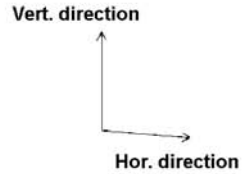
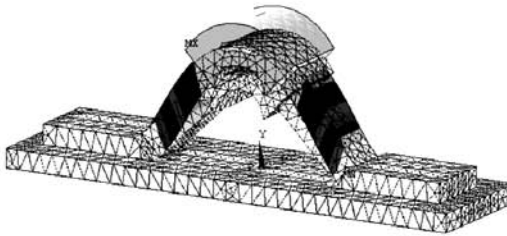
It must be emphasized that the structures presented until now have resonance frequencies which are not in the ultrasonic range. This can be obtained by restricting the variation range of the input parameter f to frequencies higher than 20kHz. After many simulations, a final structure has been obtained applying the same methodology. The results are presented in the following section.

Model:

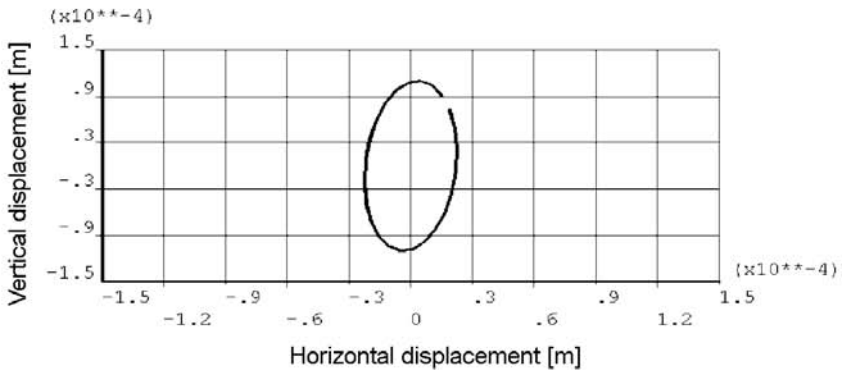


Final parameters: $U = 30 \text{ V}$
 $f = 11.79 \text{ kHz}$
 $N = 50.0 \text{ N}$
 $D = 11.0 \text{ mm}$
 $B = 6.0 \text{ mm}$
 $H = 8.6 \text{ mm}$
 $L = 19.1 \text{ mm}$
 $E = 3.7 \text{ mm}$
 $G = 1.79 \text{ mm}$
 $\alpha = 23.0^\circ$
 $R_2 = 8.51 \text{ mm}$
 $C = 1.7 \text{ mm}$

Deformation:



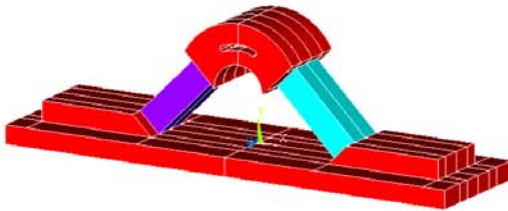
Elliptical trajectory of a surface point:



Deformation amplitude: $111.5 \mu\text{m}$

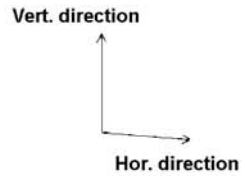
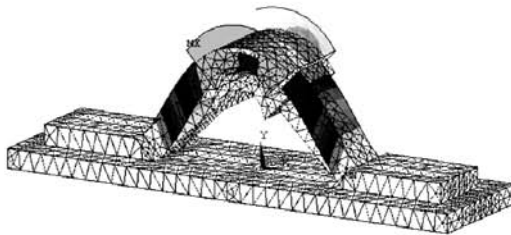
Fig. 5.17: FE Optimization (structure with a hole): first order method

Model:

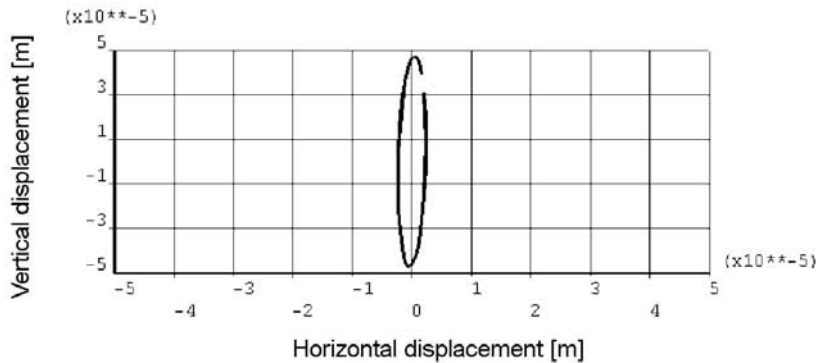


Final parameters: U = 30 V
 f = 11.8 kHz
 N = 50.0 N
 D = 11.0 mm
 B = 6.0 mm
 H = 8.6 mm
 L = 19.1 mm
 E = 3.7 mm
 G = 1.79 mm
 $\alpha = 23.0^\circ$
 R₂ = 8.51 mm
 C = 1.2 mm

Deformation:



Elliptical trajectory of a surface point:



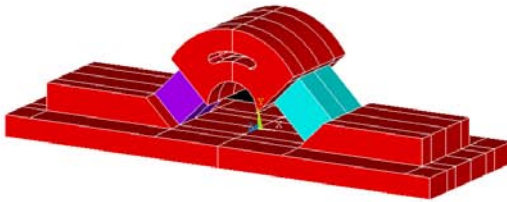
Deformation amplitude: 47.4 μm

Fig. 5.18: FE Optimization (structure with a hole): factorial method

Final structure

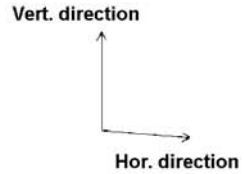
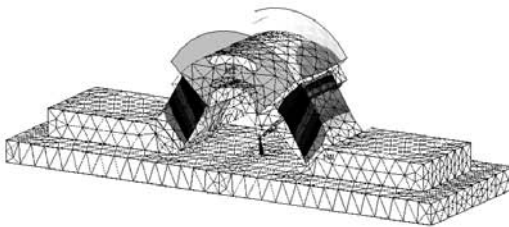
This section presents the results obtained when the frequency is forced to be higher than $20kHz$. This has been done with the aim of obtaining a motor operating in the ultrasound range. The same methodology has been applied, i.e. sensitivity analysis and FE optimization. Only the result of the final structure obtained after the FE optimization using the first order method is presented. Figure 5.19 shows the model with the values of the different parameters, the deformation obtained at the resonance frequency (about $20.32kHz$) and the elliptical trajectory of a surface point of the resonator. Then, Fig. 5.20 summarizes the results obtained throughout the chapter. The different structures are compared in terms of deformation amplitude. The results in the left part of the graph correspond to the initial structure (simulated deformation amplitude of $3.3\mu m$ for an applied voltage of $90V$). The right part of the graph shows the results of the final structure (simulated deformation amplitude of $97.8\mu m$ for an applied voltage of $30V$). It means that by applying our optimization methodology, the value of the deformation amplitude has been increased by a factor 30 while decreasing the applied voltage of a factor 3. These results are discussed in the next section.

Model:

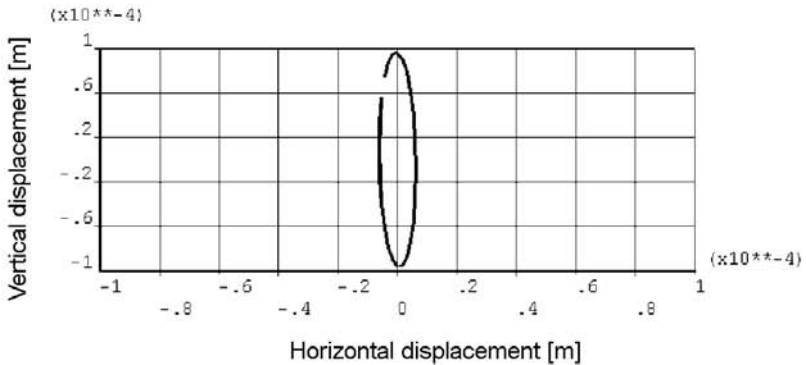


Final parameters: $U = 30 \text{ V}$
 $f = 20.32 \text{ kHz}$
 $N = 50.0 \text{ N}$
 $D = 9.91 \text{ mm}$
 $B = 7.14 \text{ mm}$
 $H = 10.52 \text{ mm}$
 $L = 9.45 \text{ mm}$
 $E = 3.83 \text{ mm}$
 $G = 1.7 \text{ mm}$
 $\alpha = 24.6^\circ$
 $R_2 = 8.61 \text{ mm}$
 $C = 1.71 \text{ mm}$

Deformation:



Elliptical trajectory of a surface point:



Deformation amplitude: $97.8 \mu\text{m}$

Fig. 5.19: FE Optimization: final structure

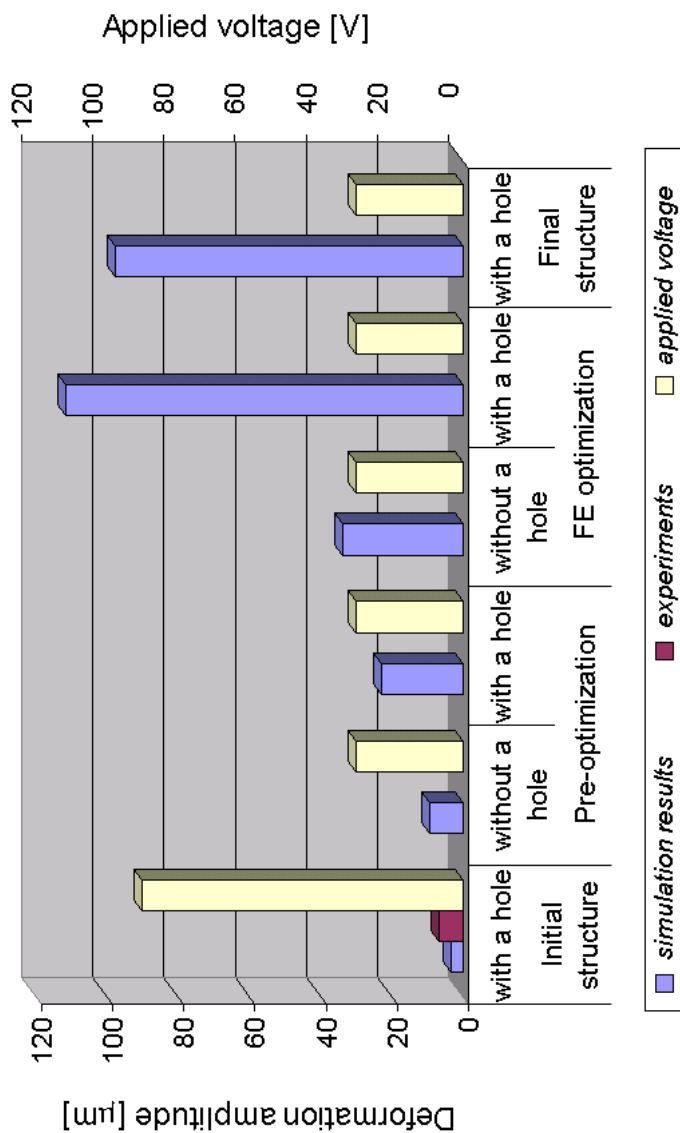


Fig. 5.20: Structures comparison: initial, pre-optimization, FE optimization and final

5.5 Discussion and methodology validation

As the first results showed it, the pre-optimization stage already allows an improvement of the deformation amplitude of the motor vibrating body but FE optimization makes it possible to obtain a bigger deformation amplitude. Results obtained with the first order method give a bigger deformation amplitude, which shows that this optimization method is better than the factorial one, although computing time is much longer. Indeed, for the case of a structure with a hole, one optimization simulation takes around 8 hours for 10 iterations. This is due to the fact that there are more input parameters for a structure with a hole but also the mesh size is lower in this case, which implies more computing time necessary to complete the optimization.

However, methodology used appears to be very efficient and already allows to:

- i. multiply the deformation amplitude by a factor 30 (from $3.3\mu\text{m}$ to $97.8\mu\text{m}$) compared to the initial design model and respecting the ultrasound range
- ii. reduce the voltage applied to the piezoceramics by a factor 3 (from 90V to 30V)

It should be noted that simulations have been done considering maximum stresses in the piezoceramics. Furthermore, a damping coefficient of 1% (see end of section 4.2) has been taken into account in our simulations. This coefficient is difficult to determine and measurements are necessary to determine it precisely (the manufacturer of the piezoceramics was not able to give us a value). Moreover, a feasibility study should be achieved before designing the motor. Indeed, some structures found by applying our methodology should be the subject of a thorough analysis by means of the mechanical constraints acting on the vibrating piece, in particular by realizing various prototypes for experimental measurements. This part has not been carried out within the framework of this thesis, considering the difficulty in building prototypes within the laboratory but also the cost and the necessary time to realize them.

The different developments and results obtained and described in the previous sections have been also the subject of two publications ([Fer05] and [Fer08]).

Moreover, the choice has been made for this study to take the deformation amplitude of the vibrating body as objective function. But other objective functions could be easily introduced while using the same methodology, in particular for a multi-objective optimization. Some considerations about multi-objective optimization methods will be discussed at the end of this chapter. Furthermore, other parameters could be easily changed, such as the materials of the vibrating body or the piezoceramics for example.

The optimization methodology presented in this chapter will now be applied for a concrete case, that is, the optimization of an ultrasonic linear motor for the auto-focus function of an optical system. Developments are presented in the next section with the aim of demonstrating the validity of the proposed methodology.

5.6 Application case: optimization of an ultrasonic linear motor for the auto-focus function of an optical system

5.6.1 Introduction

This section presents the application of the methodology suggested in this chapter for the optimization of an ultrasonic linear motor used for the auto-focus function of an optical system. Figures 5.21 and 5.22 show the entire system, including the ultrasonic motor, the slider composed of a spring for the contact, a coil to increase the input voltage coming from the battery and the lens of the optical system. More precise schemes of the parts of the system will be given in the following sections. The ultrasonic motor has been invented and patented by MINISWYS SA [MINIS] in 2005. MINISWYS SA is a spin-off company of Creaholic SA which develops and markets a new generation of piezoelectric motors based on an innovating technology. This type of motor is different from current piezoelectric motors because of its specific construction, low energy consumption, low cost and it can be easily manufactured. MINISWYS SA wishes to optimize the characteristics of the ultrasonic motor, in particular the displacement amplitude of the lens for a future zoom application.

So, the approach adopted for the optimization study of the MINISWYS ultrasonic

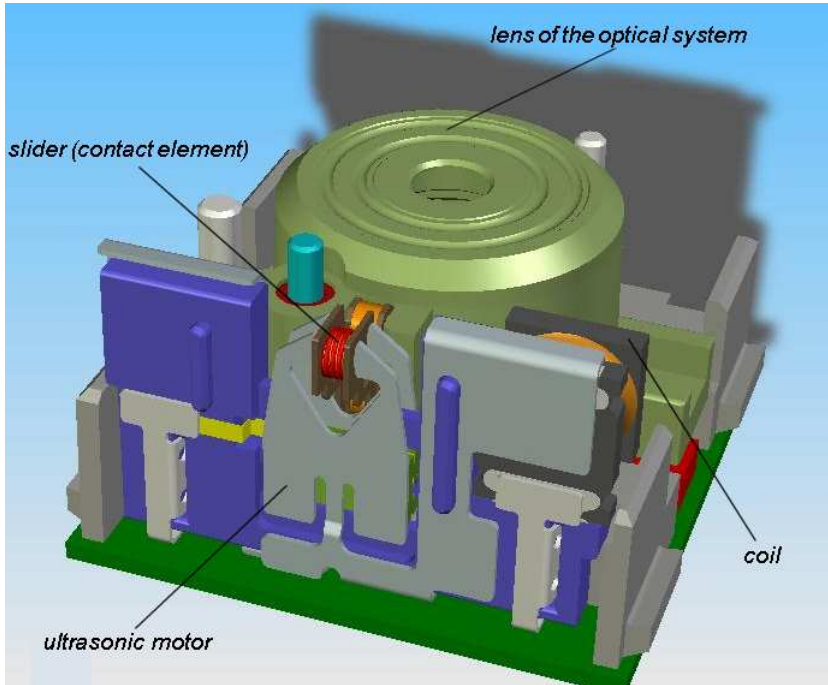


Fig. 5.21: Application case: linear motion of the lens of an optical system

motor (MUM) is divided into three stages: initially, an analysis of the current structure of the motor will be carried out using FEM to find out the vibration modes and the actual movement amplitudes; then, the behavior of the MUM according to its geometrical parameters will be undertaken, in particular using design of experiments (DOE); finally, the FE optimization will be carried out. These different stages of the study are presented in the following sections.

5.6.2 The MINISWYS Ultrasonic Motor (MUM)

The MINISWYS ultrasonic motor (see Fig. 5.23, 5.24 and 5.25) has two functional resonance frequencies, allowing both forward and backward motions.

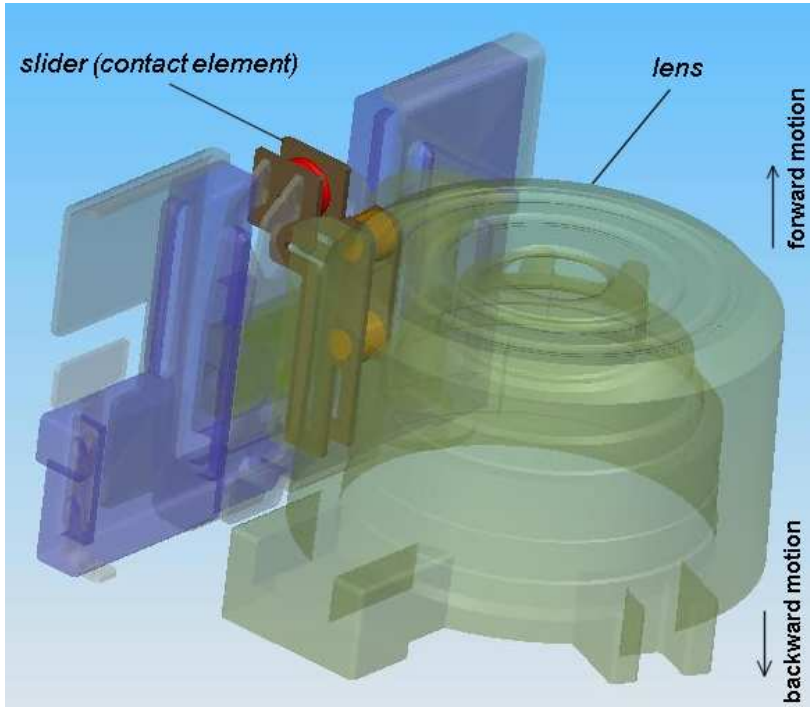


Fig. 5.22: Scheme of the motion transmission

Moreover, the motor is based on a PZT807 piezoelectric ceramic (see Appendix C). Figure 5.26 shows the layout and the polarization of the piezoelectric ceramics. They are actually composed of 2 elements working in opposite directions with a common middle electrode. The ceramics are glued between the two chucks (made of Pfnodal copper alloy) with the support, made of a non electrically-conducting material. The glue contains some small metallic balls making an electric connection between the piezoceramics electrodes and the chucks. The two electrodes are connected, one to the inductor and the other to the middle of the ceramic. A coil is used to increase the voltage because the battery output voltage is not high enough. Indeed, a minimum voltage of 20V is necessary to supply the piezoceramics to reach the desired specifications.

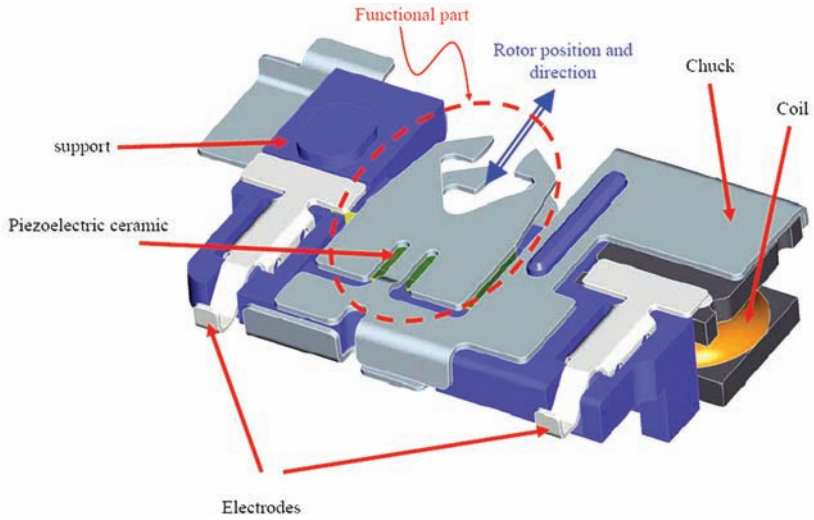


Fig. 5.23: The MINISWYS Ultrasonic Motor (MUM)

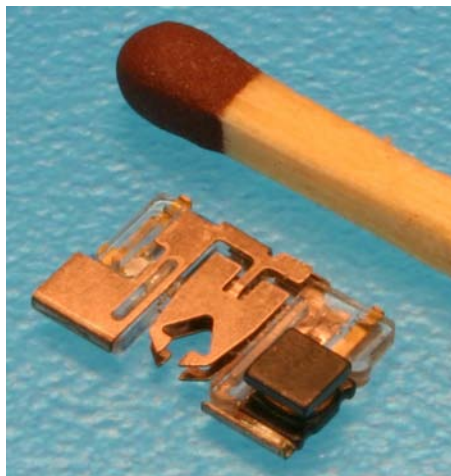


Fig. 5.24: MUM prototype

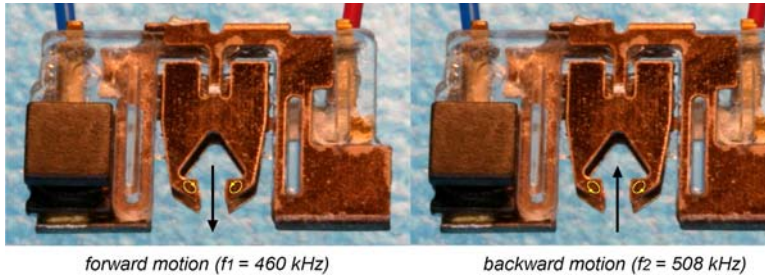


Fig. 5.25: Forward and backward motions of the MINISWYS motor

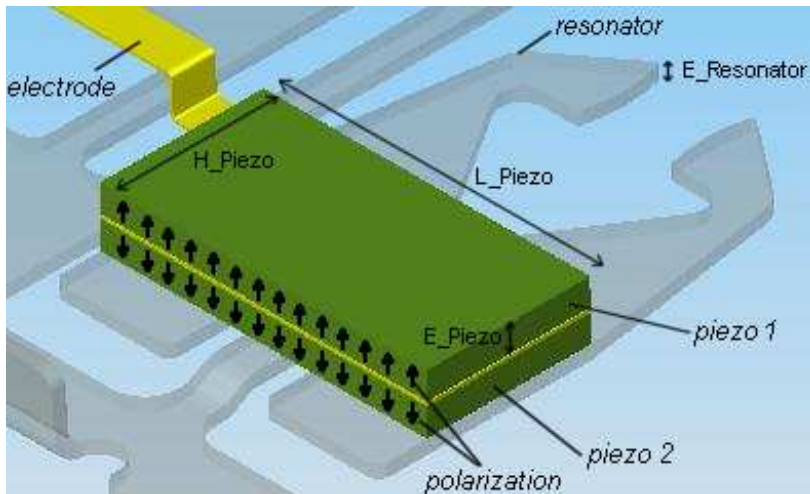


Fig. 5.26: MUM: piezoelectric elements and polarization

Deformations obtained for both resonance frequencies are presented in Fig. 5.27. These vibrations modes have been obtained in a previous work carried out in the Swiss Federal Institute of Technology in Zürich (ETHZ) by H. Widmer. He developed a simulation method (based on superimposed eigenmodes) to calculate the mechanical properties of vibrational impact motors [WD04]. Thanks to his study, it is possible to determine the motor characteristics such as speed, torque,

power and also electrical properties directly from the design characteristics of any new motor design. He used ANSYS and Matlab softwares for these calculations. ANSYS is used for the modal analyses and the responses of these different modes are calculated with Matlab. Then, a program developed in Matlab and which takes the description of the modes provided by ANSYS makes it possible to obtain the transient behavior of the motor, taking into account the moving part. Figure 5.28 depicts the result found after the transient simulation carried out by H. Widmer for the initial structure of the motor. The displacement of the motor moving part is obtained by applying a voltage of $20V$ during $4ms$. As it is shown, the moving part moves about $23\mu m$ in the forward direction ($f_1 = 460kHz$) and about $10\mu m$ in the backward direction ($f_2 = 508kHz$). Values of the driving force for both forward and backward motions have also been determined (about $3mNm$ and $4.7mNm$ respectively).

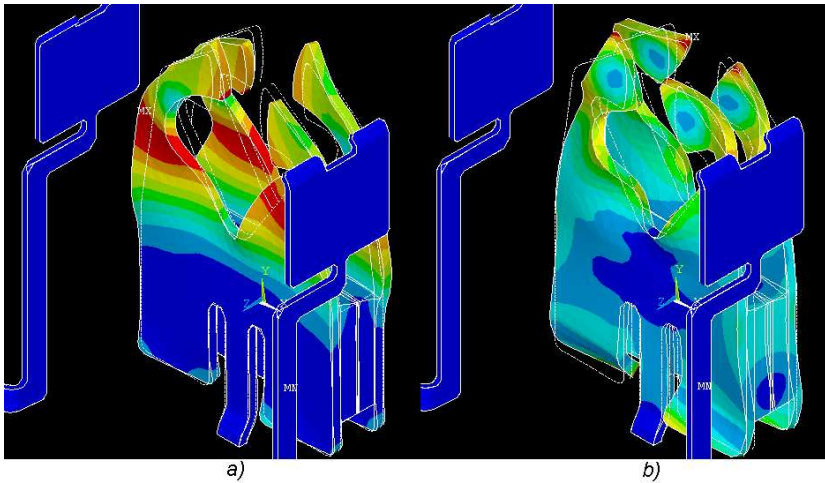


Fig. 5.27: FEM results obtained for the actual structure: a) forward motion ($f_1 = 460kHz$), b) backward motion ($f_2 = 508kHz$)

To verify his model, many experiments on different prototypes have been carried out and it has been demonstrated that the simulations performed lead to a

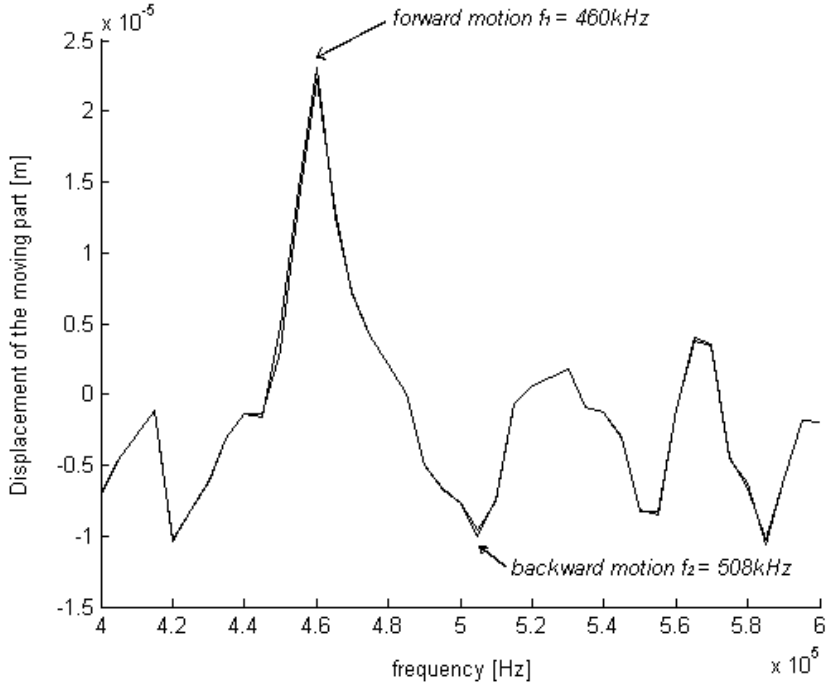


Fig. 5.28: Transient simulation of the initial structure: displacement of the motor moving part obtained by applying a voltage of 20V during 4ms

good agreement with the experimental data. So, the method has been validated by MINISWYS SA. In this manner, the designs found after the pre-optimization and FE optimization stages of our study will be simulated by the method proposed by H. Widmer for the results validation. This will be presented in the optimization and validation sections. Furthermore, some other projects dealing with the analysis of the characteristics and the control of the motor have been carried out ([AP05] and [BW05]), but no optimization study has been undertaken yet. So, in a first approach, only the displacement amplitude of the lens will be optimized, even if the torque or the speed of the motor could also be optimized applying the same reasoning. First of all, the numerical modeling of the motor has been performed. Indeed, even if some results have already been presented

previously about the work carried out by H. Widmer, a new FE model has been built, in particular to allow the parametrization of the motor. This is presented in the next section.

5.6.3 Numerical modeling of the motor

Dimensions and material properties of the simulated motor are presented in Table 5.5 and in Appendix C. These dimensions are also referred to Fig. 5.29.

Table 5.5: Dimensions and materials of the simulated structure of the MUM

Parameter	Value
L_Piezo	3.0mm
H_Piezo	1.5mm
E_Piezo	0.25mm
E_Resonator	0.13mm
L_Resonator	3.0mm
L1	0.42mm
L2	0.43mm
L3	1.0mm
L4	1.22mm
H_Resonator	4.5mm
H1	1.2mm
H2	0.75mm
H3	1.0mm
H4	2.55mm
H5	2.75mm
Material of the resonator: copper	
Density	8900 kg/m ³
Young's modulus	1.24 · 10 ¹¹ N/m ²
Poisson's ratio	0.364

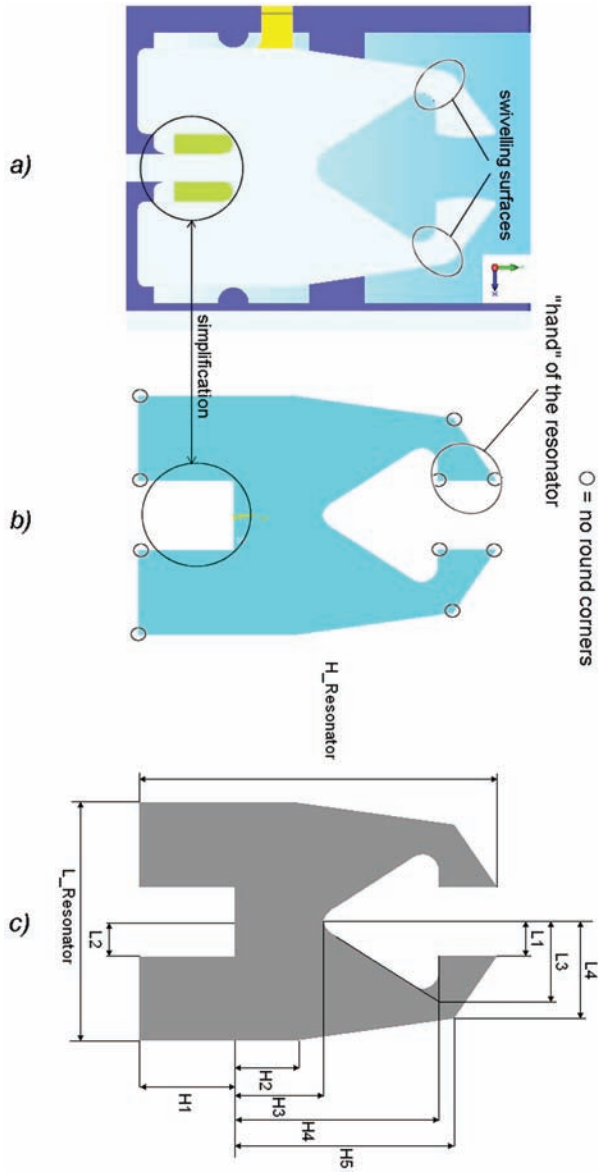


Fig. 5.29: MUM: a) initial design; b) numerical model; c) parametrization

Moreover, Fig. 5.29 shows the initial design and the numerical model built as well as the parametrization of the motor. As it is shown, some simplifications have been made in the numerical model (no round corners, simplified base of the motor), in particular for an easier parametrization.

The analysis of the present structure (initial) of the MINISWYS motor had two goals. On one hand, the aim was to determine its working principle and identify the role of the different parts constituting the motor. In the other hand, it was interesting to study the possibility of using a less complex structure presenting a behavior similar to that of the present structure. The first part of the analysis gave us the possibility to understand the behavior of the MINISWYS motor according to its geometrical parameters and also allowed us to know the direction to take for the pre-optimization stage of the study (variation of the input parameters according to their influences on the displacement amplitude). Figure 5.30 shows the vibration modes obtained (forward and backward motions).

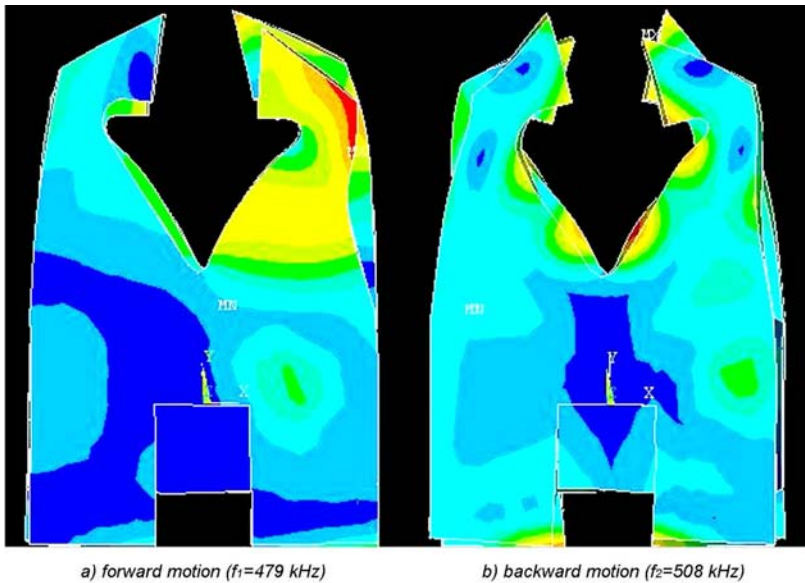


Fig. 5.30: Initial structure: vibration modes for the forward and backward motions

As it is shown, results are quite similar to those obtained by H. Widmer and presented in Fig. 5.27. The frequency deviation for the forward motion can be explained by the simplifications made in the construction of the numerical model. But that is not important considering the fact that the aim of the study remains the optimization of the displacement amplitude of the lens and with this intention, dimensions of the motor will be varied thereafter.

The second part of the analysis was to find equivalent structures or even new structures less complex than the initial one with the aim of reducing the computing time necessary to carry out a simulation, in particular in sight of the FE optimization stage of the study which requires significant computing times. For that purpose, many simulations have been carried out. The results are not presented here but can be found in Appendix D and in [BerMs]. They have shown that the whole structure needs to be simulated (and not only a half or a quarter resonator) but also that the motor could operate at frequencies lower than those present ones (in particular, this could be interesting to reduce the losses due to an operation at high frequencies). But we decided only to study the case of an operation frequency around the two values already determined (f_1 and f_2) and which are those for which the motor is sure to operate (validated experimentally by MINISWYS SA).

After the modal analyses carried out to determine the vibration modes of the resonator of the MINISWYS motor, harmonic responses have been obtained by applying a voltage of 20V to the piezoceramics. Then, some nodes of the structure have been chosen and the mean value of the displacements in the three directions have been obtained. Figure 5.31 shows the different points at the extremities of the vibrating parts of the resonator taken into account for the calculation of the displacements. Points at the four extremities have been taken into account for a more accurate analysis. Then, using Matlab, the mean values of the movement amplitudes in the three directions have been calculated (absolute values). Figure 5.32 shows the results obtained. The values found for the two operating frequencies of the present structure of the resonator are given in Table 5.6. These values are absolute values. As the results show it, the movement amplitude is bigger in the y direction, which implies, intuitively, that the motion of the moving part of

the motor is mainly due to the vertical displacements of the vibrating extremities of the resonator. Some analysis of the trajectory of the points at the extremities of the resonator has been undertaken but no conclusion could be drawn. So, the movement of the extremities of the resonator is rather chaotic. Another interesting point which can be raised from Fig. 5.32 is that there are two frequencies for which the displacements in the y direction are bigger compared to the other directions (about $250kHz$ and $300kHz$) and that could be interesting for an operation of the motor at lower frequencies. But this observation should be verified experimentally and for the continuation of the work, we decided to focus us on the two well known operation modes.

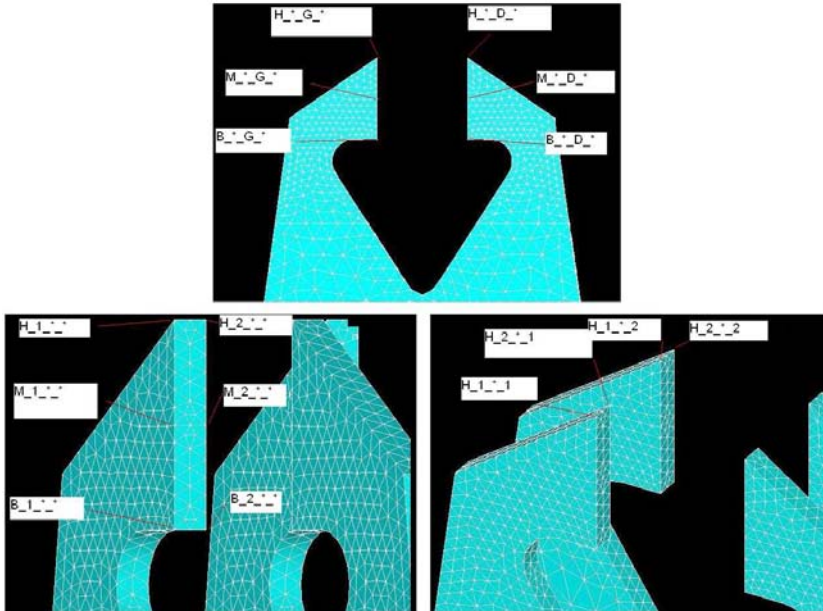


Fig. 5.31: Points at the extremities of the resonator taken into account for the calculation of the mean value of the displacements in the three directions

So, with the aim of increasing the motion of the lens (in both directions), an

Table 5.6: Values of the displacements found for the initial structure

Vibration mode	x direction	y direction	z direction
1 (forward)	$5.1 \mu\text{m}$	$5.6 \mu\text{m}$	$4.1 \mu\text{m}$
2 (backward)	$1.2 \mu\text{m}$	$2.7 \mu\text{m}$	$1.5 \mu\text{m}$

optimization study has been carried out. To maximize the displacement of the moving part of the motor, we made the hypothesis that by amplifying the displacements of the extremities of the resonator in the y direction, that would lead to increase the displacement amplitude of the lens. In the next section, a sensitivity analysis is first of all carried out. Then, using the results obtained in this pre-optimization stage, FE optimization is performed and results are presented.

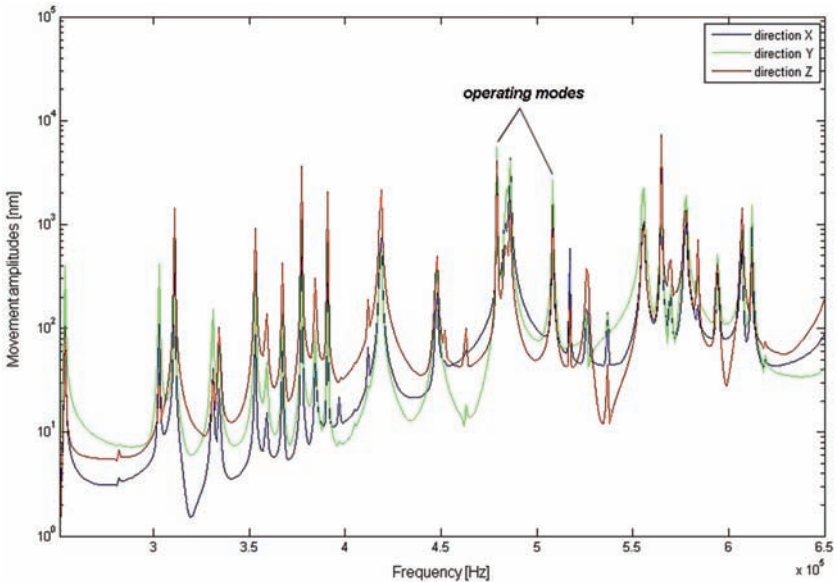


Fig. 5.32: Initial structure: movement amplitudes (absolute values) in the three directions

5.6.4 Optimization

Sensitivity analysis (pre-optimization)

As already explained in the previous sections, only the design of the resonator will be taken into account for the optimization study. Indeed, the interaction between the vibrating part of the motor and the moving part is not taken into account because it would be very complex and would also need high computing times. Moreover, the operating hypothesis formulated previously allows to say that if the type of movement observed at the extremities of the resonator is similar to the one simulated with the present structure (for the two operation frequencies f_1 and f_2), then the new designed motor will work. Indeed, if a bigger deformation amplitude in the y direction is simulated without the interaction, then the displacement of the moving part taken the interaction into account will be bigger too.

Furthermore, the piezoelectric ceramics used in the initial motor will be kept unchanged in our simulations. It is obvious that an improvement of the deformation amplitude could be reached by changing the piezoelectric material (by using multilayered piezoelectric ceramics for example). But this point will remain for a further investigation. Moreover, the whole size of the resonator will not exceed that of the present one because the available space in the optical module is limited and so some dimensional constraints have been introduced in the sensitivity analysis as well as in the FE optimization. So, parameters $E_{Resonator}$, $L_{Resonator}$ and $H_{Resonator}$ have been fixed to their initial values.

The pre-optimization carried out with ANSYS and Matlab has been initially based on many simulations performed, in particular to study the vibration modes obtained due to the variation of the different parameters used in the parametrization of the resonator (see Fig. 5.29). These simulations have shown [BerMs] that the parameters $H1$, $H2$ and $L2$ had to be fixed during the optimization process because their influence on the operating modes of the resonator were too important and that would imply a change of the operating frequencies which would not enable us to affirm with certainty that the motor would work.

So, after these considerations, Doehlert method has been used to obtain the influences of the remaining parameters (H3, H4, H5, L1, L3 and L4) on the movement amplitude in the y direction obtained at the extremities of the resonator. In a first approach (simplified case), only the principal relative effects have been calculated and taken into account for the study. Figures 5.33 and 5.34 show the results obtained.

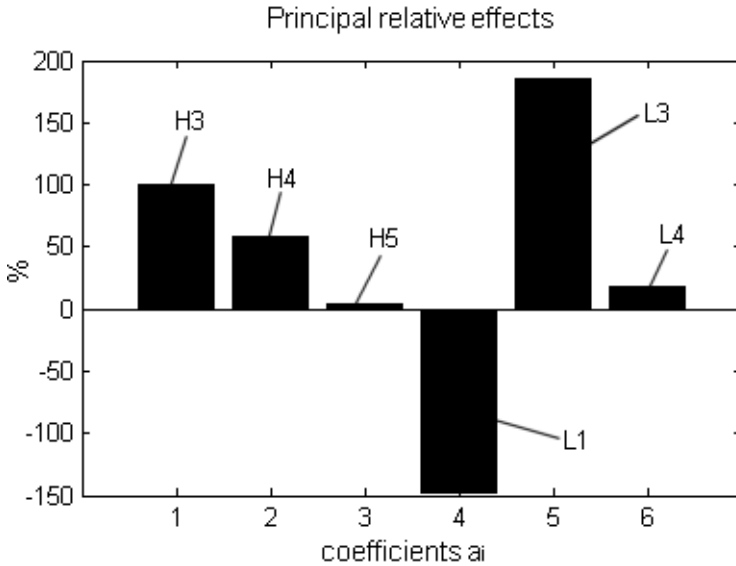


Fig. 5.33: Principal relative effects for the first vibration mode (f_1)

The results obtained show that there are four parameters that have an important influence on the movement amplitude for the two operating frequencies. Indeed, the values of H4 and L3 indicate that it is necessary to decrease the swivelling surfaces of the resonator (see Fig. 5.29). By decreasing these surfaces, the mechanical resistance to the movement is also decreased and so the movement amplitude is increased. The value of L1 indicates that it would be necessary to increase the length of the "hands" of the resonator. Indeed, by increasing this length, the extremities of the resonator will be more distant from the rotation center around

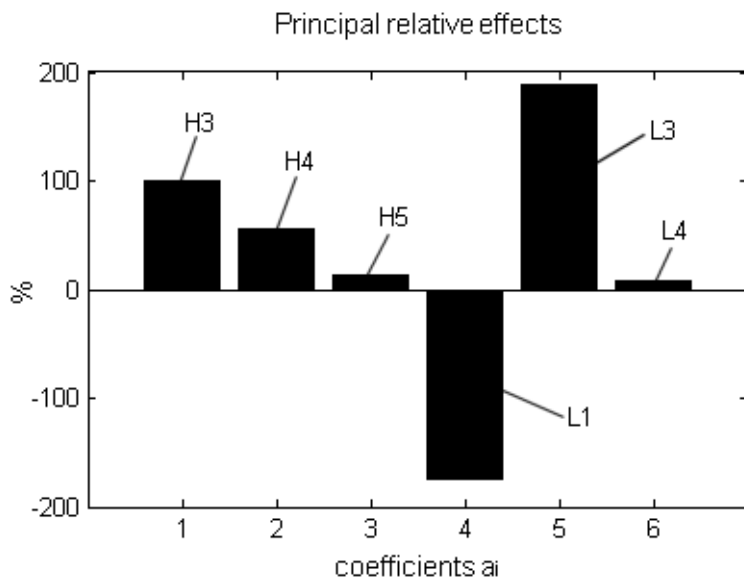


Fig. 5.34: Principal relative effects for the second vibration mode (f_2)

the swivelling surface and thus the movement at the extremities of the "hands" will be amplified. Moreover, the value of H3 indicates that the "hands" of the resonator should be thinner and thus their weight will decrease. The effect will be to decrease the mechanical inertia to the movement and thus increase the movement amplitude at the extremities of the resonator. With regard to the parameters L4 and H5, they have not a significative influence on the movement amplitude and will be fixed during the FE optimization.

According to the results obtained thanks to the sensitivity analysis, a pre-optimized structure has been obtained. The dimensions and the model of the simulated structure are presented in Table 5.7 and in Fig. 5.39, respectively. Moreover, Fig. 5.35 shows the deformations obtained for the two operating frequencies. The results show an important improvement of the movement amplitudes in the vertical direction at the extremities of the resonator (see Table 5.8 and Fig. 5.40 in the "Results summary" section).

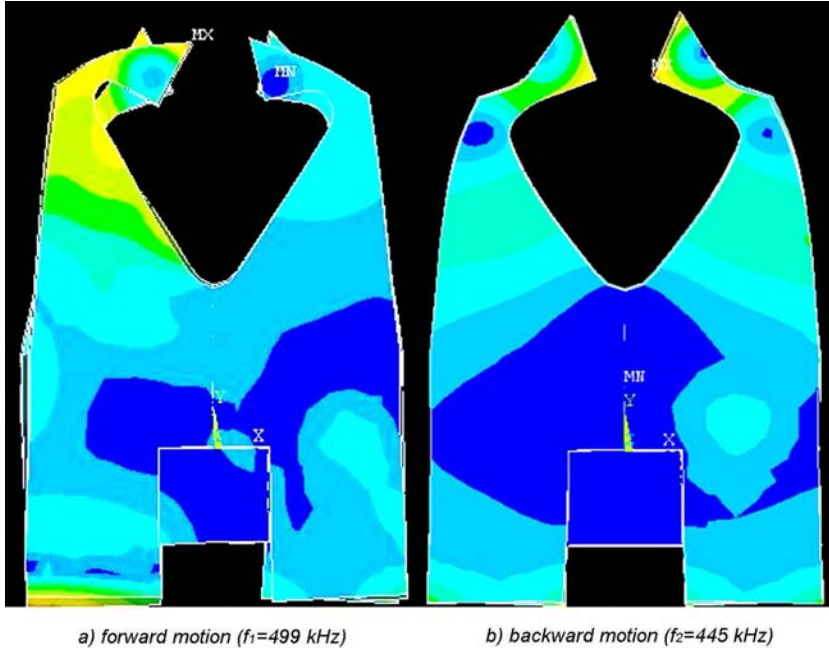


Fig. 5.35: Pre-optimized structure: vibration modes for the forward and backward motions

Then, the results found after the pre-optimization stage have been simulated using the program developed by H. Widmer (taking into account the moving part of the motor). Figure 5.36 depicts the displacement of the moving part when a voltage of 20V is applied to the piezoceramics during 4ms. As the results show it, the displacement amplitude of the moving part has been strongly increased but only for the forward motion ($f_1 = 499$ kHz). The backward motion is not present for the second vibration mode (around 510 – 520 kHz) for which the motor should work. A frequency of about 445 kHz has been obtained instead. The different results are presented in Table 5.8 and in Fig. 5.41.

The results show that the vibration modes obtained with the pre-optimized structure are different from the operating modes of the initial structure, in particular

for the second operating mode. This change in the deformation does not allow predicting if these two vibration modes will make it possible to obtain the two desired motions for the motor. In order to obtain an answer to this question, measurements on prototypes will be very helpful (see the "Discussion and validation" section). Nevertheless, the results obtained after the pre-optimization stage are helpful to carry out the FE optimization. The goal of this part of the study is to try to increase even more the movement amplitudes of the moving part but also obtain the two motions (forward and backward) at the operating frequencies of the initial structure of the motor.

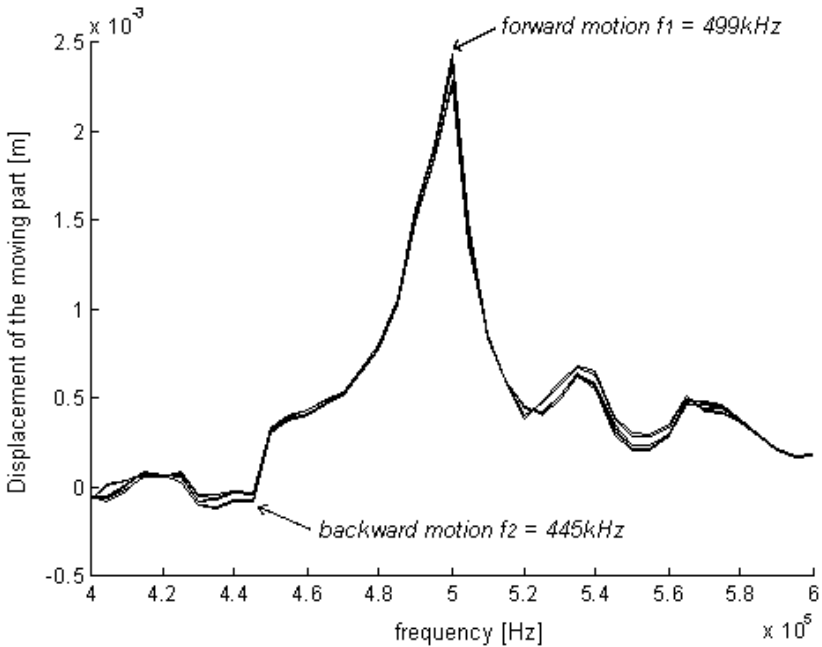


Fig. 5.36: Transient simulation of the pre-optimized structure: displacement of the motor moving part obtained by applying a voltage of 20V during 4ms

FE optimization

The variation range of the six most influential parameters has been fixed to $\pm 5\%$ of their initial values. These values have been chosen according to the results obtained after the pre-optimization stage. The other parameters have been fixed. First order method has been chosen for the FE optimization. Figure 5.37 shows the deformations obtained for the forward and backward motions.

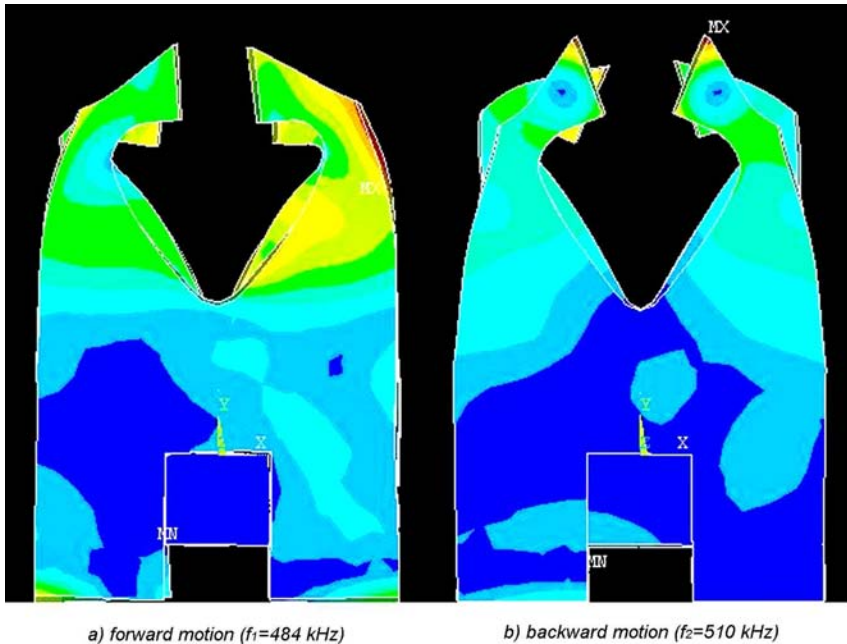


Fig. 5.37: FE optimized structure: vibration modes for the forward and backward motions

The structure obtained after the optimization process, makes it possible, contrary to the pre-optimized structure, to find similar operating modes to those present in the initial structure. This allows us to affirm that the probability that this optimized structure design will effectively work is quite important. However, this will be confirmed by the measurements on a prototype presented later. Moreover,

the different results obtained with the optimized structure are presented in Table 5.8 and in Fig. 5.41.

Finally, the results found after the FE optimization stage have been also simulated using the program developed by H. Widmer. Figure 5.38 shows the result obtained. The different results are also presented in Table 5.8 and in Fig. 5.41.

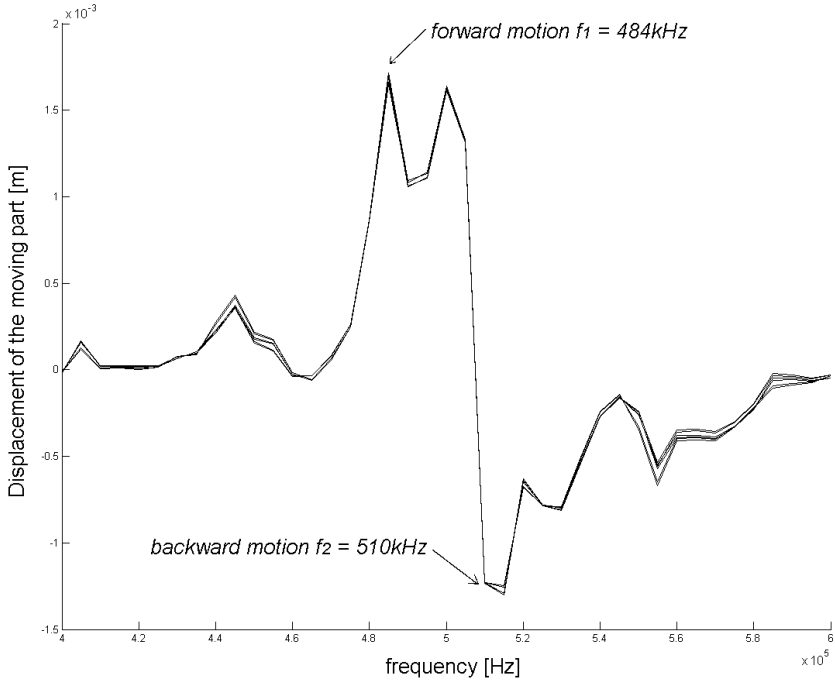


Fig. 5.38: Transient simulation of the optimized structure: displacement of the motor moving part obtained by applying a voltage of 20V during 4ms

Results summary

As the optimized structure obtained shows it, the optimization of the MINISWYS motor has been performed. In spite of the high complexity of the structure and

the different possible vibration modes, it has been demonstrated that it is possible to significantly improve the movement amplitudes of the moving part (motion of the lens). First of all, Table 5.7 summarizes the dimensions of the simulated structures, from the initial one to the final optimized structure. Then, Fig. 5.39 shows these different structures to emphasize the differences in the resonator designs. Finally, Table 5.8, Fig. 5.40 and Fig. 5.41 summarize the different results obtained throughout the study of this application case.

Table 5.7: Dimensions of the simulated structures

Initial structure		Pre-optimized structure		FE optimized structure	
Parameter	Value	Parameter	Value	Parameter	Value
E_Resonator	0.13mm	E_Resonator	0.13mm	E_Resonator	0.13mm
L_Resonator	3.0mm	L_Resonator	3.0mm	L_Resonator	3.0mm
L1	0.42mm	L1	0.378mm	L1	0.399mm
L2	0.43mm	L2	0.43mm	L2	0.43mm
L3	1.0mm	L3	1.1mm	L3	1.05mm
L4	1.22mm	L4	1.22mm	L4	1.22mm
H_Resonator	4.5mm	H_Resonator	4.5mm	H_Resonator	4.5mm
H1	1.2mm	H1	1.2mm	H1	1.2mm
H2	0.75mm	H2	0.75mm	H2	0.75mm
H3	1.0mm	H3	1.1mm	H3	1.05mm
H4	2.55mm	H4	2.805mm	H4	2.55mm
H5	2.75mm	H5	2.75mm	H5	2.268mm

Table 5.8: Results comparison of the simulated structures

Structure	Initial		Pre-optimized		FE optimized	
	1	2	1	2	1	2
Vibration mode	1	2	1	2	1	2
Frequency [kHz]	479	508	499	445	484	510
Displ. y direction [μ m]	5.6	2.7	247.8	2.1	3365.0	25.6
Displ. moving part [mm]	0.023	-0.01	2.4	-0.1	1.7	-1.25

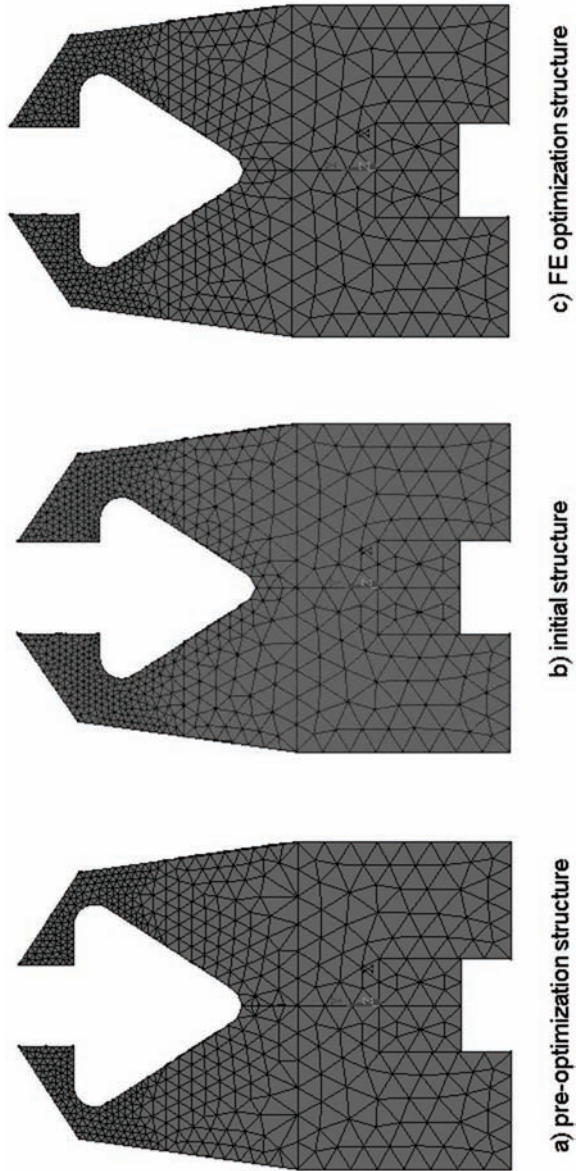


Fig. 5.39: Structures comparison: a) pre-optimized structure, b) initial structure, c) FE optimized structure

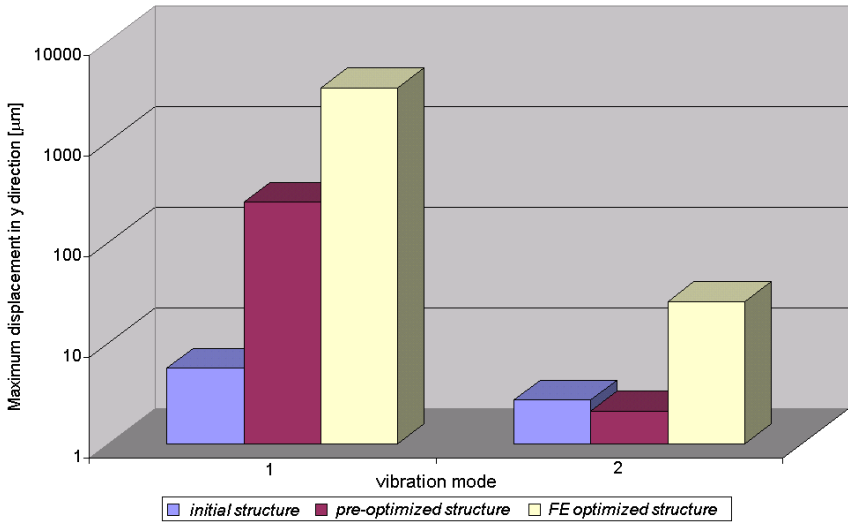


Fig. 5.40: Structures comparison (resonator) : initial, pre-optimized, FE optimized

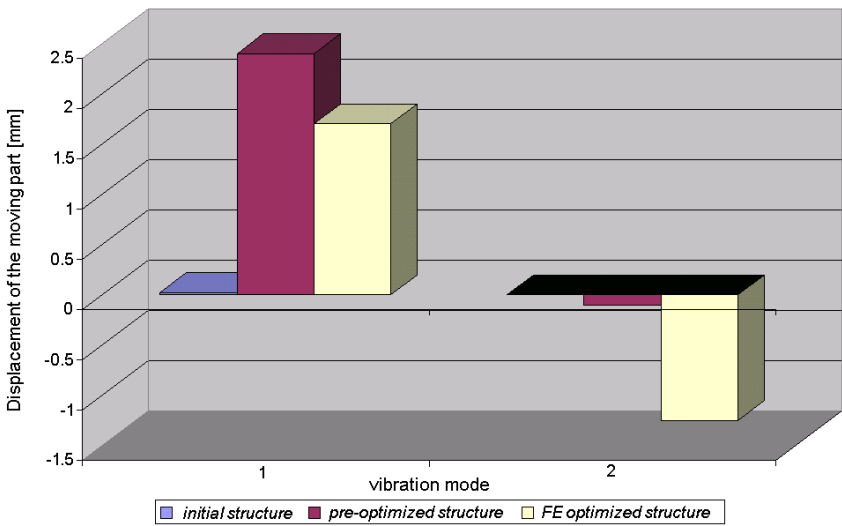


Fig. 5.41: Structures comparison (moving part): initial, pre-optimized, FE optimized

5.6.5 Methodology validation

Experimental results

In the previous section, optimization results of the MINISWYS ultrasonic motor have been presented. These results have been obtained using a numerical model of the motor and performing transient simulations. Even if this method has been validated by MINISWYS SA, some experiments are necessary to corroborate the optimization methodology presented. Indeed, as it is known, some hypotheses made for the simulations (no damping coefficient has been taken into account in the simulations for example) are too restrictive but necessary to simplify the model. Thus, some measurements have been realized on a prototype built thanks to the results obtained by the FE optimization. Figure 5.42 shows the design of the resonator chosen for building the prototype. This structure has the same dimensions as the design model presented in Fig. 5.39c (round corners have been added).

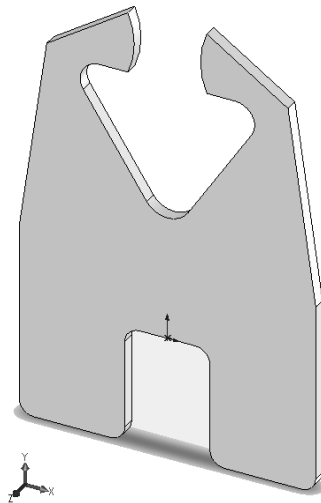


Fig. 5.42: Design of the resonator built for measurements

In order to compare the results obtained with the structure found by FE optimization and the initial structure, some experiments have been also carried out on a motor with a resonator designed like the one presented in Figures 5.29 and 5.39 b. These measurements have been made by MINISWYS SA using in particular the LabView software. Indeed, for confidentiality reasons, we could not have access to the different prototypes nor the possibility of testing them ourselves. Nevertheless, some measurements on both structures (initial and optimized) could be obtained. Results are presented in Figures 5.43 and 5.44 for a motor using the initial design for the resonator and in Fig. 5.45 for a motor using the optimized resonator design.

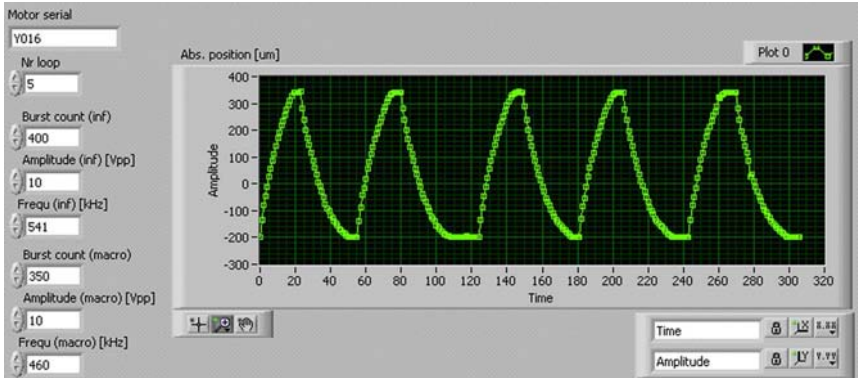


Fig. 5.43: Measurement obtained with the initial structure using a coil to increase the input voltage (\Rightarrow applied voltage to piezoceramics of 20V)

Figure 5.43 depicts the position of the moving part of the motor as a function of the time when a coil is used. The coil allows to increase the voltage applied to the piezoceramics by a factor 6. So, in this case, the voltage before the coil was 10V pick to pick and approximately 20V (RMS value) across the piezoceramics. Then, Fig. 5.44 shows the results for the same structure but without using a coil and with a voltage of 7V applied to the piezoceramics. Finally, Fig. 5.45 depicts the results obtained with the optimized structure of the resonator and without using a coil (voltage of 5V applied to the piezoceramics). One can notice that

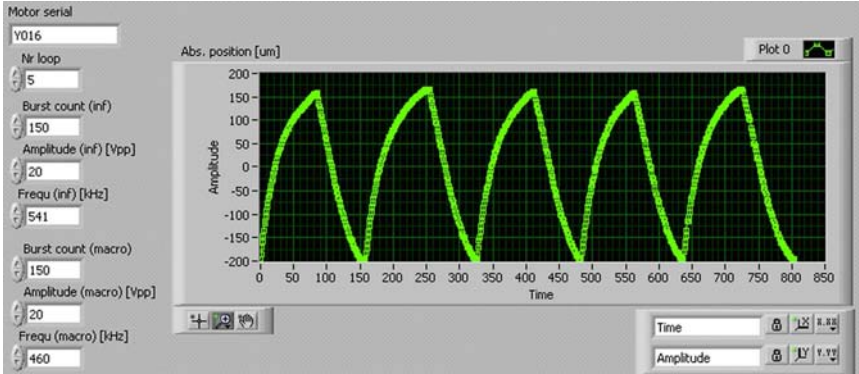


Fig. 5.44: Measurement obtained with the initial structure without using a coil to increase the input voltage (\Rightarrow applied voltage to piezoceramics of 7V)

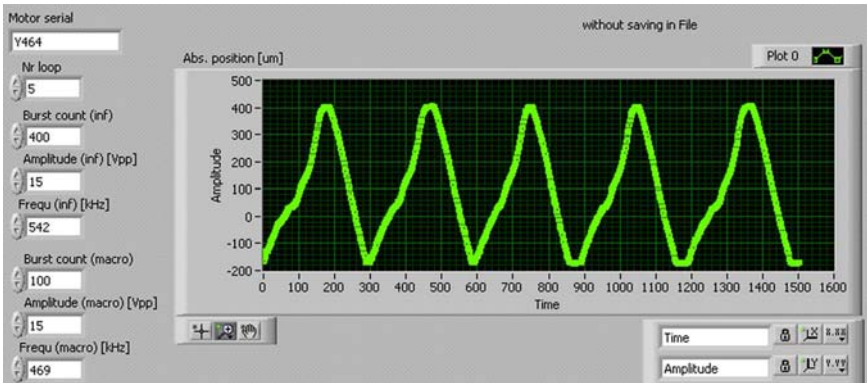


Fig. 5.45: Measurement obtained with the optimized structure without using a coil to increase the input voltage (\Rightarrow applied voltage to piezoceramics of 5V)

on the left ascending side of the triangle curve (Fig. 5.45), a slight mechanical friction point is present. Furthermore, the differences between the curves of Fig. 5.44 and Fig. 5.45 can be explained by the fact that the motor operates at slightly different frequencies and that the friction forces vary from one case to another.

These different results are summarized in Table 5.9 and are discussed in the fol-

lowing section.

Table 5.9: Results comparison of the tested structures

Structure	Initial				FE optimized	
	1	2	1	2	1	2
Vibration mode	1	2	1	2	1	2
Frequency [kHz]	460	541	460	541	469	542
Applied voltage [V]	7	7	20 (coil)	20 (coil)	5	5
Displ. moving part [μm]	165	-200	350	-200	420	-180

Discussion

First of all, as Table 5.9 shows it, the results obtained with the optimized structure of the resonator are better than those obtained by using the initial design. On one hand, it can be noticed that to travel the full stroke imposed by MINISWYS SA ($550\mu\text{m}$), it is necessary for the initial motor to use a coil to increase the input voltage to 20V. On the other hand, for a motor using the optimized structure of the resonator, the full stroke is widely reached ($600\mu\text{m}$) for an applied voltage of 5V without needing to use a coil. On the contrary, in the case of using the initial resonator design and without the use of a coil, the motor travels only $365\mu\text{m}$ for an applied voltage of 7V.

Normally, with the original resonator geometry, an applied voltage of about 11V is necessary to obtain a full stroke (MINISWYS SA measurements) without using a coil. So, there is more than 50% less voltage needed to obtain the same value in the case of using the optimized structure. Now, if a coil is used, the needed voltage would be only about 1V to supply the motor with the optimized design of the resonator. Moreover, within sight of the results, for the same voltage applied to the piezoelectric ceramics, the motion of the moving part is increased by a factor higher than 2 if the optimized structure of the resonator is considered. Thus, it means that the optimization of the travel range of the motor has been reached.

Validation

As it has been demonstrated with the experimental results, an optimized structure of the resonator of the MUM has been obtained. Now, if the results of Table 5.9 are compared to those found by simulation and presented in Table 5.8, we can see that there are some differences between the simulated structures and the measurements. Indeed, the resonance frequencies of both vibration modes simulated are slightly different with those measured, approximately 3% to 4% for the forward motion and around 6% for the backward motion. These differences can be explained by considering the small variations between the structure simulated (numerical model) and the structure that has been built for the measurements and also by the assumptions made for the simulations.

So, the program of Heinz Widmer and our simulations proved to be a good way to model the MUM and the results found are in agreement with the measurements and can then be validated. Moreover, the optimization methodology presented in this thesis work has shown its potential and has become an interesting working tool for MINISWYS SA.

Nevertheless, this is only a first study on the optimization of the MUM [Fer09]. Indeed, one of the essential points for a future optimization of the MINISWYS motor is to integrate the mechanical constraints and the resistance of materials in the process of optimization. In the same direction, other objectives like decreasing the operation frequency of the motor (around 200kHz - 300kHz to minimize the losses) or replacing the coil by a piezoelectric transformer, allowing for example to obtain a more compact system (a saving in space) or a better efficiency, are some aspects to be retained for future developments.

The following section presents some methods which could be applied for this purpose to carry out a multi-objective optimization of the MUM. In addition, chapter 6 presents a study on piezoelectric transformers which could be in particular an interesting alternative to increase the voltage applied to the piezoceramics in the case of the MUM.

5.7 Multi-objective optimization methods

5.7.1 Introduction

In this section, some multi-objective optimization methods are presented and described. This is done with the aim of showing that it is possible to apply the methodology of design of experiments and then FE optimization for problems where several objective functions need to be taken into account and not only one as it has been the case in the preceding sections.

The Multi-Objective Problem (MOP) is an extension of the single-objective optimization problem. In the MOP, several objective functions are to be solved simultaneously. In the single-objective optimization, one can find a solution which is absolutely best with respect to all other alternatives. In the MOP, because of incommensurability and conflict among objectives, it is not always possible to find a solution for which each objective function gets its optimal value simultaneously. It means that no improvement in any objective function is possible without deterioration of at least one of the other objective functions. The solutions of a MOP are therefore given in the non-dominance or Pareto optimality sense. Definitions and explications about non-dominance and Pareto optimality can be found in [Mie99] and [Deb02].

Then, to solve a MOP, an appropriate optimization method is needed. Many multi-objective optimization methods have been developed over the past decades. Some of them, which are most commonly used in engineering will be described in the next paragraphs, based on a thesis work carried out recently [Fu05].

5.7.2 Traditional multi-objective optimization methods

There are many kinds of methods for handling MOPs. The most traditional ones convert a MOP into a single (scalar) or a family of single objective optimization problems by using some user-defined preference structures and then solve the problem using the widely developed methods for single objective optimization. This can be a good solution in our case, using FE optimization taking into account different objective functions. In the following, some most commonly used meth-

ods are briefly described with the aim of giving the reader a basic idea of how to solve a multi-objective optimization problem in the framework of a possible development of our study. More details can be found in [Fu05], [Mie99], [GC00] and [Deb02].

Weighted sum method

The weighted sum method scalarizes a set of objectives into a single objective by assigning weights to each objective function. This method is the simplest and the most widely used.

ϵ -Constraint method

ϵ -Constraint method can overcome some of the problems which can be encountered with the weighted sum method. In this method, a MOP is reformulated just by keeping one of the objectives and transfer the others into constraints.

Value function method

In the value function method, a preference structure is mathematically represented using a value function which maps solutions in the objective space into a real number so that the bigger the number, the more preferred the solution in the objective space is.

In addition to the above described methods, there are many other conventional approaches that are discussed in [Mie99].

5.7.3 Multi-objective evolutionary algorithms

Conventional multi-objective optimization methods solve a MOP by scalarization. For these methods, many difficulties in finding multiple Pareto optimal solutions exist. Over the past decades, Multi-Objective Evolutionary Algorithms

(MOEAs) have been developed. The basic feature of MOEAs is multiple directional and global search through maintaining a population of potential solutions from generation to generation [GC00]. Furthermore, MOEAs can find multiple and different Pareto optimal solutions. The general procedure to follow in a Pareto-based MOEA is composed by the following steps:

1. **Initialization:** An initial population of individuals (solutions) is generated randomly. Each individual refers to a design which contains several design variables. Each individual is represented by a chromosome (string) which contains several segments corresponding to the different design variables.
2. **Evaluation:** During evaluation, each individual is evaluated to give some measure of its fitness. In an unconstrained single-objective optimization problem, the fitness of a solution is assigned a value which is a function of the value of the corresponding objective function. In MOPs, special approaches are needed to determine the fitness value of a solution according to multiple objectives (see [GC00] and [GR87] for details).
3. **Selection:** The primary task of the selection operator is to select and duplicate good solutions to create a new set of parent solutions. To do this, it exists a number of selection methods: tournament selection, proportionate selection and ranking selection are some common types. Details can be found in [Deb02].
4. **Generation:** Here, the goal is to generate offspring using the crossover and mutation operators. The crossover operator provides the search mechanism of the EA. It creates new solutions (offspring) by exchanging features of two parent solutions picked randomly from the set of parent solutions. There exists many crossovers, such as single- or two-point crossover operators, linear crossover, blend crossover, boundary crossover, simulated binary crossover, unimodal normally distributed crossover, fuzzy connectives based crossover or direction-based crossover. For details, refer to [GC00]. Then, the mutation operator is used to perform a local search to find an improved solution.

The above three operators, namely selection, crossover and mutation constitute the main part of a EA. Through them, a new population is created in every generation (iteration).

5. **Termination:** Then, termination conditions are checked. It means that if the specified maximum number of generations is reached, or another stopping criterion is satisfied, the iteration stops. Otherwise, the surviving population becomes the starting population for the next generation and one returns to step 2.
6. **Determination of the preferred solution:** Finally, a best solution is selected for implementation.

Figure 5.46 shows a standard MOEA flowchart.

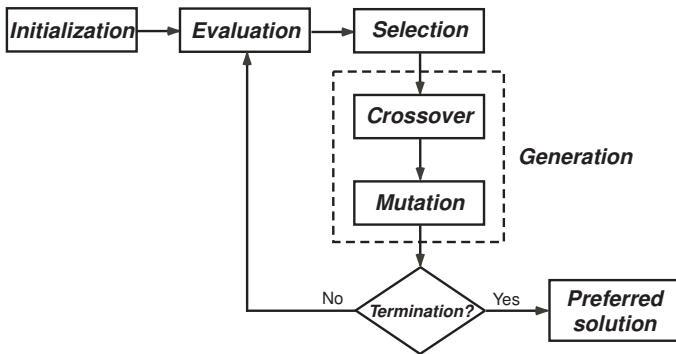


Fig. 5.46: Standard MOEA flowchart

The best known evolutionary algorithms include genetic algorithms (GAs), evolution strategies and evolutionary programming. GAs are the most widely used EAs in the field of optimization. They are described in the following paragraph.

5.7.4 Multi-objective genetic algorithms

Genetic Algorithms were invented by John Holland in the 1960's and were further developed by him, students and colleagues during the 1960's and 1970's. Genetic algorithms were not intended to be used for solving a specific problem like evolutionary strategies and evolutionary programming, but rather to study adaptation and evolution in nature. Holland's original genetic algorithm had three operators, crossover, mutation and inversion. These were used on genes (represented by bits) of a population of chromosomes. The population was allowed to reproduce and statistically the fitter genomes produced more offspring than the less fit genomes. Holland's major innovation was to use crossover and a population that was larger than two individuals. In recent years, the use of genetic algorithms has been booming. Genetic algorithms have successfully been applied to a wide range of problems and have in the latter part of the 1990's become a major research area in computer science.

The idea behind genetic algorithms is to mimic evolution in nature. A population is created and the individuals of the population compete, leaving the fittest to reproduce and the least to die. Evolution will then push the population to become fitter and fitter. For a more detailed introduction to genetic algorithms, see [BBM93], [Gol89] and [KG92] or [Mit98]. As genetic algorithms are close to evolution and genetics, it has borrowed many terms from these fields. In order to solve a problem with a genetic algorithm, a way of encoding a solution to the problem in a sequence of properties has to be found. This encoding is called the genotype of the solution. The encoding for each property is called a gene and the different values that the gene can have are called alleles. The encoding of the genes can be anything from a string of bits to instances of objects. When an encoding has been set, ways of combining and changing solutions must be devised. For evolution to work there has to be a measure of how good one genotype is compared to another. This measure is called fitness. It is generally easy to find a way to measure fitness, but often the fitness has to be scaled to get the best results.

The combining of two (or more) genotypes is called crossover. To start the evolution, an initial (often random) population is created. The population is then eval-

uated, i.e. fitness is assigned to each of its members. A new population is then created by letting the old population reproduce. A general improvement in fitness is guaranteed by letting the fitter individuals of the population have a higher probability of reproduction. The theory behind genetic algorithms is mostly non-existent. However, there have been some attempts to explain how they work and from where they get their power. Most notably is the Schema Theory of Holland (see [Mit98] for a detailed overview). The Schema Theory was developed for genomes using bit representation, but some attempts to convert it to a general representation have been carried out. A scheme is a pattern for the solution. In each position of the genome, the schema could have the value 1, 0 or *. The * means that the schema allows the genome to have any value (i.e. 1 or 0). The theory states that the genetic algorithm implicitly samples the different schemas for their usefulness in producing highly fit genomes. The genetic algorithm starts by exploring short schemas and builds longer schemas with the help of crossover and mutation.

This method could be also applied in the case of design optimization (thus for our case). By the way, the application of GAs for optimal placement of two piezoelectric actuators on a simply supported plate is in particular an example [SWW99].

5.8 Conclusion

Simulation works should incorporate a sensitivity analysis indicating the confidence limits of output data. This can be done efficiently by using up-to-date statistical techniques as it is done in other fields [FR95]. Sensitivity analysis must also be considered when developing models as well as when beginning a new study. In our case, some of these techniques have been applied to carry out the sensitivity analysis of piezoelectric motors. Design of experiments applied as a pre-optimization stage and then FE optimization method are a very interesting way to maximize the deformation amplitude of ultrasonic motors and show good complementarity. Design of experiments makes it possible to simplify the problem by reducing the variation ranges of the input parameters used to carry

out the FE optimization. The results obtained have shown that this optimization methodology is efficient. In particular, in the case of the MUM optimization, experimental results made it possible to validate the simulation results and therefore also the proposed methodology. Moreover, design methodology and optimization methods described in this work made it possible to explore a new way in the optimization field of smart ultrasonic actuators [Fre03]. Furthermore, some concepts of multi-objective optimization have been introduced. Basic ideas behind various multi-objective optimization methods using the scalarization technique, evolutionary algorithms or genetic algorithms have been briefly described, in particular in sight of considering a later multi-objective optimization study of the ultrasonic motors presented in this chapter.

In the next chapter, a new way to supply ultrasonic motors using piezoelectric transformers will be presented. As in the case of the MINISWYS motor, where a coil is used to increase the voltage given by a battery, it is possible to integrate a piezoelectric transformer to obtain the desired input voltage. Indeed, electromagnetic transformers have become obstacles to progress power supply miniaturization. Thus, piezoelectric transformers, which are more compact, immune to magnetic field and that present a high galvanic insulation, become more and more an alternative to electromagnetic transformers. Two different piezoelectric transformers are presented and compared: a Rosen type and a radial mode type.

6. PIEZOELECTRIC TRANSFORMERS: A NEW WAY TO SUPPLY ULTRASONIC MOTORS

6.1 Introduction

Recent progress on electrical power applications, particularly in the domain of the miniaturization of both electrical and electromechanical devices, has enabled envisaging the development of very compact systems (microcomputers, microsystems, cellular phones, etc.). The supply, storage and transformation of electrical power in these systems must respect this trend. However, the miniaturization of classical electromagnetic transformers raises certain problems such as manufacture both the coils and the magnetic core, increase in the losses and especially electromagnetic pollution of the environment. One interesting solution consists in using a piezoelectric transformer (PT) [HLW02], [HaS98]. This will insure an electrical-mechanical and mechanical-electrical double conversion of energy with a transformation ratio that allows adapting the output voltage being used. This kind of transformer is more compact, lends itself better to miniaturization, in addition to displaying the attractive characteristics of immunity to the magnetic field and a high galvanic insulation.

In this chapter, the study of two different piezoelectric transformers is presented. A Rosen type transformer, which is frequently employed in applications requiring considerable transformation ratios, and a radial mode type transformer, which is rather used when there is the need of having a high output power at high frequencies. After a general description of the transformers working principles, two

approaches will be presented. The first one, analytical modeling, is inspired by the technique used in electroacoustics and allows to build an electric equivalent circuit of the vibrating structure. The second approach deals with numerical finite element method using ANSYS software. A three-dimensional finite element model of each transformer is then simulated to find out the resonance frequency but also to determine the transformation ratio as a function of the frequency for several values of the load resistance. In order to validate the models, experiments will be performed. Measurements of the voltage gain, output power and efficiency of both piezoelectric transformer types will be compared taking into account their characteristics. Finally, applications of both radial mode type and Rosen type piezoelectric transformers will be briefly presented, in particular in sight of the integration of a PT for the ultrasonic motor power supply.

6.2 Working principle of the piezoelectric transformers

6.2.1 Rosen type

From a geometrical point of view, the Rosen type piezoelectric transformer is a piezoceramic divided into two parts and which is excited in a longitudinal vibration mode. In the example shown in Fig. 6.1, the left part, polarized in the thickness direction, represents the primary whereas the right part, polarized in the length direction, represents the secondary. If a voltage is applied between the input electrode and the ground (V_{in}), the left part will become deformed in its length. This deformation is proportional to the coupling coefficient d_{31} . This will contract the right part and as this one is polarized in its length direction (the electric field is directly proportional to the deformation and inversely proportional to the coupling coefficient d_{33}), a voltage between the output electrode and the ground will appear. This output voltage is directly proportional to the length to which the field is applied. Thus, the transformation ratio G_a can be expressed, in a first approximation, by the following equation:

$$G_a \propto \frac{PT's \text{ length}}{PT's \text{ thickness}} \cdot \frac{d_{31}}{d_{33}} \quad (6.1)$$

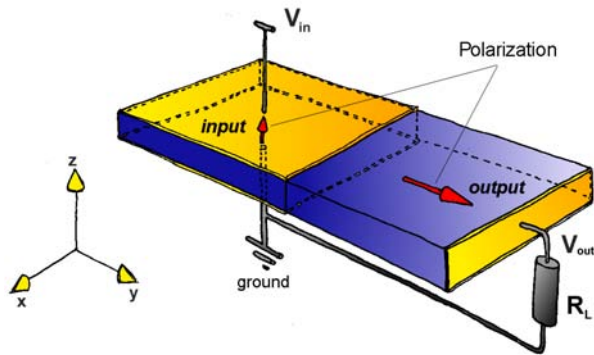


Fig. 6.1: Working principle of a Rosen type piezoelectric transformer

By changing the PT's dimensions or material, one can easily reach a large range of transformation ratios. We can also use a multilayered ceramic which allows to increase the electric field and so imply higher transformation ratios.

Two Rosen type transformers have been chosen for our study (see Fig. 6.2). A Noliac Ceramic Multilayer Transformer (CMT) [NoI] and a Transoner Rosen type multilayer transformer [Tra].

The different properties and characteristics of both Rosen type piezoelectric transformers can be found in Appendix E and F.

6.2.2 Radial mode type

One can find different radial mode type transformers, all characterized by a specific material, dimensions, polarization and configuration of their electrodes. Fig. 6.3 shows the Transoner T6 non-isolated radial mode type transformer [Tra]. This piezoelectric transformer is composed of six layers separated by electrodes. Four input layers (two at each end) and two output layers (in the middle). Each layer is polarized in the direction indicated by the figure. Moreover, one can find the different properties and characteristics of this PT in Appendix G (same piezoelectric material properties as the Transoner Rosen type PT).

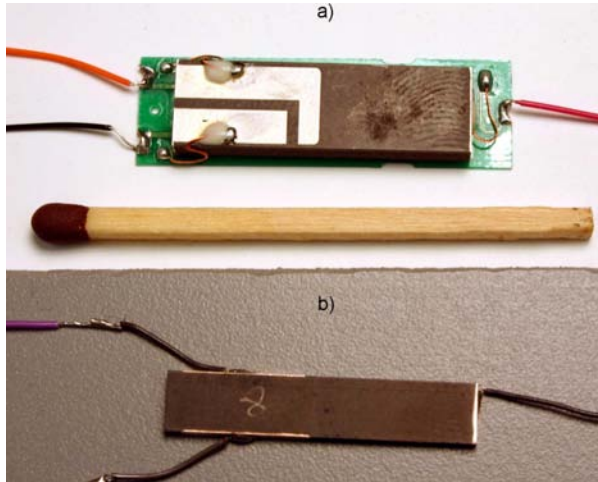


Fig. 6.2: Rosen type piezoelectric transformers: a) Transoner, b) Noliac CMT

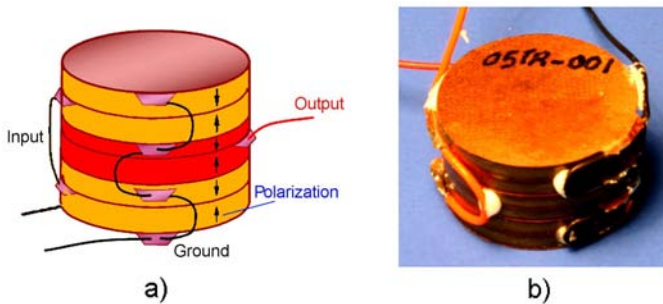


Fig. 6.3: a) working principle of a radial mode type transformer, b) Transoner radial mode type piezoelectric transformer

Due to the voltage applied, the deformation of the input layers is transmitted to the output layers which will generate a displacement electric field, i.e. an output voltage. Obviously, the connection between the layers must be rigid to ensure a perfect coupling and so, minimal losses. A transformer having more input layers than output layers is a step-up transformer. In a first approximation, a linear

transformation ratio can be expressed by eq. (6.2). However, this is valid only if there is an alternate polarization of the piezoelectric layers.

$$G_a \propto \frac{\#input\ layers}{\#out\ put\ layers} \quad (6.2)$$

Now, to approach the aspect of modeling, two methods are used. The first one is the analytical way, in particular using an electric equivalent circuit. The second one is the finite element method, performing numerical simulations using ANSYS software [Ans81]. These two approaches are presented in the next sections.

6.3 Analytical and numerical modeling

6.3.1 Introduction

In this section, analytical and numerical modeling are presented. Analytical modeling is carried out by using linear piezoelectric equations combined with the theory of elasticity, and an equivalent circuit model has been deduced. Indeed, as explained in chapter 4 (section 4.2.2), it is possible to determine an electric equivalent circuit characterizing the piezoelectric transformer near its resonance frequency [Rose64], [Fuk98], [Bak02]. Then, numerical modeling is performed building a three-dimensional finite element model and simulating it using ANSYS to find out the resonance frequency but also the transformation ratio as a function of the frequency.

6.3.2 Analytical modeling

Electric Equivalent Circuit (EEC)

According to piezoelectric transformers theory and [Bak02], it is possible to represent a PT by an electric equivalent circuit. Figures 6.4a and 6.4b show respectively the electric equivalent circuits of a PT without and with the dielectric losses taken into account.

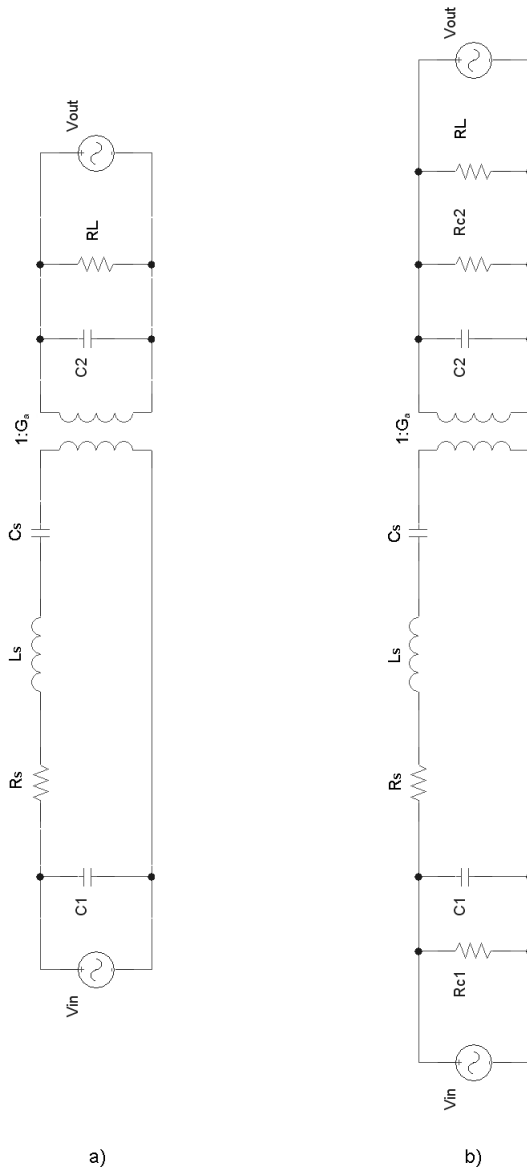


Fig. 6.4: Electric equivalent circuits of a PT: a) without diel. losses, b) with diel. losses

In this models, we consider a single vibration mode, neglecting coupling phenomena along the other axes. The elements values are approximated near the resonance frequency. The resistance R_S permits to take into account the mechanical losses. The capacitances C_1 and C_2 represent the capacitive nature of the device. The inductance L_S and the capacitance C_S model inertial and potential mechanical energies. Resistances R_{C_1} and R_{C_2} represent the dielectric losses in the material. Except the load resistance R_L , all the elements are directly related to the dimensional and piezoelectric properties of the transformer. In the case of a Rosen type PT, the way to calculate the different elements can be easily found in the literature ([Fuk98], [Rose64] and [Mas64]). In the case of the radial mode type PT, they can be calculated by using the following formulas [SVC05]:

$$R_S = \frac{\sqrt{2\rho_p s_{11}^E{}^3}}{16Q_m(N_1 d_{31})^2} \frac{N_1 t_1 + N_2 t_2}{r} \quad (6.3)$$

$$L_S = \frac{\rho_p s_{11}^E{}^2}{8\pi(N_1 d_{31})^2} (N_1 t_1 + N_2 t_2) \quad (6.4)$$

$$C_S = \frac{16(N_1 d_{31})^2}{\pi s_{11}^E} \frac{r^2}{N_1 t_1 + N_2 t_2} \quad (6.5)$$

$$C_1 = N_1 \pi \epsilon_{33}^T \left(1 - \frac{d_{31}^2}{\epsilon_{33}^T s_{11}^E}\right) \frac{r^2}{t_1} \quad (6.6)$$

$$C_2 = N_2 \pi \epsilon_{33}^T \left(1 - \frac{d_{31}^2}{\epsilon_{33}^T s_{11}^E}\right) \frac{r^2}{t_2} \quad (6.7)$$

$$R_{C_1} = \frac{1}{\omega_S C_1 \tan \delta} \quad (6.8)$$

$$R_{C_2} = \frac{1}{\omega_S C_2 \tan \delta} \quad (6.9)$$

$$G_a = \frac{N_1}{N_2} \quad (6.10)$$

Where:

- ρ_p : density of the PT material
- t_1 : thickness of the input layer
- t_2 : thickness of the output layer
- r : radius of the radial mode type PT
- N_1 : number of input layers
- N_2 : number of output layers
- ω_s : angular frequency of the source

The electric equivalent circuits presented in Fig. 6.4 are easily enough exploitable with an electric circuit simulator. Results are presented in the following paragraph (taking into account the dielectric losses in the EEC).

Results

The results obtained by simulating the EEC are depicted in Figures 6.5 and 6.6 for the case of the Noliac Rosen type PT. The first graph shows the variation of the transformation ratio as a function of the frequency and the load resistance. The second graph depicts the transformation ratios obtained by simulating the EEC using the calculated elements as well as the elements measured with an impedance analyzer for the specific case of a load resistance R_L of $200\text{k}\Omega$. The values of these elements are given in Table 6.1. The differences between the calculated and the measured values of the elements can be explained by the fact that the analytical formulas used for the calculation are only approximate formulas. Moreover, the measurements made also vary according to the overheating of the transformer and this can be a source of errors. But in general, measured and calculated values are in the same range. Obviously, other results such as the input/output impedance can be obtained in an analytical way. These results are not presented here but are detailed in [StuSe] for the case of the Rosen PT from Noliac and in [HolSe] for that of Transoner.

For the case of the radial mode type PT of Transoner, results are depicted in Figures 6.7 and 6.8. In the second graph, a load resistance R_L of 500Ω has been chosen. The values of the elements of the EEC are also given in Table 6.2.

Table 6.1: Calculated and measured elements of the EEC for the Noliac Rosen type PT

	Calculated elements	Measured elements
R_S	51.3 Ω	12.3 Ω
L_S	46.9 mH	23.4 mH
C_S	3.6 nF	6.18 nF
C_1	83.5 nF	140 nF
C_2	3.16 pF	5.5 pF
R_{C_1}	7.6 k Ω	4.1 k Ω
R_{C_2}	200 M Ω	105 M Ω

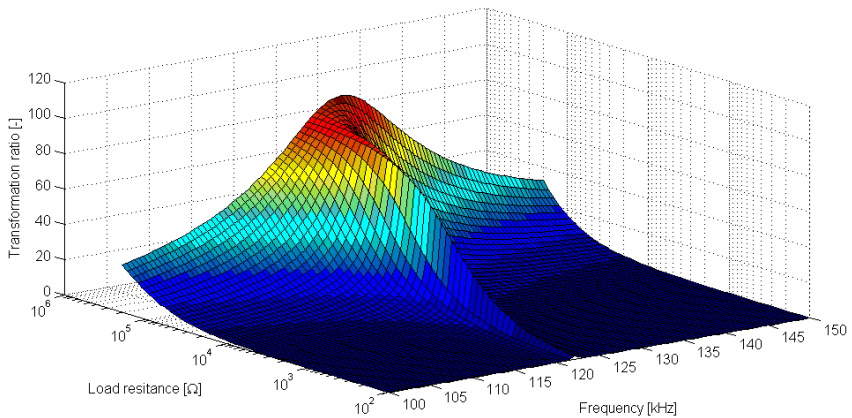


Fig. 6.5: Transformation ratio of the Noliac Rosen type PT (1)

As for the case of the Rosen type piezoelectric transformer, other results for the radial mode type PT can be obtained analytically. They are not presented here but can be found in [HolSe].

To complete the study of the piezoelectric transformers presented in this chapter, FE simulations have been carried out. Next section deals with this aspect of the modeling.

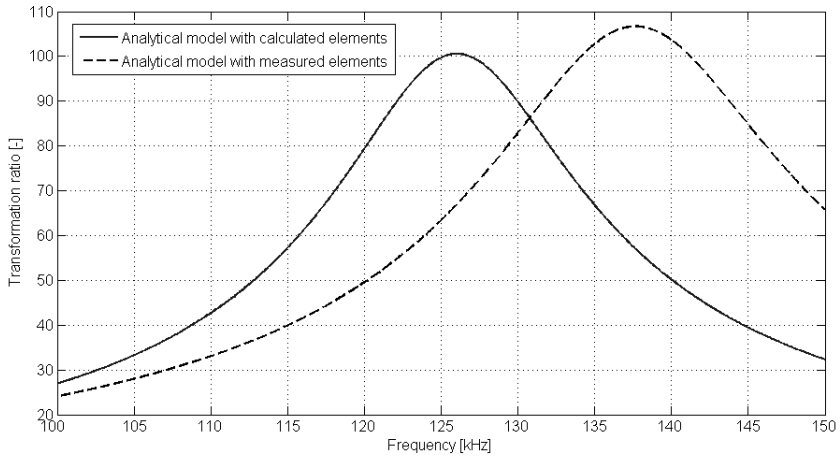


Fig. 6.6: Transformation ratio of the Noliac Rosen type PT (2)

Table 6.2: Calculated and measured elements of the EEC for the radial mode type PT

	Calculated elements	Measured elements
R_S	5.9 Ω	5.1 Ω
L_S	3.1 mH	2.5 mH
C_S	0.62 nF	1.27 nF
C_1	2.6 nF	8.6 nF
C_2	1.47 nF	3.83 nF
R_{C_1}	1.65 k Ω	0.62 k Ω
R_{C_2}	2.95 k Ω	1.40 k Ω

6.3.3 Numerical modeling

FE simulations

The analysis of the piezoelectric transformers presented in the previous section has been based on the well-accepted equivalent circuit. However, the electric

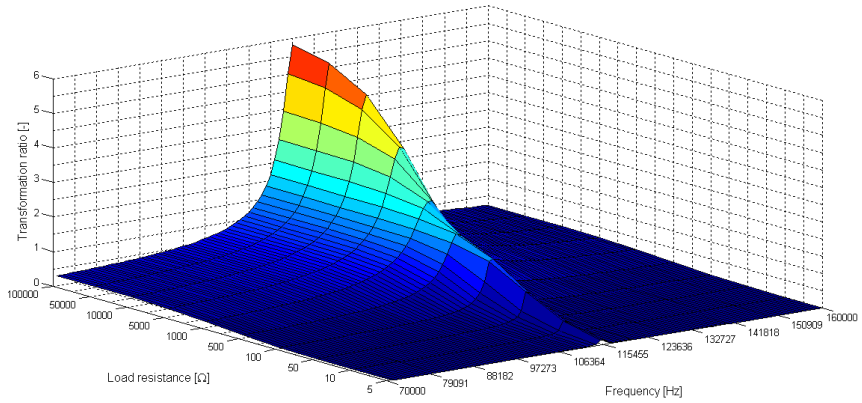


Fig. 6.7: Transformation ratio of the Transoner radial mode type PT (1)

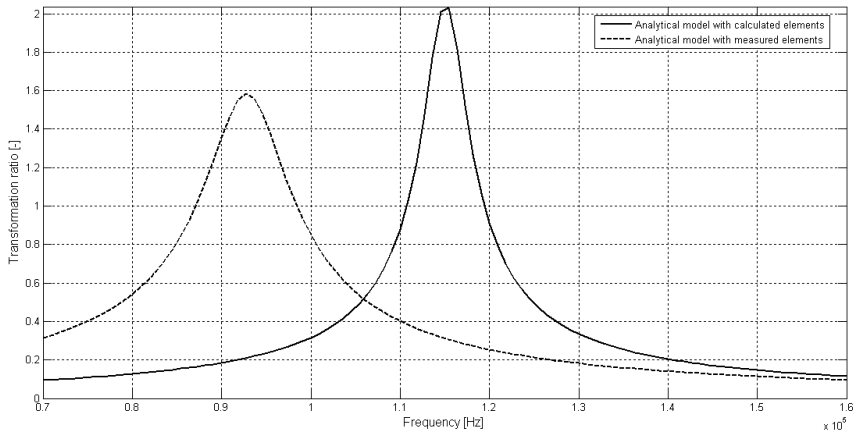


Fig. 6.8: Transformation ratio of the Transoner radial mode type PT (2)

equivalent circuit is derived from a 1-D model or assumption, the vibration of the PT is actually on all three dimensions. At higher order modes, the activities of all the directions are comparable and should not be neglected. This is why the use of a 3-D FEM analysis is valuable in such cases. The commercial ANSYS software [Ans81] has been used to carry out the simulations. Piezoelectric prob-

lems are solved as an extend elastic-electric coupling. Couple-field elements that can include both mechanical and electrical degrees of freedom (DOF) are used to construct the PT models. Figure 6.9 shows the models built for the Rosen type and the radial mode type piezoelectric transformers.

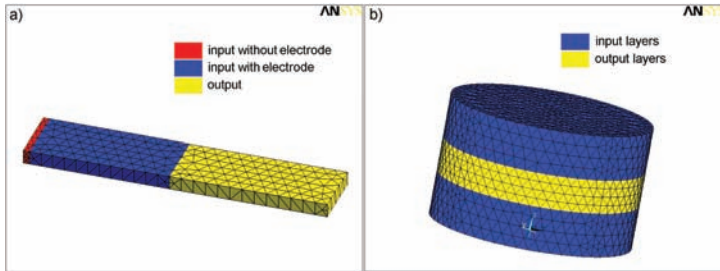


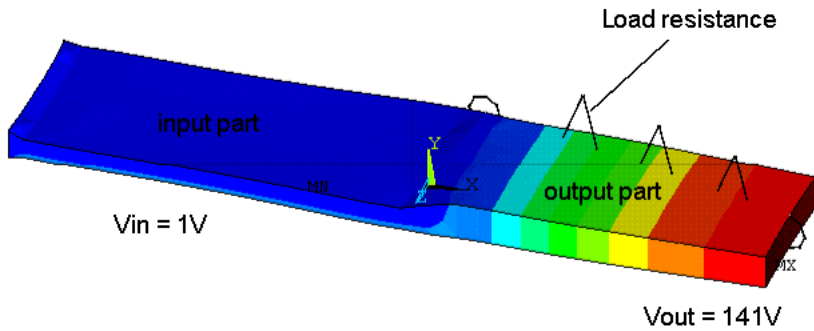
Fig. 6.9: FE models of the PTs: a) Rosen type, b) radial mode type

Results

Figures 6.10 and 6.11 show finite element simulations of the Transoner Rosen type PT and the Transoner radial mode type PT, respectively. In Fig. 6.10a, the nodal solution of the electric potential is depicted. A voltage of 1 V has been applied to the input part of the transformer and a voltage of about 141 V has been obtained at the output part when a load resistance of 500 k Ω is used. Fig. 6.10b shows then the transformation ratio as a function of the frequency. Results using the Noliac Rosen type PT are not presented here, but can be obtained using a similar model (see [StuSe] for details). Then, same results are presented in Figures 6.11a and 6.11b for the radial mode type PT and a load resistance of 500 Ω (transformation ratio of about 2 obtained at the resonance frequency ($f_r = 107.1$ kHz)).

The results obtained with both modeling methods (analytical and numerical) already enable us to characterize the piezoelectric transformers. In order to validate these results, some experiments are necessary. The following section presents the measurements carried out with the different piezoelectric transformers as well as the results comparison in order to validate the modeling methodology.

a)



b)

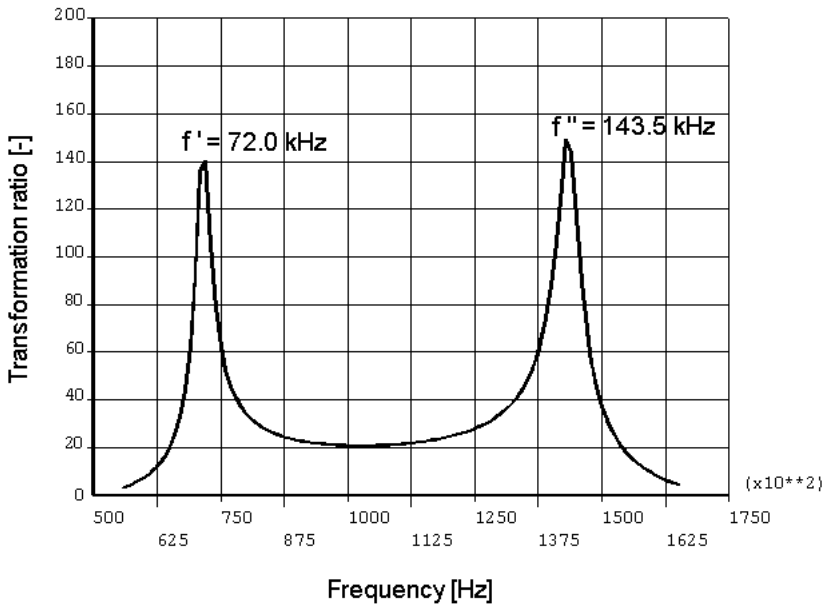


Fig. 6.10: FE simulation of the Transoner Rosen type PT: a) electric potential at first resonance frequency ($f' = 72.0 \text{ kHz}$), b) transformation ratio for $R_L = 500 \text{ k}\Omega$

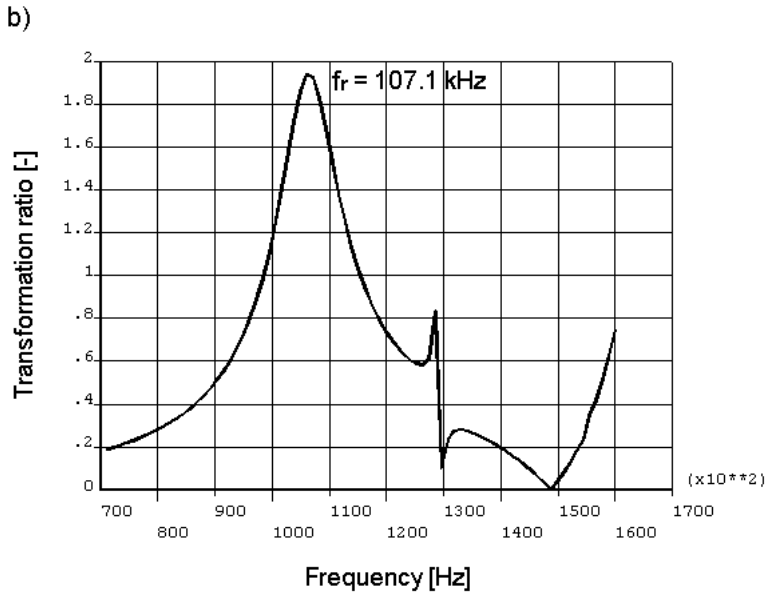
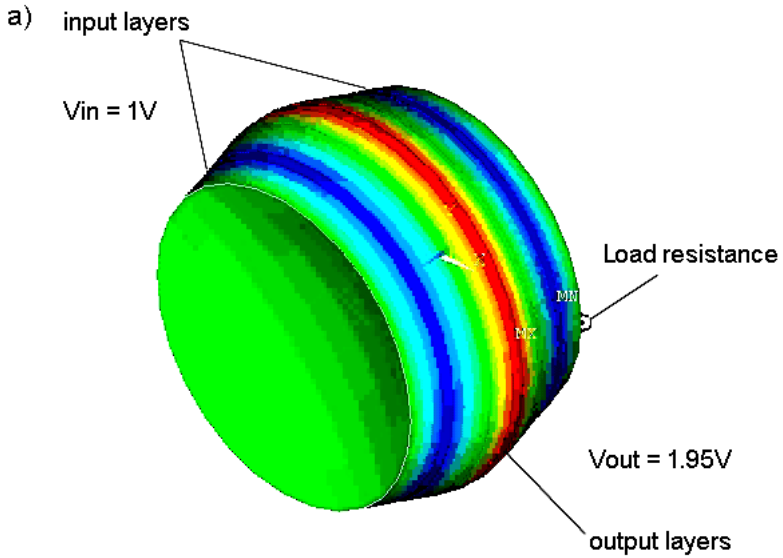


Fig. 6.11: FE simulation of the Transoner radial mode type PT: a) electric potential at resonance frequency ($f_r = 107.1 \text{ kHz}$), b) transformation ratio for $R_L = 500\Omega$

6.4 Experimental results and validation

6.4.1 Introduction

In order to compare the calculated and simulated results to validate the modeling methodology, some experiments on the different piezoelectric transformers presented in this chapter have been performed. First, some measurements using a precise impedance analyzer have been done to find out the input/output impedance of the piezoelectric transformers. Secondly, the transformation ratio versus frequency, under different load resistance values, has been measured and finally other characteristics like output voltage, input/output current, power and efficiency have been obtained.

6.4.2 Measurements

Not exhaustive but significant results are now presented. Figures 6.12 and 6.13 show typical measurements done with both Transoner piezoelectric transformers. Moreover, measurements of the input and output impedances as well as the determination of the values of the elements of the EEC can be obtained (see Table 6.1, Table 6.2 and [HolSe]). Measurements are made for the Rosen type PT with a load resistance of $500\text{ k}\Omega$ and a frequency $f' = 65.5\text{ kHz}$ and for the radial mode type transformer with a load resistance of 500Ω at the resonance frequency of the transformer ($f_r = 94.8\text{ kHz}$). As Fig. 6.13 shows it, the output current signals are often very disturbed. This implies measurement errors that can lead to obtain results that do not correspond exactly to the simulated or calculated values. Furthermore, some measurements are made according to the load resistance R_L and the frequency. In particular, one is interested in obtaining the values of the transformation ratio, power and efficiency of the PTs. Figure 6.14 depicts the characteristics and performances of the Transoner radial mode type PT. Note that the units of power and voltage are to be multiplied by the factor indicated in the figure to obtain the correct values. Same characteristics can be obtained for the two Rosen type PTs but are not given here (see [StuSe] and [HolSe]).

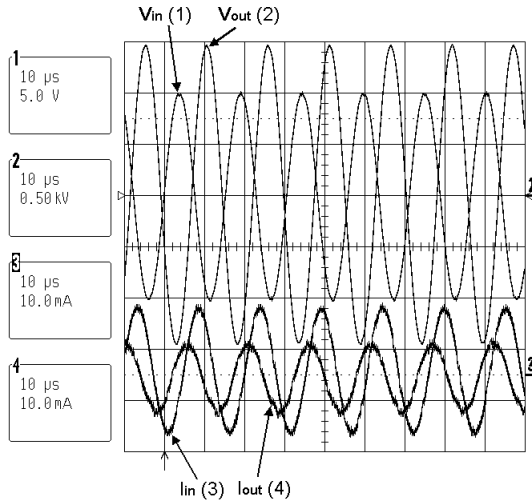


Fig. 6.12: Input/output voltages and currents measured for the Transoner Rosen type PT for $R_L = 500\text{k}\Omega$ and $f' = 65.5\text{kHz}$

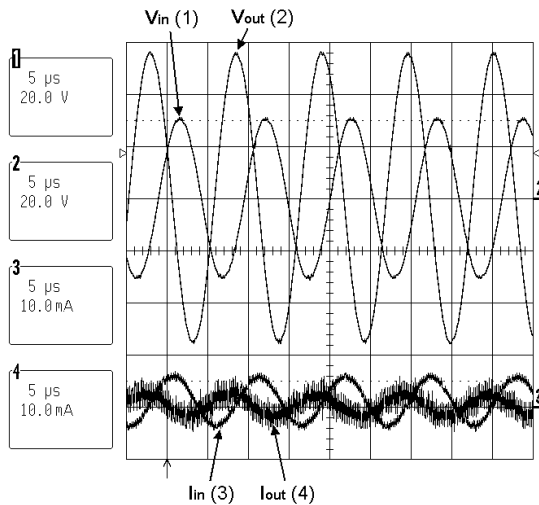


Fig. 6.13: Input/output voltages and currents measured for the Transoner radial mode type PT for $R_L = 500\Omega$ and $f_r = 94.8\text{kHz}$

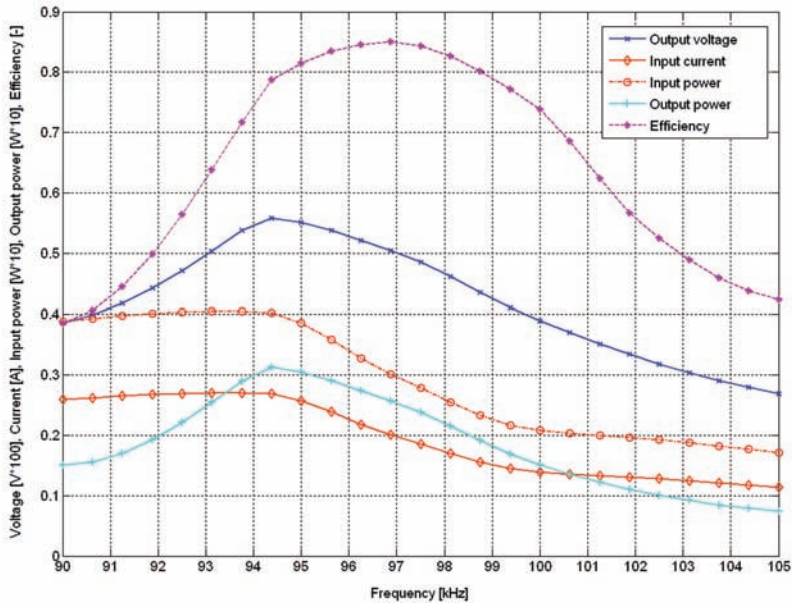


Fig. 6.14: Characteristics of the Transoner radial mode type PT for an input voltage $V_{in} = 30V$ and a load resistance $R_L = 500\Omega$

It can be noticed that the maximum of efficiency (about 85%) is obtained at about $97kHz$. Moreover, the maximum amplification of the output voltage does not coincide with the maximum of efficiency. Furthermore, by following the evolution of the transformation ratio, one can notice that at the frequency of maximum efficiency, the transformation ratio is about $\frac{V_{out}}{V_{in}} = 1.7$. These results correspond rather well with the values given by the manufacturer (see Appendix G).

6.4.3 Comparison and validation

Figures 6.15, 6.16 and 6.17 show the comparison of the results for the two Rosen type piezoelectric transformers and also for the radial mode type PT. The curves of the transformation ratio (vs. frequency) obtained with the modeling approach (analytical and numerical) and by measurements are represented.

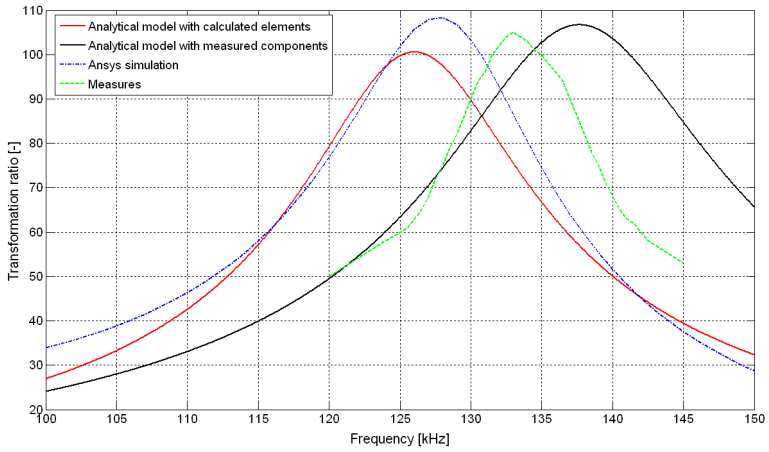


Fig. 6.15: Comparison of the results obtained with the Noliac Rosen type PT

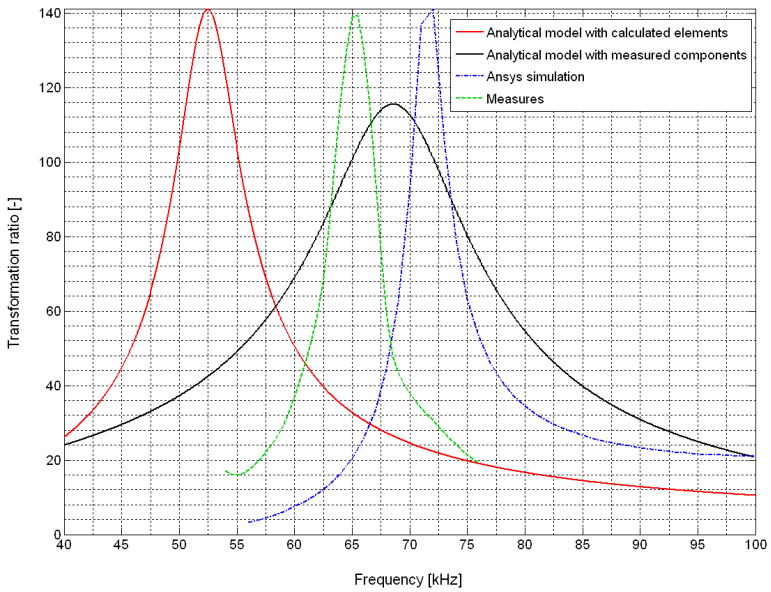


Fig. 6.16: Comparison of the results obtained with the Transoner Rosen type PT

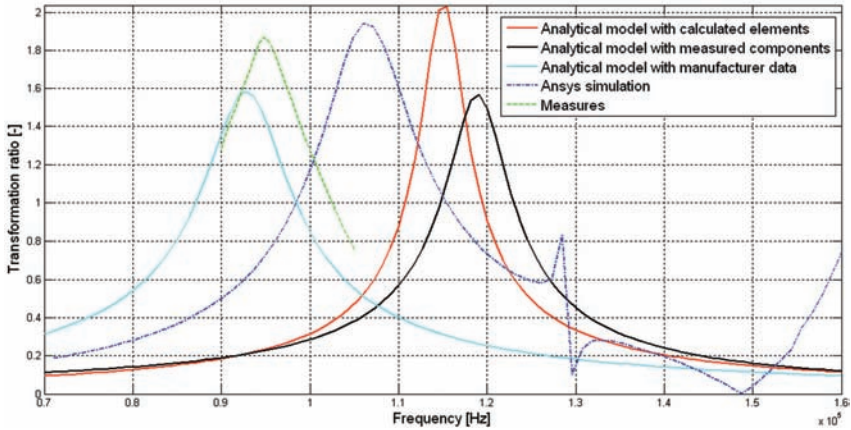


Fig. 6.17: Comparison of the results obtained with the Transoner radial mode type PT

As we can see, experimental, calculated and simulated results are quite similar despite few differences. Nevertheless, the approximation of measurements by the analytical model and FE simulations is rather good. Especially in the case of the radial mode type PT (see Fig. 6.17), the correspondence between the analytical model calculated with the elements given by the manufacturer (magenta), our measurements (green) and the values indicated in Appendix G shows that the model used is a good approximation. Otherwise, the other curves are shifted slightly in frequency. Moreover, FE simulations give also good results, taken into account the assumptions made. However, the numerical model is better than the analytical approach with the elements of the EEC calculated thanks to the analytical formulas (blue curve compared to red curve).

It is clear, in sight of the results obtained, that analytical modeling and FE simulation give only approximate results of the reality. To compare these results to the values of the real transformers characteristics, it is important to keep in mind the different sources of errors, related in particular to the approach used. Indeed, under some assumptions, one can possibly validate a model whose results do not correspond exactly to reality in a first approach and then explain these differences. Thus, Table 6.3 presents the hypotheses and the different observations

classified as a function of the approach chosen for our study of the piezoelectric transformers.

Table 6.3: Hypotheses made and observations about the study of the PTs

Rosen type and radial mode type PTs study	
Analytical modeling	<ul style="list-style-type: none"> ● Simplified model (EEC) ● Elements of the EEC approximated near the resonance frequency ● Single mode of vibration is considered (coupling phenomena along the other axes are neglected)
FE simulations	<ul style="list-style-type: none"> ● Size of the mesh chosen (not so thin) ● Sampling of the values ● Multilayers not simulated in the case of the Rosen type PT (result multiplied then by the number of layers)
Measures	<ul style="list-style-type: none"> ● Measurements errors (precision) ● Overheating of the PTs during measurements ● Sampling of the values

Indeed, with regard to the analytical model, one supposes that there is a perfect coupling between the layers. Moreover, it is admitted that the vibrations in the

desired mode do not generate vibrations in other directions. Actually, these two assumptions cannot be regarded as true. The losses at the interface of the layers are minimal but are present. Furthermore, other vibration modes can also be excited. As an example, in the radial mode, the retraction of the matter in one moment results inevitably in an expansion in the direction of the thickness (also related to the Poisson's effect).

In the case of the FE simulations, the mesh size used was quite coarse (due to computing time). Moreover, one is limited to calculate the response for certain values of frequency. This causes a sampling of the output signal (in our case, a sampling step of 1 kHz was generally used). In the case of the Rosen type PT, the numerical model built does not correspond exactly to the transformer in reality. There is a difference in the arrangement of the electrodes between the real PT (multilayered) and the model (monolayered). The choice has been motivated by the fact that computing time is much more important if all layers are simulated. This is why only one layer has been simulated and then the result has been multiplied by the number of input layers.

Finally, it is clear that any measurement is accompanied by errors even if one tries to avoid them as well as possible. Moreover, it should be considered that during the measurements of the transformers, the phenomenon of overheating has been observed and this can explain some differences between our measures and the results given by the manufacturers. Nevertheless, the different approaches presented in this chapter already allow to give an idea of how PTs can be analyzed and the results presented are satisfactory in qualitative and quantitative points of view.

Once the modeling and the analysis of the piezoelectric transformers presented, let us look now for which type of applications they are used. The following section presents some known application fields and in particular that which consists in using a PT for the power supply of ultrasonic motors, which is particularly interesting in our case.

6.5 Applications

6.5.1 Introduction

Considering its recent development, the radial mode type PT has not yet many applications. But a recent application dealing with a new driving method for ultrasonic motors has emerged. Indeed, instead of a DC/AC converter type driver using a conventional electromagnetic transformer, a radial mode type PT is used to obtain a very simple drive circuit, both motor and PT operating in the same radial vibration mode. This solution has many advantages as explained in [MLU02]. Furthermore, for low voltage and high power applications like battery chargers, AC/DC adapters, laptop computers or even cellular phones, this PT type could be an interesting solution. With regard to the Rosen type PT, it is used in high voltage applications like for cold cathode fluorescent lamps used in liquid crystal displays, power supplies or even ion generators. In the next sections, some of these application fields are described more in detail, in particular the use of a PT for the power supply of ultrasonic motors.

6.5.2 Ultrasonic motors power supply

Usually, an ultrasonic motor requires high AC voltages of the order of 50 – 300 V for generating traveling or standing waves to drive a rotor or a slider. In order to generate this high voltage from an usual DC power supply, step-up transformers are required. Previously, piezoelectric transformers have not been used in driving circuits because of the limitation that they work effectively only near the resonance frequency. So far, piezoelectric transformers have been commercially used in some particular applications that require high voltages and no magnetic noise interference, such as back-light inverters for LCDs, switching converters, switching regulated power supplies, notebook computers and powering neon lamps (these applications will be described in the following sections). Nevertheless, if the resonance frequency of the piezoelectric transformer is tuned with that of the ultrasonic motor, it is possible to use the piezoelectric transformer for driving the ultrasonic motor without any extra frequency control circuit that re-

quires electromagnetic transformers. The basic concept is illustrated in Fig. 6.18. When the transformer operating frequency is fitted exactly to the same frequency of the ultrasonic motor resonance, it can be used as a drive system, or obtain a transformer-integrated motor [MLU02].

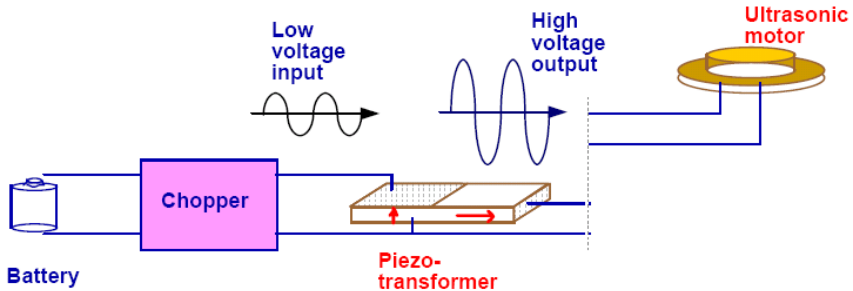


Fig. 6.18: Basic concept of UM drive system using a PT

There are three typical types of piezoelectric transformers that can be used for this purpose: Rosen type, thickness vibration mode type and radial vibration mode type. Two of them have been described and analyzed in this chapter. It has been noticed that in the case of Rosen type PTs, the optimal efficiency can be obtained by using a high load (around 100 – 200 k Ω) because of its inherent high voltage gain. The piezoelectric transformer operating in a thickness vibration mode type (not treated in our work) is known as a low voltage PT and its optimal efficiency can be obtained by using a lower load (around 10 k Ω) because of its inherent low voltage gain [Ohn92]. With regard to the radial vibration mode PT, the optimal load is between 100 Ω and 10 k Ω . Now, as an example, let us consider the annular plate-type ultrasonic motor presented in [Kim02] and operating in a non-axisymmetric radial vibration mode. Figure 6.19 shows the integration of the piezoelectric transformer and the ultrasonic motor. The resonance impedance (load) of the motor is around 0.5 k Ω , which is near the range of the radial vibration mode piezoelectric transformers. Thus, the disc-shaped piezoelectric transformer has been used for driving the annular plate-type ultrasonic motor. The voltage transformation ratio of 4 (step-up) could provide a voltage of

40V, high enough for the motor drive, starting from a battery. So, a disc-type PT operating in the radial vibration mode can effectively drive an annular plate-type UM. Thus, one can affirm that this new way of driving UMs is very promising and could be applied for the power supply of other ultrasonic motors, in particular in the case of the MINISWYS motor. Indeed, the coil used for increasing the voltage applied to the piezoceramics (see section 5.6.2 and Fig. 5.23) could be replaced, in an efficient way, by a piezoelectric transformer.

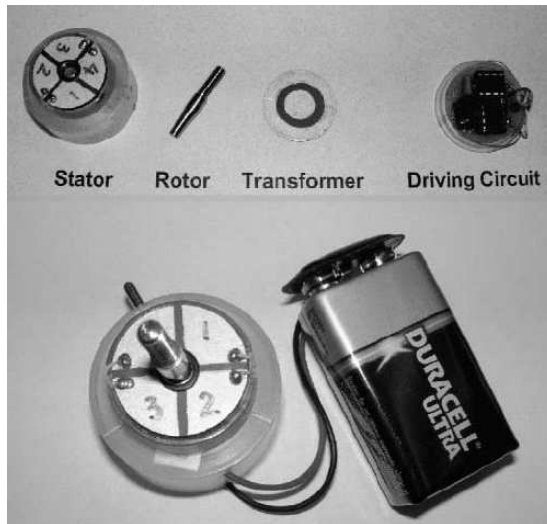


Fig. 6.19: Application of a PT for the UM drive [Kim02]

6.5.3 High voltage applications

Piezoelectric transformers, based on the original Rosen type or in the various multilayers configurations, are generally known to be an excellent way to obtain a high voltage transformation. Thus, this characteristic has made this type of PT suitable for applications in LCD back-lighting, high voltage generators for TV sets, air cleaners, copy machines or even ion generators. The output

power levels are typically in the range of $0.5 - 5\text{ W}$ with power densities of about $5 - 10\text{ W}/\text{cm}^3$. This type of PT is also widely used in cold cathode fluorescent lamps (CCFLs). CCFLs are commonly used as a back-light source for color liquid crystal displays (LCDs) used in notebook computers and portable electronic devices. These lamps require a high AC voltage for ignition and operation. The required ignition voltage is typically double than the operating voltage and increases at cold temperatures. The lamp requires a sinusoidal voltage to provide the best electrical-to-optical energy conversion. The lamp and display enclosures used for the next generation of portable products are becoming increasingly narrow, generating the need for a low-profile CCFL power supply. Advances in both magnetic and ceramic piezoelectric transformers have enabled efficient and smaller back-light converters to be built. The choice of the transformer depends on several factors including cost, size and efficiency. Nevertheless, the piezoelectric transformer has the advantages of inherently sinusoidal operation, high strike voltage, non flammability and no electromagnetic noise. Some examples of transformers used in notebook computer applications are shown in Fig. 6.20 [Tex02].

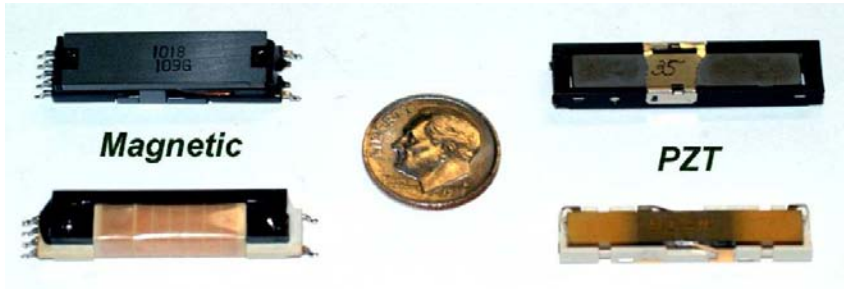


Fig. 6.20: Comparison of magnetic and piezoelectric transformers for CCFL applications

6.5.4 Low voltage and high power applications

In many modern consumer electronic applications, for example power supplies for portable equipment, there is a strong need for low voltage transformers with power levels above 10 W , and there is thus an extremely large potential use of

PTs. As a demonstration of this technology, the miniaturization of an AC/DC converter for charging mobile phone batteries is presented in Fig. 6.21a. The PT could then be successfully implemented in an AC/DC converter prototyped by Alcatel (Spain), shown in Fig. 6.21b. Typical values obtained using this type of PT are: input voltage $84 - 264V$ AC, output voltage $12V$ DC, output power $> 10W$ and a power density of about $40 - 50 W/cm^3$ [Bov00].

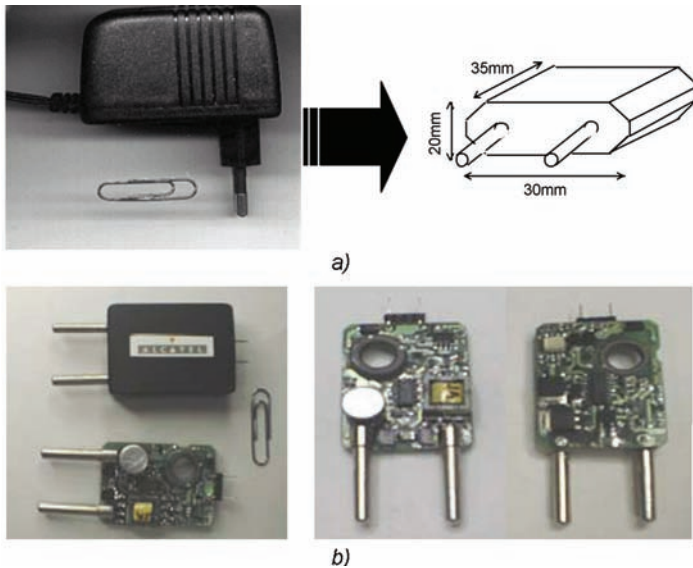


Fig. 6.21: AC/DC converter for mobile phone battery charging: a) objective (miniaturization of a conventional AC/DC converter through implementation of a PT), b) overview pictures of the prototyped AC/DC converter [Bov00]

Moreover, this type of PT is frequently used in notebook computers, where AC-adapters which supply DC voltage to such computers need to be smaller and lighter than those used these last years. Figure 6.22 depicts an example of the use of such a PT. More details can also be found in the literature about this application field (see [Zai97]).

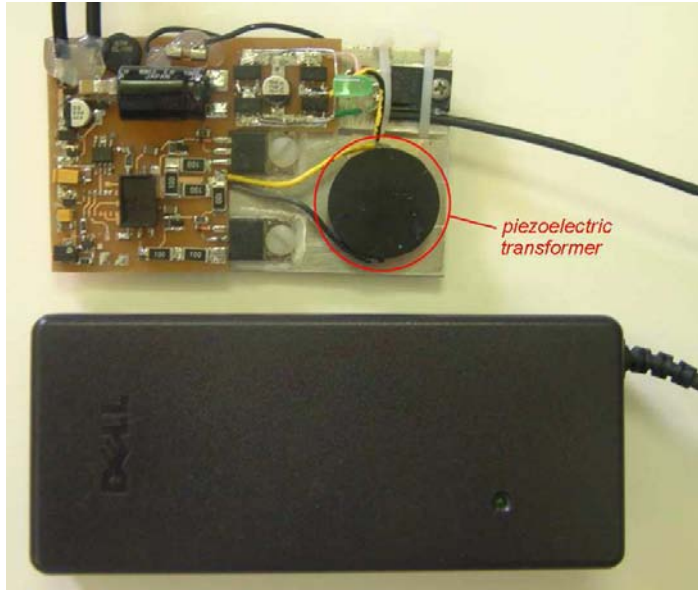


Fig. 6.22: AC/DC adapter for notebook computers [Del]

Furthermore, in order to improve the transformer performances, various proposals have been made: improvement in piezoceramics with higher mechanical toughness and low losses (high Q_m), selection of a vibration mode and an electrode configuration to separate the nodal point from the maximum residual stress point or even selection of a vibration mode with higher electromechanical coupling. As shown in Fig. 6.23, though this device has been widely manufactured, the application is still limited due to the power capability [CU01]. The development of PTs operating in thickness extensional vibration mode has been also widely treated [Ohn92].

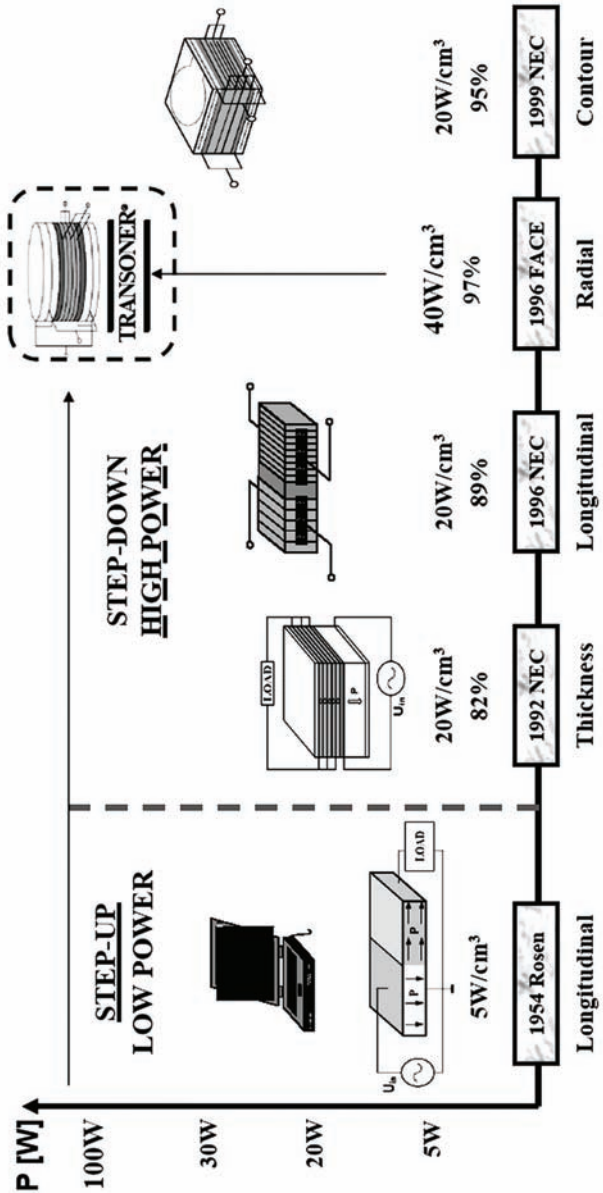


Fig. 6.23: High power applications of piezoelectric transformers [CU01]

6.6 Conclusion

In this chapter, calculated, simulated and experimental characteristics of two different piezoelectric transformer types have been presented (see also [Fer07]). The modeling approach developed was to use an electric equivalent circuit and the finite element method. Furthermore, some experiments have been carried out. All results are in good adequation despite few differences in resonance frequency and transformation ratio, due to the assumptions made. The analytical model is restrictive because only one vibration mode is taken into account. But results show that this method is a good approximation and can be used as a fast tool to characterize a PT. FE method is interesting to find out local values such as the electric potential as well as the coupling phenomena in the 3-D structure of the PT. Furthermore, the transformer operation mode could be chosen according to the desired application: maximum output/power voltage required or best efficiency desired, and this by changing the value of the load resistance. Moreover, some application fields where piezoelectric transformers are used have been described, in particular its use for the ultrasonic motors power supply.

Then, by considering the optimization methodology presented in the preceding chapter, it would be also possible to optimize the performances of piezoelectric transformers by applying design of experiments as well as optimization by finite elements. Even better, the integration of a piezoelectric transformer and an ultrasonic motor could be considered as an entire system, making it possible to optimize even more efficiently the performances.

7. CONCLUSION AND PERSPECTIVES

7.1 Overview

Ultrasonic motors have received much attention these last years in response to their specific characteristics which differentiate them from conventional electromagnetic motors. The main advantages of this type of motors are that they present a simple mechanical structure, a large speed range without any gear-mechanism, a high force density and a braking force without energy supply. Furthermore, they are noiseless in the audible range, insensitive to electromagnetic fields and they present negligible electromagnetic emissions. They also become more and more interesting for applications requiring miniaturized devices. This thesis work describes the study, the modeling and the optimization of linear ultrasonic motors. A comparison of the different types of existing motors, using standing or traveling waves, micro-push working principles or even operating in the stick and slip mode, has been carried out and presented in the early stage of the study.

Many researches have been carried out in order to find out analytical models or determine theoretical models based on numerical approaches which use finite element methods. So, analytical modeling has been also briefly presented. This methodology uses simplifying assumptions which make it possible to characterize the motor in a simple way but it often does not give satisfactory results. Nevertheless, the method which is based on the use of an electric equivalent circuit has been described more in detail and has been used to study the behavior of piezoelectric transformers. Within sight of the results obtained, this methodology remains limited and needs to take into account some phenomena that are often neglected. However, in a first approximation, this method remains inter-

esting. Within the framework of this thesis work, numerical modeling has rather been selected instead. By building a three-dimensional model, it is then possible to simulate it using the finite element method (FEM). In particular, this method allows to take into account the geometrical details of a motor design for a better accuracy. While choosing this modeling strategy, it is then possible to undertake an optimization study in an easier way.

An adequate model is fundamental for the formulation of optimization problems and it has been decided to use a numerical model, as already mentioned. If optimization problems are formulated by means of the FEM, the number of variables (input parameters) is usually very large. Then, the cost of numerical computation in the FEM can be a drawback. Therefore, to make FEM more suitable in the optimization study of ultrasonic motors, sensitivity analysis has been introduced. After a parametrization stage, design of experiments have been used to carry out this analysis, in particular using factorial designs and the surface responses method (Doehlert). This pre-optimization stage has been introduced before carrying out the optimization using the finite element method in order to reduce the variation ranges of the input parameters but also to find out the most influential parameters. Then, FE optimization has allowed, as well in the case of the linear ultrasonic motor developed in the laboratory as for the MINISWYS ultrasonic motor, to obtain good results making it possible to validate the methodology proposed in this thesis work.

7.2 Main results and innovative contribution

This thesis work made it possible to deal with the modeling and optimization of piezoelectric motors. FE method has been chosen for the study of the ultrasonic motors. The results obtained have shown a good similarity between experiments and simulations and allowed to validate this modeling method. However, the most important contributions of the work presented in this dissertation are related to the development of a new optimization methodology that presents the following originalities:

- Pre-optimization using design of experiments applied to finite element simulations is an innovative way to find out the sensitivity of the design parameters of an ultrasonic motor.
- The finite element method used in this thesis work makes it possible to simulate complex structures. Then FE optimization is possible thanks to the results obtained in the pre-optimization stage, allowing to optimize ultrasonic motors designs. Since only the most influential parameters are taken into account and the variation ranges are better defined, computing time needed for an optimization is reduced.
- Some studies about optimization of ultrasonic motors have been undertaken in the last years but no concrete results have been obtained. Indeed, most of the time, the way to obtain better performances of ultrasonic motors was to build various prototypes with different designs and then test them. This is expensive and takes sometimes a lot of time. The methodology presented in this thesis work introduces a new way to model and design ultrasonic motors, in particular for a better approach and analysis before the construction of prototypes, which could significantly reduce production costs.

In addition, the developed methodology made it possible to improve the performances of the MINISWYS ultrasonic motor, both forward and backward motion amplitudes of the slider being increased. Indeed, simulation results have shown that the slider displacement is about 1.7 mm in the forward direction and about 1.25 mm in the backward direction, which represents on average an increase of a factor 100 compared to the initial design. With regard to the experiments carried out, they have shown that the optimized structure of the resonator gives better results than those obtained by using the initial design. Indeed, the full stroke imposed by MINISWYS SA ($550\mu\text{m}$) is reached by applying an input voltage of 5 V (without the use of a coil). On the contrary, in the case of the initial motor and without the use of a coil, the motor travels only $365\mu\text{m}$ for an applied voltage of 7 V . Furthermore, it has been obtained that the motion of the moving part is increased by a factor higher than 2 if the optimized structure of the resonator

is considered. Thus, it means that the optimization of the travel range of the motor has been reached. So, FE method proved to be a good way to model the MUM. Moreover, the results found allowed us to obtain good enhancements and therefore the optimization methodology has been validated.

Finally, it has been shown that it is possible to use a piezoelectric transformer to increase the voltage needed to supply the motor. Indeed, electromagnetic transformers have become obstacles to progress power supply miniaturization and this is why PTs become more and more an interesting alternative. The optimization methodology presented in this work would then make it possible to improve the performances of piezoelectric transformers. Still better, by considering a system integrating at the same time a piezoelectric transformer and an ultrasonic motor, this would be a very interesting concept, completely innovating.

7.3 Perspectives and future developments

According to the results obtained in this thesis work, it appears judicious to incorporate a sensitivity analysis in the modeling and simulation of ultrasonic motors. Design of experiments applied as a pre-optimization stage and then FE optimization method have shown good complementarity and make this methodology very interesting for further applications. Indeed, other types of ultrasonic motors or even piezoelectric transformers could be optimized using the same reasoning. Nevertheless, the results obtained by using this optimization methodology should be validated systematically by experimental measurements on prototypes. Indeed, the assumptions and the simplifications made, in particular during the modeling part of the study, should be checked by experiments in order to validate the methodology.

Furthermore, a first optimization of the MINISWYS ultrasonic motor has been performed. In spite of the great complexity of the structure and the different possible vibration modes, it has been demonstrated that it is possible to significantly improve the movement amplitudes of the moving part (motion of the lens). That demonstrates the validation of the optimization methodology, but the study should go on in order to reach even better performances, by means of the

speed, the driving force, the efficiency or even the materials used for the motor (cost). For this purpose, multi-objective optimization could be applied. Indeed, weighted sum method or even genetic algorithms, which have been briefly described at the end of chapter 5, could be the subject of a study in itself.

Finally, one must keep in mind that the optimization of ultrasonic motors is not so obvious. One has to take into account the contact between the stator (resonator) and the rotor (slider). Indeed, in our case, only the vibrating part (resonator) of the motor has been considered for the optimization. However, the phenomena existing in the contact zone between the vibrating part and the moving part represent a very important aspect in the operation of the motor and should be taken into account. This point has not been treated in this thesis work (in particular because some assumptions about the contact zone would need to be validated through experimental results and this is not very easy in our case). Therefore, this aspect of the study could be the subject of future developments.

BIBLIOGRAPHY

- [Abb98] N. N. Abboud, G. L. Wojcik, D. K. Vaughan, J. Mould, D. J. Powell and L. Nikodym, *Finite element modelling for ultrasonic transducers*, Proceedings of the International Symposium on Medical Imaging, SPIE, 1998.
- [AH70] H. Allik, J. R. Hughes , *Finite Element for Piezoelectric Vibration*, International Journal Numerical Methods of Engineering, n°2, pp. 151-157, 1970.
- [Ans81] ANSYS Multiphysics 8.1 version, User manual, ANSYS Inc., 2004.
- [AP05] M. Ayoub and C. Péclat, *Piezoelectric Motor - Analysis and characterization*, Intermediate report, Helbling Technik Bern AG, 2005.
- [Bak02] E. M. Baker, W. Huang, D. Y. Chen and F. C. Lee, *Radial mode piezoelectric transformer design for fluorescent lamp ballast applications*, IEEE, 2002.
- [Bar73] H. V. Barth, IBM Tech. Disclosure Bull. 16 2263, 1973.
- [Bar00] R. Barboni, A. Mannini, E. Fantini and P. Gaudenzi, *Optimal placement of PZT actuators for the control of beam dynamics*, Smart Materials and Structures, vol.9, pp. 110-120, 2000.
- [Bau01] M. G. Bauer, *Design of a linear high precision ultrasonic piezoelectric motor*, Thesis Dissertation, North Carolina State University, 2001.

- [BBM93] D. Beasley, D. R. Bull and R. R. Martin, *An Overview of Genetic Algorithms, Part 1 and 2*, University Computing, 1993.
- [BC98] J.-M. Breguet and R. Clavel, *Stick and slip actuators: design, control, performances and applications*, Proceedings of the 1998 International Symposium on Micromechatronics and Human Science, pp. 89-95, 1998.
- [BD87] G.E.P. Box, N. Draper, *Empirical model building and response surfaces*, Wiley Series in Probability and Mathematical Statistics, John Wiley and Son, New-York, 1987.
- [Ber04] A. Bergander, W. Driesen, T. Varidel and J.-M. Breguet, *Monolithic piezoelectric actuators for miniature robotic systems*, Actuator 04, 9th International Conference on New Actuators, Bremen, Germany, 114-117, 2004.
- [BerMs] L. A. Berger, *Etude et optimisation d'un actionneur linéaire piézoélectrique*, Master project, EPFL-STI-IPR-LAI, 2006.
- [BF02] S. Bharti and M. I. Frecker, *Topology optimization and detailed finite element modeling of piezoelectric actuators: effect of external loads and detail geometers on actuator output*, Proceedings of SPIE, vol.4693, pp. 124-135, 2002.
- [BHH78] G.E.P. Box, W.G. Hunter, J.S. Hunter, *Statistics for Experimenters: An Introduction to design, data analysis and model building*, John Wiley, New York, USA, 1978.
- [Blu82] A. J. Blundell, *Bond Graphs for Modelling Engineering Systems*, Ellis Horwood Publishers, Chichester, United Kingdom, and Halsted Press, New York, 1982.
- [Bov00] T. Bove, W. Wolny, E. Ringgaard and K. Breboel, *New Type of Piezoelectric Transformer With Very High Power Density*, Proc. IEEE International Symposium on Applications of Ferroelectrics, vol. 1, pp. 321-324, 2000.

- [Bul05] M. Bullo, *Modélisation et commande du moteur piézoélectrique à onde progressive*, EPFL Thesis, n°3348, 2005.
- [BS03] M. P. Bendsoe and O. Sigmund, *Topology Optimization - Theory, Methods and Applications*, Springer-Verlag Berlin Heidelberg, 2003.
- [BW05] M. Bhend and S. Wehren, *Messungen der elektrischen Eigenschaften eines Ultrasonic Motor fr Autofocuslinsen bei Mobilgeräten*, Semester project, HTA Biel, 2005.
- [Cad64] W. Cady, *Piezoelectricity*, Dover Publications, New-York, 1964.
- [CF00] S. Canfield and M. Frecker, *Topology optimization of compliant mechanical amplifiers for piezoelectric actuators*, Structural and Multidisciplinary Optimization, vol.20, pp. 269-279, 2000.
- [CL87] E. F. Crawley and J. Luis, *Use of piezoelectric actuators as elements of intelligent structures*, AIAA Journal, vol.25, pp. 1373-1385. 1987.
- [Cla99] F. Claeysen, R. Le Letty, F. Barillot, N. Lhermet, M. Debarnot, M.F. Six, G. Thomin and M. Privat, *Piezoelectric Actuators for Direct Drive Applications*, Cedrat Recherche, <http://www.cedrat-grenoble.fr>, 1999.
- [Cra94] E. F. Crawley, *Intelligent structures for aerospace: a technology overview and assessment*, AIAA Journal, vol.32, n°8, pp. 1689-1699, 1994.
- [CTS02] C. Chee, L. Tong and G. P. Steven, *Piezoelectric actuator orientation optimization for static shape control of composite plates*, Composite structures, vol.55, pp. 169-184, Elsevier, 2002.
- [CU01] A. V. Carazo and K. Uchino, *Novel Piezoelectric-Based Power Supply for Driving Piezoelectric Actuators Designed for Active Vibration Damping Applications*, Journal of Electroceramics, vol. 7, pp. 197-210, 2001.

- [Deb02] K. Deb, *Multi-objective Optimization using Evolutionary Algorithms*, John Wiley & Sons, 2002.
- [Del] <http://www.dell.com>.
- [DS83] J. E. Dennis, R. B. Schnabel, *Numerical Methods of Unconstrained Optimization and Nonlinear Equations*, Prentice-Hall, Englewood Cliff, NJ, 1983.
- [Du00] H. Du, G. K. Lau, M. K. Lim and J. Qui, *Topological optimization of mechanical amplified for piezoelectric actuators under dynamic motion*, Smart Materials and Structures, vol.9, pp. 788-800, 2000.
- [Ellip] Elliptec Resonant Actuator AG, <http://www.elliptec.com>.
- [FerMs] J. Fernandez, *Paramétrisation et validation d'un modèle équivalent mécanique d'un moteur piézoélectrique*, Master project, EPFL-STI-IPR-LAI, 2002.
- [Fer01] J. Fernandez and Y. Perriard, *Comparative Analysis and Modeling of Both Standing and Traveling Wave Ultrasonic Linear Motor*, in Proceedings of the IEEE International Ultrasonics Symposium, Honolulu, USA, 5-8 October 2003, vol.2, pp. 1770-1773.
- [Fer02] J. Fernandez and Y. Perriard, *Characteristics, Modeling and Simulation of a Traveling Wave Ultrasonic Linear Motor*, in Proceedings of the IEEE International Ultrasonics, Ferroelectrics, and Frequency Control 50th Anniversary Joint Conference, Montreal, Canada, 23-27 August 2004, vol.3, pp. 2247-2250.
- [Fer03] J. Fernandez and Y. Perriard, *Numerical Analysis and Simulation of Ultrasonic Linear Actuators*, World Congress on Ultrasonics / Ultrasonic International, Beijing, China, 28th August - 1st September 2005.
- [Fer04] J. Fernandez and Y. Perriard, *Sensitivity Analysis of an Ultrasonic Linear Actuator Using Design of Experiments*, World Congress on

Ultrasonics / Ultrasonic International, Beijing, China, 28th August - 1st September 2005.

- [Fer05] J. Fernandez, Y. Ruffieux and Y. Perriard, *Design Optimization Analysis of a Standing Wave Ultrasonic Linear Actuator*, in Proceedings of the IEEE International Ultrasonics, Ferroelectrics, and Frequency Control Conference, Rotterdam, The Netherlands, 18-21 September 2005, vol. 1, pp. 311-314.
- [Fer06] J. Fernandez, M. Krummen and Y. Perriard, "Analytical and Numerical Modeling of an Ultrasonic Stepping Motor Using Standing Waves", in Proceedings of the IEEE International Ultrasonics, Ferroelectrics, and Frequency Control 50th Anniversary Joint Conference, Montreal, Canada, 23-27 August 2004, vol.2, pp. 1173-1176.
- [Fer07] J. Fernandez, J. Holzbecher, M. Stutz, and Y. Perriard, *Modeling and Characteristics Comparison of Two Different Piezoelectric Transformers*, in Proceedings of the IEEE International Ultrasonics, Ferroelectrics, and Frequency Control Conference, Rotterdam, The Netherlands, 18-21 September 2005, vol. 3, pp. 1530-1533.
- [Fer08] J. Fernandez and Y. Perriard, *Sensitivity Analysis and Optimization of a Standing Wave Ultrasonic Linear Motor*, IEEE Transactions on Ultrasonics, Ferroelectrics and Frequency Control, vol.53, n°7, pp. 1352-1361, 2006.
- [Fer09] J. Fernandez, L. A. Berger and Y. Perriard, *Optimization of a New Type of Ultrasonic Linear Motor*, accepted for IEEE International Ultrasonics Symposium, Vancouver, Canada, 3-6 October, 2006.
- [Fis71] R. A. Fisher, *The design of experiment*, Hafner press, Collier Macmillian publishers, 9th edition, London, 1971.
- [Fly92] A. M. Flynn, L. S. Tavrow, S. F. Bart, R. A. Brooks, D. J. Ehrlich, K.R. Udayakumar and L. E. Cross, *Piezoelectric Micromotors for Microrobots*, IEEE Journal of Microelectromechanical Systems, vol.1, n°1, pp. 44-51, 1992.

- [FMP83] D. Feneuille, D. Mathieu, R. Phan-Tan-Luu, *Méthodologie de la recherche expérimentale*, Laboratoire de Prospective Réactionnelle et d'Analyse de l'Information, Aix-en-Provence, France, 1983.
- [FP04] J. M. Fuerbringer and A. Persily, *Sensitivity analysis of VOC measurement*, EPFL, 2004.
- [FR95] J.-M. Fuerbringer, C.-A. Roulet, *Comparison and Combination of Factorial and Monte-Carlo Design in Sensitivity Analysis*, Building and Environment, vol.30, n°4, pp. 505-519, 1995.
- [Fre03] M. I. Frecker, *Recent Advances in Optimization of Smart Structures and Actuators*, Journal of Int. Mat. Syst. and Struct., vol.14, 2003.
- [Fu05] B. Fu, *Piezoelectric Actuator Design via MultiObjective Optimization Methods*, Thesis dissertation, University of Paderborn, germany, 2005.
- [Fuk98] H. Fukunaga, H. Kakehashi, H. Ogasawara and Y. Ohta, *Effect of Dimension on Characteristics of Rosen-Type Piezoelectric Transducer*, IEEE International Ultrasonics Symposium, 1998.
- [GC00] M. Gen and R. Cheng, *Genetic algorithms and engineering optimization*, Wiley-Interscience Publication, USA, 2000.
- [Gol89] D. E. Goldberg, *Genetic Algorithms in Search, Optimization & Machine Learning*, Addison-Wesley, 1989.
- [GR87] D. Goldberg and J. Richardson, *genetic algorithm with sharing for multi-modal function optimization*, in Proceedings of the 2nd International Conference on Genetic Algorithms, pp. 41-49, 1987.
- [Gra77] K. F. Graff, *Wave Motion in Elastic Solids*, Clarendon, Oxford, 1975.
- [Gun93] B.H. Gunter, *How experimental design concepts can improve experimentation in the physical sciences*, Computer in Physics, vol.7, n°3, 1993.

- [HA95] N. W. Hagood and J. Andrew, *Modeling of a Piezoelectric Rotary Ultrasonic Motor*, IEEE Transactions on Ultrasonic, Ferroelectrics, and Frequency Control, vol.42, n°2, pp. 210-224, 1995.
- [HaS98] S. Hallaert, E. Sarraute, *Piezoelectric transformers: principles, structures and modeling*, Actuators 98, pp. 337-340, 1998.
- [Hel74] D. Hellwege, *Piezoelectric Ignition Elements*, Feinwerktechnik & Messtechnik 82, pp. 223-226, 1974.
- [Hel98] P. Hélin, V. Sadaune, C. Druon and J. -B. Tritsch, *A Mechanical Model for Energy Transfer in Linear Ultrasonic Micromotors Using Lamb and Rayleigh Waves*, IEEE/ASME Transactions on Mechatronics, vol.3, n°1, pp. 3-8, 1998.
- [HK93] N. Hoshi and A. Kawamura, *Plane Ultrasonic Piezoelectric Actuators*, PCC-Yokohama, 1993.
- [HKU98] Y. Hashimoto, Y. Koike, S. Ueha, *Transporting objects without contact using flexural traveling waves*, The Journal of the Acoustical Society of America, vol.103, issue 6, pp.3230-3233, 1998.
- [HL99] J. H. Han and I. Lee, *Optimal placement of piezoelectric sensors and actuators for vibration control of a composite plate using genetic algorithms*, Smart Materials and Structures, vol.8, pp. 257-267, 1999.
- [HLH03] Y. Hsu, C. Lee and W. Hsiao, *Optimizing piezoelectric transformer for maximum power transfer*, Smart Materials and Structures, vol.12, pp. 373-383, 2003.
- [HLW02] T. Hemsel, T. Littmann, J. Wallaschek, *Piezoelectric Transformers - State of the art and development trends*, Proc. IEEE Ultrasonics Symposium, pp. 645-648, vol.1, 2002.
- [HM03] D. Halim and S. O. Moheimani, *An optimization approach to optimal placement of collocated piezoelectric actuators and sensors on a thin plate*, Mechatronics, vol.13, pp. 27-47, 2003.

- [HolSe] J. Holzbecher, *Etude d'un transformateur piézoélectrique à très haute fréquence*, Semester project, EPFL-STI-IPR-LAI, 2005.
- [Hos89] K. Hosoe, *An Ultrasonic Motor for Use in Autofocus Lens Assemblies*, Techno, pp. 36-41, 1989.
- [HS96] M. Hermann, W. Schinkothe, *Piezoelectric Travelling Wave Motors Generating Direct Linear Motion*, Actuator 96, Germany, 1996.
- [HSH98] M. Hermann, W. Schinkothe, J. Haug, *Properties of a Piezoelectric Travelling Wave Motor Generating Direct Linear Motion*, Actuator 98, Germany, 1998.
- [HU93] H. Hirata and S. Ueha, *Characteristics estimation of a travelling wave type ultrasonic motor*, IEEE Transactions on Ultrasonic, Ferroelectrics, and Frequency Control, vol.40, n°4, pp. 402-406, 1993.
- [HU95] H. Hirata and S. Ueha, *Design of a travelling wave type ultrasonic motor*, IEEE Transactions on Ultrasonics, Ferroelectrics, and Frequency Control, vol.42, n°2, pp. 225-231, 1995.
- [Hu01] J. Hu, G. Li, H. L. W. Chan and C. L. Choy, *A Standing Wave-Type Noncontact Linear Ultrasonic Motor*, IEEE Trans. Ultrason. Ferroelect. Freq., vol.48, n°3, pp. 699-708, 2001.
- [HW92] P. Hagerdorn and J. Wallaschek, *Mechanical Vibration Aspects of Piezoelectric Travelling Wave Motors*, Actuator 96, 4th International Conference on New Actuators, Bremen, Germany, 32-37, 1992.
- [HW00] T. Hemsel and J. Wallaschek, *State of the Art and Development Trends of Ultrasonic Linear Motors*, Proceedings of the IEEE Ultrasonics Symposium, vol.1, pp. 663-666, 2000.
- [HYO93] S. Hirose, Y. Yamayoshi and H. Ono, *A small noncontact ultrasonic motor*, Proc. IEEE Ultrasonics Symposium, vol.1, pp. 453-456, 1993.

- [IEE87] Standard on Piezoelectricity, American Standards National Institute, New-York, 1987.
- [Iij87] T. Iijima, M. Wada, Y. Nakagawa and H. Itoh, *Ultrasonic Motor Using Flexural Standing Wave*, Proc. 7th Symp. Ultrasonic Electronics, Kyoto, Japanese Journal of Applied Physics, vol.26, suppl.26-1, pp. 191-193, 1987.
- [Ike96] T. Ikeda, *Fundamentals of Piezoelectricity*, Oxford University Press, 1996, ISBN 0-19-856339-6.
- [Ina87] R. Inaba, A. Tokushima, O. Kawasaki, Y. Ise and H. Yoneno, *Piezoelectric Ultrasonic Motor*, Proceedings of the IEEE Ultrasonics Symposium, pp. 747-756, 1987.
- [JC71] B. Jaffe and W. R. Cook, *Piezoelectric Ceramics*, Academic Press, 1971, ISBN 0-12-379550-8.
- [Jeo97] S. H. Jeong, H. K. Lee, Y. J. Kim, H. H. Kim, and K. J. Lim, *Vibration analysis of the stator in ultrasonic motor by FEM*, Proceedings of the 5th International Conference on Properties and Applications of Dielectric Materials, pp. 1091-1094, 1997.
- [JNL00] T. Y. Jiang, T. Y. Ng and K. Y. Lam, *Optimization of a piezoelectric ceramic actuator*, Sensors and actuators, vol.84, pp. 81-94, 2000.
- [Kas92] M. Kasuga, T. Satoh, J. Hirotohi and M. Kawata, *Development of Ultrasonic Motor and Application to Silent Alarm Analog Quartz Watch*, 4th Congrès Européen de Chronométrie, Lausanne, Switzerland, pp. 53-56, 1992.
- [KG92] K. Krishankumar and D. E. Goldberg, *Control system optimization using genetic algorithms*, AIAA J. Guidance, Contr. Dynam. vol.15, pp. 735739, 1992.
- [Kim02] H. W. Kim, S. Dong, P. Laoratanakul and K. Uchino, *Novel Method for Driving the Ultrasonic Motor*, IEEE Trans. Ultrasonics Ferroelec. Freq. Cont., vol. 49 (10), pp. 13561362, 2002.

- [Kle82] P. Kleinschmidt, *Piezokeramische Sensoren*, NTG-Fachberichte 79, pp. 189-195, 1982.
- [KruMs] M. Krummen, *Etude d'un moteur ultrasonique pas à pas nanométrique*, Master project, EPFL-STI-IPR-LAI, 2004.
- [KT91] A. Kawamura and N. Takeda, *Linear Ultrasonic Piezoelectric Actuator*, IEEE Trans. on Industry Applications, vol.27, n° 1, pp. 23-26, 1991.
- [KTH96] M. Kurosawa, M. Takahashi and T. Higuchi, *Friction Drive Surface Acoustic Wave Motor*, Ultrasonics 34, 243-246, 1996.
- [KUM85] M. Kuribayashi, S. Ueha and E. Mori, *Excitation conditions of flexural traveling waves for a reversible ultrasonic linear motor*, Journal of the Acoustic Society of America, vol.77, pp. 1431-1435, 1985.
- [Kum85] A. Kumada, *A piezoelectric ultrasonic motor*, Japanese Journal of Applied Physics, vol.24, suppl.24-2, pp. 739-741, 1985.
- [Kur98] M.K. Kurosawa, O. Kodaira, Y. Tsuchitoi and T. Higuchi, *Transducer for high speed and large thrust ultrasonic linear motor using two sandwich-type vibrators*, IEEE Trans. Ultrasonics Ferroelec. Freq. Cont. 45 (5), pp. 1188-1195, 1998.
- [KW95] J. W. Krome and J. Wallaschek, *Influence of the piezoelectric actuator on the vibrations of the stator of a traveling wave motor*, IEEE Ultrasonics Symposium, vol.1, pp. 413-416, 1995.
- [Lau00] G. K. Lau, H. Du, N. Guo and M. K. Lim, *Systematic design of displacement-amplifying mechanisms for piezoelectric stacked actuators using topology optimization*, Journal of Intelligent Material Systems and Structures, vol.11, pp. 685-695, 2000.
- [Ler90] R. Lerch, *Simulation of piezoelectric devices by two- and three-dimensional finite elements*, IEEE Transactions on Ultrasonics, Ferroelectrics and Frequency Control, vol.37, pp. 233-247, 1990.

- [Let94] R. Le Letty, *Conception de moteurs piézo-actifs à l'aide de la modélisation*, Thesis Dissertation, Institut National des Sciences Appliquées, Lyon, 1994.
- [LIP98] N. Lamberti, A. Iula and M. Pappalardo, *A Piezoelectric Motor Using Flexural Vibration of a Thin Piezoelectric Membrane*, IEEE Trans. Ultrason. Ferroelect. Freq., vol.45, pp. 23-29, 1998.
- [LOM02] Y. Li, J. Onoda and K. Minesugi, *Simultaneous optimization of piezoelectric actuator placement and feedback for vibration suppression*, Acta Astronautica, vol.50, n°6, pp. 335-341, Elsevier, 2002.
- [Mas64] W. P. Mason, *Physical Acoustics: Principles and Methods*, volume I, part A, Academic Press, New-York, 1964.
- [MBB98] J. F. Manceau, S. Biwersi and F. Bastien, *On the generation and Identification on traveling Waves in non-circular structures-application to innovative piezoelectric Motors*, Smart Mater. Struct. 7, 337-344, 1998.
- [Mer81] J. Merhaut, *Theory of electroacoustics*, McGraw-Hill Company, London, 1981.
- [Mie99] K. Miettinen, *Nonlinear multiobjective optimization*, Kluwer Academic Publishers, 1999.
- [MINIS] MINISWYS SA, <http://www.miniswys.com>.
- [Mit98] M. Mitchell, *An Introduction to Genetic Algorithms*, MIT Press, 1998.
- [MK99] A. Mukherjee and R. Karmakar, *Modeling and Simulation of Engineering Systems Through Bondgraphs*, CRC Press LLC, ISBN 0-8493-0982-4, 1999.
- [MKH96] T. Morita, M. Kurosawa and T. Higuchi, *Design of cylindrical ultrasonic micromotor to obtain mechanical output*, Japanese Journal of Applied Physics, vol.35, part 1, n°5B, pp. 3251-3254, 1996.

- [MLU02] S.Manuspiya, P.Laoratanakul and K.Uchino, *Integration of a piezo-electric transformer and an ultrasonic motor*, Ultrasonics, Elsevier, vol. 41, pp. 83-87, 2002.
- [MMF96] P. Minotti, P. Le Moal and A. Ferreira, *Moteurs piézo-électriques à onde progressive: I. Modélisation de la conversion d'énergie mécanique à l'interface stator/rotor*, J. Phys. III France 6 pp. 1315-1337, 1996.
- [Mon97] D. C. Montgomery, *Design and Analysis of Experiments*, John Wiley, New York, USA, 1997.
- [MW75] A. May and G. William, *Piezoelectric electromechanical translation apparatus*, United States Patent 3902084, 1975.
- [MWH89] R.M. Moroney, R.M. White and R.T. Howe, *Ultrasonic Micromotors*, IEEE Ultrasonics Symposium, Montreal, Canada, 1989.
- [Nak97] K. Nakamura, J. Margairaz, T. Ishii and S. Ueha, *Ultrasonic Stepping Motor Using Specially Shifted Vibrations*, IEEE Trans. Ultrason. Ferroelect. Freq., vol.44, pp. 823-828, 1997.
- [Nanom] Nanomotion, <http://www.nanomotion.com>.
- [NEY90] M. Nagai, N. Endo, T. Yamada, *Fundamental Characteristics of Linear Ultrasonic Motor Driven by Travelling Wave*, IEEE International Workshop on Intelligent Motion control, Istanbul, 1990.
- [Ngu98] N. T. Nguyen, R. W. Doering, A. Lal, R. M. White, *Computational fluid dynamics modeling of flexural plate wave pumps*, Proc. IEEE Ultrasonics Symposium, vol.1, pp. 431-434, 1998.
- [Nol] <http://www.noliac.com>.
- [Ohn92] O. Ohnishi, H. Kishie, A. Iwamoto, Y. Sasaki, T. Zaitzu and T. Inoue, *Piezoelectric Ceramic Transformer Operating in Thickness Extensional Vibration Mode for Power Supply*, Proc. IEEE Ultrasonics Symposium, vol.1, pp. 483-488, 1992.

- [OM87] I. Okumura and H. Mukohjima, *A Structure of Ultrasonic Motor for Auto Focus Lenses*, Proceedings of Motor Control, 1987.
- [OWIS] OWIS, Precise mechanical and optical system engineering, <http://www.owis-staufen.de>.
- [Pec95] C. Péclat, *Conception et réalisation d'un micromoteur piézoélectrique*, EPFL Thesis, n° 1434, 1995.
- [Poh87] D.W. Pohl, *Dynamic piezoelectric translation devices*, Rev. Sci. Instrum. 58 (1), pp. 5457, 1987.
- [Pon03] J. L. Pons, H. Rodriguez, J. F. Fernandez, M. Villegas and F. Seco, *Parameter optimization of ultrasonic motors*, Sensors and actuators, vol.107, pp. 169-182, Elsevier, 2003.
- [Pre02] A. Preumont, *Responsive Systems for Active Vibration Control*, Kluwer Academic Publishers, Dordrecht, 2002.
- [Rag88] K. Ragulskis, R. Bansevicius, R. Barauskas and G. Kulvietis, *Vibromotors for Precision Microrobots*, Hemisphere Publishing Co., New York, 1988.
- [Rao84] S. S. Rao, *Mechanical vibrations*, Addison-Wesley Publishing Company, USA, 1984.
- [Ros88] J. F. Rosenbaum, *Bulk acoustic wave theory and devices*, Artech House, Inc, Boston, 1988.
- [Rose64] C. A. Rosen, *Ceramic Transformers and Filters*, Ph.D. Thesis, Syracuse University, 1964.
- [Sas83] T. Sashida, Mech. Automation of Jap. 15(2), pp. 31-36, 1983.
- [Sas85] T. Sashida, *Ultrasonic Motors*, Japanese Journal of Applied Physics, vol. 54, n°6, pp. 589-590, 1985.

- [SB82] T. Sashida, and O. Butsuri, *Trial Construction and Operation of an Ultrasonic Vibration Drive Motor: Theoretical and Experimental Investigation of its Performances*, vol. 51, n°6, pp. 713-720, 1982.
- [SC93] C. E. Seeley and A. Chattopadhyay, *The development of an optimization procedure for the design of intelligent structures*, Smart Materials and Structures, vol.2, n°2, pp. 135-146, 1993.
- [Set02] N. Setter, *Piezoelectric Materials in Devices*, EPFL, 2002, ISBN 2-9700346-0-3.
- [Shi87] Shinsei Corporation Inc., <http://www.tky.3web.ne.jp/ usrmotor>.
- [Shi89] Operation Manual for the Ultrasonic Motor, Shinsei Corporation, 1-8, Kasuya 2-chome, Setagaya-ku, Tokyo, 157 Japan, 1989.
- [SK93] T. Sashida and T. Kenjo, *Introduction to Ultrasonic Motors*, Oxford University Press, 1993.
- [Smi92] W. A. Smith, *New Opportunities in Ultrasonic Transducers Emerging from Innovations in Piezoelectric Materials*, Proc. SPIE 1733, pp. 2-26, 1992.
- [SNK00] E. Silva, S. Nishiwaki and N. Kikuchi, *Topology optimization of flextensional actuator*, IEEE Transactions on Ultrasonics, Ferroelectrics, and Frequency Control, vol.47, n°3, pp. 657-671, 2000.
- [StuSe] M. Stutz, *Transformateur piézoélectrique*, Semester project, EPFL-STI-IPR-LAI, 2004.
- [SVC05] E. Sarraute, D. Vasic and F. Costa, *Transformateurs statiques piézoélectriques*, ENS de Cachan, 2005.
- [SWW99] A. M. Sadri, J. R. Wright and R. J. Wynne, *Modelling and optimal placement of piezoelectric actuators in isotropic plates using genetic algorithms*, Smart Materials and Structures, vol.8, pp. 490-498, 1993.

- [Tak88] T. Takano, Y. Tomikawa, T. Ogasawara, S. Sugawara and M. Konnon, *Ultrasonic Motors Using Piezoelectric Ceramic Multi-Mode Vibrators*, Proc. 8th Symp. Ultrasonic Electronics, Tokyo, Japanese Journal of Applied Physics, vol.27, suppl.27-1, pp. 192-194, 1988.
- [Tex02] *Analog Applications Journal*, Texas Instruments Incorporated, 2002.
- [Tom87] Y. Tomikawa, T. Kondo, T. Ogasawara, S. Sugawara and M. Konno, *Fundamental Considerations of Excitation of a Flexural Progressive Wave and its Application*, Proc. 7th Symp. Ultrasonic Electronics, Kyoto, Japanese Journal of Applied Physics, vol.26, suppl.26-1, pp. 194-196, 1987.
- [Tom88] Y. Tomikawa, T. Ogasawara, S. Sugawara, M. Konno and T. Takano, *Construction of Ultrasonic Motors and their Application*, Proc. 8th Symp. Ultrasonic Electronics, Kyoto, Japanese Journal of Applied Physics, vol.27, suppl.27-1, pp. 195-197, 1988.
- [Tra] Face Electronics, Transoner, <http://www.transoner.com>.
- [TT95] T. Takano and Y. Tomikawa, *Characteristics of the Ultrasonic Linear Motor Using Radial and Nonaxisymmetric Vibration Modes of an Annular Plate*, Japanese Journal of Applied Physics, vol.34, part 1, n°9B, pp. 5288-5291, 1995.
- [TTK92] T. Takano, Y. Tomikawa, C. Kusakabe, *Same phase drive-type ultrasonic motors using two degenerate bending vibration modes of a disk*, IEEE Transactions on Ultrasonics, Ferroelectrics and Frequency Control, vol.39, n°2, pp. 180-186, 1992.
- [Uch97] K. Uchino, *Piezoelectric Actuators and Ultrasonic Motors*, Kluwer Academic Publishers, USA, 1997, ISBN 0-7923-9811-4.
- [UK88] S. Ueha, M. Kurosawa, *Ultrasonic motors*, Proceedings of the IEEE Ultrasonics Symposium, vol.1, pp. 519-522, 1988.

- [UNM87] S. Ueha, H. Nagashima and M. Masuda, *Longitudinal-Torsional Composite Transducer and Its Applications*, Proc. 6th Meet. Ferroelectric Materials and Their Applications, Kyoto, Japanese Journal of Applied Physics, vol.26, suppl.26-2, pp. 188-190, 1987.
- [UT93] S. Ueha and Y. Tomikawa, *Ultrasonic Motors: Theory and Applications*, Oxford University Press, 1993.
- [Vas79] P. E. Vasiliev, UK Patent Application GB 2020857 A, 1979.
- [Vil05] M. Villiger, *Moteur ultrasonique sans contact*, Semester project, EPFL-STI-IPR-LAI, 2005.
- [Vis77] V. Vishnevsky, V. Kavertsev, I. Kartashev, V. Lavrinenko, M. Nekrasov and A. Prez, *Piezoelectric Motor Structures*, U.S. Patent 4'019'073, 1977.
- [Vis81] V. Vishnevsky, L. Gultiaeva, I. Kartaschew and V. Lavrinenko, *Piezoelectric Motor*, Russian Patent CCCP No. 851560, 1981.
- [Waa91] J. W. Waanders, *Piezoelectric Ceramics - Properties and Applications*, Philipps Components, Eindhoven, 1991.
- [WD04] H. Widmer and J. Dual, *A Model of a Vibrational Impact Drive*, Proceedings of the Euromech colloquium 457 on non linear modes of vibrating systems, 2004.
- [Wer86] W. Wersing, *Composite Piezoelectrics for Ultrasonic Transducers*, Proc. 6th IEEE Int. Symp. on Appl. of Ferroelectrics, pp. 212-223, 1986.
- [Wie01] M. Wiesendanger, *Squeeze film air bearings using piezoelectric bending elements*, EPFL Thesis, n°2336 ,2001.
- [YV96] A. Yousefi-Koma and G. Vukovich, *Shape and location optimization of piezoelectric actuators in active control systems*, Proceedings of the ASME Aerospace Division, AD-vol.52, pp. 559-566, 1996.

- [Zai97] T. Zaitso, Y. Fuda, Y. Okabe, T. Ninomiya, S. Hamamura, and M. Katsuno, *New Piezoelectric Transformer Converter for AC-Adapter*, Proc. IEEE APEC97, vol. 2, pp. 568-572, 1997.
- [Zha00] H. W. Zhang, B. Lennox, P. R. Goulding and A. Y. T. Leung, *A float-encoded genetic algorithm technique for integrated optimization of piezoelectric actuator and sensor placement and feedback gains*, Smart Materials and Structures, vol.9, pp. 552-557, 2000.

LIST OF ABBREVIATIONS

CAD	Computer Aided Design
CCFL	Cold Cathode Fluorescent Lamp
CMT	Ceramic Multilayer Transformer
DOE	Design Of Experiments
DOF	Degree Of Freedom
EAs	Evolutionary Algorithms
EEC	Electric Equivalent Circuit
FE	Finite Element
FEA	Finite Element Analysis
FEM	Finite Element Method
GAs	Genetic Algorithms
HTUM	Hybrid Transducer Ultrasonic Motor
LCA	Left Clamping Actuator
LCD	Liquid Crystal Display
LPV	Longitudinal Piezoelectric Vibrator
MCUM	Mode Conversion Ultrasonic Motor

MMUM	Multi-Mode Ultrasonic Motor
MOEAs	Multi-Objective Evolutionary Algorithms
MOP	Multi-Objective Problem
MUM	MINISWYS Ultrasonic Motor
PT	Piezoelectric Transformer
PZT	Piezoelectric Zirconate Titanate
RCA	Right Clamping Actuator
RMS	Root Mean Square
SWUM	Standing Wave Ultrasonic Motor
TWUM	Traveling Wave Ultrasonic Motor
ULM	Ultrasonic Linear Motor
UM	Ultrasonic Motor

LIST OF SYMBOLS

a_0	[—]	constant effect
a_i	[—]	principal effects
a_{ij}	[—]	effects of the first order interactions
a_{ijk}	[—]	effects of the second order interactions
A	[N/V]	Force factor
b	[m]	width of the bar
B	[m]	Width of piezoceramics
C	[—]	Effects vector
C	[m]	Width of the hole
C_m	[F]	Motional capacitance
C_t	[—]	Constant
C_S	[F]	Capacitance (PT)
C_0	[F]	Static capacitance
C_1	[F]	Capacitance (primary)
C_2	[F]	Capacitance (secondary)
d	[C/N]	piezoelectric charge constant
d_{el}	[m]	Distance between the ceramic electrodes
d_v	[—]	number of design variables
D	[C/m^2]	Dielectric displacement
D	[m]	Spacing between piezoceramics
e	[C/m^2]	piezoelectric constant
E	[V/m]	Electric field strength
E_x	[—]	Experiments matrix
E	[m]	Half-thickness of the stator
E_{Piezo}	[m]	Thickness of the piezoceramics of the MUM

$E_{Resonator}$	[m]	Thickness of the resonator of the MUM
f	[Hz]	frequency of the input voltage
f_a	[Hz]	anti-resonance frequency
f_p	[Hz]	parallel resonance frequency
f_r, f', f''	[Hz]	resonance frequencies
f_s	[Hz]	series resonance frequency
f_1	[Hz]	frequency of the backward motion of the MUM
f_2	[Hz]	frequency of the forward motion of the MUM
F	[N]	Amplitude of the sinusoidal normal force
F_F	[N]	Friction force
F_m	[N]	Force at the mechanical terminal
F_N	[N]	Normal force
\mathbf{F}_V	[N]	Nodal mechanical force vector
F_0	[N]	Pre-stressing force
\mathbf{g}	[V · m/N]	piezoelectric voltage constant
G	[m]	Supplementary width added to the stator
G_a	[—]	Step-up ratio of a PT
h	[m]	thickness of the bar
H	[m]	Thickness of piezoceramics
H_{Piezo}	[m]	Width of the piezoceramics of the MUM
$H_{Resonator}$	[m]	Height of the resonator of the MUM
$H1$	[m]	Dimensional parameter of the resonator of the MUM
$H2$	[m]	Dimensional parameter of the resonator of the MUM
$H3$	[m]	Dimensional parameter of the resonator of the MUM
$H4$	[m]	Dimensional parameter of the resonator of the MUM
I	[A]	Current at the electrical terminal
I_S	[kg · m ²]	Moment of inertia of the cross section
\mathbf{k}	[—]	electromechanical coupling factor
k	[rad/m]	wavenumber
k_p	[—]	planar coupling factor
k_t	[—]	thickness coupling factor
K	[N/m]	Spring constant
\mathbf{K}_1	[N · s/m]	Damping matrix

K₂	[N/m ²]	Stiffness matrix
K₃	[C/m ²]	Piezoelectric matrix
K₄	[C · m/V]	Dielectric matrix
<i>l</i>	[m]	length of the ceramic plate
<i>L</i>	[m]	Length of piezoceramics
<i>L_m</i>	[H]	Motional inductance
<i>L_{Piezo}</i>	[m]	Length of the piezoceramics of the MUM
<i>L_{Resonator}</i>	[m]	Width of the resonator of the MUM
<i>L_S</i>	[H]	Inductance (PT)
<i>L1</i>	[m]	Dimensional parameter of the resonator of the MUM
<i>L2</i>	[m]	Dimensional parameter of the resonator of the MUM
<i>L3</i>	[m]	Dimensional parameter of the resonator of the MUM
<i>L4</i>	[m]	Dimensional parameter of the resonator of the MUM
<i>m</i>	[kg]	mass of the slider
<i>m_v</i>	[kg]	mass of the vibrator
M_M	[kg]	Mass matrix
<i>n</i>	[—]	number of simulations
<i>N</i>	[N]	Pre-stressing force
<i>N₁</i>	[—]	number of input layers of the radial mode type PT
<i>N₂</i>	[—]	number of output layers of the radial mode type PT
<i>p</i>	[m]	width of the ceramic plate
P	[C/m ²]	Polarization
<i>q</i>	[—]	number of input parameters
Q	[—]	Electrical quality factor
Q_E	[C]	Nodal electrical charge vector
Q_m	[—]	Mechanical quality factor
<i>r</i>	[m]	radius of the radial mode type PT
R	[—]	Response vector
<i>R_{C1}</i>	[Ω]	Dielectric losses (primary) resistance (PT)
<i>R_{C2}</i>	[Ω]	Dielectric losses (secondary) resistance (PT)
<i>R_L</i>	[Ω]	Load resistance
<i>R_S</i>	[Ω]	Resistance (PT)
<i>R_m</i>	[Ω]	Motional resistance

$R(x)$	$[-]$	Response of the system
R_0	$[\Omega]$	Dielectric resistance
R_1	$[rad]$	Stator's inner radius
R_2	$[rad]$	Hole's inner radius
R_3	$[rad]$	Stator's outer radius
s	$[m^2/N]$	elastic compliance
s^D	$[m^2/N]$	elastic compliance under constant electric displ.
s^E	$[m^2/N]$	elastic compliance under constant electric field
S	$[m/m]$	Strain
S_b	$[m^2]$	Cross section of the bar
S_{el}	$[m^2]$	Surface of the electrodes
t	$[m]$	thickness of the ceramic plate
t_1	$[m]$	thickness of the input layer (radial mode type PT)
t_2	$[m]$	thickness of the output layer (radial mode type PT)
T	$[N/m^2]$	Mechanical stress
u	$[m]$	longitudinal displacement
u_x	$[m]$	longitudinal displacement in the horizontal direction
u_z	$[m]$	longitudinal displacement in the vertical direction
U	$[V]$	Voltage applied to piezoceramics
U_e	$[V]$	Voltage at the electrical terminal
v	$[m/s]$	velocity at the mechanical terminal
v_x	$[m/s]$	velocity of the particles at the crests (traveling wave)
V_{in}	$[V]$	Input voltage
V_{out}	$[V]$	Output voltage
w	$[m]$	transverse displacement
$x(t)$	$[m]$	coordinate of the slider
x_i	$[-]$	input parameters
X	$[-]$	Model matrix
Y	$[N/m^2]$	Young's modulus
Y_b	$[N/m^2]$	Young's modulus of the bar
Y_m	$[S]$	Motional admittance
Y_0	$[S]$	Electrical admittance of the piezoelectric ceramic
$z(t)$	$[m]$	coordinate of the tip motion

z_0	$[m]$	amplitude of the tip motion
Z_m	$[\Omega]$	Mechanical impedance of the piezoelectric ceramic
α	$[rad]$	angle defining stator's hole
γ	$[m]$	nodal displacement vector
$\tan \delta$	$[-]$	dielectric dissipation factor
ϵ	$[C \cdot m/V]$	dielectric constant or permittivity
ϵ_r	$[F/m]$	relative permittivity
ϵ^S	$[F/m]$	Permittivity at constant strain
ϵ^T	$[F/m]$	Permittivity at constant stress
ϵ_0	$[F/m]$	free space permittivity
φ_0	$[rad]$	phase between the tip motion and the force
ϕ	$[rad]$	phase difference between u_x and u_z
λ	$[m]$	wavelength
μ	$[-]$	coefficient of friction
ξ	$[V]$	nodal potential vector
ω	$[rad/s]$	angular frequency
ω_r	$[rad/s]$	resonant angular frequency
ω_s	$[rad/s]$	angular frequency of the source
ρ	$[kg/m^3]$	density of the bar
ρ_p	$[kg/m^3]$	density of the PT material

LIST OF FIGURES

2.1	Crystal structure of a traditional piezoelectric ceramic: a) temperature above Curie point, b) temperature below Curie point . . .	7
2.2	Polarizing (poling) a piezoelectric ceramic: a) random orientation of polar domains prior to polarization, b) polarization in DC electric field, c) remanent polarization after electric field removed	7
2.3	a) hysteresis curve for polarization, b) elongation / contraction of a ceramic element	8
2.4	Impedance as a function of frequency	11
2.5	Axes notation	12
2.6	The longitudinal vibration mode	18
2.7	The transversal vibration mode	19
2.8	The shear vibration mode	19
2.9	Generator and motor actions of a piezoelectric element	20
2.10	Piezoelectric ignition system	21
2.11	Sensor constructions	22
2.12	Scheme of an ultrasound transducer	23
2.13	Principle of a Rosen type piezoelectric transformer	24
2.14	a) Traveling wave ultrasonic motor developed by Sashida, b) application in a camera auto-focusing mechanism	25

3.1	Basic scheme of ultrasonic motors	27
3.2	Ultrasonic motor by Barth	28
3.3	Example of SWUM [SB82]	30
3.4	Example of SWUM [TTK92]	31
3.5	Principle of TWUM	32
3.6	a) Configuration of longitudinal torsional vibrator b) motion of the torsional coupler	33
3.7	a) Scheme of the rotation mode b) piezoelectric element with divided electrode for the rotation mode	34
3.8	a) Scheme of the HTUM b) principle of the HTUM	35
3.9	The contact surface of the actuator at different vibration amplitude ratios: u_v is the amplitude of the vibrator and u_a the amplitude of the actuator: a) low speed, c) high speed	36
3.10	Shinsei ultrasonic motor	37
3.11	Operating principle of the step by step ultrasonic motor	38
3.12	a) prototype built at the laboratory, b) vibration mode for $n=10$ obtained with Ansys, c) experimental result through speckle interferometry	39
3.13	A non-contact type ultrasonic rotary motor	40
3.14	Traveling wave linear ultrasonic motors: a) linear TWUM with ring-type stator, b) linear TWUM with a straight rod pressed tangentially onto rotational symmetric stator	41
3.15	Schematic operation diagram of an inchworm motor	42
3.16	Micro-push motor using a piezoelectric rectangular plate	43
3.17	Micro-push motor using piezoelectric stacks	44
3.18	Elliptec motor and its operating principle	45

3.19	Elliptec actuator: a) harmonic responses, b) Elliptec prototype	46
3.20	Operating principle of a stick and slip motor	47
3.21	Application example: linear stage for micro-positioning	47
3.22	A non-contact type ultrasonic linear motor	48
3.23	Linear slider bearing: a) complete system with glass rail ; b) bottom view of the slider with five bearing elements	49
3.24	Classification of ultrasonic motors	50
4.1	Standing wave pattern	53
4.2	Motion of the motor tip for different phase angles	54
4.3	Motion model for the slider	56
4.4	Traveling wave	58
4.5	Driving process of linear traveling wave motors	59
4.6	Elliptic displacement motion	61
4.7	Electromechanical equivalent scheme	63
4.8	Ceramic plate deformed in its length	64
4.9	Electric equivalent circuit	66
4.10	FE model of the ULM	72
4.11	Operating principle of the ULM	73
4.12	Parametrization of the vibrating part of the ULM	73
4.13	Modal shape at resonance frequency	78
4.14	Vertical displacement of a surface point	78
4.15	Elliptic motion of a surface point	79
4.16	Prototype of the motor realized at the laboratory	80
4.17	Admittance versus frequency of the vibrating part of the ULM	81

4.18	Comparison of the vertical displacement versus applied voltage between ANSYS simulations and experimental data and power consumption of the motor	82
5.1	Steps of the sensitivity analysis	94
5.2	Two dimensional Doehler's network and the corresponding model matrix	98
5.3	Relative effects of the different input parameters for a structure without a hole: a) principal effects	99
5.4	Relative effects of the different input parameters for a structure without a hole: b) first order interactions effects	99
5.5	Relative effects of the different input parameters for a structure without a hole: c) second order interactions effects, d) quadratic effects	100
5.6	Input parameters influences for a structure without a hole	101
5.7	Relative effects of the different input parameters for a structure with a hole: a) principal effects	101
5.8	Relative effects of the different input parameters for a structure with a hole: b) first order interactions effects	102
5.9	Relative effects of the different input parameters for a structure with a hole: c) second order interactions effects	102
5.10	Relative effects of the different input parameters for a structure with a hole: d) quadratic effects	103
5.11	Input parameters influences for a structure with a hole	103
5.12	Structures comparison: maximum amplitude without a hole	105
5.13	Structures comparison: maximum amplitude with a hole	106
5.14	Example of iso-surfaces graph for three input parameters (B, L, D)	108
5.15	FE Optimization (structure without a hole): first order method	110

5.16	FE Optimization (structure without a hole): factorial method . . .	111
5.17	FE Optimization (structure with a hole): first order method . . .	113
5.18	FE Optimization (structure with a hole): factorial method	114
5.19	FE Optimization: final structure	116
5.20	Structures comparison: initial, pre-optimization, FE optimization and final	117
5.21	Application case: linear motion of the lens of an optical system .	120
5.22	Scheme of the motion transmission	121
5.23	The MINISWYS Ultrasonic Motor (MUM)	122
5.24	MUM prototype	122
5.25	Forward and backward motions of the MINISWYS motor	123
5.26	MUM: piezoelectric elements and polarization	123
5.27	FEM results obtained for the actual structure: a) forward motion ($f_1 = 460kHz$), b) backward motion ($f_2 = 508kHz$)	124
5.28	Transient simulation of the initial structure: displacement of the motor moving part obtained by applying a voltage of 20V during 4ms	125
5.29	MUM: a) initial design; b) numerical model; c) parametrization .	127
5.30	Initial structure: vibration modes for the forward and backward motions	128
5.31	Points at the extremities of the resonator taken into account for the calculation of the mean value of the displacements in the three directions	130
5.32	Initial structure: movement amplitudes (absolute values) in the three directions	131
5.33	Principal relative effects for the first vibration mode (f_1)	133

5.34	Principal relative effects for the second vibration mode (f_2) . . .	134
5.35	Pre-optimized structure: vibration modes for the forward and backward motions	135
5.36	Transient simulation of the pre-optimized structure: displacement of the motor moving part obtained by applying a voltage of 20V during 4ms	136
5.37	FE optimized structure: vibration modes for the forward and backward motions	137
5.38	Transient simulation of the optimized structure: displacement of the motor moving part obtained by applying a voltage of 20V during 4ms	138
5.39	Structures comparison: a) pre-optimized structure, b) initial structure, c) FE optimized structure	140
5.40	Structures comparison (resonator) : initial, pre-optimized, FE optimized	141
5.41	Structures comparison (moving part): initial, pre-optimized, FE optimized	141
5.42	Design of the resonator built for measurements	142
5.43	Measurement obtained with the initial structure using a coil to increase the input voltage (\Rightarrow applied voltage to piezoceramics of 20V)	143
5.44	Measurement obtained with the initial structure without using a coil to increase the input voltage (\Rightarrow applied voltage to piezoceramics of 7V)	144
5.45	Measurement obtained with the optimized structure without using a coil to increase the input voltage (\Rightarrow applied voltage to piezoceramics of 5V)	144
5.46	Standard MOEA flowchart	150

6.1	Working principle of a Rosen type piezoelectric transformer . . .	156
6.2	Rosen type piezoelectric transformers: a) Transoner, b) Noliac CMT	157
6.3	a) working principle of a radial mode type transformer, b) Transoner radial mode type piezoelectric transformer	157
6.4	Electric equivalent circuits of a PT: a) without diel. losses, b) with diel. losses	159
6.5	Transformation ratio of the Noliac Rosen type PT (1)	162
6.6	Transformation ratio of the Noliac Rosen type PT (2)	163
6.7	Transformation ratio of the Transoner radial mode type PT (1)	164
6.8	Transformation ratio of the Transoner radial mode type PT (2)	164
6.9	FE models of the PTs: a) Rosen type, b) radial mode type	165
6.10	FE simulation of the Transoner Rosen type PT: a) electric potential at first resonance frequency ($f' = 72.0kHz$), b) transformation ratio for $R_L = 500k\Omega$	166
6.11	FE simulation of the Transoner radial mode type PT: a) electric potential at resonance frequency ($f_r = 107.1kHz$), b) transformation ratio for $R_L = 500\Omega$	167
6.12	Input/output voltages and currents measured for the Transoner Rosen type PT for $R_L = 500k\Omega$ and $f' = 65.5kHz$	169
6.13	Input/output voltages and currents measured for the Transoner radial mode type PT for $R_L = 500\Omega$ and $f_r = 94.8kHz$	169
6.14	Characteristics of the Transoner radial mode type PT for an input voltage $V_{in} = 30V$ and a load resistance $R_L = 500\Omega$	170
6.15	Comparison of the results obtained with the Noliac Rosen type PT	171
6.16	Comparison of the results obtained with the Transoner Rosen type PT	171

6.17	Comparison of the results obtained with the Transoner radial mode type PT	172
6.18	Basic concept of UM drive system using a PT	176
6.19	Application of a PT for the UM drive [Kim02]	177
6.20	Comparison of magnetic and piezoelectric transformers for CCFL applications	178
6.21	AC/DC converter for mobile phone battery charging: a) objective (miniaturization of a conventional AC/DC converter through implementation of a PT), b) overview pictures of the prototyped AC/DC converter [Bov00]	179
6.22	AC/DC adapter for notebook computers [De1]	180
6.23	High power applications of piezoelectric transformers [CU01]	181
7.1	Example of iso-surfaces graph for three input parameters (B, D, H) and the deformation amplitude as output value	230
7.2	Example of iso-surfaces graph for three input parameters (f, G, B) and the deformation amplitude as output value	231
7.3	Example of iso-surfaces graph for three input parameters (H, E, L) and the deformation amplitude as output value	232
7.4	Example of iso-surfaces graph for three input parameters (N, D, B) and the deformation amplitude as output value	233
7.5	Example of iso-surfaces graph for three input parameters (U, f, E) and the deformation amplitude as output value	234
7.6	Example of iso-surfaces graph for three input parameters (H, U, L) and the deformation amplitude as output value	235
7.7	Example of iso-surfaces graph for three input parameters (α , G, C) and the deformation amplitude as output value	236
7.8	Example of iso-surfaces graph for three input parameters (C, f, E) and the deformation amplitude as output value	237

7.9	Example of iso-surfaces graph for three input parameters (U, N, L) and the deformation amplitude as output value	238
7.10	Example of iso-surfaces graph for three input parameters (B, H, R_2) and the deformation amplitude as output value	239
7.11	Example of iso-surfaces graph for three input parameters (α , f, G) and the deformation amplitude as output value	240
7.12	Example of iso-surfaces graph for three input parameters (D, H, L) and the deformation amplitude as output value	241
7.13	MUM initial structure: numerical model	243
7.14	MUM initial structure: movement amplitudes in the three directions	243
7.15	MUM initial structure: 254kHz mode	244
7.16	MUM initial structure: 303kHz mode	244
7.17	MUM initial structure: 486kHz mode	245
7.18	MUM initial structure: 556kHz mode	245
7.19	MUM initial structure: 578kHz mode	246
7.20	MUM initial structure: 612kHz mode	246
7.21	Structure without "feet": numerical model	247
7.22	Structure without "feet": movement amplitudes in the three directions	247
7.23	Structure without "feet": 278kHz mode	248
7.24	Structure without "feet": 351kHz mode	248
7.25	Structure without "feet": 483kHz mode	249
7.26	Structure without "feet": 516kHz mode	249
7.27	Structure without "feet": 535kHz mode	250
7.28	Structure without "feet": 557kHz mode	250

7.29	Half structure in z direction: numerical model	251
7.30	Half structure in z direction: movement amplitudes in the three directions	251
7.31	Half structure in z direction: 305 kHz mode	252
7.32	Half structure in z direction: 328 kHz mode	252
7.33	Half structure in z direction: 482 kHz mode	253
7.34	Half structure in z direction: 555 kHz mode	253
7.35	Half structure in x direction: numerical model	254
7.36	Half structure in x direction: movement amplitudes in the three directions	254
7.37	Half structure in x direction: 300 kHz mode	255
7.38	Half structure in x direction: 427 kHz mode	255
7.39	Half structure in x direction: 464 kHz mode	256
7.40	Half structure in x direction: 522 kHz mode	256
7.41	Structure with straight lines: numerical model	257
7.42	Structure with straight lines: movement amplitudes in the three directions	257
7.43	Structure with straight lines: 284 kHz mode	258
7.44	Structure with straight lines: 374 kHz mode	258
7.45	Structure with straight lines: 426 kHz mode	259
7.46	Structure with straight lines: 514 kHz mode	259
7.47	Dimensions of the Noliac Rosen type PT	260
7.48	Cross section of the input part of the Noliac Rosen type PT . . .	260
7.51	Dimensions of the Transoner Rosen type PT	264
7.56	Dimensions of the Transoner radial type PT	270

LIST OF TABLES

2.1	Characteristics of soft ceramics and hard ceramics compared . . .	9
2.2	Definition of the piezoelectric constants	17
2.3	Types of fundamental piezoelectric constitutive equations	17
2.4	Elastoelectric matrix for T and E taken as independent variables	18
3.1	Advantages and drawbacks of ultrasonic motors	28
4.1	Dimensions and materials of the simulated vibrator	74
5.1	Variation ranges of the different input parameters	92
5.2	Input parameters and maximum deformation amplitude	105
5.3	Initial values and variation ranges of the different input parameters	109
5.4	Initial values and variation ranges of the different input parameters	112
5.5	Dimensions and materials of the simulated structure of the MUM	126
5.6	Values of the displacements found for the initial structure	131
5.7	Dimensions of the simulated structures	139
5.8	Results comparison of the simulated structures	139
5.9	Results comparison of the tested structures	145
6.1	Calculated and measured elements of the EEC for the Noliac Rosen type PT	162
6.2	Calculated and measured elements of the EEC for the radial mode type PT	163

6.3 Hypotheses made and observations about the study of the PTs . 173

APPENDIX

Appendix A: Piezoelectric ceramic properties

Appendix B: Pre-optimization results

Appendix C: MINISWYS motor: piezoceramic properties

Appendix D: MINISWYS motor: structures analysis

Appendix E: Noliac Rosen type piezoelectric transformer

Appendix F: Transoner Rosen type piezoelectric transformer

Appendix G: Transoner radial mode type PT

Appendix A

Piezoelectric ceramic properties

Material data of the used stacked PZT ceramic NLA-2x3x9 from TOKIN company.

$$\text{Density: } \rho = 7700 \text{ kg/m}^3.$$

Stiffness matrix:

$$c^E = \begin{bmatrix} 12.8 & 6.8 & 6.6 & 0 & 0 & 0 \\ & 12.8 & 6.6 & 0 & 0 & 0 \\ & & 10.0 & 0 & 0 & 0 \\ & & & 2.1 & 0 & 0 \\ & & & & 2.1 & 0 \\ & & & & & 2.1 \end{bmatrix} \cdot 10^{10} \text{ N/m}^2.$$

Piezoelectric constants:

$$e = \begin{bmatrix} 0 & 0 & 0 & 0 & 11.8 & 0 \\ 0 & 0 & 0 & 11.8 & 0 & 0 \\ -6.1 & -6.1 & 15.7 & 0 & 0 & 0 \end{bmatrix} \text{ As/m}^2.$$

Dielectric constants:

$$\epsilon^S = \begin{bmatrix} 8.8 & 0 & 0 \\ 0 & 8.8 & 0 \\ 0 & 0 & 8.8 \end{bmatrix} \cdot 10^{-9} \text{ As/Vm}.$$

Appendix B

Pre-optimization results: structure without a hole

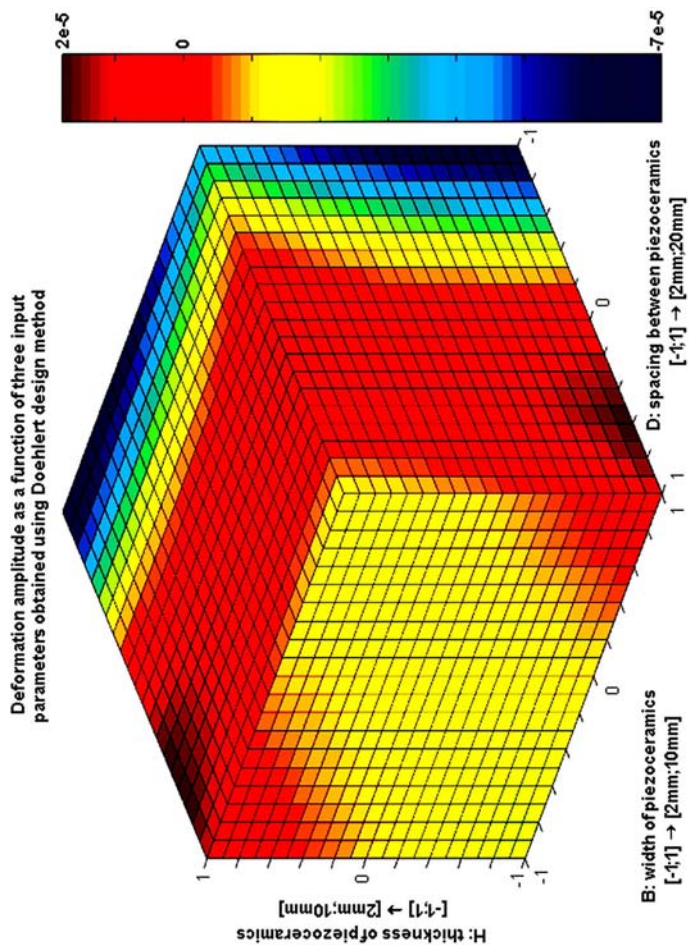


Fig. 7.1: Example of iso-surfaces graph for three input parameters (B, D, H) and the deformation amplitude as output value

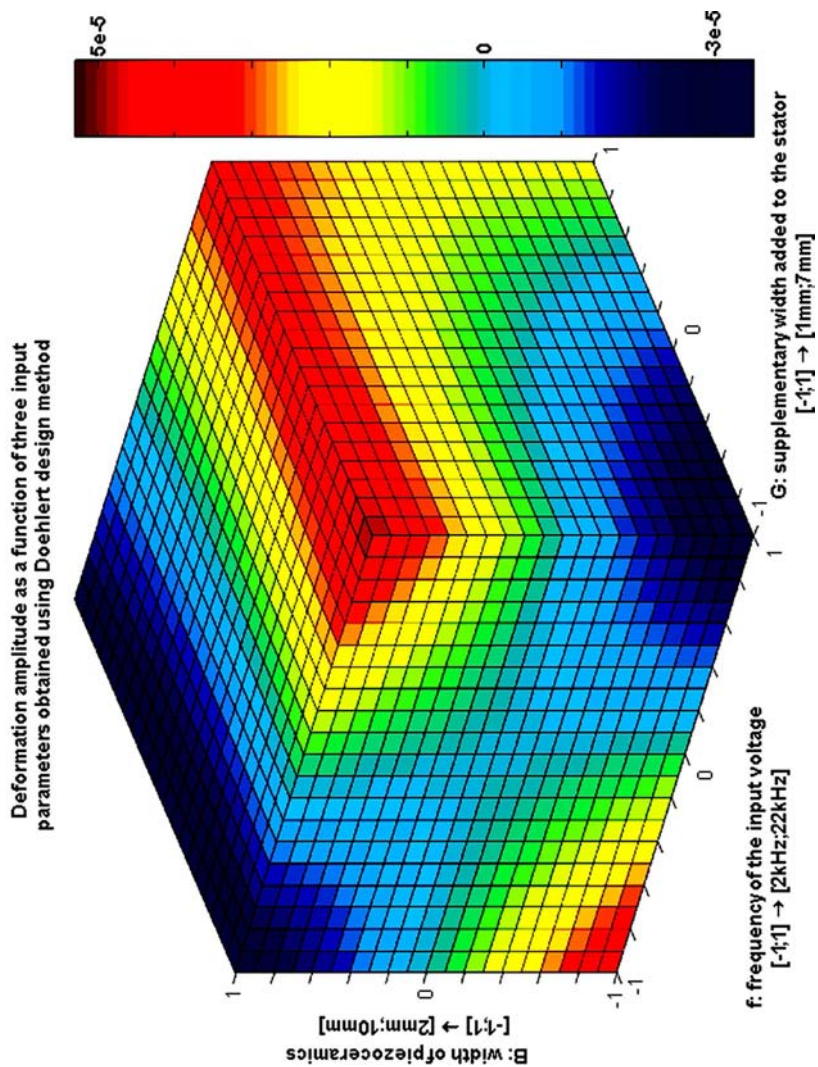


Fig. 7.2: Example of iso-surfaces graph for three input parameters (f , G , B) and the deformation amplitude as output value

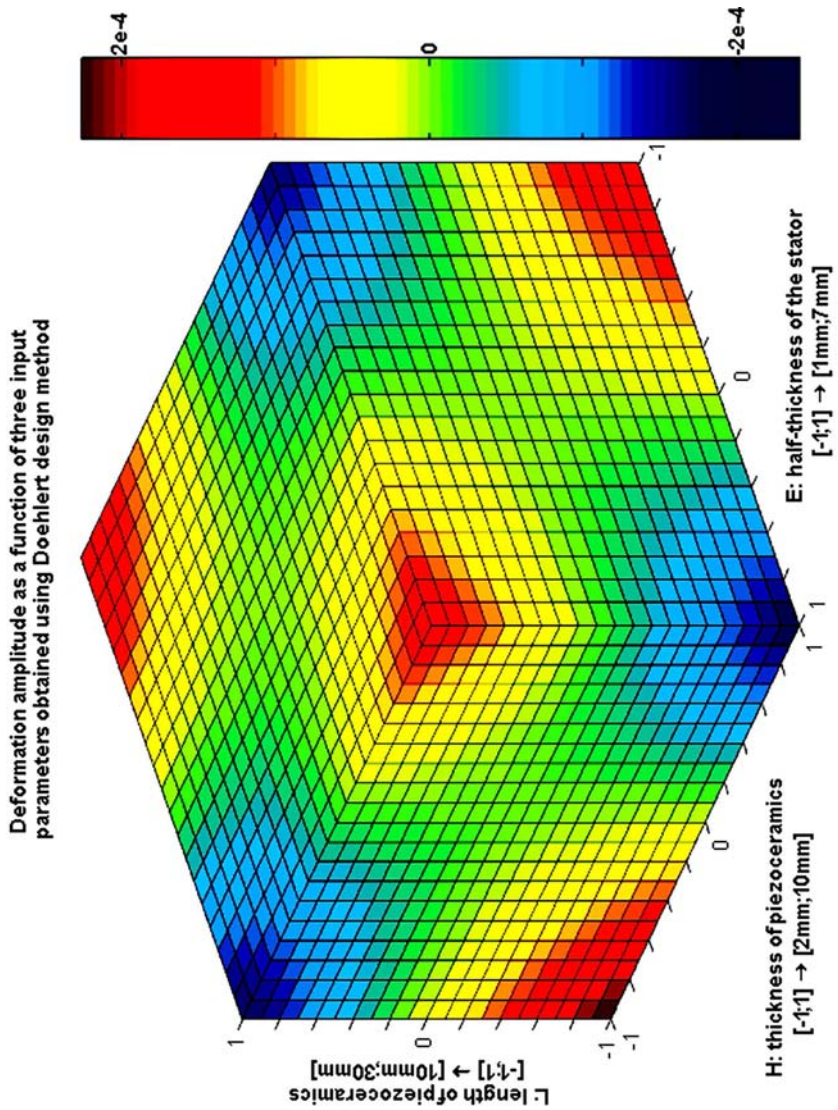


Fig. 7.3: Example of iso-surfaces graph for three input parameters (H, E, L) and the deformation amplitude as output value

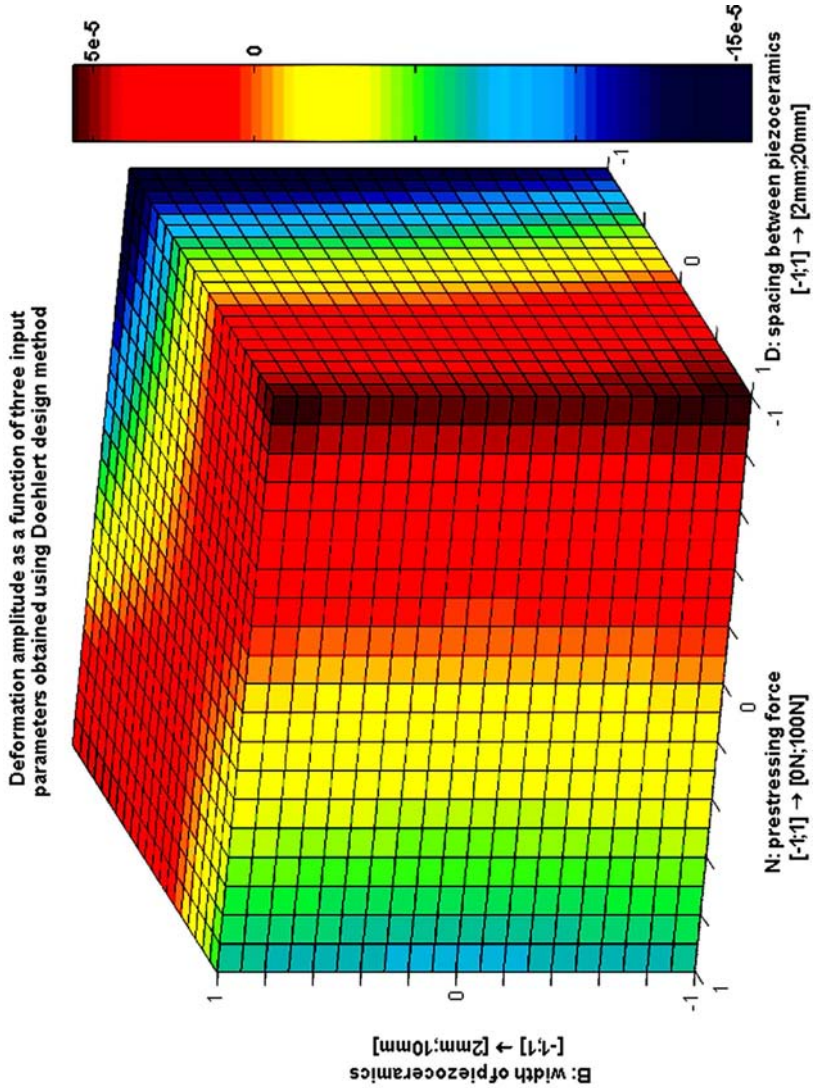


Fig. 7.4: Example of iso-surfaces graph for three input parameters (N , D , B) and the deformation amplitude as output value

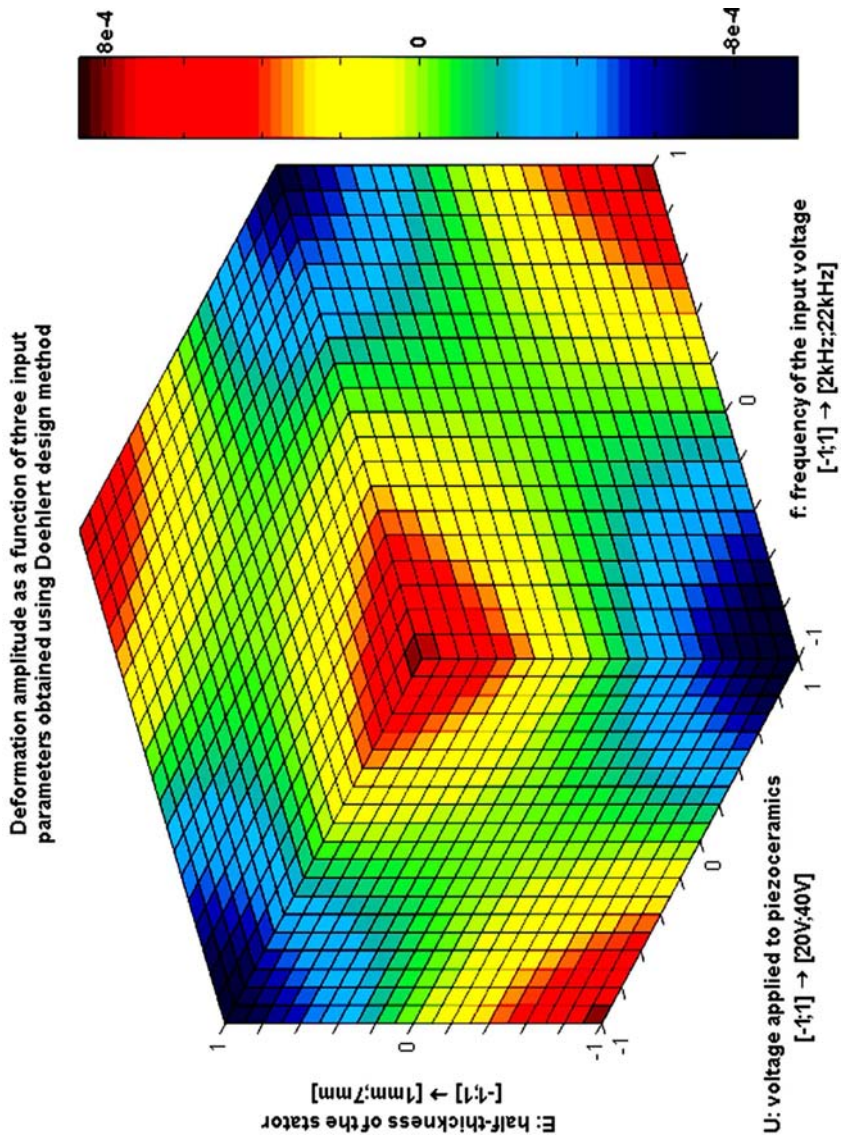


Fig. 7.5: Example of iso-surfaces graph for three input parameters (U , f , E) and the deformation amplitude as output value

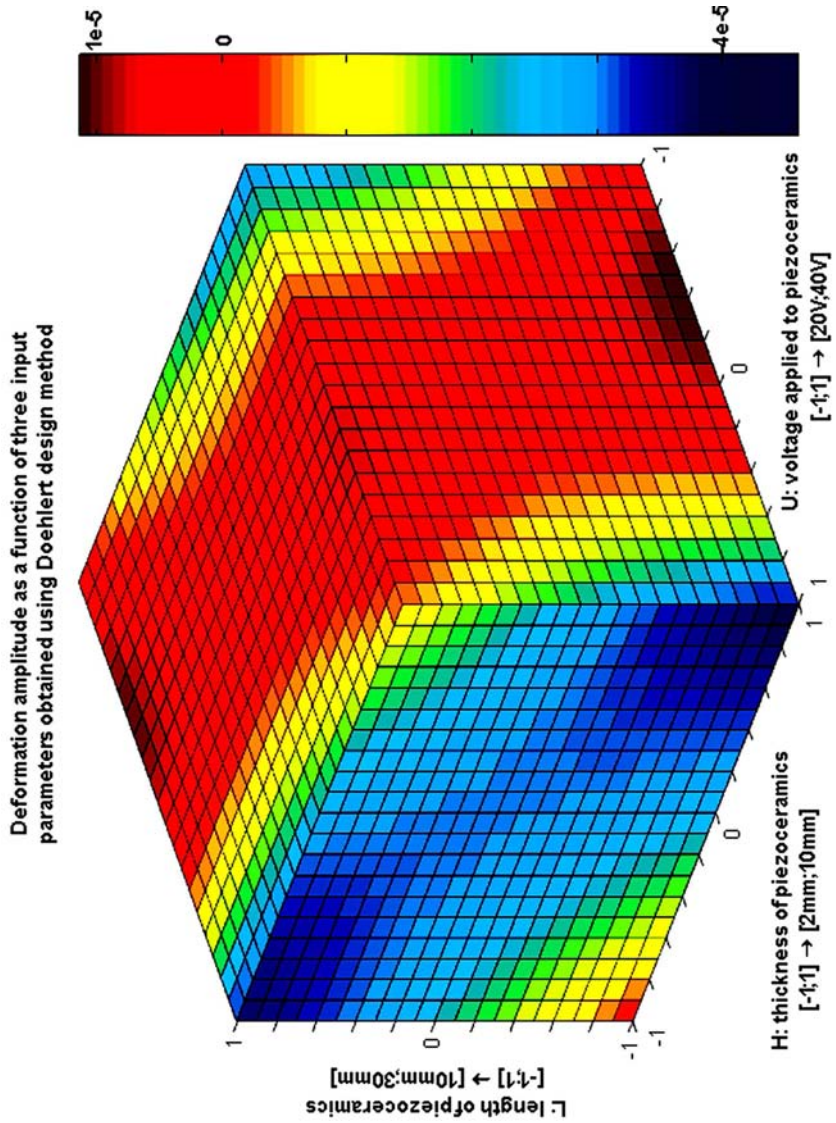


Fig. 7.6: Example of iso-surfaces graph for three input parameters (H , U , L) and the deformation amplitude as output value

Pre-optimization results: structure with a hole

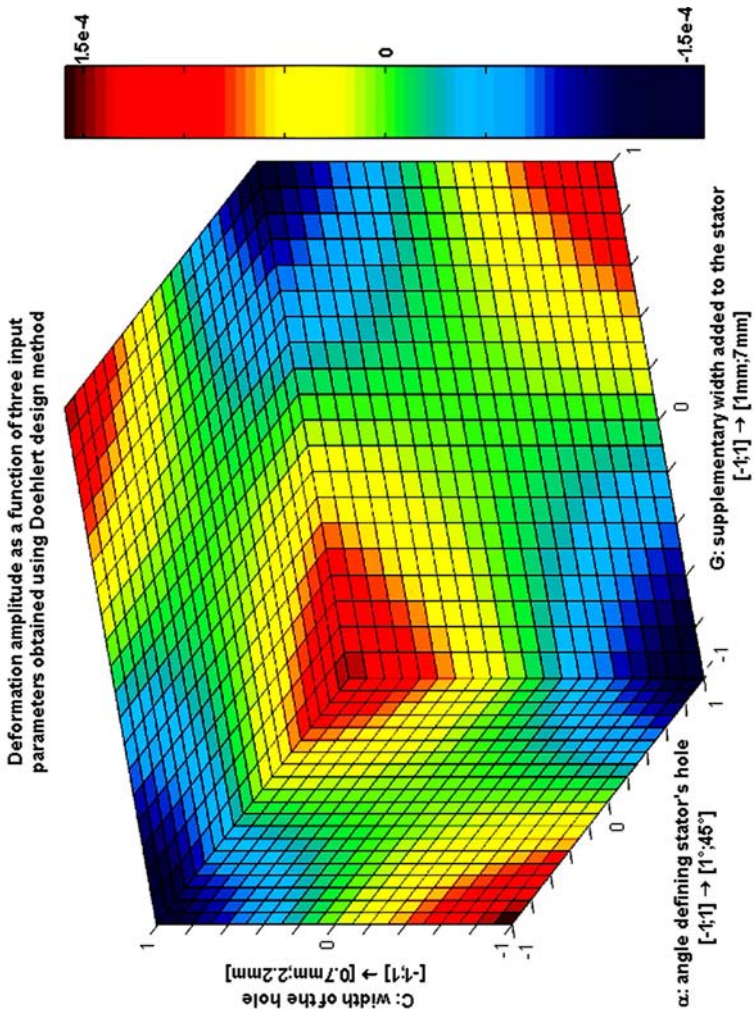


Fig. 7.7: Example of iso-surfaces graph for three input parameters (α , G , C) and the deformation amplitude as output value

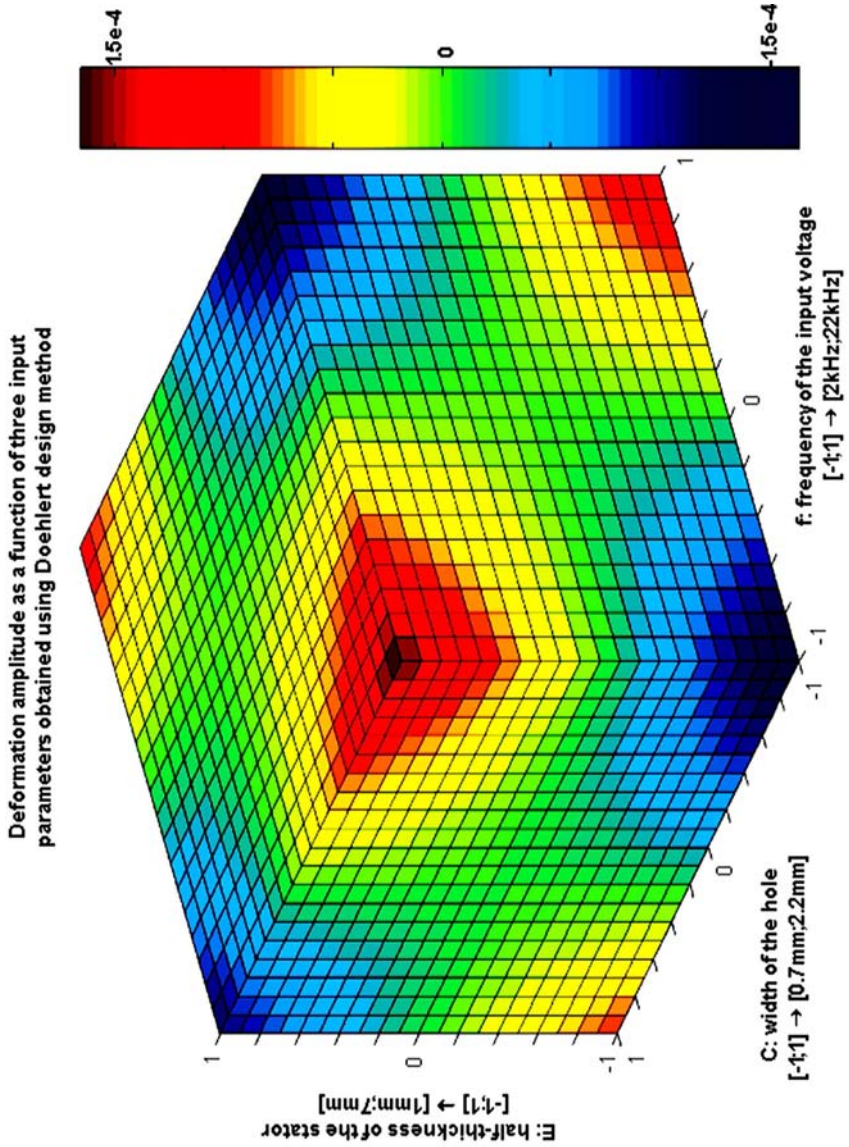


Fig. 7.8: Example of iso-surfaces graph for three input parameters (C, f, E) and the deformation amplitude as output value

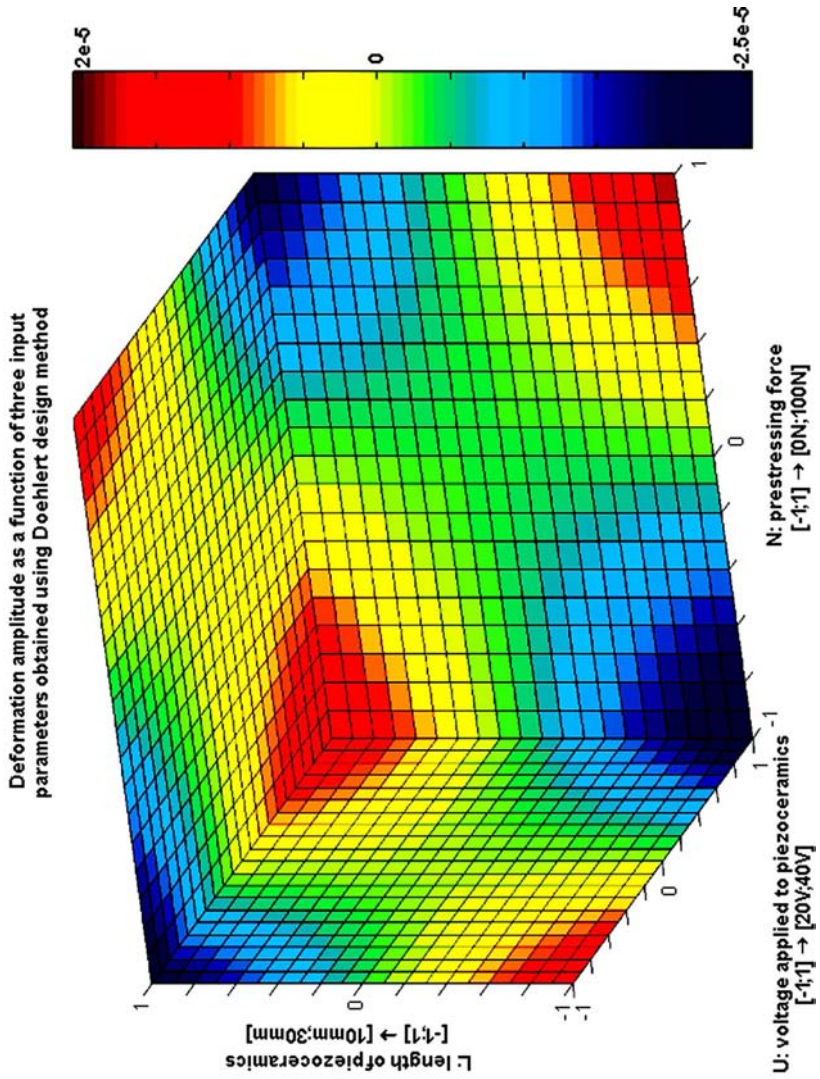


Fig. 7.9: Example of iso-surfaces graph for three input parameters (U, N, L) and the deformation amplitude as output value

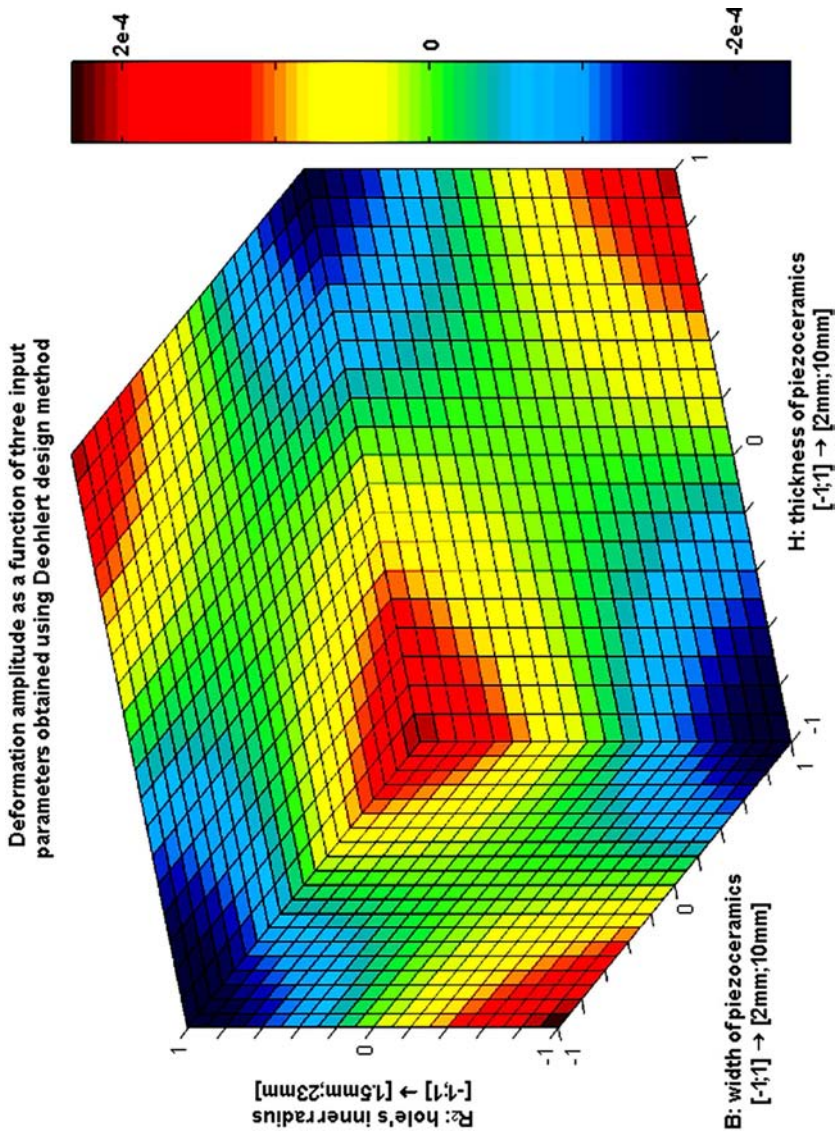


Fig. 7.10: Example of iso-surfaces graph for three input parameters (B , H , R_2) and the deformation amplitude as output value

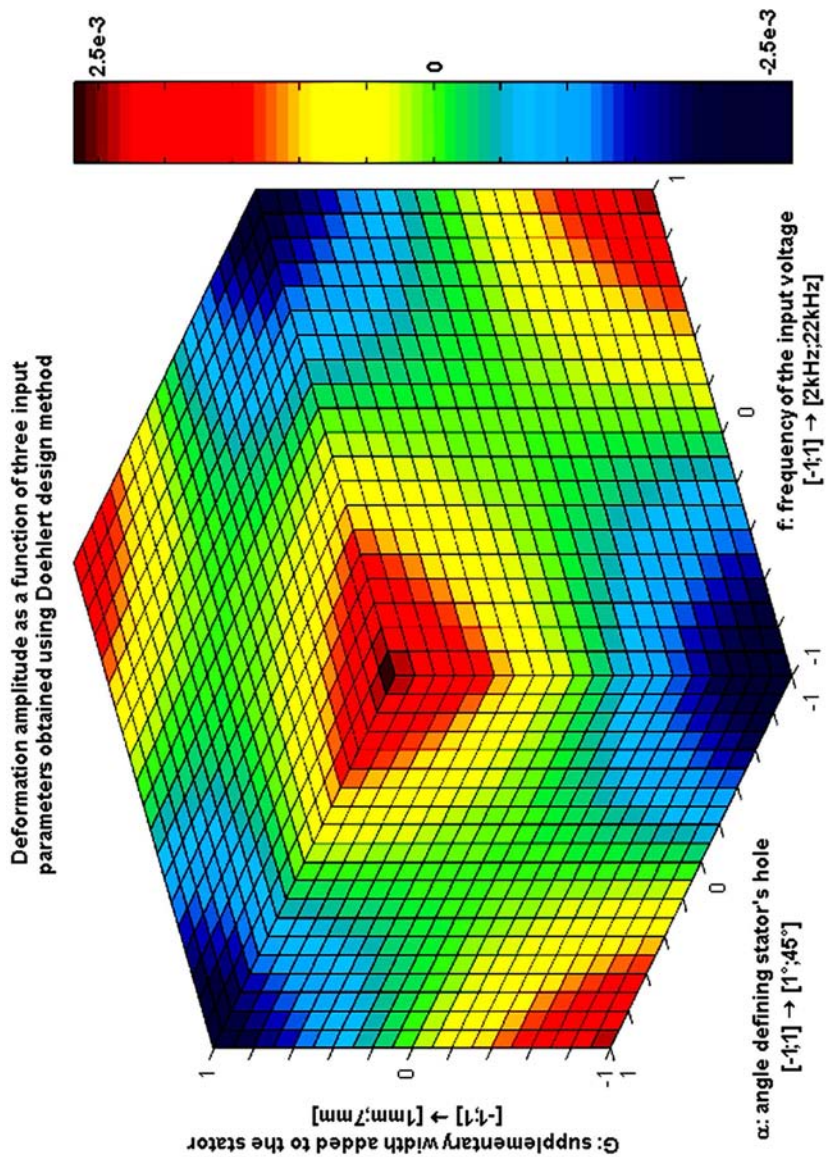


Fig. 7.11: Example of iso-surfaces graph for three input parameters (α , f , G) and the deformation amplitude as output value

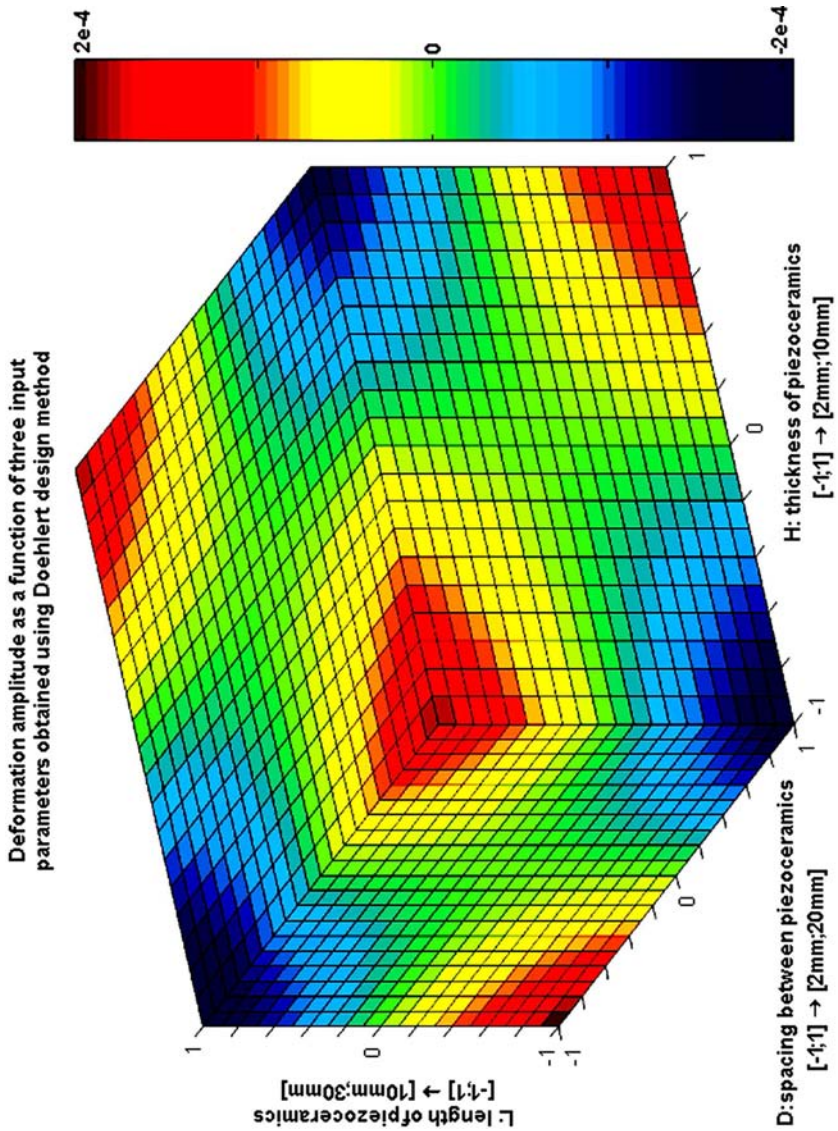


Fig. 7.12: Example of iso-surfaces graph for three input parameters (D, H, L) and the deformation amplitude as output value

Appendix C

MINISWYS motor: piezoceramic properties

Material data of the used PZT807 ceramic from Morgan Electro Ceramics company.

$$\text{Density: } \rho = 7800 \text{ kg/m}^3.$$

Stiffness matrix:

$$c^E = \begin{bmatrix} 9.1 & 3.2 & 3.7 & 0 & 0 & 0 \\ & 9.1 & 2.7 & 0 & 0 & 0 \\ & & 7.7 & 0 & 0 & 0 \\ & & & 2.9 & 0 & 0 \\ & & & & 3.5 & 0 \\ & & & & & 3.5 \end{bmatrix} \cdot 10^{10} \text{ N/m}^2.$$

Piezoelectric constants:

$$e = \begin{bmatrix} 0 & 0 & 0 & 0 & 27.8 & 0 \\ 0 & 0 & 0 & 27.8 & 0 & 0 \\ -90.9 & -90.9 & 37.0 & 0 & 0 & 0 \end{bmatrix} \text{ As/m}^2.$$

Dielectric constants:

$$\varepsilon^S = \begin{bmatrix} 8.41 & 0 & 0 \\ 0 & 8.41 & 0 \\ 0 & 0 & 8.41 \end{bmatrix} \cdot 10^{-9} \text{ As/Vm}.$$

Appendix D

MINISWYS motor: structures analysis

Initial structure



Fig. 7.13: MUM initial structure: numerical model

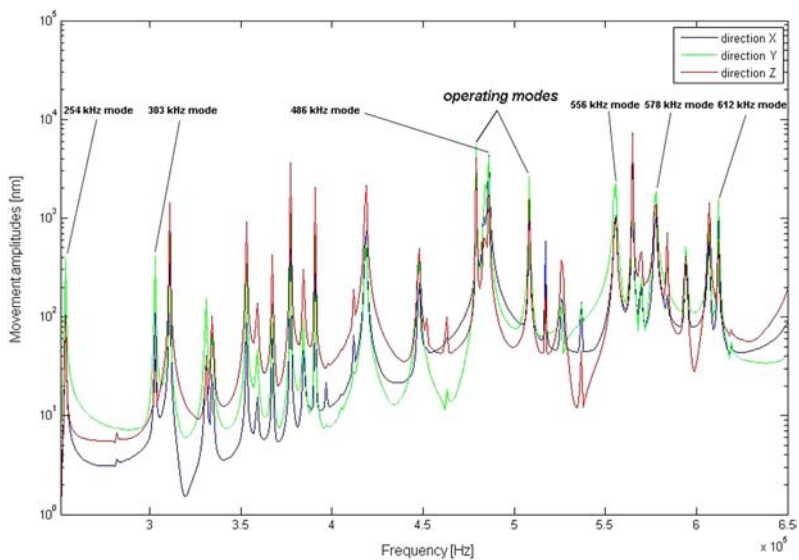


Fig. 7.14: MUM initial structure: movement amplitudes in the three directions

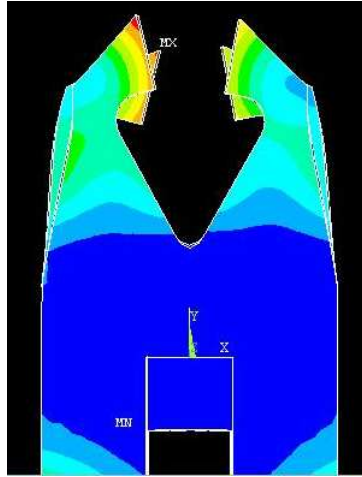


Fig. 7.15: MUM initial structure: 254 kHz mode

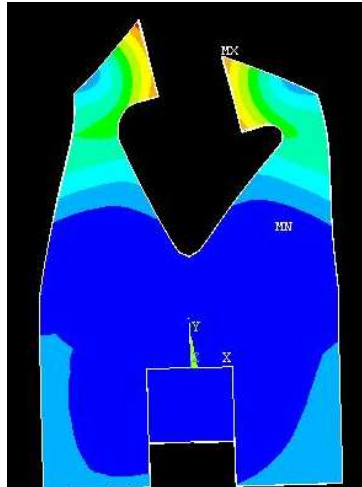


Fig. 7.16: MUM initial structure: 303 kHz mode

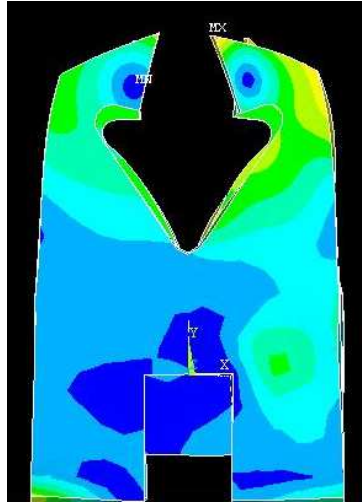


Fig. 7.17: MUM initial structure: 486kHz mode

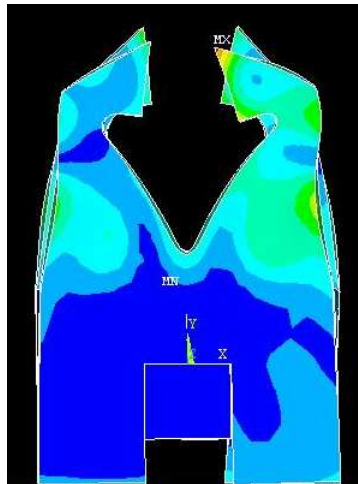


Fig. 7.18: MUM initial structure: 556kHz mode



Fig. 7.19: MUM initial structure: 578kHz mode

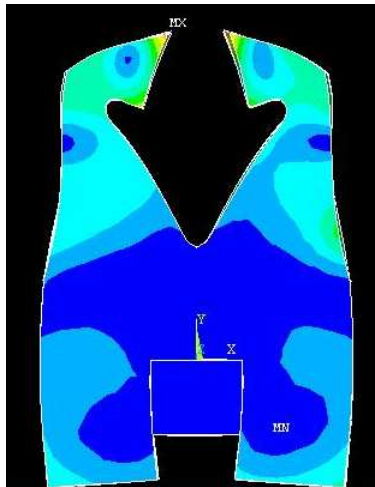


Fig. 7.20: MUM initial structure: 612kHz mode

Structure without "feet"

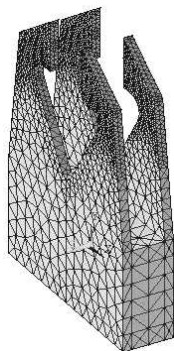


Fig. 7.21: Structure without "feet": numerical model

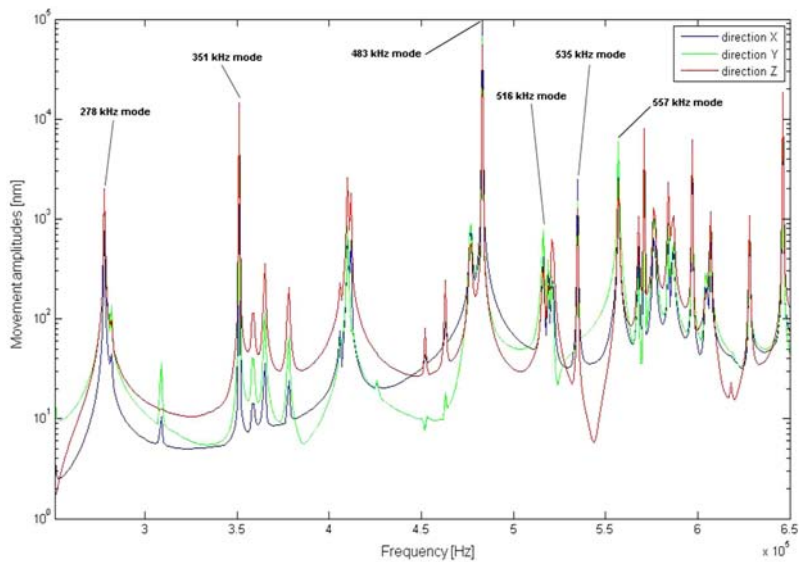


Fig. 7.22: Structure without "feet": movement amplitudes in the three directions

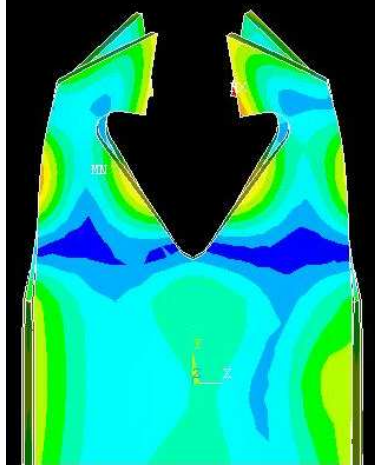


Fig. 7.23: Structure without "feet": 278 kHz mode

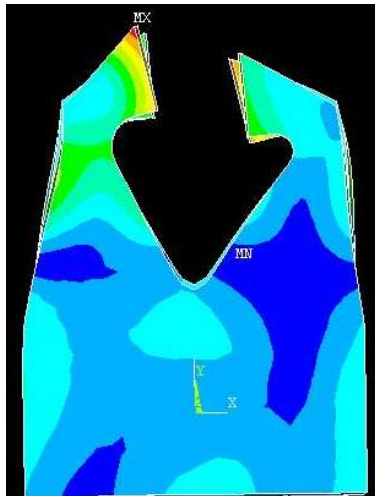


Fig. 7.24: Structure without "feet": 351 kHz mode

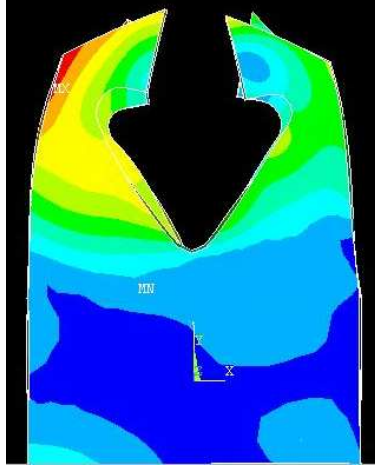


Fig. 7.25: Structure without "feet": 483 kHz mode

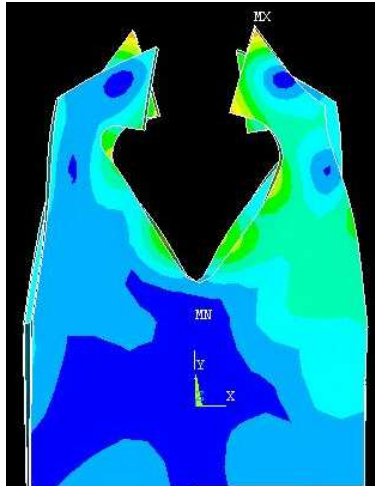


Fig. 7.26: Structure without "feet": 516 kHz mode

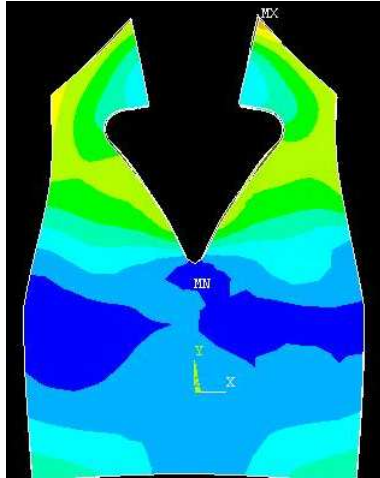


Fig. 7.27: Structure without "feet": 535 kHz mode

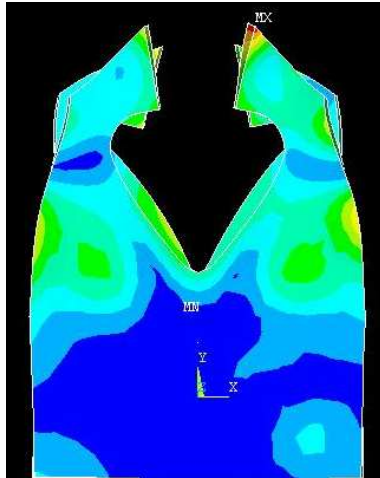


Fig. 7.28: Structure without "feet": 557 kHz mode

Half structure in z direction

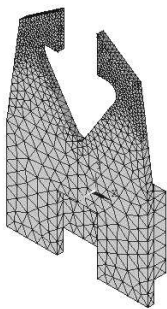


Fig. 7.29: Half structure in z direction: numerical model

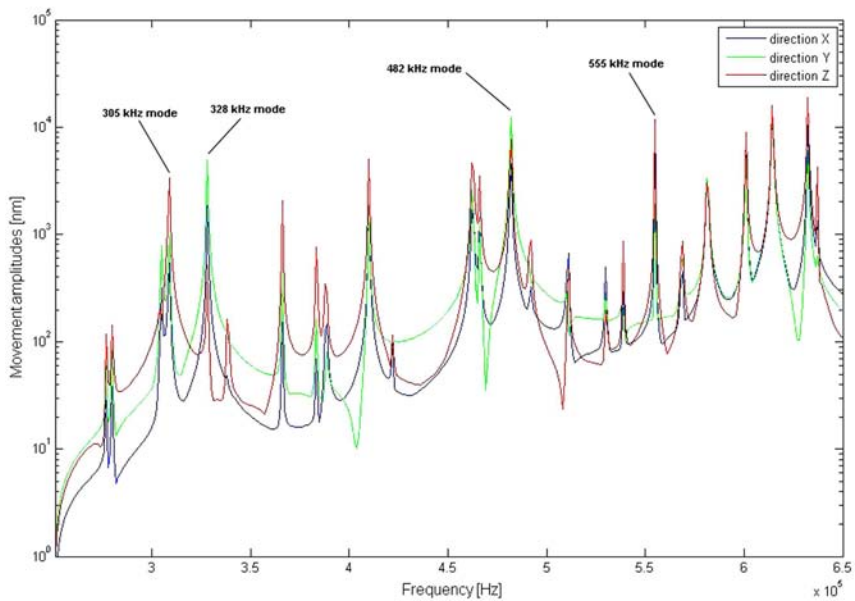


Fig. 7.30: Half structure in z direction: movement amplitudes in the three directions

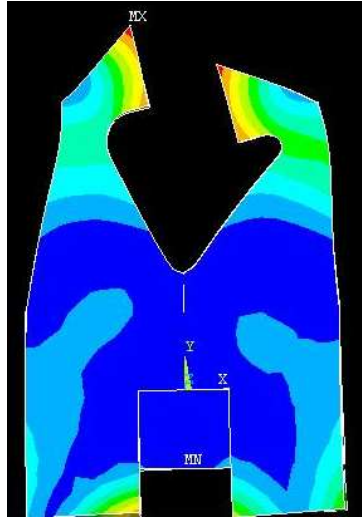


Fig. 7.31: Half structure in z direction: 305kHz mode

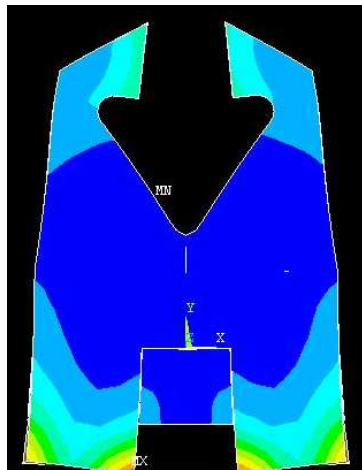


Fig. 7.32: Half structure in z direction: 328kHz mode

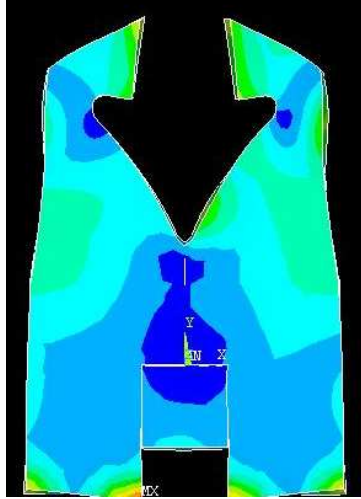


Fig. 7.33: Half structure in z direction: 482kHz mode

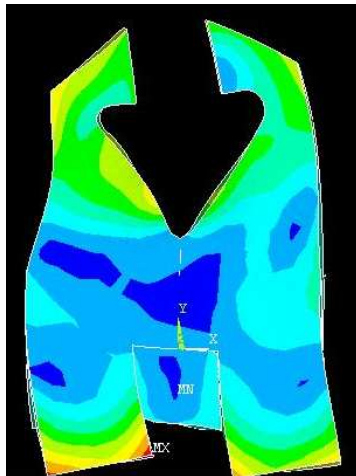


Fig. 7.34: Half structure in z direction: 555kHz mode

Half structure in x direction

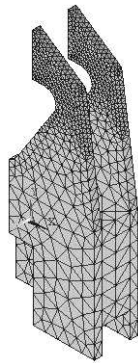


Fig. 7.35: Half structure in x direction: numerical model

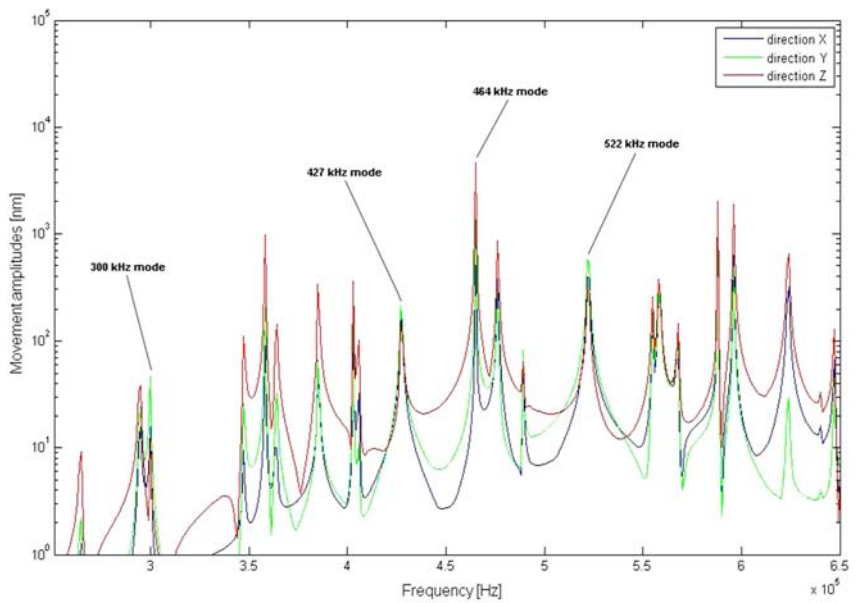


Fig. 7.36: Half structure in x direction: movement amplitudes in the three directions

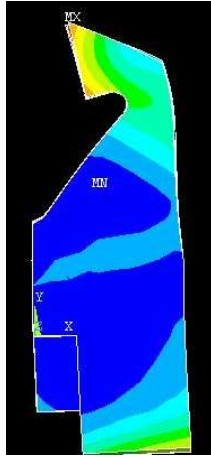


Fig. 7.37: Half structure in x direction: 300kHz mode

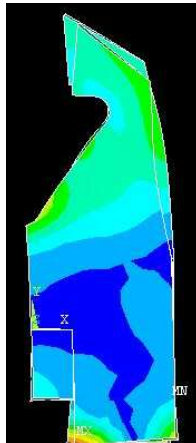


Fig. 7.38: Half structure in x direction: 427kHz mode

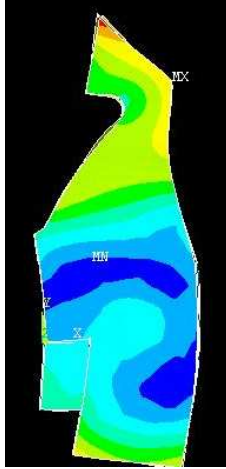


Fig. 7.39: Half structure in x direction: 464kHz mode

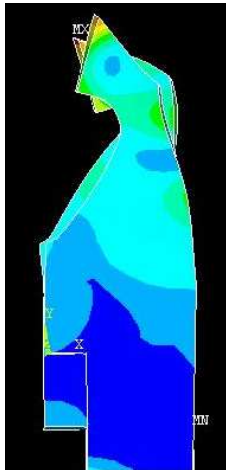


Fig. 7.40: Half structure in x direction: 522kHz mode

Structure with straight lines

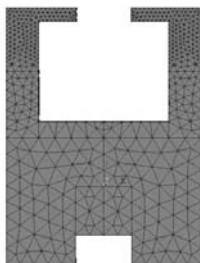


Fig. 7.41: Structure with straight lines: numerical model

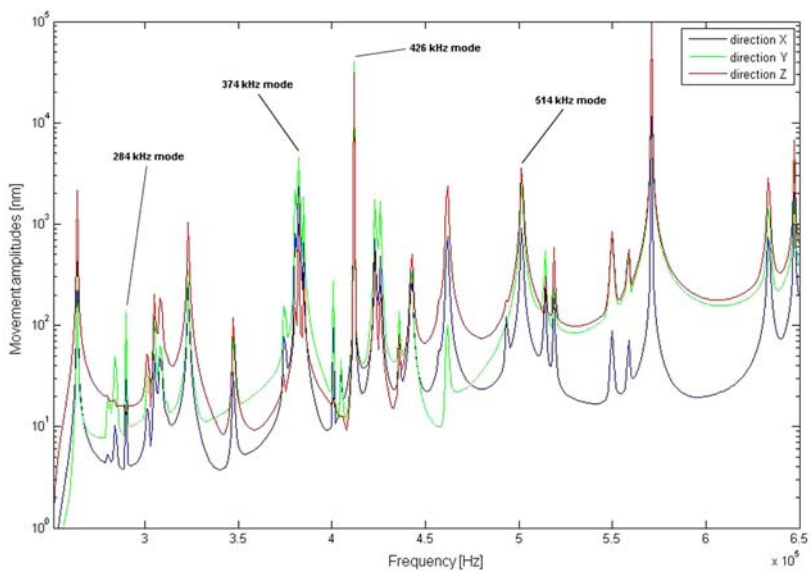


Fig. 7.42: Structure with straight lines: movement amplitudes in the three directions

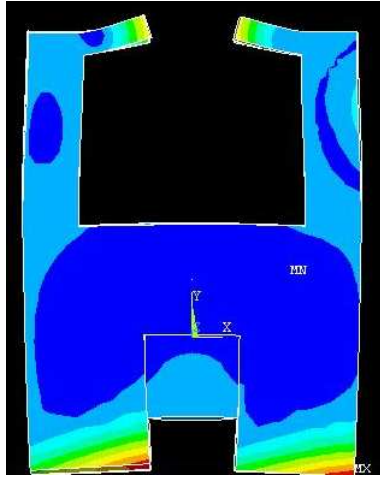


Fig. 7.43: Structure with straight lines: 284kHz mode

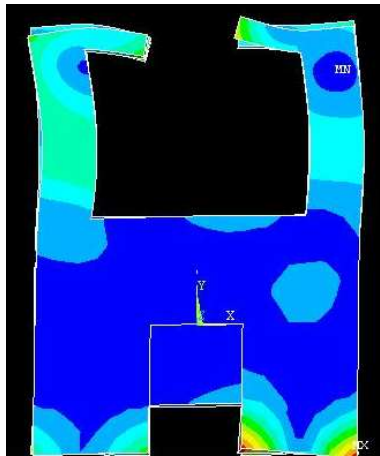


Fig. 7.44: Structure with straight lines: 374kHz mode



Fig. 7.45: Structure with straight lines: 426kHz mode

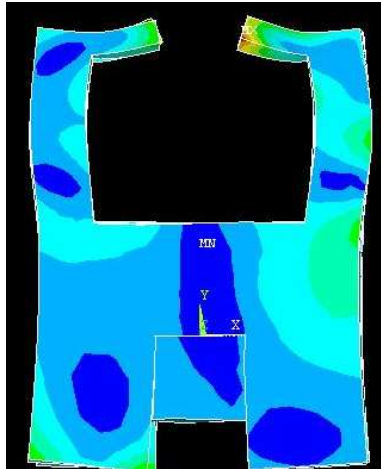


Fig. 7.46: Structure with straight lines: 514kHz mode

Appendix E

Noliac Rosen type piezoelectric transformer

Dimensions and cross section (input part) of the Noliac Rosen type PT:

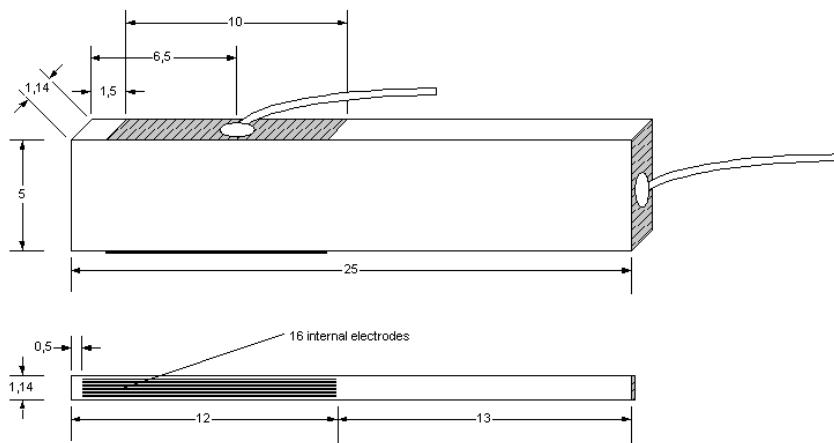


Fig. 7.47: Dimensions of the Noliac Rosen type PT

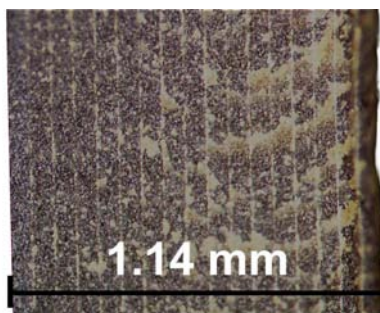


Fig. 7.48: Cross section of the input part of the Noliac Rosen type PT

Material properties of the Noliac Rosen type PT:

$$\text{Density: } \rho = 7600 \text{ kg/m}^3.$$

Stiffness matrix:

$$c^E = \begin{bmatrix} 14.1 & 8.06 & 7.87 & 0 & 0 & 0 \\ & 14.1 & 7.87 & 0 & 0 & 0 \\ & & 11.8 & 0 & 0 & 0 \\ & & & 2.11 & 0 & 0 \\ & & & & 2.11 & 0 \\ & & & & & 3.04 \end{bmatrix} \cdot 10^{10} \text{ N/m}^2.$$

Piezoelectric constants:

$$e = \begin{bmatrix} 0 & 0 & 0 & 0 & 13.3 & 0 \\ 0 & 0 & 0 & 13.3 & 0 & 0 \\ -5.16 & -5.16 & 15.5 & 0 & 0 & 0 \end{bmatrix} \text{ As/m}^2.$$

Dielectric constants:

$$\epsilon^S = \begin{bmatrix} 7.26 & 0 & 0 \\ 0 & 7.26 & 0 \\ 0 & 0 & 6.72 \end{bmatrix} \cdot 10^{-9} \text{ As/Vm}.$$

Data sheet of the Noliac Rosen type PT:

CMT/HDE/A/25/5/1.3/1.5

Noliac Rosen-type Transformer



Features

- Multilayer piezo ceramic transformer
- High conversion efficiency
- Low EMI radiation
- Low profile planar construction
- No fire hazard
- Inherent safety for an electrical short in the secondary

Application

- Backlight inverter for CCFL

SPECIFICATION (Typical)

	Typical Specification	Remark (Test Condition)
Resonant Frequency ¹⁾ [kHz]	132	RL = 200kΩ , Vin = 1Vrms
Static Input Capacitance [nF]	140	1 kHz , Vin = 1Vrms , 25°C
Static Output Capacitance [pF]	5.5	
Voltage Transfer Ratio ²⁾	105	RL = 200kΩ , Vin = 1Vrms
Output Power ²⁾ [W]	1.5	Sinusoidal input, RL = 100kΩ ~ 300kΩ
Dimension (L×w×t) [mm]	25×5×1.3	
Test Load [kΩ]	200	
Type	Rosen	
Size of LCD Panel Applicable	3.5" ~ 5"	
Application	PDA	

Notes

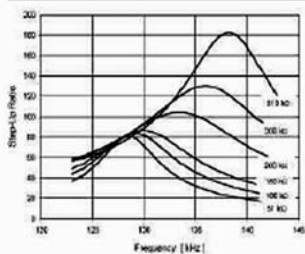
- 1), 2) Resonant frequency and voltage transfer ratio vary with load resistance.
Measured at the given test load in the table.



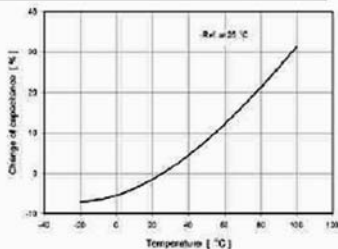
Noliac Rosen-type Transformer

OUTPUT CHARACTERISTICS

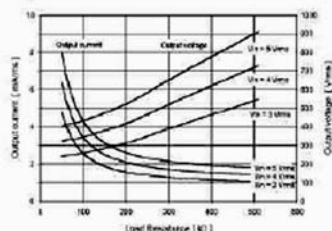
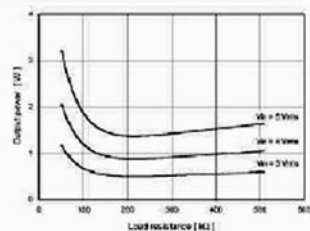
Frequency characteristic of output voltage



Change of capacitance with temperature



Output characteristic



This specification might be subject to changes without prior notice.



Hejreskovvej 18 DK-3490 Kvistgaard
 Phone +45 4912 5030 Fax +45 4912 5031
 Web www.noliac.com

Appendix F

Transoner Rosen type piezoelectric transformer

Dimensions of the Transoner Rosen type PT:

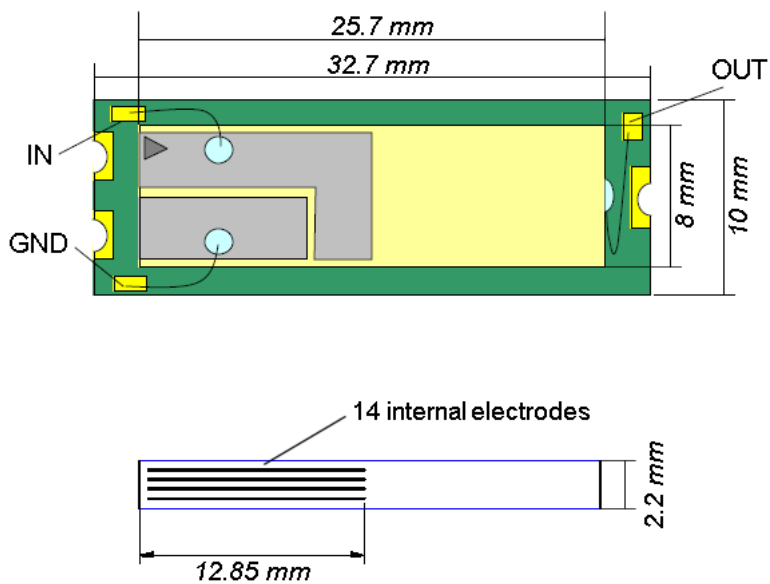


Fig. 7.51: Dimensions of the Transoner Rosen type PT

Material properties of the Transoner Rosen and radial mode type PTs:

$$\text{Density: } \rho = 7600 \text{ kg/m}^3.$$

Stiffness matrix:

$$c^E = \begin{bmatrix} 11.13 & 4.48 & 3.76 & 0 & 0 & 0 \\ & 11.13 & 3.76 & 0 & 0 & 0 \\ & & 9.12 & 0 & 0 & 0 \\ & & & 3.32 & 0 & 0 \\ & & & & 2.81 & 0 \\ & & & & & 2.81 \end{bmatrix} \cdot 10^{10} \text{ N/m}^2.$$

Piezoelectric constants:

$$e = \begin{bmatrix} 0 & 0 & 0 & 0 & 9.27 & 0 \\ 0 & 0 & 0 & 9.27 & 0 & 0 \\ -6.61 & -6.61 & 13.25 & 0 & 0 & 0 \end{bmatrix} \text{ As/m}^2.$$

Dielectric constants:

$$\epsilon^S = \begin{bmatrix} 8.36 & 0 & 0 \\ 0 & 8.36 & 0 \\ 0 & 0 & 4.59 \end{bmatrix} \cdot 10^{-9} \text{ As/Vm}.$$

Data sheet of the Transoner Rosen type PT:



Face Electronics, LC

427 W. 35th St. - Norfolk, VA 23508 USA - 757.624.2121 - Fax 757.624.2128 - www.faceco.com

Data Sheet for NA2508A – Rosen type PT

Description: High Voltage Rosen-type PT for 5W

Parameter	Value	Notes
Rating Output Power	5W	$R_L = 100\text{ k}\Omega$
Dimensions of the PT	$25.5^L \times 8.0^W \times 2.2^T\text{ mm}$	
Resonant mode	$\lambda / 2$ mode	
Resonant frequency	$63\text{ kHz} \pm 10\%$	$R_L = 100\text{ k}\Omega$
Primary Capacitance	$170\text{ nF} \pm 10\%$	1 kHz, Input 1V, 20°C
Secondary Capacitance	$20\text{ pF} \pm 10\%$	1 kHz, Input 1V, 20°C
Open Output Voltage	Over 1500 V	$R_L = 10\text{ M}\Omega$
Operating Temperature	0 ~ 50°C	

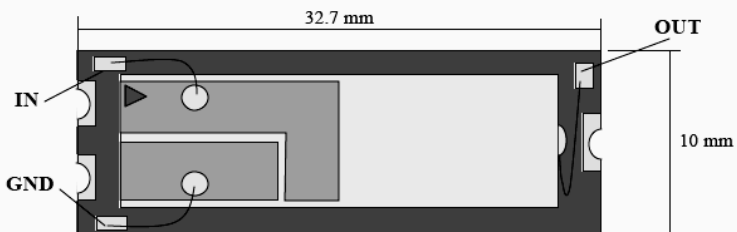
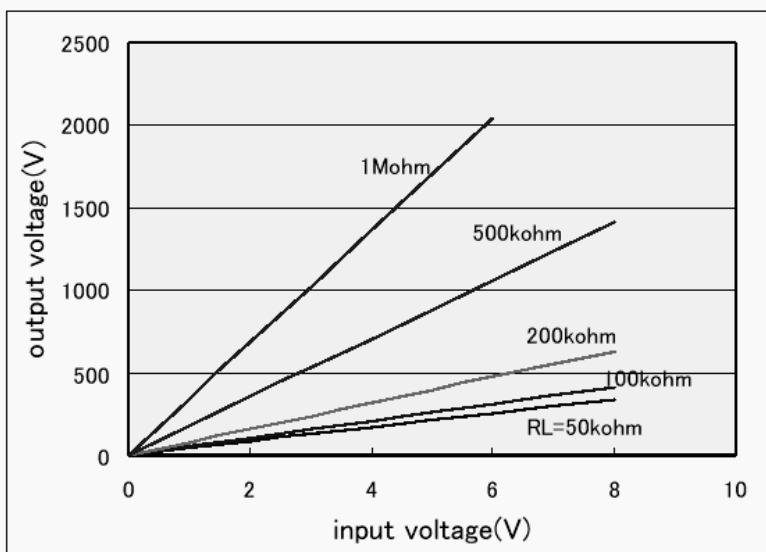
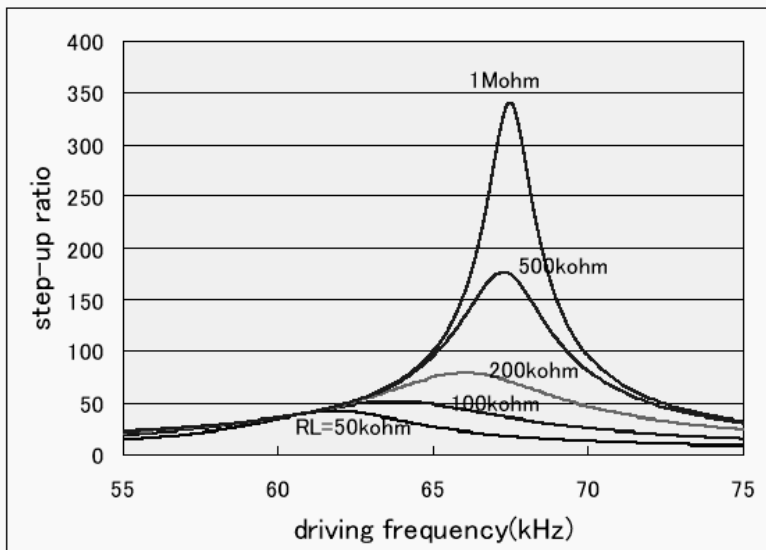


Figure 1. Dimensions including the supporting PCB

Data sheet of the Transoner Rosen type PT:

1. Electrical Characteristics



Data sheet of the Transoner Rosen type PT:

2. Equivalent Circuit

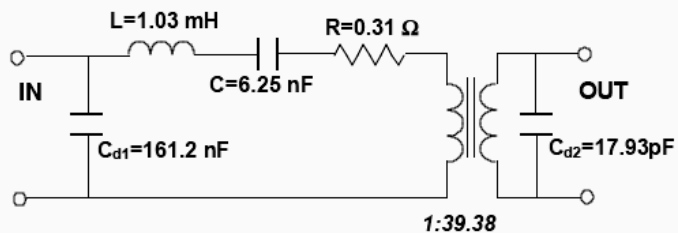
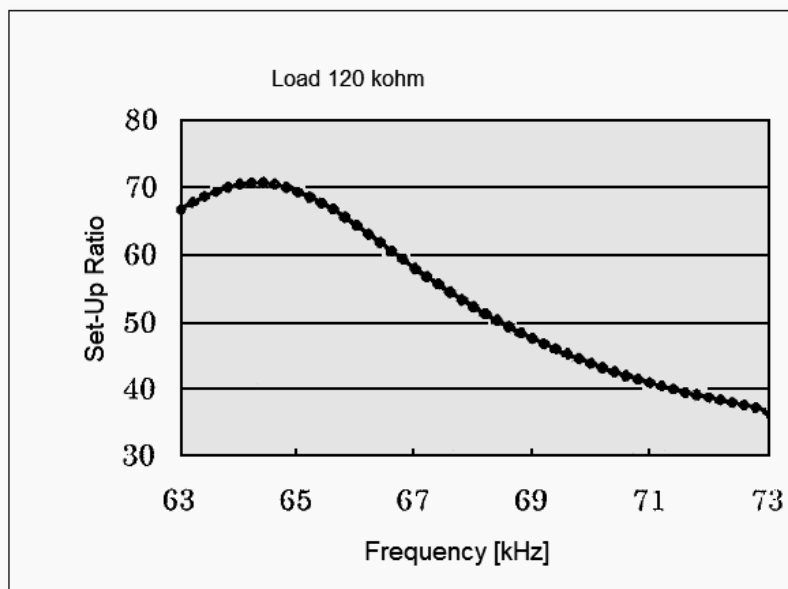
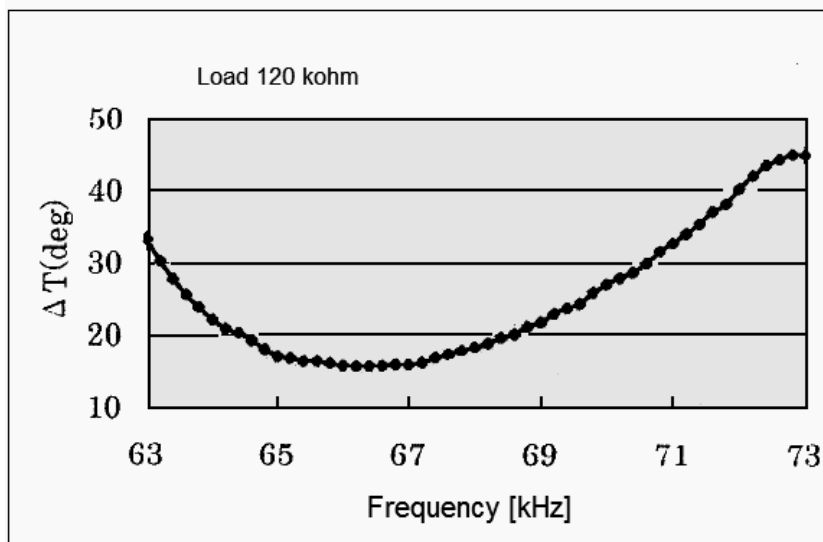
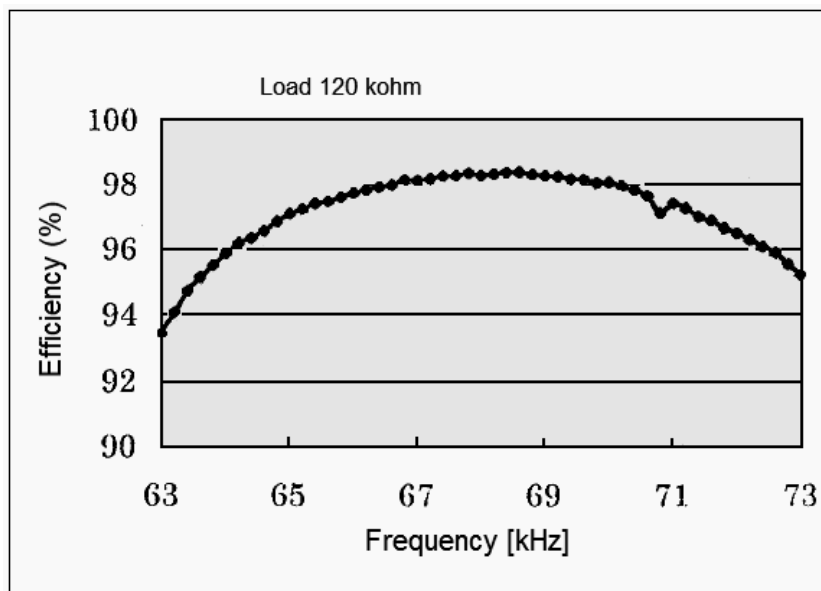


Figure 2. Equivalent circuit for the NA2508A PT. The equivalences were made using HP Impedance Analyzer 4194A under 1 Vpp input AC voltage.

3. Characteristics measured at $P_{out}=5W$ under 120 kohm load



Data sheet of the Transoner Rosen type PT:



Appendix G

Transoner radial mode type PT

Dimensions of the Transoner radial mode type PT:

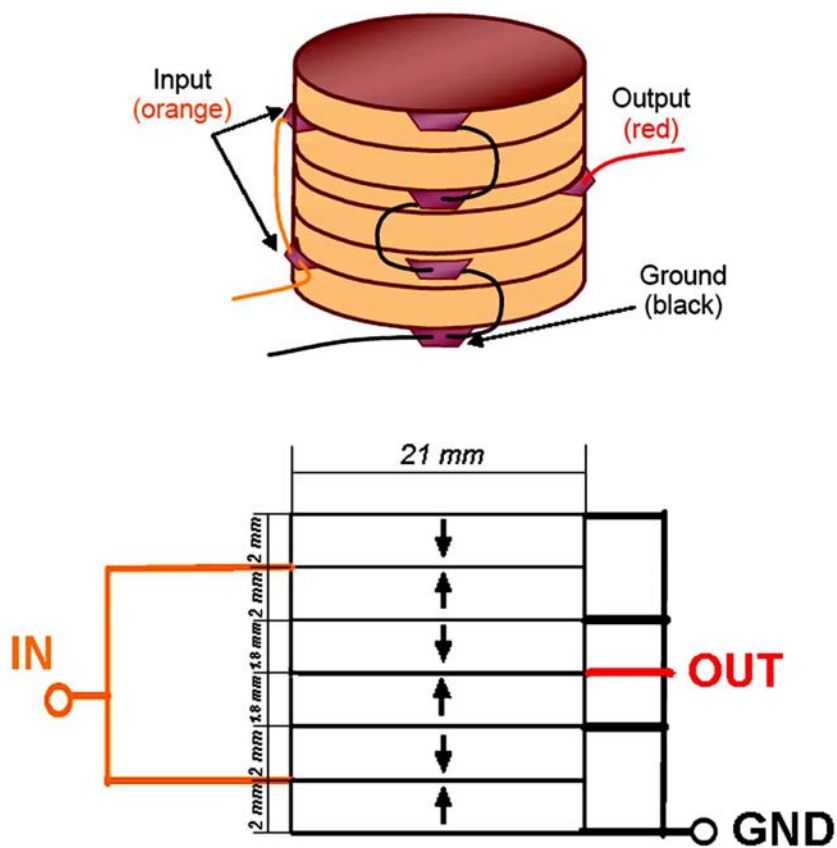


Fig. 7.56: Dimensions of the Transoner radial type PT

Data sheet of the Transoner radial mode type PT:



Face Electronics, LC

427 W. 35th St. • Norfolk, VA 23508 USA • 757.624.2121 • Fax 757.624.2128 • www.faceco.com

Transoner® Data Sheet

Date of Testing: 14-March-2005

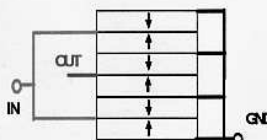
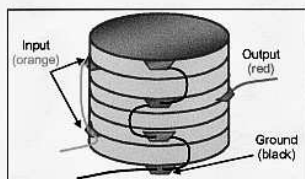
Transoner I.D.:05TR-001

Description: Transoner T6 non-isolated

Product Dimensions			
	Inches	mm	
Diameter PZT	0.825	20.955	
Input Thick. PZT	0.080	2.032	
Out. Thick. PZT	0.07	1.778	
Input layers			4
Output Layers			2
Total Mass with wires			33.67g

Typical measures at R=500Ω (Measurement Method: Power @ 20 W)	
Input Voltage (Vrms)	55
Output Voltage (Vrms)	102
Output Power (W)	20
Max. Efficiency Load (Ω)	500
Operation frequency at 500Ω (kHz)	96.5
Efficiency (%)	96-97
Temperature increase	27

Maximum ratings	
Maximum output Power peak for 2 min	45 W
Max. admissible T increase	35-40C



NOTE:

- 1) Avoid operating the Transoner at high power on hard surfaces because this will cause the Transoner to interact mechanically with the surface (chatter and bounce).
- 2) Use appropriate electrical safety precautions when operating/testing Transoner.
- 3) Maximum temperature of the sample should not exceed 35-40 degrees temperature increase, and no more than 125 C absolute body temperature (including environment temperature).
- 4) The maximum power rating should not be exceeded for more than approx. 2 minutes.

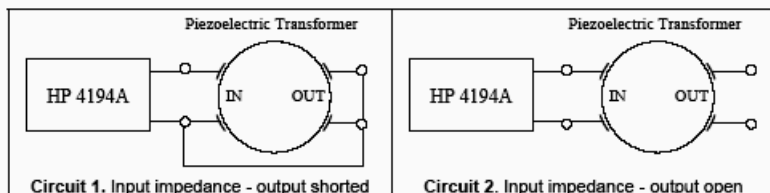
Transoner® is protected under US Patent 5,834,882 and other patents and pending patents.

Data sheet of the Transoner radial mode type PT:

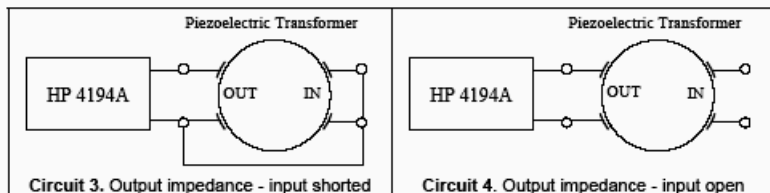
DATA SHEET

1. Test Circuits

- A. Input impedance measurements under output open-circuit conditions (Circuit 1) and output short-circuit conditions (Circuit 2):



- B. Output impedance measurements under input open-circuit conditions (Circuit 1) and input short-circuit conditions (Circuit 2):



2. Equivalent Circuit

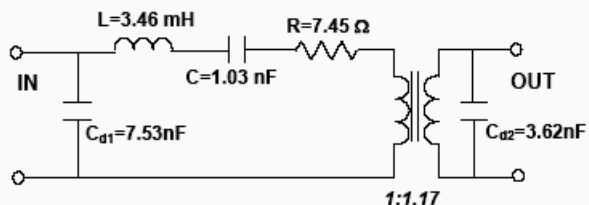


Figure 1. Equivalent circuit of T6 non-isolated TRANSONER # 04TR32. The equivalences were made using HP Impedance Analyzer 4194A under 1 Vpp input AC voltage.

Data sheet of the Transoner radial mode type PT:

3. Input and output impedance spectrum around operating resonance frequency

3.1. Input impedance (Circuits 1 & 2)

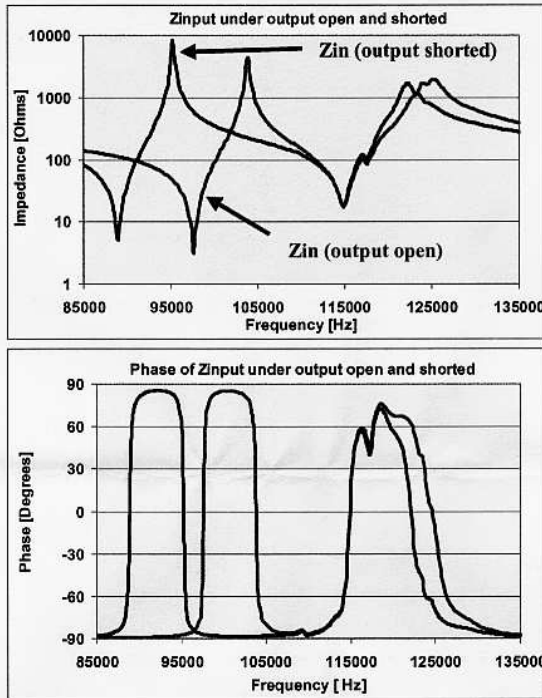


Figure 2. Input impedance-Phase vs. frequency. Measurements were taken with the HP4194A Impedance Analyzer at 1Vpp input AC voltage.

Input Impedance under output open				
fr=97647 Hz	Rr=3.16 Ω	fa=103855 Hz	Ra=4.48 kΩ	Cin (1 kHz) = 8.214 nF
Input Impedance under output shorted				
fr=88965 Hz	Rr=5.21 Ω	fa=95244 Hz	Ra=8.26 kΩ	Cin (1 kHz) = 8.261 nF

Data sheet of the Transoner radial mode type PT:

3.2. Output impedance (Circuits 3 & 4)

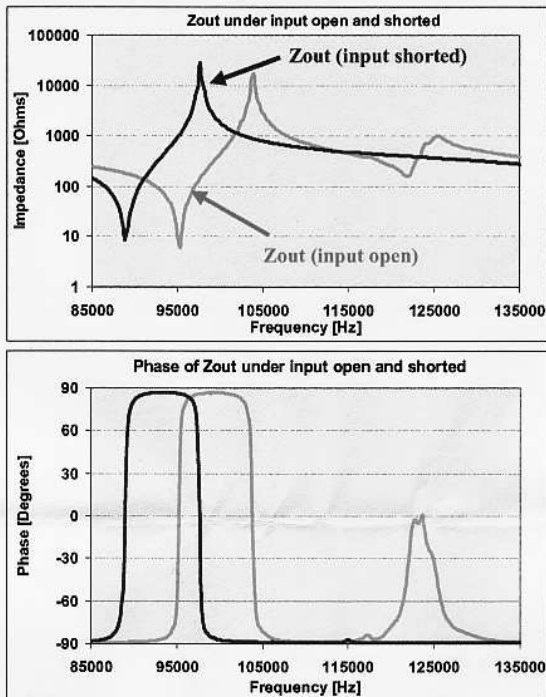


Figure 3. Output impedance-Phase vs. frequency. Measurements were taken with the HP4194A Impedance Analyzer at 1Vpp input AC voltage.

Output Impedance under input open				
fr=95244 Hz	Rr=6.02 Ω	fa=103855 Hz	Ra=17.53 kΩ	Cout (1 kHz) = 4.38 nF
Output Impedance under input shorted				
fr=88965 Hz	Rr=8.41 Ω	fa=97647 Hz	Ra=28.14 kΩ	Cout (1 kHz) = 4.41 nF

Data sheet of the Transoner radial mode type PT:

3.2. Input and output impedance under short-circuit conditions (Circuits 1 & 3)

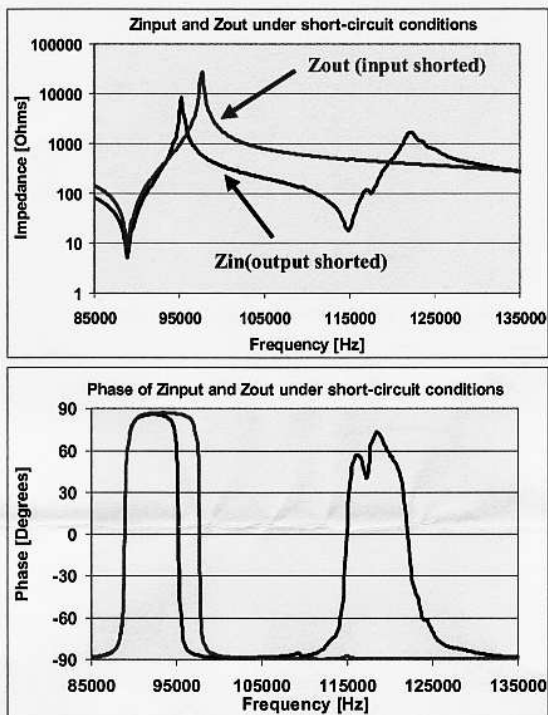


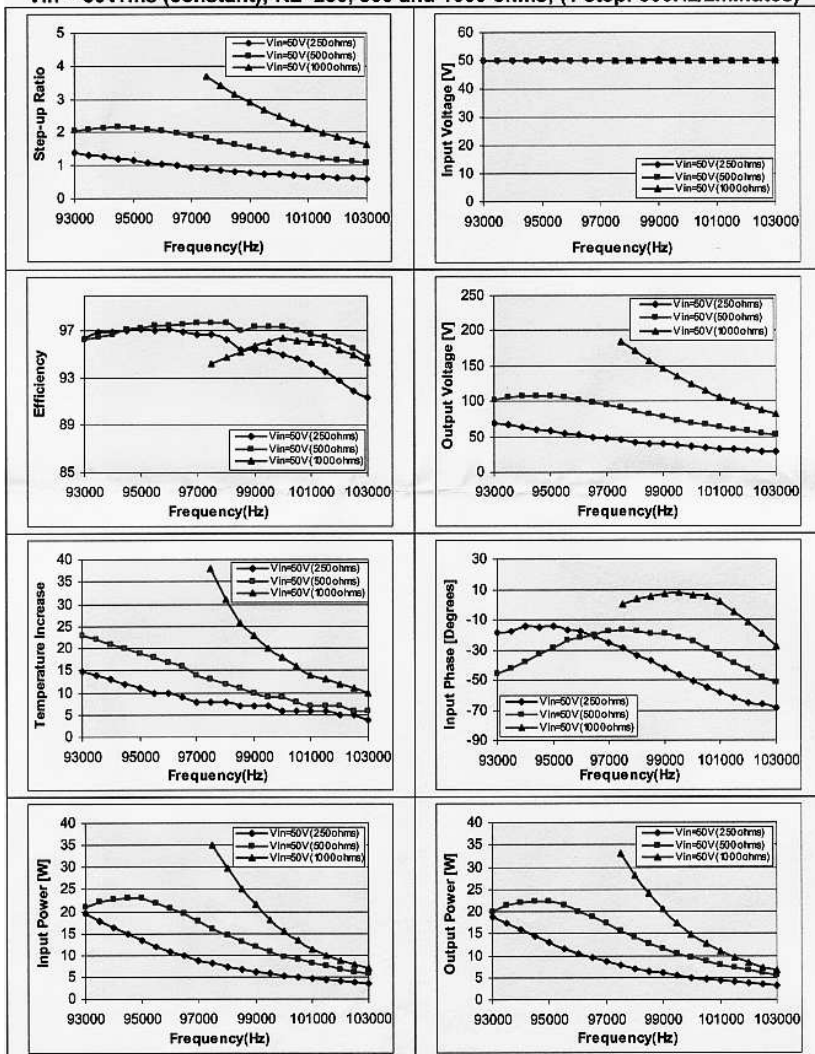
Figure 4. Input and output impedance-Phase under short circuit conditions vs. frequency. Measurements were taken with the HP4194A Impedance Analyzer at 1Vpp input having the output short-circuited to ground.

Input Impedance under output open				
fr=97647 Hz	Rr=3.16 Ω	fa=103855 Hz	Ra=4.48 kΩ	Cin (1 kHz) = 8.214 nF
Input Impedance under output shorted				
fr=88965 Hz	Rr=5.21 Ω	fa=95244 Hz	Ra=8.26 kΩ	Cin (1 kHz) = 8.261 nF
Output Impedance under input open				
fr=95244 Hz	Rr=6.02 Ω	fa=103855 Hz	Ra=17.53 kΩ	Cout (1 kHz) = 4.38 nF
Output Impedance under input shorted				
fr=88965 Hz	Rr=8.41 Ω	fa=97647 Hz	Ra=28.14 kΩ	Cout (1 kHz) = 4.41 nF

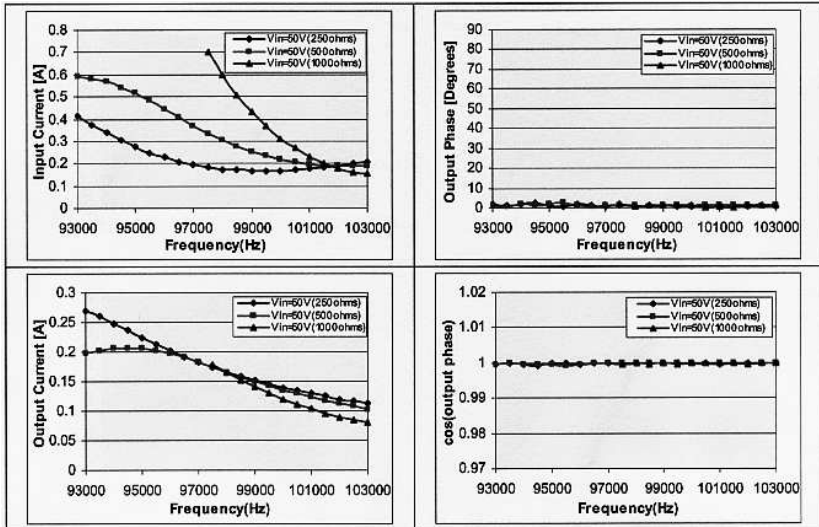
Data sheet of the Transoner radial mode type PT:

6. Power Tests at input voltage constant

$V_{in} = 50V_{rms}$ (constant); $R_L=250, 500$ and 1000 ohms; (1 step: 500Hz/2minutes)



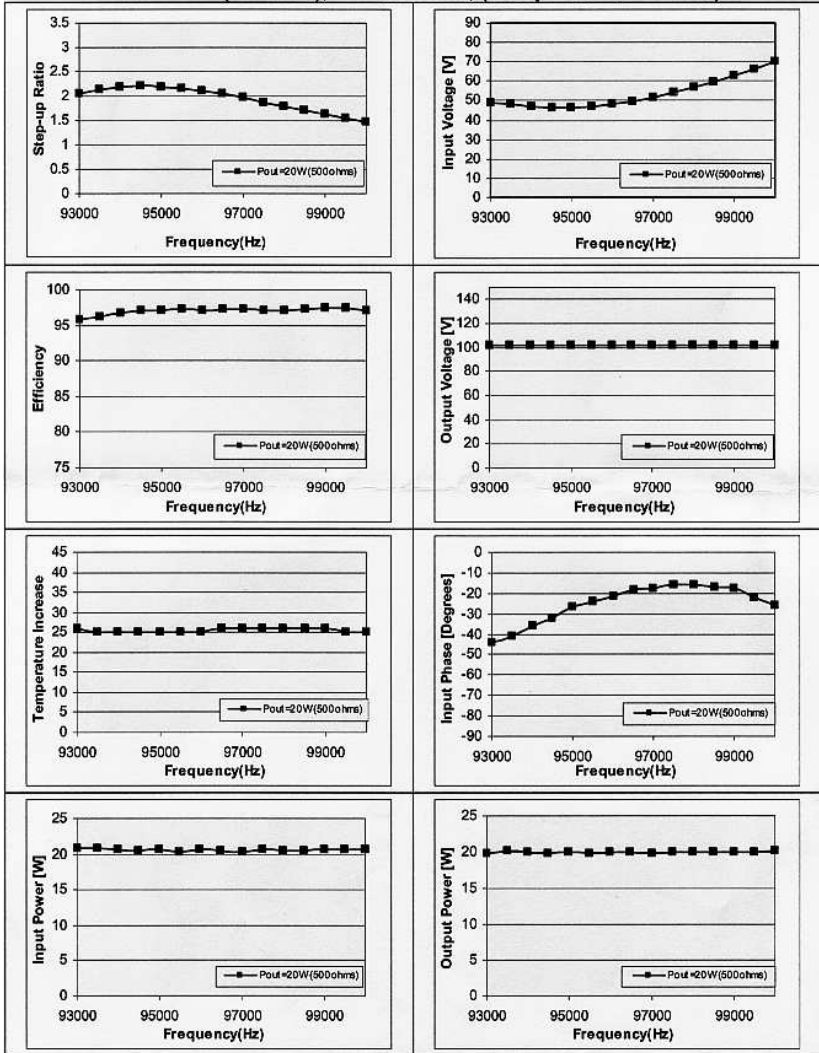
Data sheet of the Transoner radial mode type PT:



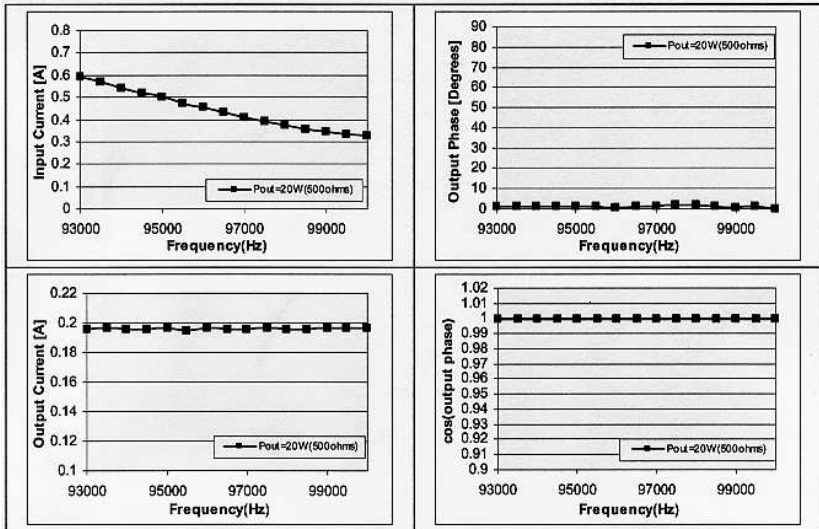
Data sheet of the Transoner radial mode type PT:

7. Power Tests at output power constant

Pout = 20W (constant); RL=500 ohms; (1 step: 500Hz/2minutes)



Data sheet of the Transoner radial mode type PT:



CURRICULUM VITAE

Personal Data

José FERNANDEZ	Ch. de Boisy 18
Nationality: Spanish	CH-1004 Lausanne / VD
Date of birth: September 14 th , 1977	Phone: +41 / 79 679.41.05
Place of birth: Lausanne, Switzerland	jose.fernandezlopez@epfl.ch

Research Activities

Modeling and Optimization of Ultrasonic Motors and Piezoelectric Transformers

Education

2002–to date	Research Assistant at the Integrated Actuators Laboratory (LAI) of the Swiss Federal Institute of Technology in Lausanne (EPFL) Responsible of supporting ANSYS software for EPFL users as well as co-organizing related courses within the school Author of 9 scientific publications
1996–2002	Swiss Federal Institute of Technology in Lausanne (EPFL) Main research projects: - Piezoelectric micro-transducer - Study of antennas applicable to networks with solar cells - Parametrization and validation of an equivalent mechanical model for a piezoelectric motor Degree: Dipl. Ing. EPFL
1993–1996	Senior High School, Lausanne Degree: Matura Typus C

Languages

French, Spanish	Mother tongues
English	Fluent
German, Italian	Good knowledge